Topics in Applied Physics
Volume 81

Available Online

Topics in Applied Physics is part of the Springer LINK service. For all customers with standing orders for Topics in Applied Physics we offer the full text in electronic form via LINK free of charge. Please contact your librarian who can receive a password for free access to the full articles by registration at:

http://link.springer.de/orders/index.htm

If you do not have a standing order you can nevertheless browse through the table of contents of the volumes and the abstracts of each article at:

http://link.springer.de/series/tap/

There you will also find more information about the series.

Springer
Berlin
Heidelberg
New York
Barcelona
Hong Kong
London
Milan
Paris
Singapore
Tokyo

Topics in Applied Physics

Topics in Applied Physics is a well-established series of review books, each of which presents a comprehensive survey of a selected topic within the broad area of applied physics. Edited and written by leading research scientists in the field concerned, each volume contains review contributions covering the various aspects of the topic. Together these provide an overview of the state of the art in the respective field, extending from an introduction to the subject right up to the frontiers of contemporary research.
Topics in Applied Physics is addressed to all scientists at universities and in industry who wish to obtain an overview and to keep abreast of advances in applied physics. The series also provides easy but comprehensive access to the fields for newcomers starting research.
Contributions are specially commissioned. The Managing Editors are open to any suggestions for topics coming from the community of applied physicists no matter what the field and encourage prospective editors to approach them with ideas.
See also: http://www.springer.de/phys/books/tap/

Satoshi Kawata (Ed.)

Near-Field Optics and Surface Plasmon Polaritons

With 136 Figures

Springer

Prof. Satoshi Kawata (Ed.)
Department of Applied Physics
Osaka University
Suita, Osaka 565-0871
Japan
kawata@ap.eng.osaka-u.ac.jp

Library of Congress Cataloging-in-Publication Data

Near-field optics and surface plasmon polaritons / Satoshi Kawata (ed.).
p. cm. -- (Topics in applied physics, ISSN 0303-4216 ; v. 81)
Includes bibliographical references and index.
ISBN 3540415025 (alk. paper)
1. Polaritons. 2. Plasmons (Physics) 3. Near-field microscopy. I. Kawata, Satoshi, 1966- II. Series.

QC176.8.P6 N43 2001
530.4'16--dc21
2001017049

Physics and Astronomy Classification Scheme (PACS):
07.79.-v; 07.79.Fc; 68.37.-d; 68.37.Uv; 73.20.Mf; 87.64.Xx; 87.80.Cc

ISSN print edition: 0303-4216
ISSN electronic edition: 1437-0859
ISBN 3-540-41502-5 Springer-Verlag Berlin Heidelberg New York

Springer-Verlag Berlin Heidelberg New York
a member of BertelsmannSpringer Science+Business Media GmbH

http://www.springer.de

Printed in Germany

Typesetting: DA-TEX Gerd Blumenstein, Leipzig
Cover design: *design & production* GmbH, Heidelberg

Printed on acid-free paper SPIN: 10778948 57/3141/mf 5 4 3 2 1 0

Preface

This book aims at organizing and developing a new concept of physics and instrumentation by comparing and combining near-field optics and surface plasmon polaritons. These two physics disciplines are well known, while they are developed quite independently. The electromagnetic evanescent field (or near-field) is known as a solution of Maxwell's equations, and appeared, for example, in Isaac Newton's book "Optics" when the frustrated total internal reflection or photon tunneling between two prisms was explained. Surface plasmon polaritons are well known in solid-state physics, appearing, for example, in Charles Kittel's Introduction to Solid State Physics. These two physics disciplines have individually found significant applications in science and industry, such as a microwave directional coupler, an optical waveguide (optical fiber), a system for infrared surface analysis, a surface affinity/immunosensor, and super-resolving microscopy and surface-enhanced Raman spectroscopy.

In the 1980s I was working on two different research topics in optics, the study of confocal laser scanning microscopy for three-dimensional macroanalysis and the development of a surface plasmon sensor as a highly sensitive surface sensor, and I happened to find an article by Fischer and Pohl on the use of a scattering plasmon probe to sense the near field for near-field imaging. In addition to the super-resolving capability as a microscope, the combination of scanning microscopy and surface plasmon polaritons was, in particular, academically impressive to me. Near-field microscopy has since been getting more popular and more important for scientists as a new scientific topic in physics and also as a new advanced tool to see or modulate nanometric structures. The surface plasmon polariton has also obtained popularity as the principle in advanced immunosensors, optoelectronic devices, and spectroscopical instruments. In addition to such individual progress for these two optical sciences, they have been evolving to merge into surface-plasmon-associated near-field microscopy and field-enhanced near-field spectroscopy.

The use of surface plasmons is now essential in near-field microscopy. At the 5th International Conference on Near Field Optics (NFO-5) held in Shirahama, Japan in December 1998, I discussed with Dieter Pohl and Ulrich Fischer the plan to edit this book, and then at the 6th conference NFO-6, these topics came to the fore with many related new results. And now our book appears for the public, with 10 contributions.

The first and second chapters were written by Dieter Pohl and myself as a historical survey of near-field optics and surface plasmon polaritons and a review of the super-resolution studies developed in imaging optics. In the following chapter, the interaction of a metallic probe at the apex with surface plasmon polaritons is described for use as a highly efficient apertureless near-field probe; this chapter was written by Yasushi Inouye. In Chap. 4, the idea of the confinement of the optical intensity in nanoscopic dimensions by using surface plasmon polaritons is developed by Ulrich Fischer et al. In Chap. 5, Shinji Hayashi discusses the electromagnetic normal modes of a metallic particle placed very near to a metallic surface, and in Chap. 6, Takayuki Okamoto describes the scattering and the absorption properties of metal particles smaller than the wavelength of light. The story extends to the application of the plasmon-excited near-field microscope to the localized radiation force. Lukas Novotny derives the conservation law for linear momentum in an optical field using classical electrodynamics in Chap. 7, and Tadao Sugiura presents laser-beam trapping of metallic nanoparticles for near-field microscope probes in Chap. 8. In Chap. 9, Masatoshi Osawa reviews the mechanism of the infrared electromagnetic interaction of the photon field with metal particles and a molecule; and, in the last chapter, the excitation of surface plasmon polaritons by a focused laser beam is described by Hiroshi Kano.

My thanks are due to my contributors for finding the time and energy to write the chapters. Among them, my colleague Dr. Yasushi Inouye spent a lot of time helping me from the planning to the final proof. I am also grateful, on behalf of all the authors, to our secretary Ms. Masae Noda for her administrative assistance in editing the manuscripts, including the LaTeXconversion, and pushing the scientists to obey the deadline.

Osaka,
April 2001 *Satoshi Kawata*

Contents

Near-Field Optics and the Surface Plasmon Polariton

Near-Field Microscope Probes
Utilizing Surface Plasmon Polaritons

Near-Field Spectral Analysis of Metallic Beads

Forces in Optical Near-Fields

Laser Trapping of a Metallic Probe for Near Field Microscopy

Surface-Enhanced Infrared Absorption

Excitation of Surface Plasmon Polaritons by a Focused Laser Beam

Near-Field Optics and the Surface Plasmon Polariton

Dieter W. Pohl

Institut für Physik, Universität Basel
Klingelbergstrasse 82, 4056 Basel, Switzerland
`Dieter.Pohl@unibas.ch`

Abstract. The history of research in surface plasmon polaritions and in near-field optics is reviewed with emphasis on their common aspects.

1 Introduction

The terms "near field optics" (NFO) and "surface plasmon polariton" (SPP) denote physical phenomena of different but related nature: Both refer to the excitation and propagation of high-frequency electromagnetic fields in environments comprising several materials. NFO describes the behavior of such fields in structures small compared with the wavelength. It is not restricted to particular materials. Plasmons are defined as electromagnetic excitations coupled to the free charges of a conductive medium, and the SPP is such a plasmon bound to an interface with a dielectric medium. An SPP may be excited in structures of any size, but excitations in small structures are distinguished by a pronounced resonant character, resulting in a variety of interesting, even spectacular optical phenomena.

Another link between NFO and SPPs are the dispersion relations of a freely propagating light wave and an SPP propagating along a plane interfac which prohibit direct coupling in general. One of the exceptions is NFO-confined light, which provides a broad spectrum of wave vectors sufficiently extended for SPP coupling.

Present-day research in NFO is strongly influenced by the development of scanning near-field optical microscopy (SNOM), also called near-field scanning optical microscopy (NSOM). This is a super-resolution optical microscopy which has enabled a variety of novel SPP experiments. The present chapter puts emphasis on these relations because of the author's personal engagement in this field. The references mainly refer to early work on the respective subjects, the more recent publications being cited adequately in the other chapters.

2 Back to the Roots...

The intimate relation between NFO and SPPs makes itself felt in the mathematical description of various electromagnetic interface phenomena. Some of

S. Kawata (Ed.): Near-Field Optics and Surface Plasmon Polaritons,
Topics Appl. Phys. **81**, 1–13 (2001)

them date back to the early days of electromagnetic research. It is interesting to note that the pioneers of electromagnetic theory expressed little interest in the properties of optical near fields because of the small dimensions involved. The divergences of interface excitations that nowadays are called SPPs were ignored, too. Still, in retrospect, it is fair to consider some of these activities early forerunners of present-day NFO and SPP research.

2.1 Rayleigh and Mie Scattering

Any particle that is small compared with the wavelength can be represented by an induced dipole to the lowest-order approximation. The field enhancement near such a submicroscopic particle is of immediate relevance to NFO microscopes using a surface protrusion as an antenna [1] or, to some extent, pointed tips [2].

In the near field, retardation effects may be ignored to first-order approximation. This reduces Maxwell's equations to the Laplacian form. Mie's theory is considerably simplified in this limit. For sufficiently small particles, only the lowest-order solution, equivalent to dipole excitation, is of significance. The scattering efficiency is proportional to $(\varepsilon_1 - \varepsilon_2)/(\varepsilon_1 + 2\varepsilon_2)$ in this case, where $\varepsilon_{1,2}$ are the dielectric constants of the particle and the surrounding medium, respectively.

2.2 Surface Plasmon Polaritons

The Rayleigh and Mie scattering theories can be readily extended to include plasmon effects. For small particles, the divergence in scattering efficiency at $\varepsilon_1 + 2\varepsilon_2 = 0$ is the condition for the lowest-order SPP resonance. Upon approach of a third medium, ε_2 becomes a weighted average of the dielectric constants of the second and the third medium. This modifies the resonance condition, as a function of distance between the particle and the third medium [3].

The optical effects caused by SPPs were recognized long ago. Excellent overviews of the early work can be found in the reviews of *Raether* [4], *Economou* and *Ngai* [5] and *Feibelmann* [6]. A detailed and up-to-date review was published recently by *Knoll* [7].

Experimental SPP studies were greatly facilitated by the excitation and observation techniques developed by *Kretschmann* and *Raether* [8], and by *Otto* [9]. These techniques allow one to launch extended plane SPP waves in a metal film and provide detailed information about thin-film SPP properties in k-space. The SNOM/NSOM techniques for SPP excitation developed recently by *Hecht* et al., *Novotny* et al., *Bouhelier* et al. [10,11,12] complement the Kretschmann and Otto schemes: They provide detailed information about thin-film SPP properties in real space.

2.3 Surface-Enhanced Raman Scattering

In the mid-1970s, opticians were surprised by the high-intensity Raman scattering from certain adsorbates on rough surfaces of copper, silver, or gold [13,14]. It was soon found that field enhancement by SPP excitation plays an important role (see, for example, the review articles of *Chang* and *Laube* [15], *Otto* [16], and *Wokaun* [17]). The SPPs are localized at small protrusions and crevices of the rough surface.

An individual protrusion can be modeled as a semi-ellipsoid on a plane. Laplace's equation can be solved analytically for this geometry [18,19]. As a general result, several plasmon resonances of approximately equal strength were found, but the field enhancement due to SPP excitation is not sufficient to explain the immense enhancement factors experiementally observed.

2.4 Resonant Interaction of Particles

2.4.1 Förster Resonant Energy Transfer (FRET)

The fluorescence of a first molecule can be quenched by placing a second molecule in its immediate proximity. This happens if the second molecule absorbs light at the emission frequency of the first. The transfer of excitation can be studied quantitatively if the second molecule is also fluorescent. This resonant energy transfer was discovered more than half a century ago by *Förster* [20,21]. The quenching increases with decreasing distance according to an inverse sixth-order power law. This is a typical near-field effect based on the well-known characteristics of dipole antennas. It was proposed several times in the past to utilize this effect for SNOM/NSOM (see, for instance *Tan* and *Kopelman* [22] and *Sekatskii* and *Letokhov* [23]) with sub-10 nm resolution. Technical difficulties have, so far, apparently prevented the successful implementation of such a Förster SNOM/NSOM.

2.4.2 Resonant Energy Transfer Between Fluorescent Molecules and Metallic Particles

Gersten and *Nitzan* [24] and *van Labeke* et al. [25] extended the above energy transfer considerations to the case of a fluorescent molecule near a small metallic particle. The fluorescence properties were found to vary drastically from those of the free molecule. This was confirmed experimentally by *Leitner* et al. [26], who studied the fluorescence of dyes adsorbed an small silver islands.

2.4.3 SPP-Coupled Small Structures

Superposition of the electro-magnetic fields of neighboring SPP-excited particles results in considerable modification of the resonance conditions. This is readily noticed in the reflection and absorption spectra of granular gold and silver films [27,28,29]. Arrays of regular, small metal structures on a dielectric substrate provide even more detailed information. A good entry into these studies is provided the papers of *Aussenegg* and coworkers, who produced such structures by electron lithography. Excitation with ultrashort laser pulses gives direct information about SPP propagation and decay [30,31].

2.5 Small Structures Next to an Interface Between Extended Media

The radio wave dipole antenna is a macroscopic analogue of a fluorescing molecule as well as of a Mie scatterer. An antenna at a near-field distance from an interface is a configuration of relevance for SPPs as well as for NFO.

2.5.1 Radio Wave Antennas Next to the Ground

The problem of the dipole antenna next to an extended body was encountered in the early days of radio telecommunication, around 1900. The relevant wavelengths in those days were kilometers rather than (sub-) micrometers, but the problems were essentially the same as in SNOM/NSOM. The question is, in both cases, 'how does the radiation characteristics of an emitter change upon variation of its environment?'

Sommerfeld and coworkers were among the first to study this subject. They considered the radiation from vertical [32] and horizontal [33] dipole antennas next to the ground, as well as various details of the general solution [34,35,36]. The discussion concentrates on the fields on the earth's surface, the only situation of relevance in the early days.

Sommerfeld's theoretical approach includes an integration in the complex plane of wave vectors $\boldsymbol{k}$ as an essential step. The value of the integral is determined by the residues of three poles located at $k_{1,2} = n_{1,2}k_0$ and $s = k_0\sqrt{\varepsilon_1\varepsilon_2/(\varepsilon_1+\varepsilon_2)}$. Here k_0 is the wave vector in a vacuum, and $\varepsilon_{1,2}$ are the dielectric constants of the air and the ground (complex), respectively. The first two poles give rise to spatial waves with wave vectors k_1 and k_2, propagating mainly into media 1 and 2, respectively. The intensity and angular distribution of the radiation depend strongly on the dielectric properties of the corresponding other medium. Thus a distant observer on side 1 can tell from the intensity of the detected radiation what the electrical (optical) properties of medium 2 are and how they may change when the dipole is moved along the surface. This is in fact the basic principle of NFO microscopy!

The third pole creates a 'ground' wave which travels along the interface with wave vector s. The amplitude of the ground wave decreases normal to the direction of propagation, as is characteristic for a bound, evanescent wave. It is intriguing to see that the ground wave amplitude diverges at $\varepsilon_1 + \varepsilon_2 = 0$, which is the condition for excitation of an SPP at a plane interface (at the limiting frequency; see, for instance, *Raether* [4]).

The amplitudes of the spatial waves vanish completely for $\varepsilon_1 + \varepsilon_2 = 0$. All the energy of the dipole is converted into SPP excitation. The situation has a striking similarity to the minimum in reflection observed in the Kretschmann prism configuration for light impinging on a glass/metal interface at the so-called plasmon angle [8].

The theory of a dipole above ground was extended to finite elevations with the utilization of shorter and shorter wavelengths in the course of the 20th century [37,38,39,40]. Overviews are found in the books of *Sommerfeld* [41] and of *Banos* [42]. An increasing elevation means a transition from near-field to far-field coupling. The transition is characterized by very strong variations for distances up to about $\lambda/2\pi$, which is the range of dominant near-field coupling, followed by undulations which can be understood on the basis of far-field interference.

2.5.2 Molecule in Front of Another Medium

The fluorescence of a molecule in front of a metallic or dielectric plane surface follows the same laws as does the radiation of a radio wave dipole above the ground, except that the relevant frequencies are 10^6 to 10^9 times larger than before, and the dielectric properties of matter are correspondingly different. In particular, metals are no longer perfect conductors but have finite complex dielectric constants with negative real parts.

Dramatic NFO effects on the fluorescent lifetime and intensity are observed with decreasing distance, in particular, the quenching of fluorescence by a sufficiently nearby metallic substrate (see, for instance, *Drexhage* et al. [43,44], *Morawitz* [45], *Drexhage* [46], *Kuhn* [47], *Tews* [48,49], *Chance* et al. [50,51], *Lukosz* and *Kunz* [52,53], *Lukosz* [54], *Kunz* and *Lukosz* [55], and *Lukosz* and *Meier* [56]). These studies were stimulated by the discovery that monolayers of fluorescing molecules can be placed at well-defined distances from a substrate, employing fatty acid salts as inert spacers in the nanometer range.

NFO effects also make themselves felt when the second medium is a non-absorbing dielectric, although proximity effects are less dramatic. Instead, evanescent waves penetrating the dielectric are converted into propagating waves, emitted at angles larger than the critical angle for total internal reflection. In SNOM/NSOM, the term ‘forbidden light’ has been used for these contributions [57]. The radiation intensity into the ‘forbidden’ directions increases with refractive index.

The theory of a fluorescing molecule near an interface was generalized to include dipoles between stratified layers of different dielectric constant instead of an infinite halfspace [58] – a geometry which comes close to a SNOM/NSOM arrangement if the fluorescing molecule is considered to be the NFO probe.

Energy transfer from an excited dye molecule to a nearby SPP-active silver film was studied by *Weber* and *Eagen* [59]. Specifically, these researchers investigated the radiation intensity emitted by the SPP into the glass substrate and its dependence on the distance of the dye molecule from the film surface. The coupling again was restricted to the NFO range $\lambda/2\pi$. Similar results were obtained by *Pockrand* et al. [60], who studied nonradiative decay of excited molecules near a metal surface.

2.5.3 SPP-Active Particle in Front of Another Medium

Ruppin [3,61] and *Royer* et al. [62] studied the influence of a nearby dielectric medium on the SPP resonances of a metallic sphere. The resonance frequency and width depend on the properties of the medium in a sensitive way. This may become of relevance for 'apertureless' SNOM/NSOM (see below).

2.6 Small Apertures

The transmission of small apertures [63,64,65,66] and slits in plane, perfect metal sheets was studied mainly in the context of shielding of electrical devices against intense pulses of electromagnetic radiation. Such pulses accompany the explosion of atomic bombs. When a bomb is detonated sufficiently far up in the stratosphere, the physical damage can be kept small but the electromagnetic shock might cause failures in the operation of computers.

Similar to the case of a scattering particle or protrusion, SPPs may play a role in the interaction of optical radiation with an aperture. Quantitative values were obtained in the electrostatic approximation by *Becker* et al. [67], who modeled the aperture screen as a single-sheet hyperboloid. The resonance frequency is considerably lower than that of the corresponding SPP at a plane interface. It is an open question, however, as to what extent electrostatic solutions are representative for a screen that is infinitely extended away from the aperture.

The idea of using a small aperture for high-resolution microscopy was formulated for the first time by *Synge*, an Irish physicist, in 1928 [68]. He proposed moving a sample along a flat screen equipped with a small aperture. In a subsequent publication, he discarded this concept — which was correct in principle — because of the technical difficulties associated. Instead, he proposed another concept for super-resolution which he believed to be superior, but which — ironically — is incorrect, ignoring the role of evanescent waves [69].

3 NFO, SPP, and SNOM/NSOM

Modern NFO and SPP research is intimately connected with the development of SNOM/NSOM. A short account of the history of SNOM/NSOM hence may be appropriate at this point.

3.1 Aperture SNOM/NSOM

In 1982, I started to investigate optical super-resolution at the IBM Research Lab in Zurich. *A. Lewis*, then at Cornell University, began to study this problem at about the same time. My first result was a patent application for a SNOM/NSOM equipped with a transparent probe, coated with metal and having a small aperture at the apex [70]. Line scans with this probe indicated a high resolution capability [71], but the first complete SNOM/NSOM images were published in 1985/86 only. A resolution in *transmission* of 20 nm [72,73] was demonstrated in those early experiments, not too far from the present limits of resolution.

The NFO probes were made from sharply pointed quartz tips coated with an opaque aluminum layer. A small aperture was generated by pressing the tip against the sample surface until the brittle quartz core began to break through the metal coating. Very small apertures were generated in this way. The technique was soon abandoned, though, because the apertures were too unstable for routine operation.

Small apertures for high-resolution microscopy were proposed independently by *Lewis* et al. [74]. The transmission of small apertures in silicon wafers was explored in particular [75]. The subsequently developed SNOM/NSOM was equipped with a metallized micropipette, similar to the ones used for patch-clamping [76,77,78]. The resolution achieved with the micropipette was not quite as high as with the pressed tip but was sufficient to demonstrate super-resolution in transmission and in fluorescence contrast.

The IBM and Cornell groups were not aware of each other's in the early phase of near-field optical microscopy. This is the reason for the introduction of two different names, 'SNOM' and 'NSOM'. The IBM group originally had coined the term 'optical stethoscope' [71] because the operating principle is similar to that of the (acoustic) stethoscope used in medicine. In later publications, the word 'stethoscope' was abandoned in favor of 'scanning near-field optical microscope', a name that emphasizes the principles in common with other scanning-probe microscopes (the scanning tunneling, force, capacitance, ion conductance, etc. microscopes). 'NSOM', on the other hand, emphasizes the near-field aspect, as opposed to the far-field techniques used in confocal scanning optical microscopy ('SOM'). Both names made their way into the literature and are still used in parallel, depending on the traditions of the different research groups. For the sake of neutrality, both acronyms are used throughout.

SNOM/NSOM imaging in *reflection* was demonstrated by *Fischer* and *Pohl* [79] with an aperture probe scheme developed by Fischer in Göttingen [80]. In contrast to transmission SNOM/NSOM, the conditions for reflection SNOM/NSOM are not well defined so far, and activities towards this goal have been sporadic; a standard method has not yet been established [81,82,83] (see also the review of *van Hulst* [84]).

In the early 1990s, *Betzig*, then at Bell Labs, perfected the aperture SNOM/NSOM. He invented the pulled-fiber probe and a process of metal evaporation that left the apex of the fiber tip uncoated. The resulting aperture was small enough to be used successfully as a SNOM/NSOM probe. *Betzig* and coworkers published a series of beautiful papers which demonstrated various possible modes of operation (e.g. fluorescence or polarization) and different possible applications, for instance in biology and lithography. This work, reviewed in [85,86], received much attention, triggering various further efforts in near-field microscopy.

3.2 'Apertureless' SNOM/NSOM

Fischer probably was the first to recognize the potential of small light-scattering particles and sharp tips for super-resolution microscopy [1]. SPP excitation increases the sensitivity of the process [1]. A scattering tip in fact is a valid alternative to the aperture probe in SNOM/NSOM. This was confirmed in later work by several authors [87,88,89]. The record high resolution reported in one case [90] however, has, remained unconfirmed so far.

3.3 Photon-Tunneling Optical Microscopes

Another interesting form of SNOM/NSOM, the 'scanning tunneling optical microscope' (STOM) or 'photon scanning tunneling microscope' (PSTM), was introduced by *Reddik* et al. [91], *Courjon* et al. [92], and *de Fornel* et al. [93]. The probe is the pointed end of an uncoated optical fiber. The sample is transparent and is illuminated in such a way that total internal reflection occurs at the sample surface. The corresponding evanescent wave field outside the sample provides the interaction with the probe tip, in strict analogy to the tunneling of electrons in an STM.

The probe in this scheme is easier to produce than the aperture SNOM/NSOM probe but resolving power and image interpretation are still under discussion. It should be noted that aperture SNOM/NSOM schemes utilizing the 'forbidden' radiation from the sample also may be categorized as photon-tunneling microscopes [94]. Photon-tunneling microscopes are excellently suited for exciting and detecting SPP excitation in thin films locally [95].

3.4 Theoretical Studies

With the increasing amount of experimental SNOM/NSOM data, the need for better theoretical understanding became obvious. A number of theoretical groups began to work on the determination of NFO field distributions in the 1990s [96,97,98,99,100,101,102,103,104,105]. The task involves massive numerical computation but is the only way to gain deeper insight into the pecularities of optical near fields, in particular about their confinement and enhancement by highly curved structures. These efforts will be instrumental in understanding the properties of SPPs in nanostructured media.

4 Summary and Outlook

The startup phase of SNOM/NSOM and NFO research culminated in the first NFO conference, a NATO workshop in 1992, bringing together the still few active parties for the first time [106]. The workshop became the birthplace of the 'NFO-X, International Conference on Near-Field Optics and Related Phenomena' conference series. The proceedings of these conferences [106,107,108] are excellent sources of information about the field.

After the first NFO conference, NFO research expanded continuously, driven by great expectations of optical characterization on the nanometer scale but delayed by problems of probe fabrication as well as of understanding. For instance, an artifact, caused by the commonly used automatic tip-positioning scheme remained unnoticed for a long time. It frequently conveyed the impression of a very high optical resolution which did not exist in reality [109,110]. Unfortunately, this initiated some activities directed into dead end roads.

The future of SNOM/NSOM will depend critically on the capability for routine operation. So far, the use of SNOM/NSOM is confined to a small community of experts. SNOM/NSOM has to be developed in the next few years to a level that allows its systematic use by biologists, medical doctors, and skilled technicians. Under these conditions, SNOM/NSOM may pave the way toward great discoveries – if not, it will vanish like many other promising techniques before.

The future of NFO and SPPs may also be seen in extensions of integrated optics towards the nanoscale. Techniques known from radio wave technology might be scaled down to submicron dimensions towards this goal. The optical antenna, the metallic optical waveguide, and optical tweezers capable of manipulating nanoscopic particles may be among the fruits of such attempts.

The increasing mastery of nanometer-scale structuring techniques may, further, allow the development of SPP functional elements such as mirrors, filters, diffraction gratings, and modulators. Implemented in thin-film structures, such elements may open new perspectives for integrated optical devices ('plasmonics'). The cross section of a planar SPP waveguide, for instance, can be kept much smaller than that of a dielectric waveguide. This will be of relevance for highly integrated optical circuitry. Another example is SPP electro-optic modulation, the efficiency of which is predicted to exceed that of conventional modulation by far [111,112,113].

References

1. U. Ch. Fischer, D. W. Pohl, Phys. Rev. Lett. **62**, 458 (1989) 2, 8
2. W. Denk, D. W. Pohl, J. Vac. Sci. Tech. B **9**, 510 (1991) 2
3. R. Ruppin, Surf. Sci. **127**, 108 (1983) 2, 6
4. H. Raether, *Surface Plasmons on Smooth and Rough Surfaces and on Gratings*, Springer Tracts Mod. Phys. **3** (Springer, Berlin, Heidelberg 1988) 2, 5
5. E. N. Economou, K. L. Ngai, *Adv. Chem. Phys.* **27**, I. Prigogine, S. A. Rice (Eds.) (Wiley, New York 1974) p. 263 2
6. P. J. Feibelamn, Proc. R. Soc. (London) **12**, 287 (1982) 2
7. W. Knoll, Ann. Rev. Phys. Chem. **49**, 569 – 638 (1998) 2
8. E. Kretschmann, H. Raether, Z. Naturforsch. **23a**, 2135 (1968) 2, 5
9. A. Otto, Z. Phys. **216**, 398-410 (1968) 2
10. B. Hecht, H. Bielefeldt, L. Novotny, Y. Inouye, D. W. Pohl, Phys. Rev. Lett. **77**, 1889 (1996) 2
11. L. Novotny, B. Hecht, D. W. Pohl, J. Appl. Phys. **81**, 1798 (1997) 2
12. A. Bouhelier, Th. Huser, J. M. Freyland, H.-J. Guentherodt, D. W. Pohl, J. Microsc. **194**, 571 (1999); Phys. Rev. B (2001) to be publ. 2
13. M. Fleischmann et al., J. Raman Spectrosc. **4**, 269 (1974) 3
14. D. J. Jeanmaire, R. P. VanDuyne, J. Electroanal. Chem. **84**, 1 (1977) 3
15. R. K. Chang, B. L. Laube, CRC Rev. Solid. State Mater. Sci. **12**, 1 (1984) 3
16. A. Otto, Adc. Chem. Phys. **27**, 263 (1974) 3
17. A. Wokaun, Mol. Phys. **56**, 1 (1985) 3
18. J. Gersten, J. Chem. Phys. **73**, 3023 (1980) 3
19. R. Ruppin, Sol. State Commun. **39**, 903 (1981) 3
20. Th. Förster, Naturwiss. **33**, 166 (1946) 3
21. Th. Foerster in *Modern Quantum Chemistry*, O. Sinanoglu (Ed.) (Academic, New York 1965) 3
22. W. Tan, R. Kopelman, *Nanoscale Imaging and Sensing by Near-Field Optics*, **137**, Chemi. Anal. Ser., X. Feng Wang, B. Herman (Eds.) (Wiley, New York 1993) p. 407 3
23. S. K. Sekatskii, V. S. Letokhov, Pis'ma Zh. Eksp. Teor. Fiz. **63**, 311 (1996) 3
24. J. Gersten, A. Nitzan, J. Chem. Phys. **76**, 1139 (1981) 3
25. D. van Labeke, Ph. Grossel, J. M. Vigoureux, Proc. SPIE **1139**, 73 (1989) 3
26. A. Leitner, M. E. Lippitsch, M. Riegler, F. R. Aussenegg, Adv. Phys. **B 36**, 105 (1995) 3
27. M. C. Buncick, R. J. Warmak, T. L. Ferrell, J. Opt. Soc. Am. B **4**, 927 (1987) 4
28. M. J. Bloemer, J. G. Mantovani, J. P. Goudonnet, D. R. James, R. J. Warmak, T. L. Ferrell, Phys. Rev. B **35**, 5947 (1987) 4
29. M. J. Bloemer, T. L. Ferrell, M. C. Buncick, R. J. Warmak, Phys. Rev. B **37**, 8015 (1988) 4
30. J. R. Krenn, W. Gotschy, D. Somitsch, A. Leitner, F. R. Aussenegg, Adv. Phys. A **61**, 105 (1995) 4
31. W. Gotschy, K. Vonmetz, A. Leitner, F. R. Aussenegg, Appl. Phys. A **63**, 381 (1996) 4
32. A. Sommerfeld, Ann. Phys. **IV**, 665 (1909) 4
33. H. von Hörschelmann, Jahrb. drahtl. Telegr. **60**, 15 (1912) 4
34. P. Epstein, Jahrb. drahtl. Telegr. **4**, 176 (1911) 4

35. A. Sommerfeld, Ann. Phys. (Leipzig) **IV, 45**, 1135 (1926) 4
36. A. Sommerfeld and F. Renner, Ann. Phys. (Leipzig) **V, 41**, 1 (1942) 4
37. M. J. O. Strutt, Ann. Phys. (Leipzig) **V, 41**, 1 (1929) 5
38. B. van der Pol and K. F. Nissen, Ann. Phys. (Leipzig) **10**, 485 (1931) 5
39. K. F. Nissen, Ann. Physik **22**, 162 (1935) 5
40. B. van der Pol, Physica **2**, 843 (1935) 5
41. A. Sommerfeld, *Partial Differential Equations in Physics, Pure and Applied Mathematics* (Academic, New York 1949) 5
42. A. Banos, *Dipole Radiation in the Presence of a Conducting Half Space, Electromagnetic Waves* (Pergamon, Oxford 1966) 5
43. K. H. Drexhage, M. Fleck, H. Kuhn, F. P. Schäfer, W. Sperling, Ber. Bunsenges. Phys. Chem. **70**, 1179 (1966) 5
44. K. H. Drexhage, M. Fleck, H. Kuhn and F. P. Schäfer, Ber. Bunsenges. Phys. Chem. **72**, 329 (1968) 5
45. H. Morawitz, Phys. Rev. **187**, 1792 (1969) 5
46. K. M. Drexhage. Prog. in Opt. **XII**, 163 (1974) 5
47. H. Kuhn, J. Chem. Phys. **53** 101 (1970) 5
48. K. H. Tews, Ann. Phys. **VII, 29**, 97 (1973) 5
49. K. H. Tews, J. Luminescence **9**, 223 (1974) 5
50. R. R. Chance, A. Prock, R. Silbey, J. Chem. Phys. **60**, 2184 (1974) 5
51. R. R. Chance, A. Prock, R. Silbey, J. Chem. Phys. **62**, 2245 (1975) 5
52. W. Lukosz, R. E. Kunz, J. Opt. Soc. Am. **67**, 1607 (1977) 5
53. W. Lukosz, R. E. Kunz, J. Opt. Soc. Am. **67**, 1615 (1977) 5
54. W. Lukosz, J. Opt. Soc. Am. **69**, 1495 (1979) 5
55. R. E. Kunz, W. Lukosz, Phys. Rev. B **21**, 4814 (1980) 5
56. W. Lukosz, M. Meier, Opt. Lett. **6**, 251 (1981) 5
57. B. Hecht, H. Heinzelmann, D. W. Pohl, Ultramicrosc. **57**, 228 (1995) 5
58. W. Lukosz, J. Opt. Soc. Am. **71**, 744 (1981) 5
59. W. H. Weber, C. F. Eagan, Opt. Lett. **4**, 263 (1979) 6
60. I. Pockrand, A. Brillante, D. Moebius, Chem. Phys. Lett. **69**, 499 (1980) 6
61. R. Ruppin, Surf. Sci. **58**, 530 (1976) 6
62. P. Royer, J. P. Goudonnet, R. J. Warmack, T. L. Ferrell, Phys. Rev. B **35**, 3753, (1987) 6
63. H. A. Bethe, Phys. Rev. **66**, 163 (1944) 6
64. C. J. Bouwkamp, Philips Res. Rep. **5**, 321 (1950) 6
65. G. A. Massey, Appl. Opt. **23**, 658 (1984) 6
66. Y. Leviatan, J. Appl. Phys. **60**, 1577 (1986) 6
67. R. S. Becker, V. E. Anderson, R. D. Birkhoff, T. L. Ferrell, PH. Ritchi, Can. J. Phys. **59**, 521 (1981) 6
68. E. H. Synge, Philos. Mag. **6**, 356 (1928) 6
69. E. H. Synge, Philos. Mag. **7**, 65 (1931) 6
70. D. W. Pohl, US Patent No. 4,604,520 (priority date Dec. 27, 1982) 7
71. D. W. Pohl, W. Denk, M. Lanz, Appl. Phys. Lett. **44**, 651 (1984) 7
72. D. W. Pohl, W. Denk, U. Dürig, Proc. SPIE **565**, 56 (1985) 7
73. U. Dürig, D. W. Pohl, F. Rohner, J. Appl. Phys. **59**, 3318 (1986) 7
74. A. Lewis, M. Isaacson, A. Muray, A. Harootunian, Biophys. J. **41**, 405a (1983) 7
75. A. Harootunian, E. Betzig, A. Muray, A. Lewis, M. Isaacson, Abstracts, 1984 Annual Meeting of the Optical Society of America (1984) p. 1293 7

76. A. Harootunian , E. Betzig , M. Isaacson, A. Lewis, Appl. Phys. Lett. **49**, 674 (1986) 7
77. E. Betzig, A. Lewis, A. Harootunian, M. Isaacson, E. Kratschmer, Biophys. J. **49**, 269 (1986) 7
78. E. Betzig, M. Isaacson, A. Lewis, Appl. Phys. Lett. **51**, 2088 (1987) 7
79. U. Ch. Fischer, U. T. Dürig, D. W. Pohl, Appl. Phys. Lett. **52**, 249 (1988) 7
80. U. Ch. Fischer, J. Vac. Sci. Technol. B **3**, 386 (1985) 7
81. S. Jiang, K. Nakagawa, M. Ohtsu, J. Appl. Phys. **33**, L55 (1994) 7
82. G. Krausch, S. Wegscheider, A. Kirsch, H. Bielefeldt, J. C. Meiners, J. Mlynek, Opt. Commun. **119**, 283 (1995) 7
83. T. J. Silva, S. Schultz, Rev. Sci. Instrum. **67**, 715 (1996) 7
84. N. F. van Hulst, M. H. P. Moers, B. Bölger, J. Microsc. **171**, 95 (1993) 7
85. E. Betzig, J. Trautman, Science **257**, 189 (1992) 8
86. J. K. Trautman, J. J. Macklin, L. E. Bruns, E. Betzig, Nature **369**, 40 (1994) 8
87. U. Ch. Fischer, *in Scanning Tunneling Microscopy and Related Methods NATO ASI Ser. E* **184**, R. J. Behm, N. Garcia, H. Rohrer (Eds.) (Kluwer, Dordrecht 1990) p. 475 8
88. P. Gleyzes, A. C. Boccara, R. Bachelot, Ultramicrosc. **57**, 318 (1995) 8
89. S. Kawata, Y. Inouye, Ultramicrosc. **57**, 313 (1995) 8
90. F. Zenhausern, M. P. O'Boyle, H. K. Wickramasinghe, Appl. Phys. Lett. **65**, 1623 (1994) 8
91. R. C. Reddick, R. J. Warmack, T. L. Ferrell, Phys. Rev. B **39**, 767 (1989) 8
92. D. Courjon, K. Sarayeddine, M. Spajer, Opt. Commun. **71**, 23 (1989) 8
93. F. de Fornel, J. P. Goudonnet, L. Salomon, E. Lesniewska, Proc. SPIE **1139**, 77 (1989) 8
94. D. Barchiesi, D. van Labeke, Ultramicrosc. **61**, 17 (1995) 8
95. S. I. Bozhevolnyi, B. Vohnsen, I. Smolyaninov, A. V. Zayats, Opt. Commun. **117**, 417 (1995) 8
96. A. Dereux, D. Pohl, *in Near-Field Optics, NATO ASI Ser. E* **242**, D. W. Pohl, D. Courjon (Eds.) (Kluwer, Dordrecht 1993) p. 189 8
97. D. Van Labeke, D. Barchiesi, *in Near-Field Optics, NATO ASI Ser. E* **242**, D. W. Pohl, D. Courjon (Eds.) (Kluwer, Dordrecht 1993) p. 157 8
98. H. Hori, *in Near-Field Optics, NATO ASI Ser. E* **242**, D. W. Pohl, D. Courjon (Eds.) (Kluwer, Dordrecht 1993) p. 189 8
99. J. M. Vigoureux, C. Girard, F. Depasse, J. Mod. Opt. **41**, 49 (1994) 8
100. L. Novotny, D. W. Pohl, P. Regli, J. Opt. Soc. Am. A **11**, 1768 (1994) 8
101. C. Girard and A. Dereux, Rep. Prog. Phys. **59**, 657 (1996) 8
102. D. Barchiesi, Ch. Girard, O. J. F. Martin, D. van Labeke, D. Courjon, Phys. Rev. E **54**, 4285 (1996) 8
103. J.-J. Greffet, R. Carminati, *in NATO ASI Ser. E* **319**, M. Nieto-Vesperinas, N. Garcia (Eds.) (Kluwer, Dordrecht 1996) 8
104. O. J. F. Martin, Ch. Girard, Appl. Phys. Lett. **70**, 705 (1997) 8
105. A. Madrazo, M. Nieto-Vesperinas, Appl. Phys. Lett. **70**, 31 (1997) 8
106. D. W. Pohl, D. Courjon (Eds.), *Near-Field Optics*, NATO ASI Ser. E **242** (Kluwer, Dordrecht 1993) p. 189 9
107. M. Paesler, N. van Hulst (Eds.), Proc. 3rd Int'l Conf. on Near-Field Optics (NFO III), Ultramicrosc. **61** (1–4) (1995) 9
108. S. Kawata (Ed.), Proc. 5th Int'l Conf. on Near-Field Optics (NFO V), J. Microsc. **194**, Parts 2/3 (1999) 9

109. B. Hecht, H. Bielefeldt, Y. Inouye, D. W. Pohl, L. Novotny, J. Appl. Phys. **81**, 2492 (1997) 9
110. V. Sandoghdar, S. Wegscheider, G. Krausch and J. Mlynek, J. Appl. Phys. **81**, 2499 (1997) 9
111. J. Takahara, S. Yamagishi, H. Taki, A. Morimoto, T. Kobayashi, Opt. Lett. **22**, 475 (1997) 9
112. J. Takahara, S. Yamagishi, T. Kobayashi, CLEO/Pacific Rim'97 Tech. Dig. (1997) p. 42 9
113. T. Yamauchi, H. Yoshimura, J. Takahara, H. Murata, T. Kobayashi, *5th Int. Conf. on Near-Field Optics, Shirahama 1998*, Tech. Dig. (1998) p. 469 9

Near-Field Microscope Probes Utilizing Surface Plasmon Polaritons

Satoshi Kawata

Department of Applied Physics, Osaka University
Suita, Osaka 565-0871, Japan
`kawata@ap.eng.osaka-u.ac.jp`

Abstract. The near-field microscope is characterized by its super-resolution capability. It exceeds the classical limit of spatial resolution of the light microscope due to the wave nature of photons or the diffraction of light. In this chapter, a general review of the methods for super-resolution in imaging optics is given, and how near-field optics enables the super-resolution is explained using the Ewald sphere. The common and distinctive mechanisms and functions of different near-field probes are compared using eight configurations including the probes associated with surface plasmon polaritons.

The imaging mechanism of the near-field optical micrscope is different from the classical light microscope; the light intensity is detected as a result of strong electromagnetic interaction between the probe and the sample structure in the near-field via evanescent photons, so that the system is not a linear passive one but a more complex one. Since this microscope uses photons to see the structure, the energy or wavelength range in the optical spectrum is an important issue to be discussed. This chapter describes these topics as an introduction to the following chapters.

1 Super-Resolution and Wavelength Shortening

Although optical microscopy has been widely used for observing small structures, there is a strict limitation of an spatial resolution with type of this microscopy. Owning to the diffraction of light, the smallest structure of the sample that can be resolved with a conventional optical microscope is a half wavelength of light, or a few hundred nanometers in the visible wavelength region. This limit is not small enough to observe the structures of interest in current advanced science and technology, such as protein molecules, quantum nano-devices, and self-assembled molecules.

There have been a variety of attempts historically to attain super-resolution imaging in optical microscopy. On the basis of Abbe's diffraction theory, the resolution limit can be increased by choosing a shorter wavelength for the light. In photolithography for semiconductor patterning, ultraviolet (UV) and deep-UV lasers, such as KrF (wavelength 248 nm) and ArF (193 nm) excimer lasers and the solid-state Nd:YAG laser with fourth-harmonic generation (266 nm), are used to obtain sub-micron resolution. In optical data storage, the GaN blue laser (395–415 nm) is the most promising light source for

S. Kawata (Ed.): Near-Field Optics and Surface Plasmon Polaritons,
Topics Appl. Phys. **81**, 15–27 (2001)

future high-density optical data-storage [1]. However, for optical-microscopic applications, UV illumination has not been much used, because most materials are opaque in the UV region, and such illumination may even damage the specimen.

In optical microscopy, a common technique to shorten the wavelength is to place oil in the gap between the sample (in practice, the cover glass over the sample) and the objective lens. Since the refractive index of the oil is around 1.5, the wavelength of light is shortened by a factor of 1.5 without changing the optical frequency. A solid can be used instead of oil [2,3]. A version of this configuration for near-field microscopy will be described later in this chapter.

Frequency mixing to convert a high-spatial-frequency component of the sample structure to a detectable low frequency is another approach to overcoming the diffraction limit. Figure 1 shows an example of a configuration used to realize super-resolution by frequency mixing. A high-spatial-frequency component can be passed through the diffraction-limited optics by mixing with a high-frequency reference grating. This is equivalent to moiré-imaging. The idea was the first proposed by *Lukosz* and *Marchand* in 1963 [4].

The spatial resolution can be also increased if the light amplitude is multiplied by itself. The square of the amplitude of a monochromatic plane wave $\cos(kr+\omega t)$ with a spatial frequency k is converted to the wave $\cos(2kr+2\omega t)$ with a spatial frequency $2k$. Imaging of a sample with photons of the second-harmonic frequency of the incident-light frequency should provide a resolution twice that obtained with the incident light [5]. A nonlinear response with a threshold also exhibits super-resolution. This is commonly used in optical data-storage for recording and reading with super-resolution [6]. Photo-induced transparency and a thermally assisted phase transition, used to open a small aperture on the mask layer to the recording layer, are used this purpose [7].

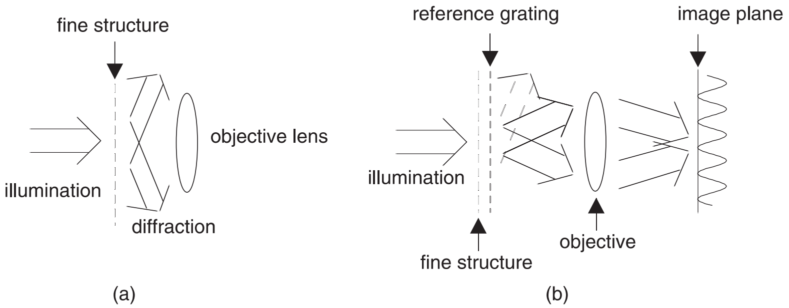

Fig. 1. Frequency mixing to enable the imaging of fine structure. (**a**) Conventional diffraction-limited optics with a lens do not image very-high-frequency components through the lens; (**b**) the reference grating down-converts the high-frequency signal by th moiré effect

2 Near-Field Imaging for Super-Resolution

Another method to shorten the wavelength, besides the methods described above, is the generation or the conversion of an evanescent wave. An evanescent wave, or evanescent field, is an electromagnetic field with an imaginary momentum component p_z in the direction z transverse to the direction of wave propagation x, and with an imaginary wavenumber k_z. Since the momentum is imaginary, a photon does not propagate towards z, even though the field exists. The amplitude of the field is given by

$$\exp[-\mathrm{j}(k_x x + k_x y + k_z z - \omega t)] = \exp[-\mathrm{j}(k_x x + k_y y - \omega t)]\, \exp(-z/d)\,, \quad (1)$$

where $d = -\mathrm{j}/k_z$, the decay length. Equation (1) indicates that the amplitude of the evanescent field decreases exponentially as z increases. This means that the evanescent field exists only in the near-field of the surface of the structure, so that it is not detected by ordinary far-field diffraction-limited optics. However, since the evanescent field is a physically existing light field, it can interact with another structure, which may be the probe of a near-field microscope, if this other structure is located in the near-field of the sample surface, and then a photon tunnels out to the far field.

In (1) the wavenumber components k_x and/or k_y associated with propagation in the x and y direction can be larger than the wavenumber $k = |\boldsymbol{k}|$, i. e.,

$$k_x > k\,, \qquad \text{and/or} \qquad k_y > k\,, \quad (2)$$

to accommodate the dispersion relationship,

$$k^2 = (2\pi/\lambda)^2 = k_x^2 + k_y^2 + k_z^2 = (\omega/c)^2\,. \quad (3)$$

The corresponding wavelength components λ_x and λ_y are hence shorter than the wavelength $\lambda = 2\pi/k$, i. e.,

$$\lambda_x < \lambda\,, \qquad \text{and/or} \qquad \lambda_y < \lambda\,. \quad (4)$$

Here the wavelength λ can be much shortened in the propagation direction x or y. The large-wavenumber or short-wavelength component indicates that the speed of this wave is slower than that ofordinary propagation, and the large momentum $p_x = \hbar k_x$ implies that the corresponding photon is heavier than the ordinary photon.

An evanescent wave, a solution of Maxwell's electromagnetic equations, can be generated when the condition for light propagation is not satisfied, such as in total internal reflection. In total internal reflection of light at a boundary between a dielectric prism and air, the wavelength of the evanescent wave in the air is shorter than the wavelength of propagation of light in the air; it is as short as the wavelength of light in the prism.

An evanescent field can be also generated at a grating with a period finer than the wavelength of light. If the period of the grating is finer than the wavelength of light, there is no direction of radiative diffraction. Nevertheless, there still exists a field which is modulated with this fine grating. This field corresponds to non-radiative diffraction or to an evanescent field near the grating with a wavelength equal to the period of the grating. Figure 2 shows a comparison between Bragg, Raman–Nath, and non-radiative diffraction. When the grating modulation is thick, the light diffracts only when the grating vector $\boldsymbol{k}_g$ which starts at the end of the wave vector k_i of the incident light is on the Ewald sphere, as shown in Fig. 2a. This is the condition of Bragg diffraction. When the grating modulation is not thick enough, diffraction occurs even if the grating vector $\boldsymbol{k}_g$ is off the Ewald sphere, as shown in Fig. 2b. In this case, the grating vector $\boldsymbol{k}_g$ is spread out and its end becomes a plane in two dimensions (shown in the figure as a line, i. e., a crossection of a plane), and the diffraction vector $\boldsymbol{k}_\mathrm{d}$ should meet this plane on the Ewald sphere. This is the case of Raman–Nath diffraction.

When the grating period is shorter than the wavelength of light, the grating vector $\boldsymbol{k}_\mathrm{g}$ is longer than the wave vector of the light, as shown in Fig. 2c, and then the spread-out end of the grating vector does not meet the Ewald sphere. As a result, neither the Bragg diffraction condition nor the Raman–Nath diffraction condition is satisfied. Nevertheless, there must be an electromagnetic field at the grating. Since this field does not satisfies either the

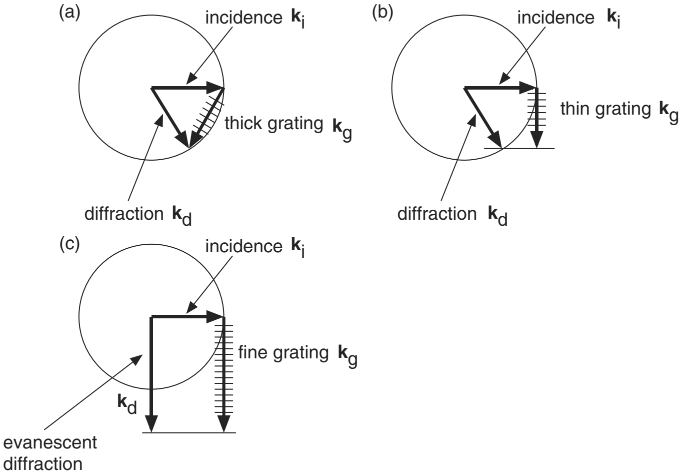

Fig. 2. Ewald sphere and diffraction condition for three cases. (**a**) Bragg diffraction. The two wave vectors, corresponding to incidence and diffraction, and the grating vector close a triangle. (**b**) Raman–Nath diffraction. Since the grating modulation is thin, the end of the grating vector has some extent, so that diffraction may be generated with an open triangle. (**c**) Non-radiative diffraction or evanescent diffraction is generated by ultrafine grating with a period shorter than the wavelength of light

Bragg or the Raman–Nath condition, the diffraction does not radiate but is evanescent.

Not only a regularly aligned grating but also any subwavelength structure generates an evanescent field; such structures include a small scattering particle and a small aperture. The decay length is proportional to the period or to the size of the structure. In conclusion, the evanescent field governs the behavior near a subwavelength structure at distances comparable to the size of the structure.

3 Surface Plasmon Polaritons

A collective oscillation of electrons or a plasma wave near the surface of a metal, known as a surface plasma wave, is necessarily associated with an electromagnetic wave (see Fig. 3). The speed of such a surface wave, or of a surface plasmon polariton, its quantum, is slower than the speed of light in the medium adjacent to the metal surface, so that the electromagnetic field is evanescent. The field distribution can be derived by a classical analysis of a multilayer system with the Fresnel formula and appropriate boundary conditions. The wavenumber of the surface plasma wave is given by [8]

$$K_{\mathrm{SP}}(\omega) = \frac{\omega}{c}\sqrt{\frac{\varepsilon_{\mathrm{m}}(\omega)\varepsilon_{\mathrm{s}}}{\varepsilon_{\mathrm{m}}(\omega)+\varepsilon_{\mathrm{s}}}}\,, \tag{5}$$

where ω is the angular frequency of the surface plasma wave, $\varepsilon_{\mathrm{m}}(\omega)$ is the complex dielectric constant of the metal, and ε_{s} is the dielectric constant of the surrounding medium. Figure 4 is a plot of the ω–k dispersion relationship. Since the surface plasmon polariton is associated with an evanescent field, it can be excited by irradiation with an evanescent light wave satisfying the dispersion relationship at the boundary between the metal and the dielectric. Excitation of the surface plasmon polariton can be performed with the evanescent field generated by either total internal reflection, a fine grating, or any other subwavelength structure. The conditions on the angle, wavelength and refractive index of the metal and prism are extremely severe for the resonance of the plasmon polariton. Figure 5 shows a plot of the reflectance of

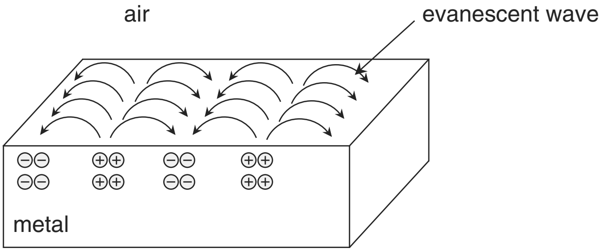

Fig. 3. Surface plasmon polariton

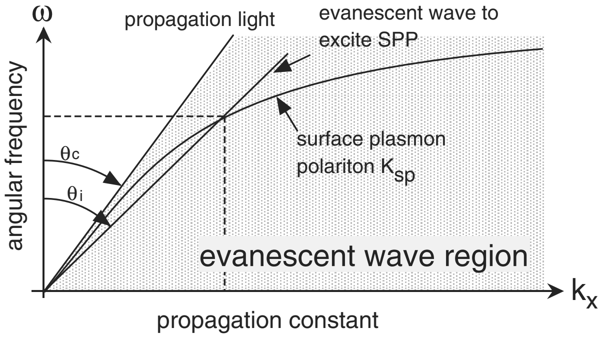

Fig. 4. ω–k dispersion relationship of surface plasmon polariton

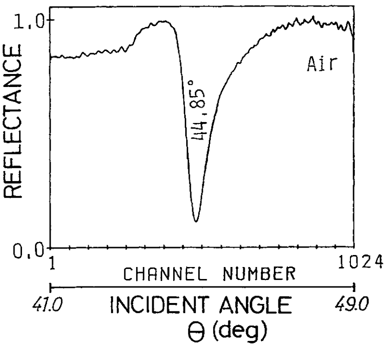

Fig. 5. Reflectance of light incident on a silver film as a function of incidence angle. At the angle of the dip in the plot, the surface plasmon polariton is excited and an evanescent electromagnetic wave is associated with it [9]

light incident on a prism coated with a thin metal film to excite the surface plasmon polariton, as a function of the incidence angle. At an angle less than the citical angle for total internal reflection the reflectance is given by the Fresnel formula. At an angle over the critical angle, the reflectance is 100% except at the angle of surface plasmon resonance. At the angle of surface plasmon resonance, incident photon excites the plasmon polariton and the photon energy is transferred to the plasmon polariton, resulting in a dip in the reflection curve. The sharpness of the dip depends on the ratio of the imaginary part to the real part of the dielectric constant of the metal. Silver exhibits a very sharp dip in the visible region, gold reasonably sharp dip, while aluminum exhibits a broad dip. A sharp dip represents a strong resonance of the plasmon, or a high intensity of the field. The plasmon polariton can hence be used for amplifying or enhancing the light intensity in the local and near-fields of a metallic structure.

4 A Family of Near-Field Probes

Figure 6 shows a family of near-field probes for generation and detection of evanescent photons near a subwavelength structure. A highly refractive prism is the simplest probe for generating or coupling out subwavelength evanescent field (Fig. 6a). The resolution enhancement is not significant; it is only by a factor equal to the refractive index of the prism [3], similarly to the oil immersion objective lens described in the introduction. In the arrangement shown in Fig. 6a, the angular component at angles lower than the critical angle is stopped [10]. A grating with a subwavelength period can be also a near-field probe (Fig. 6b). This is similar to Lukosz's super-resolution or moiré imaging with a grating, which has been described in the introduction, but the gap between the probe grating and the specimen can as large as the grating period. This probe is strongly polarization sensitive, and has been used as an efficient polarizer in the infrared region, where a metal material was used. The polarization perpendicular to the grating lines is transmitted while that parallel to the grating is reflected. Figure 6c shows a concentric circular grating with a subwavelength pitch used for a scanning probe. This can be regarded as an extreme version of a Fresnel lens for which the focus is at the center and at the surface, or an extreme case of a conical lens called an 'axicon' [11,12] where the refraction of the light by the lens has become total internal reflection [13]. The period of the conical grating is constant and less than the wavelength.

An aperture smaller than the wavelength of light can be the probe of a near-field scanning optical microscope. Figure 6d shows a screen with a subwavelength aperture in an opaque (conductive) flat screen, and Fig. 6e a metal-coated conical probe (or an optical fiber with a sharpened end) with a subwavelength aperture at the tip. In both probes, a virtual dipole is generated in the aperture by the incidence of light. In contrast to such an aperture probe, a scattering probe which is a real dipole (recently called an 'apertureless probe' [14]) can be also used as a near-field probe. The ideal apertureless probe for generating or detecting (or interacting with) evanescent photons is an extremely small scatterer or Rayleigh scatterer (Fig. 6f), which is complementary to the aperture probe shown in Fig. 6d. The material can be either a dielectric [15] or a metal [16]; a metallic bead is much better in terms of high scattering efficiency owning to the field enhancement by the local mode of the surface plasmon polariton of the metal bead. Such an isolated, single, small scattering probe is suspended and scanned near the sample surface with the aid of laser trapping technology [16]. A focused beam from a near-infrared laser is used to trap the probe and to control the position of it in a liquid medium. The details are described in the chapter by Sugiura. The trapping of such a probe is limited to situations in which the sample is immersed in a liquid. Biological samples are mostly in such a condition. For imaging non-biological samples in vacuum or in air, a metallic needle with a sharpened tip, as shown in Fig. 6g, has been proposed [17]. This apertureless probe has a

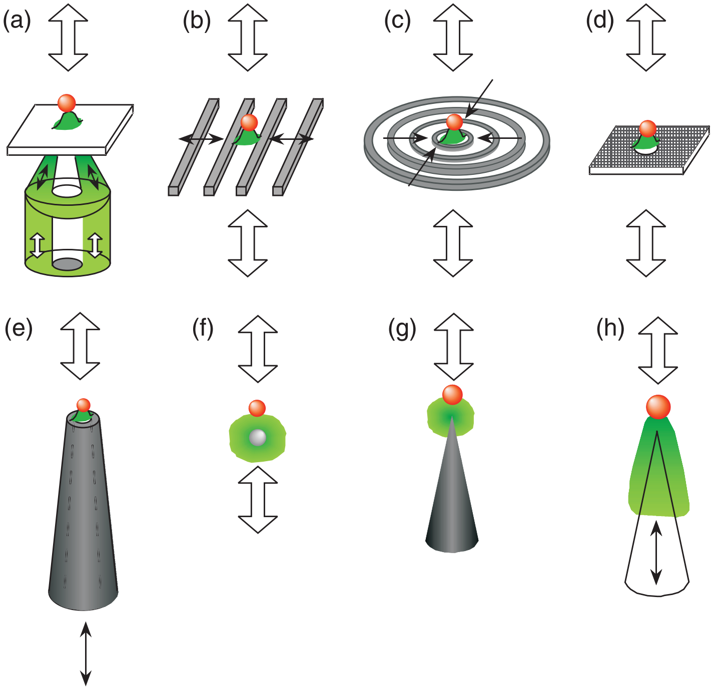

Fig. 6. A family of near-field probes. The *red particle* represents a small structure and the *green color* evanescent photons used for probe–sample interaction. (**a**) A hemisphere prism probe with a high-numerical-aperture lens. The light component incident on the prism surface at angles lower than the critical angle is stopped by a mask to provide an evanescent spot on the prism surface owing to the total internal reflection of light [10]. (**b**) A grating of subwavelength period. Diffraction is evanescent. (**c**) A concentric blazed grating of subwavelength period [13]. (**d**) An opaque screen with a subwavelength aperture. The original configuration of the near-field microscope [5,18,19,20]. (**e**) A metal-coated dielectric (fiber) probe with a subwavelength aperture at the end. The most popular near-field probe [21,22]. (**f**) A scattering probe of subwavelength diameter. An ideal probe in terms of resolution and local field intensity. The material can be a metal [16] or a dielectric [15]. Laser trapping technology is required to suspend and scan this isolated nanoprobe. (**g**) An apertureless probe. A semiconductor [14] or metal [17,23] needle with a sharpened end is used. The highest resolution [24] is attainable. High optical throughput and high field enhancement make two-photon fluorescent imaging [25], surface-enhanced Raman spectroscopic imaging [26], and high-resolution fabrication [27] possible. (**h**) A dielectric probe. This configuration is known as a photon STM [28,29]

similar configuration to that of a metal-coated fiber probe with an aperture, while it has the following significant advantages compared with an aperture probe:

1. The optical throughput or photon collection/illumination efficiency of an apertureless probe is much higher than that of a fiber probe coated with metal because of the use of external wide-angle optics to illuminate and/or collect the photons. The metal-coated fiber has a cutoff optical frequency for light transmission; the inner diameter of the waveguide strictly limits the wavelength of transmittable light. There is no such a limitation on a scattering probe because the waveguide mode is not used for light transmission.
2. Owing to the local mode of the surface plasmon at the probe tip, the electromagnetic field is significantly enhanced. This effect will be explained in detail in the chapter by Novotny [30] and by Inouye [17]. By utilizing the field-enhancement effect, even Raman spectroscopy [26] and two-photon spectroscopy [25] are made possible on the nanometer scale.
3. The spatial resolution can be much higher than that of an aperture probe, because of the small radius of the tip apex. The radius of a scattering probe without an aperture can be made much smaller than that of an aperture probe with an aperture and a metal coating surrounding the aperture. The metal coating for an aperture probe needs to be thick enough to stop the penetration of the light through the metal. This thickness of the aperture probe at the apex may cause an artifact in the imaging.

A metallic probe has been applied for imaging of semiconductors with regulation of the gap by STM (scanning tunneling microscope) [31] and for infrared imaging with high resolution [23,32]. The advantages of high throughput and of field enhancement with an apertureless metallic probe have been successfully utilized for two-photon-excited fluorescence imaging [30] and the Raman-scattering imaging with regulation by AFM (atomic force microscopic) [26].

The material for an apertureless probe can be a semiconductor [14] or a dielectric [28,29]. A dielectric fiber probe with a sharpened end, without a metal coating, can also be successfully used for near-field imaging with waveguide light transmission. This configuration shown in Fig. 6h, has been called photon STM, but did not have much claim to the above advantages 1–3. However, this configuration still contains the above three advantages to some extent. The resolution may be degraded by photons coupled into the fiber from/to the side of the probe, while there is no cutoff in transmission, owing to the absence of a metal coating. The field enhancement factor of a dielectric is not as high as that of a metal, although there still exists some enhancement for a small or sharp scatterer [33].

5 Imaging Theory of Near-Field Microscopy

The near-field image is given by the scanned light intensity detected at a detector in the far field as the probe scans over the sample surface. This image is different from the intensity distribution of the evanescent field modulated by (or generated by) the subwavelength structure. The intensity distribution modulated by the sample structure is modulated again by the subwavelength probe, resulting in the output intensity at the detector.

This near-field interaction has been known for a long time from the experiment of Newton's frustrated internal reflection [34]. Figure 7 shows a plot of the transmittance of evanescent photons through two prisms with a small gap between them as a function of the distance between two prisms [34]. The light is incident on the surface of the first prism condition of total internal reflection so as to generate the evanescent field, and the second prism reads this evanescent field and emits it to the far field. As the gap between two prisms decreases, the transmittance increases exponentially, except in the near-field region where the curve deviates from an exponential decay. Dipoles in the surface of the second prism, excited by the evanescent field on the surface of the first prism surface, generate another evanescent field, which re-excites the dipoles of the surface of the first prism. As a result, strong interaction occurs between the two prism surfaces via the evanescent field, resulting in the deviation of the transmittance curve.

Similarly to the experiment of the coupling of two prisms, near-field imaging with a probe is very complicated because of the strong interaction between the probe and the structure. Figure 8 illustrates the coupling or interaction between two structures via evanescent photons. This coupling could produce an artifact in the image, altrought in practice the image obtained represents the sample structure rather than the complicated field distribution [36].

6 Spectroscopic Issues

In contrast to the topographic imaging of the STM and AFM, a near-field optical microscope aims at imaging of the nanometric distribution of the local response of the sample to photon excitation. By choosing the optical frequency of the light, selected information, such as selected molecules and selected molecular bonds, selected conformations of molecules, and selected bands of a semiconductor, can be excited to provide the image contrast. Selection of the probe is therefore particularly important for near-field microscopy, as it must cover or discriminate in the spectroscopic range of interest. As in described in the previous section, a metal-coated fiber probe with an aperture has a cutoff limit on the transmittable optical frequency or on the wavelength, set by the diameter of the waveguide.

Since an apertureless metallic probe does not have a cutoff, such a probe has been used for molecular imaging. The metallic probe provides a reasonable contrast in the near-field infrared spectrum and image owing to the high

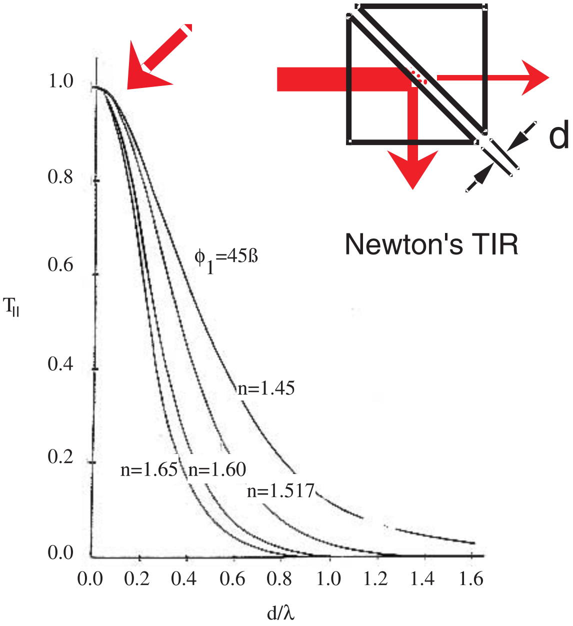

Fig. 7. Photons tunnel out between two prisms under a condition of total internal reflection [34]. The transmittance as a function of distance between the two prisms does not show an exponential decay when the two prisms are in the near-fields of each other [35]

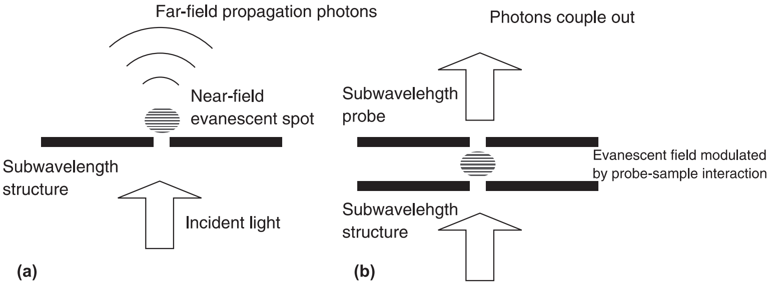

Fig. 8. (**a**) Light is incident on a subwavelength structure (small aperture). Light intensity is detectable in the far field, although it does not contain a subwavelength component, which is localized near the structure as an evanescent photon. (**b**) When a probe (a subwavelength aperture) approaches the structure, evanescent photons couple out through the probe. As a result, near-field subwavelength information can be detectable in the far field, while it is modulated owing to the probe–sample interaction

photon collection and scattering efficiency. Even the extremely weak signal of a Raman scattering spectrum and image can be detected by a metallic probe, thanks to the field enhancement of a metal particle. The scattering coefficient is a function of the wavelength, determined by the resonance of the plasmon polariton in the surrounding medium. The spectrum of scattering is given by the *Maxwell–Garnett* theory for any given complex dielectric constant and size parameter of a metallic sphere [37]. The ellipticity of a single metallic bead changes the factor of scattering (field enhancement) and spectral shift [38]. The field enhancement for a sharpened metallic needle will be described in the chapter by Novotny.

A possible problem in the use of a metal for a near-field probe lies in the fact that in fluorescence near-field microscopy the fluorescent photon energy may transfer to the metallic probe, leading to a quenching effect [39].

References

1. S. Nakamura, Jpn. J. Appl. Phys. **31**, 8 (1993) 16
2. J. M. Guerra, Photon tunneling microscopy, Appl. Opt. **29**, 3741–3752 (1990) 16
3. T. Nakano, S. Kawata, Evanescent-field scanning microscope with fourier-transform infrared spectrometer, Scanning **16**, 368–371 (1994) 16, 21
4. W. Lukosz, M. Marchand, *Foundations for Microwave Engineering* (McGraw Hill, London 1963) 16
5. R. E. Collin, Opt. Acta. **10**, 241 (1963) 16, 22
6. K. Aratani, A. Fukumot, Ohta, M. Kaneko, K. Watanabe, SPIE **1449**, 209-215 (1991) 16
7. T. Tsujioka, M. Kume, Y. Horikawa, A. Ishikawa, M. Irie, Super-Resolution Disk with a Photochromic Mask Layer, Jpn. J. Appl. Phys. **36**, 526-529 (1997) 16
8. H. Raether, *Sufrace Plasmons on Smooth and Rough Surfaces and on Gratings* (Springer, Berlin, Heidelberg 1988) 19
9. K. Matsubara, S. Kawata, S. Minami, Optical chemical sensor based on surface plasmon measurement, Appl. Opt. **27**, 1160-1163 (1988) 20
10. N. Hayazawa, Y. Inouye, S. Kawata, Evanescent field excitation and measurement of dye fluorescence in metallic probe near-field scanning optical microscope, J. Microsc. **194**, 472–476 (1999) 21, 22
11. J. H. McLeod, J. Opt. Soc. Am. **44**, 592–597 (1954) 21
12. R. Arimoto, C. Saloma, T. Tanaka, S. Kawata, Imaging Properties of Axicon in a Scanning Optical System, Appl. Opt. **31**, 6653–6657 (1992) 21
13. S. Kawata, Grating for superresolution, O. plus E. **154**, 173–180 (1992) 21, 22
14. F. Zenhausern, M. P. O'Boyle, H. K. Wickramasinghe, Apertureless near-field optical microscope, Appl. Phys. Lett. **65**, 1623–1625 (1994) 21, 22, 23
15. S. Kawata, Y. Inouye, T. Sugiura, T. Near-field Scanning Optical Microscope with a Laser Trapped Probe, Jpn. J. Appl. Phys. **33**, L1725–L1727 (1994) 21, 22
16. T. Sugiura, T. Okada, Y. Inouye, O. Nakamura, S. Kawata, Gold-bead scanning near-field optical microscope with laser-force position control, Opt. Lett. **22**, 1663–1665 (1997) 21, 22

17. Y. Inouye, S. Kawata, Near-field Scanning Optical Microscope using a Metallic Probe Tip, Opt. Lett. **19**, 159–161 (1994) 21, 22, 23
18. E. H. Synge, A Suggested method for extending microscopic resolution into the ultra-microscopic region, Philos. Mag. **6**, 356 (1928) 22
19. J. A. O'keffe, J. Opt. Soc. Am. **46**, 359 (1956) 22
20. E. A. Ash, G. Nicholls, Super-resolution Aperture Scanning Microscope, Nature **237**, 510 (1972) 22
21. D. W. Pohl, W. Denk, M. Lanz, Appl. Phys. Lett. **44**, 651–653 (1984) 22
22. A. Lewis, M. Isaacson, A. Harootunian, A. Muray, Ultramicrosc. **13**, 227–232 (1984) 22
23. A. Lahrech, P. Bachelot, P. Gleyzes, A. C. Boccara, Infrared-reflection-mode near-field microscopy using an apertureless probe with a resolution of $\lambda/600$, Opt. Lett. **21**, 1315–1317 (1996) 22, 23
24. F. Zenhausern, Y. Martin, H. K. Wickramasinghe, Scanning interferometric apertureless microscopy: optical imaging at 10 angstrom resolution, Science **269**, 1083–1085 (1995) 22
25. E. J. Sánchez, L. Novotny, X. S. Xie, Near-Field Fluorescence Microscopy Based on Two-Photon Excitation with Metal Tips, Phys. Rev. Lett. **82**, 4014–4017 (1999) 22, 23
26. N. Hayazawa, Y. Inouye, Z. Sekkat, S. Kawata, Metallized tip amplification of near-field Raman scattering, Opt. Commun. **183**, 333–336 (2000) 22, 23
27. J. Jersch, Nanostructure fabrication using laser field enhancement in the near-field of a scanning tunneling microscope tip, Appl. Phys. Lett. **68**, 868–870 (1996) 22
28. D. Courjon, Sarayeddine, M. Spajer, Scanning tunneling optical microscopy, Opt. Commun. **71**, 23–28 (1989) 22, 23
29. R. C. Reddick, R. J. Warmack, T. L. Ferrell, New form of scanning optical microscopy, Phys. Rev. Lett. **39**, 767–770 (1989) 22, 23
30. L. Novotny, R. X. Bian, X. S. Xie, Theory of Nanometric Optical Tweezers, Phys. Rev. Lett. **79**, 645–648 (1997) 23
31. Y. Inouye, S. Kawata, A Scanning near-field optical microscope having scanning electron tunneling microscope capability using a single metallic probe tip, J. Microsc. **178**, 14–19 (1995) 23
32. B. Knoll, F. Keilmann, Near-field probing of vibrational absorption for chemical microscopy, Nature **399**, 134–137 (1999) 23
33. H. Furukawa, S. Kawata, Local field enhancement with an apertureless near-field-microscope probe, Opt. Commun. **148**, 221–224 (1998) 23
34. I. Newton, *Optick, 4 ed.* (1730) (Dover, New York 1952) 24, 25
35. S. Zhu, A. W. Yu, D. Hawley, R. Roy, Frustrated total internal reflection: a demonstration and review, Am. J. Phys. **54**, 601–606 (1986) 25
36. H. Furukawa, S. Kawata, Analysis of image formation in a near-field scanning optical microscope: Effects of multiple scattering, Opt. Commun. **132**, 170–178 (1996) 24
37. J. C. Maxwell-Garnett, Colours in Metal Glasses and in Metallic Films, Philos. Trans. **203**, 385–420 (1906) 26
38. T. Okamoto, I. Yamaguchi, Field enhancement by a metallic sphere on dielectric substrates, Opt. Rev. **6**, 211–214 (1999) 26
39. X. S. Xie, R. C. Dunn, Probing Single Molecule Dynamics, Science **265**, 361–364 (1994) 26

Apertureless Metallic Probes for Near-Field Microscopy

Yasushi Inouye

Department of Applied Physics, Osaka University
Suita, Osaka 565-0871, Japan
ya-inoue@ap.eng.osaka-u.ac.jp

Abstract. In this chapter, I will show an apertureless metallic probe which enhances the electromagnetic field locally at its apex and achieves nanometric spatial resolution for near-field optical microscopy. The principle of the apertureless metallic probe and its features are described. Several near-field optical images are shown, and the contrast mechanism of microscopy is discussed.

The application to Raman spectroscopy is also described for molecular imaging and sensing.

1 Introduction

A small metallic structure a size of which is smaller than the wavelength of light scatters light field and enhances the electric field intensely, owing to the strong interaction between the light field and the metal structure, when light is incident on such a structure. For example, a thin metallic film with atomic-scale roughness enhances Raman scattering from molecules that are adsorbed on the film. The enhancement is by a factor of 10^4–10^6 relative to ordinary Raman scattering. This is well-known phenomenon, known as Surface-Enhanced Raman Scattering (SERS) [1]. One of the reasons for such an enhancement of Raman scattering is that localized surface plasmon polaritons (SPPs) are excited on small metallic structures and the incident light field is enhanced strongly. The electric field which is coupled to the localized SPPs at the metallic structures comprises an evanescent field. Since the evanescent field is localized around these structures, a super-resolution capability can be attained by detecting this field. We proposed such a near-field scanning optical microscopy (NSOM) using a metallic probe with a tip that enhances the electric field locally and strongly [2].

The NSOM described here is so-called apertureless NSOM, and the resolution is determined by the radius of the tip. In this chapter, we shall show the principle and features of an apertureless NSOM using a metallic probe, as well as several near-field images obtained with our system. Furthermore, we shall discuss near-field nanospectroscopy for chemical analysis of organic materials and molecules with the aid of our experimental data.

S. Kawata (Ed.): Near-Field Optics and Surface Plasmon Polaritons,
Topics Appl. Phys. **81**, 29–48 (2001)

2 Apertureless Metallic-Probe NSOM

2.1 Field Enhancement due to an Apertureless Metallic Probe

The apex of a metallic probe, such as the tip of a Scanning Tunneling Microscope (STM), functions as a scatterer by enhancing electric field locally. Shown in Fig. 1a is the intensity of a light field scattered at a tip, obtained from a numerical analysis. Figure 1b shows the model used for the analysis. A silver metallic tip of radius 20 nm is placed in contact with a glass substrate (refractive index:1.5). The silver tip is illuminated by plane wave traveling from the substrate. The wavelength of the incident field is 488 nm and its polarization is in the TM mode (i. e. p-polarization). The incidence angle is 45 degrees. An evanescent field is generated over the surface of the glass substrate because the incidence angle satisfies the condition of total internal reflection. The finite-differential time-domain (FDTD) method was employed in the calculation [3]. A localized and enhanced field spot is observed around the tip in the figure. The size of the small spot is about 30 nm, which corresponds approximately to the radius of the tip. The peak intensity of the small spot is enhanced by a factor of ca. 80 compared with the intensity of the incident field. If, instead, the tip is a glass probe with the same tip radius of 20 nm, the enhancement factor is 7 when the illuminating is in the TM mode [4]. No enhancement of the electric field is induced, when the TE mode (i. e. s-polarization) is used for illumination in the calculation [4,5]. These analyses show that strong enhancement of the localized field requires use of a metallic tip and TM mode illumination for an apertureless probe, and that the small-scale light field spot strongly enhanced at the tip is caused by excitation of a localized SPP.

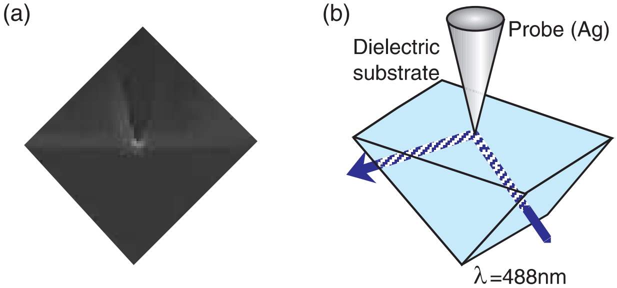

Fig. 1. Enhanced electric-field intensity localized at a silver probe tip, calculated by the FDTD method

2.2 Principle of an Apertureless NSOM

A structure $\boldsymbol{P}(\boldsymbol{r})$ of an apertureless probe tip is expressed by

$$\boldsymbol{P}(\boldsymbol{r}) = \int \boldsymbol{P}'(\boldsymbol{K}_{\text{prob}}) \exp(\mathrm{i}\boldsymbol{K}_{\text{prob}} \cdot \boldsymbol{r})\, \mathrm{d}\boldsymbol{K}_{\text{prob}} \ , \tag{1}$$

where $\boldsymbol{P}'(\boldsymbol{K}_{\text{prob}})$ is the spatial spectrum of the tip according to scalar theory [6]. When an incident light field, whose wave vector is represented by $\boldsymbol{k}_{\text{inc}}$ is scattered by the tip, the scattered field is given by

$$\int \boldsymbol{P}'(\boldsymbol{K}_{\text{prob}}) \exp[\mathrm{i}(\boldsymbol{K}_{\text{prob}} - \boldsymbol{k}_{\text{inc}}) \cdot \boldsymbol{r}]\, \mathrm{d}\boldsymbol{K}_{\text{prob}} \ . \tag{2}$$

The scattered field, of which the wave vector $|\boldsymbol{K}_{\text{prob}} - \boldsymbol{k}_{\text{inc}}|_x$ is imaginary, is converted into an evanescent field and is localized around the tip as shown in Fig. 2a. $|\boldsymbol{K}_{\text{prob}} - \boldsymbol{k}_{\text{inc}}|_x$ is euqal to $|\boldsymbol{K}_{\text{prob}}|_x$, that is, $|\boldsymbol{k}_{\text{inc}}|_x$ is negligible if the tip apex is much smaller than wavelength of the light field. This means that the size of the small light spot is approximately equal to the tip radius.

A sample having structures smaller than the wavelength is described similarly by

$$\boldsymbol{S}(\boldsymbol{r}) = \int \boldsymbol{S}'(\boldsymbol{K}_{\text{str}}) \exp(\mathrm{i}\boldsymbol{K}_{\text{str}} \cdot \boldsymbol{r})\, \mathrm{d}\boldsymbol{K}_{\text{str}} \ , \tag{3}$$

where $\boldsymbol{S}'(\boldsymbol{K}_{\text{str}})$ is the spatial spectrum of the sample. As the sample is placed in the vicinity of the tip, the small spot around the tip is scattered by the sample structure. If the lateral component of the spatial spectrum satisfies

$$|(\boldsymbol{K}_{\text{prob}})_x - (\boldsymbol{K}_{\text{str}})_x| < \frac{\omega}{c} = \frac{2\pi}{\lambda} \ , \tag{4}$$

the scattered field is converted into a propagating field, as shown in Fig. 2b. A near-field optical image is obtained by gathering the scattered field with external collection optics and detecting it in the far-field region while the tip or sample is scanned. Equation (4) represents the condition that the evanescent field around the tip is scattered by sample structures of which the spatial frequency is almost the same as the wavenumber of the evanescent field. In other words, the tip functions as a spatial band filter; if you want to observe a sample with 30 nm resolution, you should employ a metallic probe with a 30 nm radius. As the tip radius decreases, the tip can convert evanescent fields of higher spatial frequency into a propagating field, and the resolution of the NSOM becomes higher.

2.3 Features of the Metallic Probe

The basis of the metallic-tip NSOM is the scattering of the evanescent field localized around the tip due to the sample structure or the scattering of the evanescent field localized around the sample structure due to the tip.

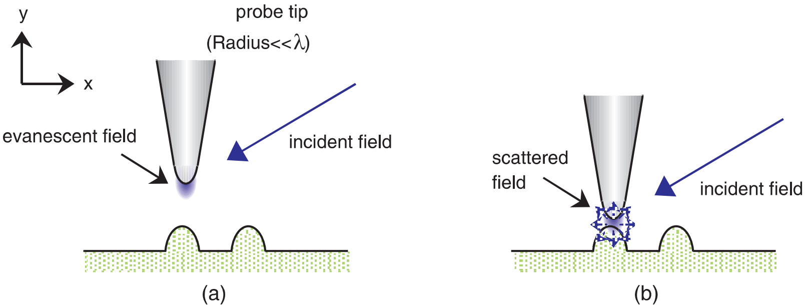

Fig. 2. Principle of an apertureless NSOM, (**a**) a small spot is generated at the tip, but does not interact with the sample, because the tip is far from the sample surface. (**b**) The localized spot is rescattered by the sample structure as the tip is in the vicinity of the sample

The function of the metallic tip is the same as that of an aperture probe, which is used for the generation of an evanescent field or conversion of an evanescent field into a propagating field at the aperture. A difference between the metallic tip and the aperture probe is whether it functions as a waveguide for illumination/detection or not.

Compared with the aperture probe, the metallic tip has several features, as follows,

1. Higher resolution is obtainable by making the tip sharper, because the resolution of an NSOM with a metallic tip is determined by the radius of the tip. Atomic resolution is achievable, provided that the tip apex is processed at the atomic level. So far, the accomplishment of imaging with 1 nm resolution has been reported [7,8]. On the other hand, the resolution of the NSOM with an aperture probe is limited to several tens of nanometers because the size of the aperture is restricted by the skin depth of the metal coated around the fiber [9].
2. The collection of the light field scattered at a metallic tip is efficient if external collection optics are used, while light field is strongly absorbed during waveguide transmission by the metal film coated around the fiber tip during waveguide transmission. The collection efficiency is getting better as higher-NA lenses are employed.
3. A metallic tip can produce a more intense scattered field than a tip made from an other material can [10] because a metal scatters the light field more efficiently than other materials as mentioned above.
4. A metallic tip can be sharpened more finely and easily than an aperture probe. An aperture probe has larger effective diameter than a pure metal tip because the former has metal coating that has to be thicker than the skin depth of light. Hence, the metallic tip can be scanned over steep areas of a sample when the tip is regulated by AFM or STM. Furthermore, atomic contact between the tip and sample or single-channel transport

of tunneling electrons is possible with a sharp metallic tip, while a light field is scattered at the tip [11]. This means that scattering center of the evanescent field coincides with the contact point or electron channel. Thus, the near-field optical image corresponds to the topography obtained with an AFM or a STM. In contrast, an aperture probe does not always provide a single contact point or elctron channel, owing to thickness of the probe, as shown in Fig. 3. This means that the probe–sample distance may not be controlled and regulated precisely and reliably. As a result, the near-field optical image and the topography of the same sample surface can exhibit different characteristic responses [12].

5. The spectral responses of near-field detection with a metallic tip ranges from the ultraviolet to the infrared because of the use of external optics (e.g. a Cassegrain objective mirror or a lens made of an appropriate material), while the spectral response of an aperture probe is limited by the material of the waveguide. Because the scattering efficiency of a metal is higher in the infrared region than in the visible, then the use of metallic probe tip can be beneficial in infrared microspectroscopy [13,14].

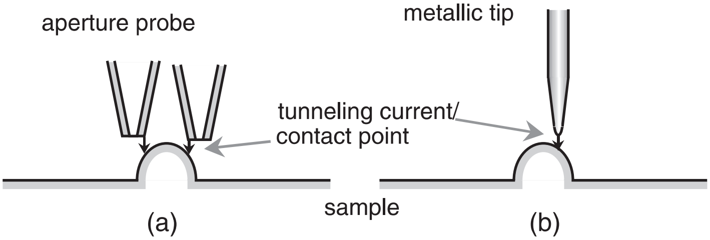

Fig. 3. Operation of NSOM probe tips as STM/AFM probes: (**a**) a fiber probe with a coated metal film, and (**b**) a metallic tip

3 Near-Field Imaging Using a Metallic Tip

In this section, we describe an NSOM that use a metallic tip, and several near-field optical images obtained with it. The contrast of near-field imaging is also discussed.

3.1 Scattering of an Evanescent Field at a Metallic Tip

Figure 4 shows the configuration of the system that we developed [2]. A laser diode ($\lambda = 670\,\mathrm{nm}, 10\,\mathrm{mW}$) illuminates the sample above the critical angle so as to achieve dark-field illumination. The evanescent field generated over the sample surface is scattered by the insertion of a platinum–iridium probe tip. The scattered field is collected towards a photomultiplier tube (PMT) by a long-working-distance objective lens (NA = 0.35, 20×). The PMT is

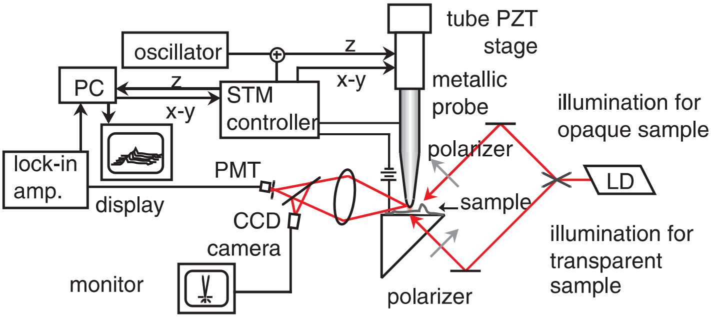

Fig. 4. NSOM system combined with STM

electronically cooled to reduce thermal noise. The probe tip is scanned in three dimensions, using a tube-type piezoelectric transducer stage.

Figure 5a shows a photograph of a metallic tip which is shining by the scattering of evanescent field. This was taken by the CCD camera shown in Fig. 4. There was not any particular sample on the prism surface; the illumination light was incident on the surface of the prism at an angle larger than the critical angle. The very small area of light is well seen on the tip of the probe. The size of the scattering area of the light was actually much smaller than the radius of the tip, while in the figure we have integrated the weak intensity in a long-time exposure so that the area visible in the figure is larger than the actual size seen in the experiment. Figure 5b shows a photograph of the same tip, but purposely illuminated with a fiber-bundle illuminator beside the probe and the sample to show the shape of the tip. The lower half of the photograph shows a mirror image of the tip reflected in the prism surface.

In any configuration of an NSOM with a metallic tip, unwanted stray light from the sample surface exists. Such stray light has to be eliminated to enhance the signal-to-noise ratio of the near-field signal. Evanescent illumination using total internal reflection is one of the methods to reduce the unwanted scattered light. However, all stray light is not necessarily elimi-

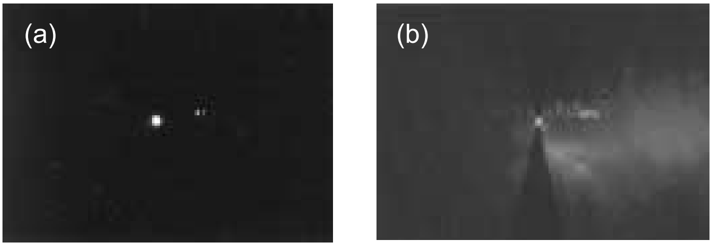

Fig. 5. (**a**) Photograph of a probe tip shining in the evanescent field, and (**b**) the tip illuminated by an external light; reflection of the tip is visible as the reflection

nated by using such illumination, as shown in Fig. 5. Another method for rejection of the stray light is a lock-in detection technique. To recover only the scattered evanescent signal, we vibrate the probe tip along the z axis at a certain frequency and with nanometric amplitudes, and the detected signal is demodulated with a lock-in detection technique. Only the scattered evanescent field is recovered, because the intensity distribution of the light field localized on the surface decays rapidly along the z axis. In contrast, the intensity of the non-evanescent waves does not decay at subnanometric resolution. As a result, unwanted contributions from scattered non-evanescent photons, as well as background stray light, are eliminated in the measured signal.

We performed an experiment to measure the exponential decay of the evanescent field produced by the total internal reflection with this NSOM. Figure 6a shows the experimental result for the light intensity (with lock-in-amplified detection) as a function of the distance between the tip and the surface. To show the reproducibility of the experiment, two curves obtained in two separate experiments are shown in this figure. The sample surface was BK7 glass with a surface precision of $\lambda/4$. The amplitude of tip vibration was 4.7 nm at a frequency of 2.5 kHz. This plot shows good agreement with the exponentially decaying curve of the evanescent field; the incidence angle calculated from the data is 46.9 degrees, and experimentally it is ∼47 degrees. Even though the light intensity when modulated by tip vibration is not sinusoidal, the lock-in detection picks up only the component at the fundamental frequency, and hence distortion should not occur in the results.

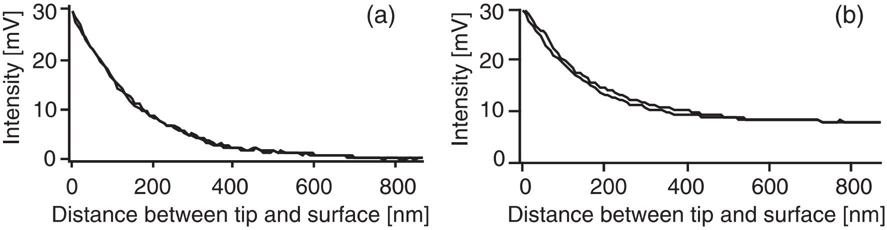

Fig. 6. Experimental result for the light intensity as a function of the distance between tip and surface; (**a**) with tip vibration (2.5 kHz) and lock-in detection, and (**b**) without tip vibration but with laser-diode flickering (2.5 kHz) instead. The sample was BK7 glass with a precision of $\lambda/4$

There is another way to modulate the intensity of the detected signal; to modulate the laser-light intensity. Figure 6b shows a plot for the same sample with the same experimental setup, except that the modulation was performed by intensity modulation of the laser diode at 2.5 kHz (the probe was stationary). Although the result shown in Fig. 6b looks similar to Fig. 6a, it contains a biased component due to the scattering of light coming out of the probe tip. This result indicates that intensity modulation does not work at all for measuring the true distance between tip and surface.

3.2 Observation of Surface Wave on a Periodic Structures

We analyzed the surface of a periodic structure (i.e. a grating) using the NSOM system [11]. Sample was placed on a triangular prism (BK7, refractive index = 1.513), and oil was introduced to match the refractive indices of the sample and the prism. A gold film was coated onto the sample surface with a thickness of 20 nm in order that the tip position along the z axis could be held constant using servo control of the STM operation, and that the amount of evanescent photons would be large enough to penetrate the metal coating from the prism side to the probe side.

Figure 7 shows an NSOM image of the sample surface, obtained using the STM feedback mode. The entire image has surface dimensions of 5µm × 5µm and sampling was done at scanning steps of 10 nm. The guide grooves, which are separated at intervals of 1.6µm, can be seen in the observed image.

A Pt–Ir probe tip with a diameter of 70 nm at its apex was used in the experiment. The tip was axially modulated at 10 kHz with an amplitude of 0.5 nm. The tunneling current and the bias voltage were selected as 0.5 nA and 1.0 V, respectively.

In the figure, the sample was illuminated from right to left, in a direction perpendicular to the groove orientation. The illumination light was in the TE mode (s-polarized), but an analyzer was not employed during detection.

Because the tip–sample distance was always held constant by regulating the STM tunneling current, the image does not describe the surface profile of the sample, but only the distribution of the localized fields at its surface. Groove edges are imaged more brightly than the central regions because the latter contain only the evanescent field produced by total internal reflection at the surface. On the other hand, the grooves are imaged more intensely because the evanescent field generated by the higher spatial frequencies constituting the structure of the groove edge is characterized by a wave vector that is larger in a certain direction than that of the illuminating light.

Fringes with a period of about 260 nm can also be seen in the central regions. The fringes are formed by interference between the light field diffracted by the periodic groove structures. These fields are evanescent because they are scattered at high diffraction orders.

Figure 8 shows a STM image which represents the surface profile of the same area as analyzed in Fig. 7. Note that the central regions bounded by pairs of grooves have a measured width of about 1.1µm. The grooves themselves have widths of about 0.5µm.

Figure 9 presents a NSOM image obtained using the same STM regulation of the tunneling current as in Fig. 4, but with TM mode (p-polarized) illumination. The scattered light intensity is ten times larger than what was obtained in the image shown Fig. 7. Note that the fields at the groove edges

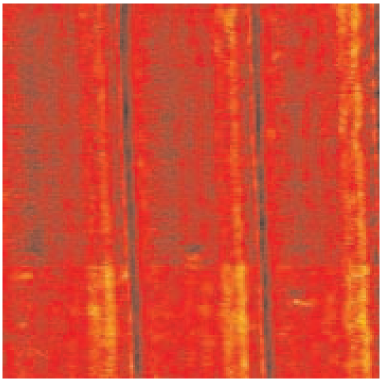

Fig. 7. NSOM image (5µm × 5µm) of a grating in the STM feedback mode. An s-polarized illumination was used

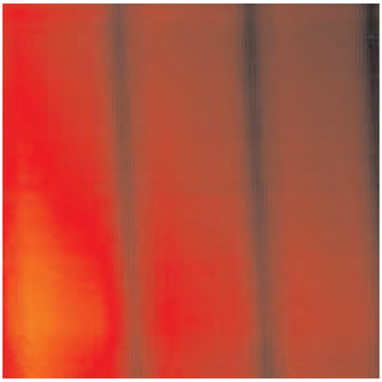

Fig. 8. STM image of the same portion of the grating as shown in Fig. 7

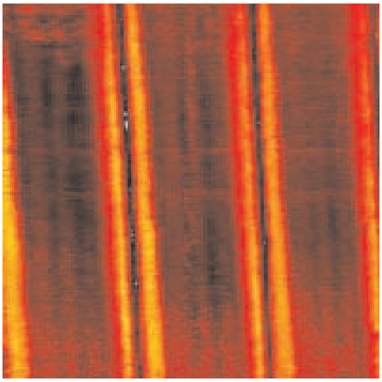

Fig. 9. NSOM image of the grating in the STM feedback mode. A p-polarized illumination was used

are imaged much more brightly than the other regions of the surface. Figures 7 and 9 illustrate that NSOM imaging is strongly polarization-dependent.

In Figs. 10a and 10b are single scan profiles (from left to right) of the images shown in Figs. 9 and 8, respectively. No averaging or smoothing has been done in these profiles. The NSOM profile in Fig. 10a clearly illustrates the localization of the evanescent field at the groove edges. Interference fringes can be also observed in Fig. 10a. Figure 10b correctly indicates an inclination of the sample surface, which a NSOM image does not detect. Thus STM and NSOM images can provide unique information about the sample surface.

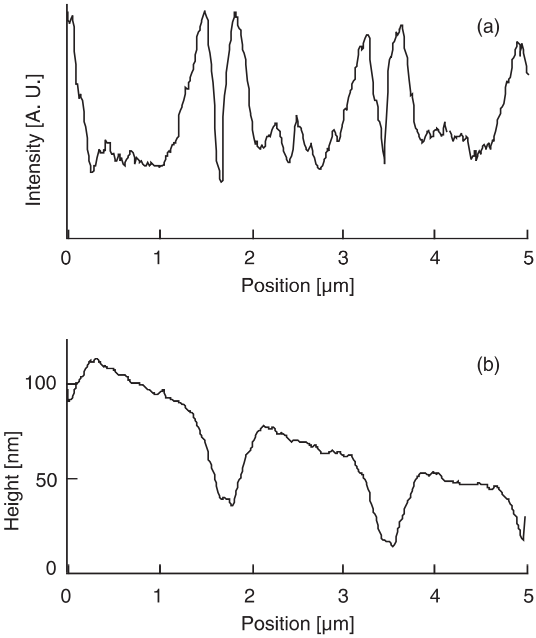

Fig. 10. Single scans from (**a**) the NSOM image in Fig. 9 and (**b**) the STM image in Fig. 8

3.3 Biological Sample

Figure 11a shows an NSOM image of a murine embroynal myocardial cell. In this figure, the sample was illuminated from the right to the left. The illumination light was in the TM mode (p-polarized). The scattered light from the scatterer was detected with an analyzer in the p polarization. The entire image has surface dimensions of 10μm × 10μm and was sampled at scanning steps of 40 nm. Figure 11b shows an STM image which represents the geometric surface structures of the same area as shown in Fig. 11a. Unlike the STM image, the NSOM image does not represent the geometric structure of the sample, but represents the localized evanescent field near the sample.

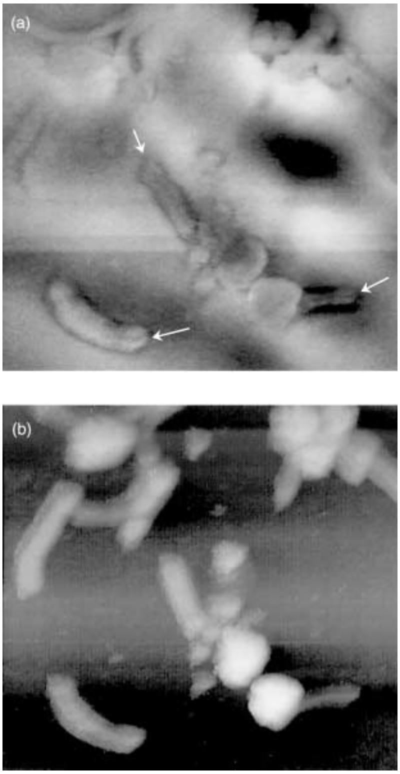

Fig. 11. (**a**) NSOM image and (**b**) topography of a murine embroynal myocardial cell

This image corresponds to the distribution of the effective refractive index of the sample. In particular, as shown by the white arrows in Fig. 11a, narrow channel structures were observed in the NSOM image, but not seen in the STM image, which means that these structures correspond to fine variations of the refractive index in the cells.

3.4 NSOM Imaging in Reflection Mode

A metallic tip can also be used for analyzing opaque samples such as semiconductors and metals in the reflection mode. Figure 12 illustrates a configuration employed in constructing a reflection mode apertureless NSOM [15]. The sample surface nearest to the probe tip is illuminated by light that is incident at a large angle relative to the surface plane. The light field that is scattered by both the probe tip and the sample is collected into a photo detector using external optics. The tip is scanned across the sample surface to produce a near-field optical image of the sample surface. Specular reflection of the incident light cannot enter the photo detector if the angle of incidence is made larger than the observation angle of the external optics. Undesirable stray light contributions from sample regions not within the proximity of the

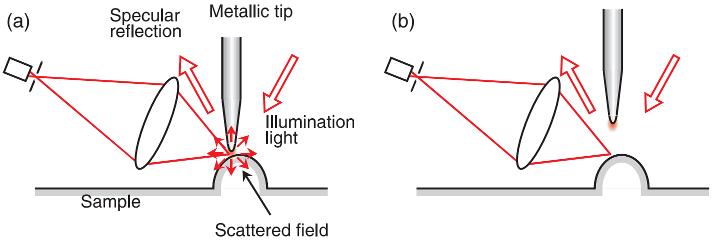

Fig. 12. Illustration of the principle of the reflection mode NSOM that employs a single metallic probe tip. (**a**) When the tip is near the sample surface, and (**b**) When the tip is far from the sample surface and it does not scatter the evanescent field

tip apex are minimized by vibrating the probe tip and employing the lock-in detection technique [2].

The experimental setup that we used was the same as that in Fig. 4 except for the illumination optics. The sample is illuminated at an incidence angle of about 50 degrees to achieve the desired dark-field illumination. The sample was a fine-pitched silicon grating (period 240 nm) which was fabricated using a laser holographic lithography technique. Details of the sample fabrication are described in [16]. Figure 13a presents a near-field image obtained under p-polarized illumination and with the tunneling current kept constant at 0.5 nA, while Fig. 13b presents an STM image of the same surface area (tunneling current = 0.5 nA, bias voltage = 2.0 V). Both of these images have surface dimensions of 1 μm × 1 μm and were sampled at scanning steps of 2 nm in the x directioan and of $8nm$ in y direction. The illumination light was incident, in this figure, from the left of the surface normal. Figures 13c and 13d show representative cross sections of the images in Figs. 13a and 13b, respectively. The STM image indicates a rectangular profile for the sample, while the electromagnetic field is localized more intensely near the edges of the grating structures. This is because the edges have geometrical structures that are smaller than the illumination wavelength, which is a condition for producing a strong localization of the evanescent field.

The electromagnetic field that was localized at the edge, with dimensions of about 60 nm, could be observed clearly, as shown in Fig 9. This size is, according to the STM image, equivalent to the size of the grating groove. This result indicates that our system has an image resolution of at least 60 nm or $\lambda/11$ for ligth of wavelength 670 nm light. Although we did not examine our system with a test sample having much finer structures, the result in Fig. 13a implies that the resolution of our system could be as fine as 6 nm or $\lambda/100$.

3.5 Multiheight Imaging

A NSOM changes the light field on an extremely small area of the sample surface by inserting a probe tip into the near-field of the sample surface.

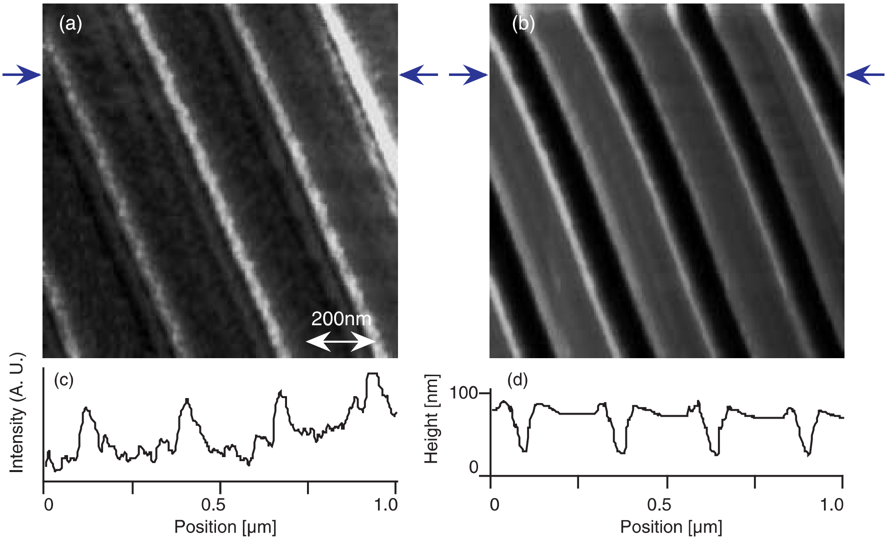

Fig. 13. Images (1 μm × 1 μm) of a fine-pitched grating (period = 240 nm): (**a**) STM image representing a topographic image of the sample surface, (**b**) near-field optical image obtained with p-polarized illumination (STM feedback mode), (**c**) cross section of Fig. 13a, and (**d**) cross section of Fig. 13b

Since the tip and the sample are very near each other, much nearer than the wavelength of the incident light, the photons scattered at the probe are rescattered by the sample structure and subsequently scattered again by the probe. Near-field imaging is based on multiple scattering, or interaction of photons with the total system, including the probe and sample. The image obtained from a NSOM is very dependent on the size of the gap between the probe and the sample surface, which makes it difficult to interpret NSOM images. Experiments were conducted to investigate the sensitivity of NSOM imaging to experimental parameters, including the polarization of the illumination as shown in Figs. 7 and 9, and the angular dependence of the detection [17]. In this section, we show our experimental results for NSOM imaging with our NSOM (see Fig. 4), with which we can obtain images of the sample with various gaps between the probe and the sample surface [18].

Figure 14 shows the scanning sequence of the system developed. First, the metallic tip is brought to position A near the sample surface, where the tunneling current between the tip and the sample surface reaches a value specified by the computer. Then the tip is lifted to positions B, C, and D sequentially by application of a series of bias voltages to the piezo transducer. The sequence of bias voltages is preset by a computer program. The number of positions at a single point is also programmable. At every height an optical signal is detected with a PMT. After the signals have been collected at the same location for the different heights, the probe returns to the initial height

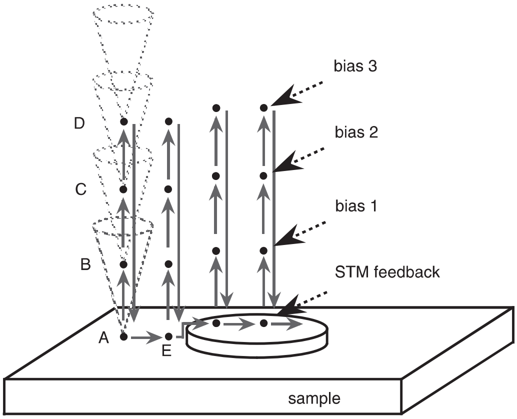

Fig. 14. Scanning sequence of the multi-height NSOM

at which the tunneling current is controlled, and then moves to the next point E. After the experiment is completed, images of the same sample at different heights are reconstructed from the measured data series. The exact height (or size of the gap) as a function of the bias voltage applied to the piezo tube was calibrated in advance by measurement of the movement of the piezo.

Using this system, we measured optical images of a grating coated with a 40 nm thick gold film with 40 nm deep grooves of period 1.6µm. Figure 15 shows a series of near-field optical images, with STM images at the top. The laser used for illumination was a laser diode with a wavelength of 670 nm. The sample was illuminated with p-polarized light in a direction perpendicular to the groove orientation. The probe tip was an apertureless platinum–iridium tip with a apex of 50 nm diameter. The scanned area was 3µm × 0.25µm, or 256 × 20 pixels, with each pixel measuring 12 nm × 12 nm.

In the STM image shown at the top of Fig. 15, the longitudinal grooves are clearly seen at the ends and at the center. The other 13 images are optical images measured at various sizes of the gap. The size of the gap is shown to the left of every image. The value of 0 nm indicates the position at which the STM image was detected, which was ~ 1 nm from the surface.

Fine structures with sizes near 400 nm, which is finer than the diffraction limit of the light, can be seen in all images measured at gaps between 0 and 10 nm. There is no such fine structure contained in this grating, as can be seen in the STM image. The fine structures represent a surface standing wave caused by interference between the high-order diffracted fields that are generated by the periodic structure of the sample, as mentioned above. Since this interference is formed by the surface wave or the evanescent wave, it disappears in the images as the tip moves up. The effective depth of this evanescent wave is ~ 10 nm according to these results.

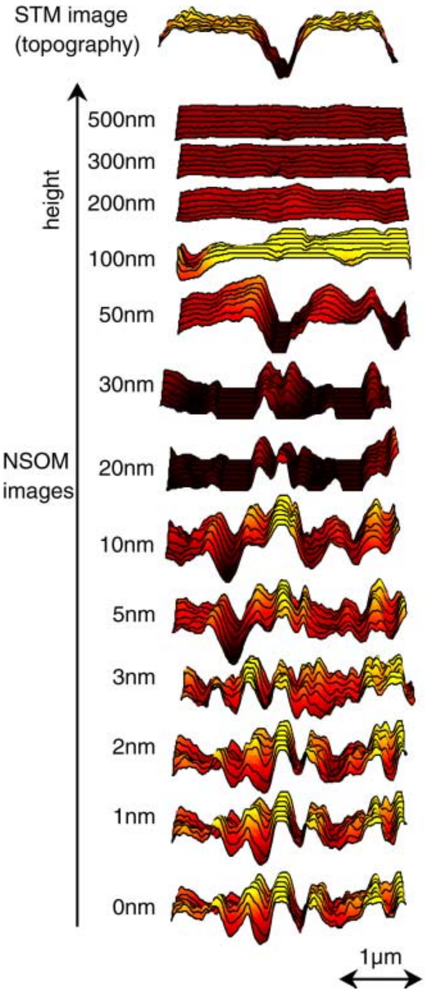

Fig. 15. Near-field optical images of a gold-coated glass grating (1.6μm pitch) at various sizes of the gap. The value to the *left* of each near-field image indicates the measured height relative to the position at which STM image was detected

The image at 50 nm is the one most similar to the STM image or to the topography of the sample structure. A resonance effect [19] may occur within the gap, diameter of the probe tip and the sample structure (groove depth), because they have similar dimensions. When the distance between the tip and the sample surface is larger than 100 nm, the image contrast does not reflect information from the sample.

Figure 16 shows the spatial-frequency distribution (or the one-dimensional Fourier transform) of the images shown in Fig. 15 with respect to the hori-

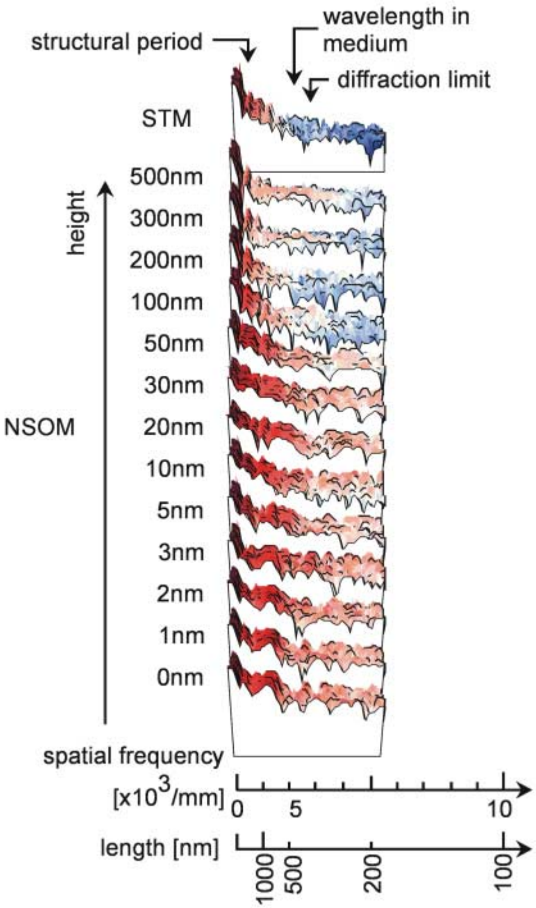

Fig. 16. Spatial-frequency distribution of the data shown in Fig. 15

zontal axis. As the probe approaches the surface the high-frequency components (on the right of the plots) increase compared with the lower-frequency components (on the left of the plots). The plot for a distance of 50 nm most resembles the STM image. In the images obtained with the tip located at less than 50 nm from the surface, components that are higher than the diffraction limit are included. The frequency of the diffraction limit ($\lambda/2 = 335$ nm) and that of the wavelength in the sample medium ($\lambda/1.5 = 450$ nm) are marked in the STM plot at the top of Fig. 16. For a super-resolution image beyond the diffraction limit, the gap between the probe and the sample must be smaller than ~ 50 nm. In the images in which the gap is larger than 200 nm, the low-frequency component representing the background image intensity dominates the spectrum.

We must point out that a single NSOM image is insufficient for reconstructing optical-constant distributions. Multiple images, observed with different known parameters, are necessary for reconstructing the original topographical (height) and material (or optical-constant) distribution of the sample surface.

4 Near-Field Spectroscopy Using a Metallic Tip

NSOM allows molecular imaging and the detection of molecular dynamics with super-resolution capability, e.g. single-molecule detection. Several researchers have succeeded in determining the orientation of an isolated fluorescent molecule [20], measurement of the lifetime in the excited state [21], and observation of energy transfer mechanisms between donor and acceptor fluorophores [22] by applying NSOM to fluorescent spectroscopic measurements.

Another alternative for molecular imaging and detection on the molecular scale is available through the combination of NSOM with vibrational spectroscopy. Raman spectroscopy is an especially promising candidate for near-field vibrational spectroscopy because a visible laser is available and because rich information about molecular vibration is obtained directly by measuring the Raman spectrum. In this section, we describe near-field Raman spectroscopy performed by using an NSOM with a metallic tip. The strongly localized field and the surface-enhanced field caused by metallic islands (SERS, surface-enhanced Raman scattering) compensates for the very low cross section for Raman scattering ($10^{-30}\,\mathrm{cm}^2$), which is much smaller than that for fluorescence ($10^{-16}\,\mathrm{cm}^2$).

Figure 17 shows the configuration of our NSOM, with a metallized cantilever which is operated in AFM mode. A light field from an Ar ion laser ($\lambda = 488\,\mathrm{nm}$, power 10 mW, polarization linear) enters the epi-illumination optics after being expanded and collimated. That part of the illumination light which corresponds to an NA smaller than 1.0 is rejected by inserting a mask (shown in the inset of Fig. 17) in front of a beam splitter [23]. Then, the annular illumination light is focused onto the sample surface by using an oil-immersion objective lens (NA 1.4, magnification 60×). The focused light spot consists of only an evanescent field because only the component of the illumination which corresponds to NA > 1.0 is transmitted by the mask. The size of the focused spot can be as small as $\lambda/2$. When the cantilever approaches this evanescent focused spot, part of the evanescent light is scattered and converted into propagating light. The scattered light is collected by the same objective lens or another long-working-distance objective lens to the side of the cantilever, and detected with PTMs or with a polychromator with a CCD camera equipped with an image intensifier, for spectroscopy. Excitation light and Rayleigh scattering are rejected completely by a notch filter ($\lambda = 488\,\mathrm{nm}$, full width at half maximum 15 nm). Light from the laser diode which is used

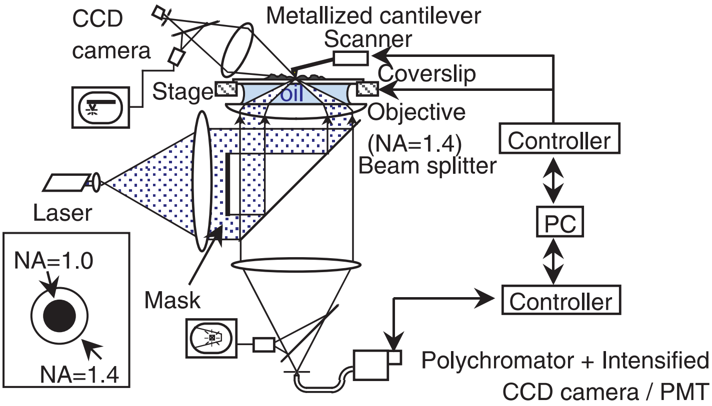

Fig. 17. Experimental setup for near-field spectroscopy

for AFM control is also eliminated through a long-wavelength-cutoff filter. The cantilever was monitored with CCD cameras during operation. A pinhole was placed in front of each PTM to reduce stray light. A silicon cantilever coated with a silver film of 40 nm thickness was used in the experiment, because the scattering efficiency of silver is highest at 488 nm. The sample was scanned with piezoelectric transducers in the $x - y$ plane while the cantilever was regulated by AFM feedback in the z direction.

Figure 18 shows a near-field SERS spectrum of rhodamine 6G obtained with the NSOM system that we developed, using the silver-coated cantilever [24,25]. This spectrum was obtained by subtracting the spectrum obtained without the silver-coated cantilever from the one obtained with the silver-coated cantilever. The spectrum in Fig. 18 consists of only the near-field-excited SERS signal, while the spectrum obtained with the silver-coated cantilever includes not only the near-field-excited SERS signal, but also the SERS signal excited by the evanescent focused spot, as mentioned earlier. Eight Stokes-shifted Raman lines were observed at 611 cm^{-1}, 771 cm^{-1}, 1190 cm^{-1}, 1313 cm^{-1}, 1364 cm^{-1}, 1512 cm^{-1}, 1574 cm^{-1}, and 1653 cm^{-1} in the spectrum. These Raman lines correspond to the stokes shift of the C–C stretching vibration mode. The exposure time for obtaining the spectra was 5 seconds and no data accumulation was used. This time was shorter than that necessary with an aperture probe [26]. From the experimental results, we estimate the factor of enhancement to be 40 by assuming that the size of the focused spot 400 nm and the radius of the tip is 20 nm.

Figure 19 shows a near-field spectrum of the same sample as in Fig. 18, but was obtained using a silicon cantilever. No Raman line is observed in the spectrum. The reason is that the silicon cantilever does not enhance the electric field at the tip apex sufficiently for the Raman lines to be measurable.

We also measured the SERS spectra of the sample while the cantilever was scanned over the evanescent focused spot. Figure 20 shows line images of

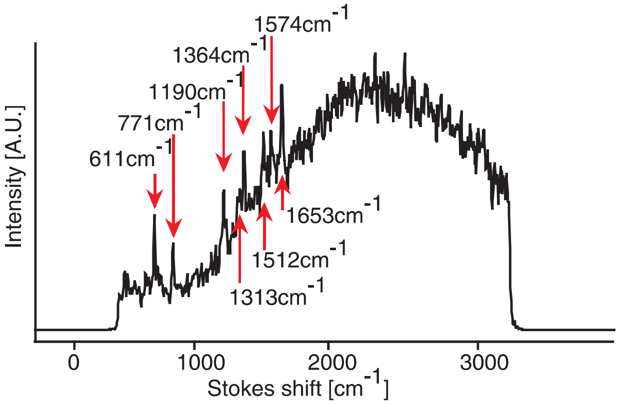

Fig. 18. Near-field SERS spectrum obtained with a silver-coated cantilever

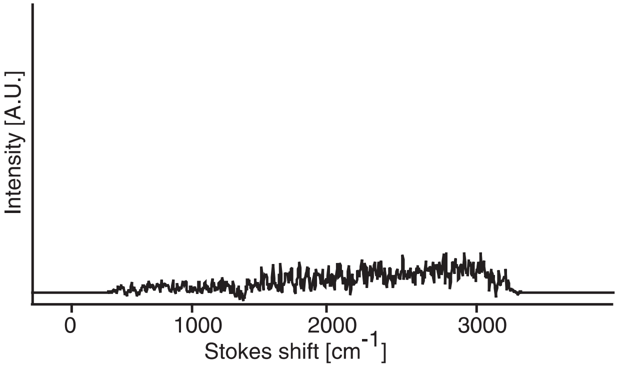

Fig. 19. Near-field SERS spectrum obtained with a silicon cantilever

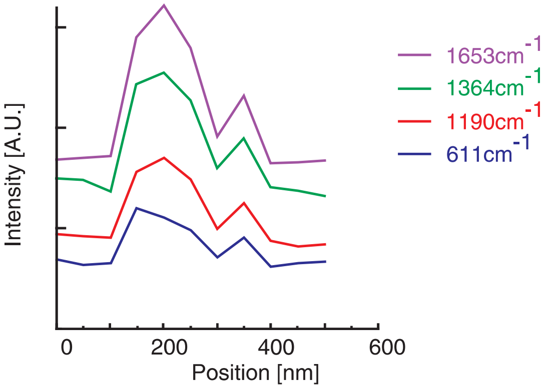

Fig. 20. Plots of typical Stokes shift lines

four near-field Raman shift peaks at 611 cm^{-1}, 1190 cm^{-1}, 1364 cm^{-1}, and 1653 cm^{-1}. A lateral resolution of ~ 50 nm is achieved in this experiment.

Near-field SERS spectra which are enhanced by a silver-coated cantilever have been shown above. The spectra give direct information about molecular vibrations. Near-field vibrational spectroscopy has the advantage of not subjecting the samples to photobleaching, and sample staining is not necessary.

References

1. R. K. Chang, T. E. Furtak, (Eds.), *Surface Enhanced Raman Scattering* (Plenum, New York 1982) 29
2. Y. Inouye, S. Kawata, Opt. Lett. **19**, 159–161 (1994) 29, 33, 40
3. H. Furukawa, S. Kawata, Opt. Commun. **132**, 170–178 (1996) 30
4. H. Furukawa, S. Kawata, Opt. Commun. **148**, 221–224 (1998) 30
5. O. J. F. Martin, C. Girard, Appl. Phys. Lett. **70**, 705–707 (1998) 30
6. J. W. Goodman, Introduction to Fourier Optics (McGraw-Hill, San Francisco 1968) 31
7. F. Zenhausern, Y. Martin, H. K. Wickramasinghe, Science **269**, 1083–1085 (1995) 32
8. J. Koglin, U. C. Fischer, H. Fuchs, Phys. Rev. B **55**, 7977–7984 (1997) 32
9. J. P. Fillard, *Near Field Optics and Nanoscopy* (World Scientific, Singapore 1996) 32
10. F. Zenhausern, M. P. O'Boyle, H. K. Wickramasinghe, Appl. Phys. Lett. **65**, 1623–1625 (1994) 32
11. Y. Inouye, S. Kawata, J. Microsc. **178**, 14–19 (1995) 33, 36
12. K. Lieberman, A. Lewis, Appl. Phys. Lett. **62**, 1335–1337 (1993) 33
13. A. Lahrech, P. Bachelot, P. Gleyzes, A. C. Boccara, Opt. Lett. **21**, 1315–1317 (1996) 33
14. B. Knoll, F. Keilmann, Nature **399**, 134–137 (1999) 33
15. Y. Inouye, S. Kawata, Opt. Commun. **134**, 31–35 (1997) 39
16. Y. Nakayama, K. Toyoda, Proc. SPIE **2196**, 74–84 (1994) 40
17. B. Hecht, D. W. Pohl, H. Heinzelmann, L. Novotny, "Tunnel" near-field optical microscopy: TNOM-2., in *Photon and Local Probes*, O. Marti, R. Moller (Eds.), NATO ASI Series E **300**, 93–107 (Kluwer Academic, Dordrecht 1995) 41
18. H. Hatano, Y. Inouye, S. Kawata, Opt. Lett. **22**, 1532–1534 (1997) 41
19. M. Xiao, Opt. Commun. **136**, 213–218 (1997) 43
20. E. Betzig, R. J. Chichester, Science **262**, 1422–1427 (1993) 45
21. X. S. Xie, R. C. Dunn, Science **265**, 361–364 (1994) 45
22. T. Ha, Th. Enderle, D. F. Ogletree, D. S. Chemla, P. R. Selvin, S. Weiss, Proc. Natl. Acad. Sci. (USA) **93**, 6264–6268 (1996) 45
23. N. Hayazawa, Y. Inouye, S. Kawata, J. Microsc. **197**, 472–476 (1997) 45
24. N. Hayazawa, Y. Inouye, Z. Sekkat, and S. Kawata, Opt. Commun. **183**, 333–336 (2000) 46
25. N. Hayazawa, Y. Inouye, Z. Sekkat, and S. Kawata, Chem. Phys. Lett. **335**, 369–374 (2001) 46
26. V. Deckert, D. Zeisel, R. Zenobi, T. Vo-Dinh, Anal. Chem. **70**, 2646–2650 (1998) 46

Controlling Light Confinement by Excitation of Localized Surface Plasmons

Ulrich Ch. Fischer[1], Alain Dereux[2], and Jean-Claude Weeber[2]

[1] Physikalisches Institut, Westfälische Wilhelms Universität
Wilhelm Klemmstrasse 10, 48149 Münster, Germany
[2] Laboratoire de Physique, Optique Submicronique,
Université de Bourgogne, 21004 Dijon, France
`fischer@nwz.-uni-muenster.de`

Abstract. Localized surface plasmons can be used to control near-field optical phenomena in the subwavelength range. Specifically, this chaper reviews recent results which show that localized surface plasmons can confine the optical intensity down to nanoscopic dimensions. The discussion first considers how a collection-mode near-field optical microscope can observe the squeezing of the plasmon field of metallic nanostructures deposited on a flat surface. Numerical simulations then provide illustrations of the confined fields associated with nanostructures which are feasible using current microfabrication techniques. Finally, we present arguments which explain how localized surface plasmons can deliver a significant amount of power to the very end of a tetrahedral tip used as the light source of an illumination-mode near-field optical microscope.

1 Introduction

Localized surface plasmons have been used and/or observed since the early development of near-field optical microscopy. In this context, localized surface plasmons not only are interesting as fundamental phenomena to be studied per se, but also turn out to be useful for controlling near-field optical phenomena in the subwavelength range.

Both collection [1,2,3,4,5,6,7,8] and illumination [9,10] mode near-field optical microscopes (see [11] for a classification of the various setups of near-field optical microscopes) have been used to study the basic properties of localized surface plasmons related to micro- and nanostructures deposited on surfaces. The principle of controlling near-field optical phenomena on the basis of plasmon properties appears not only in some near-field optical microscopes which exploit directly a signal relying on localized surface plasmons [12,13,14,15] but also in the suggestion of optical microdevices relying on surface plasmons [16] as well as in the recent direct observation of controlled plasmon coupling [17].

Among the possible applications of localized surface plasmons, this chapter reviews specifically those recent results which show that localized surface plasmons can confine the optical field intensity down to nanoscopic dimensions. By ‘confined optical field intensity’, we mean here that the spatial distribution of the optical field intensity, *in the near-field zone*, close to an

S. Kawata (Ed.): Near-Field Optics and Surface Plasmon Polaritons,
Topics Appl. Phys. **81**, 49–69 (2001)

underlying small particle, shows a sharp peak which extends over a volume whose typical diameter is of the order of the transverse size a of the said small particle. We shall refer to 'squeezing' of the field when this phenomenon of field confinement is reduced to a size smaller than a.

Confined or, even better, squeezed fields are desirable for at least two purposes. First, spatial confinement of the optical field is a prerequisite for achieving the miniaturization of optical and optoelectronic devices [18,19,20]. Second, in illumination-mode Scanning Near-Field Optical Microscopes (SNOMs), obtaining confined fields at the apex of the local probe tip is the key property for achieving high spatial resolution.

Section 2 will first consider the squeezing of the plasmon field as observed by a collection-mode Photon Scanning Tunneling Microscope (PSTM). Numerical simulations presented in Sec. 3 will demonstrate that confined plasmon fields may be achieved with several kinds of nanostructures. Finally, Sec. 4 will discuss how localized surface plasmons may bring a significant amount of power to the very end of a tetrahedral tip used as the light source of a SNOM.

2 Squeezing of the Plasmon Field

Using a collection-mode near-field optical microscope such as the PSTM [21], it is possible to observe, in the near-field zone, the distribution of the optical field associated with the localized surface plasmons of resonant metallic nanostructures. Indeed, when a bare elongated optical fiber is used as the local probe, the images recorded by a PSTM can be directly compared with the near-field distribution of the electric field intensity $|\boldsymbol{E}(\boldsymbol{r})|^2$ associated with the optical field, as calculated by the numerical solution of the Maxwell equations [22,23,24]. Experiments have shown that the spatial distribution of $|\boldsymbol{E}(\boldsymbol{r})|^2$ close to resonant small metal micro- and nanostructures is not always confined to the dimensions of the structure. Independently of the broadening related to the finite size of the local probe, the spatial distribution of the localized surface plasmon field outside a small particle may often be spread over an area of the order of λ^2, where λ is the incident wavelength. In order to observe confinement or to obtain squeezing of the near-field distribution of $|\boldsymbol{E}(\boldsymbol{r})|^2$, well-defined conditions must be searched for. We report here the recent work of *Krenn* et al. [17], which illustrates this point.

Au particles were deposited on an ITO (Indium Tin Oxide)-doped glass substrate by a microfabrication process. Their geometry was checked by scanning electron microscopy and Atomic Force Microscope (AFM) measurements. The particle shape was found to be akin to half on oblate spheroid (cut by the plane of the substrate). Their typical sizes were $100 \times 100\,\mathrm{nm}^2$ in section and 40 nm in height. A microspectrometer located in the far-field measured the plasmon peak of the single particles at a wavelength of 640 nm.

The plasmon resonance of the Au particles is associated with a large lateral variation of the intensity in the near-field zone so that image acquisition cannot be performed efficiently at constant intensity. To record the spatial distribution of $|\boldsymbol{E}(\boldsymbol{r})|^2$ close to a particle, the tip was thus scanned at a constant height above the sample surface while monitoring the light intensity level. Successive images were recorded while bringing the tip closer to the sample surface by 5 nm steps. The series of images terminated when the tip touched a particle. The last complete image which was recorded before the tip crash was retained.

On the basis of the results found for dielectric samples [23], the use of sharpened, bare (uncoated) optical fiber tips in PSTM leads us to compare the experimental image with the theoretical distribution of $|\boldsymbol{E}(\boldsymbol{r})|^2$, as provided by a solution of the Maxwell equations *which does not include any tip.* In the computation, the p-polarized incoming field ($\lambda = 633$ nm) was adjusted to fit the experimental conditions: total internal reflection with an angle of incidence equal to 55 degrees, and with the projection of the incident wave vector onto the surface of the substrate pointing mostly towards the y direction but with a slight tilt towards the upper left corner of the images. The numerical solution was obtained by applying Green's dyadic technique [25], discretizing a single Au particle into $10 \times 10 \times 10$ nm^3 cubic cells.

Figure 1 compares a theoretical computation with an experimental PSTM image recorded above an isolated Au particle. Figure 1b maps the distribution of the normalized intensity of the electric field associated with the optical wave ($|\boldsymbol{E}(\boldsymbol{r})|^2/|\boldsymbol{E}_0(\boldsymbol{r})|^2$) at a constant height $z = 140$ nm above the glass substrate. This constant height does not correspond to the experimental tip-to-sample distance, which was determined to be less than 45 nm since the experimental image displayed in Fig. 1 was the last one recorded before the tip touched the particle, when the tip approached 5 nm closer to the sample. The height $z = 140$ nm was found to provide the best agreement between the computed image and the experimental one after the computed distribution patterns in planes parallel to the substrate surface at heights ranging between 0 and 200 nm were examined systematically. Since, in this height range, the distribution patterns are very similar from one plane to another, the best agreement was defined as that obtained when the pattern exhibited contrast between the lowest and the highest intensity which is closest to the experimental image. We justify this procedure by the fact that the tip is not included in the calculation. Since the tip integrates the optical field over a certain volume, the height $z = 140$ nm should be interpreted as a rough modeling of the averaging process occurring inside the tip.

The agreement between the patterns of the calculated and the experimental images is excellent. Since the simulation has not included the tip, the experimental image exhibits a broader and less contrasty pattern. The simulation recovers successfully the interference between the incident surface optical wave and the wave scattered by the Au particle. The computation

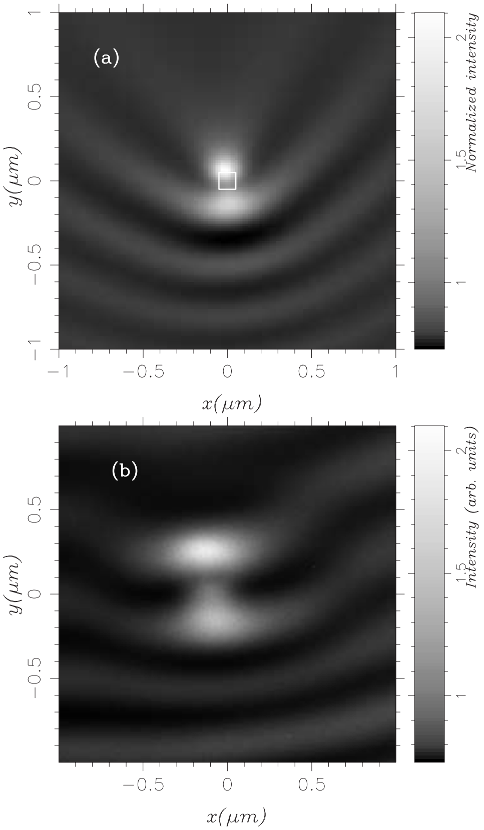

Fig. 1. Comparison of a theoretical computation (**a**) with an experimental PSTM image recorded at constant height (**b**) of an Au particle ($100 \times 100 \times 40\,\mathrm{nm}^3$) deposited on an ITO glass substrate. The particle is centered at the origin of the coordinate system in the computation (**a**) (the surface projection of the model particle corresponds to the *white square*) while it is slightly translated to the left in the experimental image (**b**)

fixes the exact position of the particle to be between the two central bright spots. We conclude that the near-field optical signature of such an isolated resonant Au particle is much larger than the size of the underlying particle.

However, Au particles identical to the one described above may be arranged in order to construct a squeezed distribution of $|\boldsymbol{E}(\boldsymbol{r})|^2$. This can be achieved by aligning 10 000 of such particles in a row with a spacing of 100 nm. In this configuration, the localized plasmons of each individual particle may couple to each other and setup a hybrid plasmon mode. The observed image, using the same illumination and detection conditions as in the preceding section, is shown in Fig. 2a. The main feature of this coupling is the transverse squeezing of the optical field distribution which contrasts

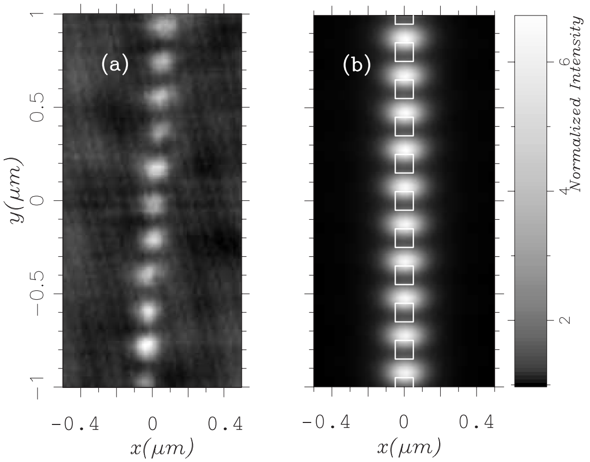

Fig. 2. (**a**) Constant-height PSTM image recorded above a chain of Au particles (individual size: $100 \times 100 \times 40\,\mathrm{nm}^3$) separated from each other by a distance of 100 nm and deposited on an ITO glass substrate. A comparison with a numerical simulation (**b**) shows that the bright spots are not on top of the Au particles (the surface projections of the particles correspond to the *white squares*). The intensity scale of the experimental data (**a**) is normalized to that of the numerical calculation

with the broad spots found above a single particle (see Fig. 1). Indeed, the tip has integrated the detection of the optical field over its own volume at least. Consequently, the field distribution in the absence of the tip is probably narrower. The model calculation (Fig. 2 (b)) confirms that the spots are narrower than in the case of the single Au particle (Fig. 1). However, the calculated squeezing is not as narrow as in the experiment, since the modeling involved only 30 particles instead of the 10 000 present in the experiment. The squeezing probably increases as the chain length grows.

In this section, we have thus provided an illustration of the fact that obtaining a confined or squeezed field close to structures which can sustain surface plasmons requires one to search for particular conditions.

3 Localized Plasmons around Lithographically Designed Nanostructures

To show that confined plasmon fields may be achieved with several kinds of nanostructures, this section presents numerical simulations of the excitation of localized surface plasmons in nanostructures deposited on a flat, transparent substrate. As in the preceding section, the numerical simulations rely on Green's dyadic technique [25]. The chosen example, borrowed from [20], discusses the excitation of a single particle using metal nanowiress.

Such structures may be fabricated by currently available techniques such as electron beam lithography.

Let us consider a gold wire with a volume of $1000 \times 30 \times 20\,\mathrm{nm}^3$ deposited on a glass substrate. As stated in the preceding section, the excitation of the surface plasmons can be achieved under particular conditions. For the given geometry of the wire, we computed a spectrum in order to determine the incident wavelengths which can excite localized surface plasmons. The spectrum shown in Fig. 3 was obtained when one end, which are call the 'entrance', of the nanowire was excited by a focused beam. A model describing such an incident field has been developed by *Török* et al.to study the structure of the electric field associated with a plane wave focused through an interface between two materials with different refractive indexes [26,27,28]. The incident plane wave is linearly x-polarized and the objective lens has a numerical aperture of 0.9. The spectrum in Fig. 3 is related to the computed intensity at the other end, called the 'exit', of the nanowire when the incident wavelength is swept from the visible to the near infra-red. To compute this spectrum, the center of the incident beam was shifted away from the 'entrance' end of the wire in order to reduce the area of the particle illuminated by the incident light. The shift was chosen to be λ-dependent and was fixed at $\lambda/4$ in order to compensate for the spot size growing with increasing wavelength. Because the volume of the wire is large enough to exclude intrinsic size effects, we used the bulk tabulated values to describe the dielectric function of gold [29]. The computed signal Q versus the wavelength is defined as

$$Q(\lambda) = \frac{1}{S} \int_s \frac{\mid \boldsymbol{E}(x, y, z_{\mathrm{obs}}, \lambda) \mid^2}{\mid \boldsymbol{E}_0(x_{\mathrm{b}}, y_{\mathrm{b}}, z_{\mathrm{obs}}, \lambda) \mid^2} \mathrm{d}S \,, \tag{1}$$

where S is an area of $100 \times 50\,\mathrm{nm}^2$ located above the 'exit' end of the nanowire at a distance of 10 nm from the top of the nanowire.

$\boldsymbol{E}_0(x_{\mathrm{b}}, y_{\mathrm{b}}, z_{\mathrm{obs}}, \lambda)$ is the electric field associated with the incident wave at a point located in the observation plane $z = z_{\mathrm{obs}}$ above the 'entrance' of the wire, while $\boldsymbol{E}(x_{\mathrm{b}}, y_{\mathrm{b}}, z_{\mathrm{obs}}, \lambda)$ is the total field at a point located in the observation plane $z = z_{\mathrm{obs}}$ above the 'exit' of the wire; λ is the wavelength of the incident light in vacuum. The quantity $Q(\lambda)$ can be understood as a kind of near-field scattering coefficient that measures the near-field response at the 'exit' end of the wire relative to a given local excitation at the 'entrance'. This coefficient is proportional to the signal that would be detected by a PSTM. The spectrum plotted in Fig. 3 exhibits severals peaks in the red and near-infra-red regions. Because the peaks occur at low frequency, we can assume that they are related to longitudinal eigenmodes, i. e. excitation with the electric field parallel to the long axis x of the nanowire [30,31]. This assumption is supported by the fact that no significant signal is detected at the 'exit' end of the wire if the incident beam is mostly polarized in the transverse y direction.

On the basis of the reference spectrum of Fig. 3, we chose an incident wavelength of $\lambda = 770$ nm and computed the near-field intensity in an obser-

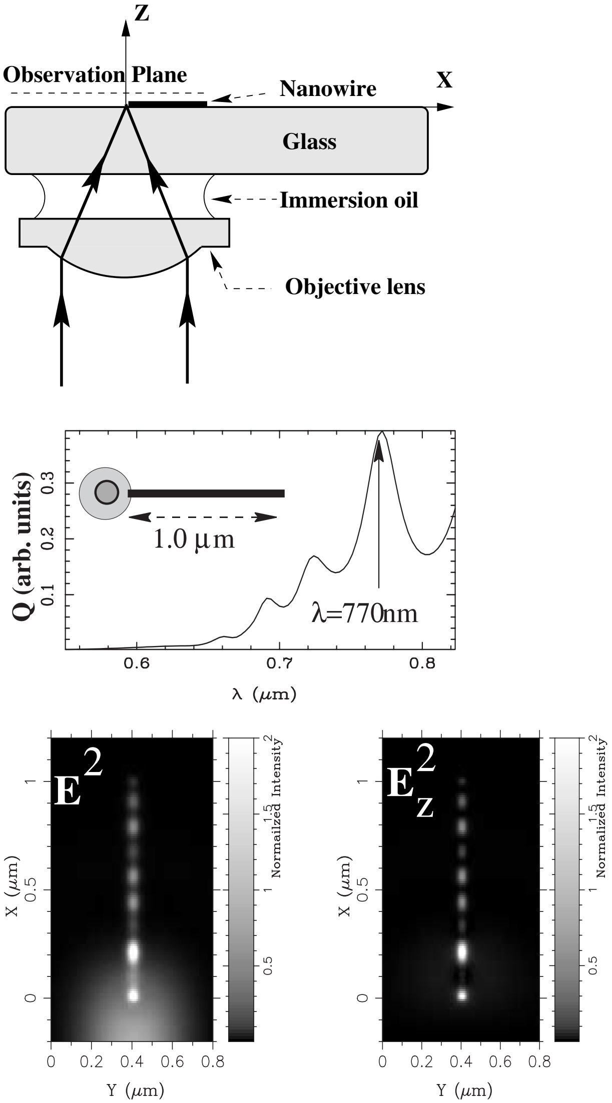

Fig. 3. *Top:* diagramnatic view of the local illumination of a nanowire by a focused plane wave. *Middle:* near-field spectrum of a 1.0µm long nanowire. *Bottom:* normalized intensity for $\lambda = 770$ nm. The observation plane is located 20 nm above the top of the object

vation plane located 20 nm above the top of the object. The $|E|^2$ and $|E_z|^2$ maps reported in Fig. 3 are plotted with the same gray-scale. It turns out that the z component of the electric field supports most of the intensity detected over the nanowire. At the 'exit' end of the wire, more than 90% of the total intensity is due to the z component. Note that this behavior is not inconsistent with an excitation of the x axis of the wire. A small prolate ellipsoid excited at the resonance frequency of its long axis can also scatter an electric near-field that ist locally strongly polarized along a direction perpendicular to the excited axis. This result suggests that the electric field of the electromagnetic mode supported by the wire could be used to excite the z axis of a metallic particle placed close to the end of the nanowire. In order to check this hypothesis, we considered the situation depicted in Fig. 4. At the end of two 1µm long nanowires, we have placed two gold particles elongated in the z direction. Both particles, denoted α and β in Fig. 4, have a height of 100 nm. Particle β has a rectangular section of $20 \times 30\,\mathrm{nm}^2$, while the section of particle α is square with a surface of $30 \times 30\,\mathrm{nm}^2$. Computed spectra show that the z axis resonances of particles α and β occur at $\lambda_\alpha = 730\,\mathrm{nm}$ and $\lambda_\beta = 820\,\mathrm{nm}$ respectively. Note that even if these two wavelengths do not correspond to maxima of resonance peaks of the 1µm long nanowire (see Fig. 3), the quantity Q has a significant value for both λ_α and λ_β. These two wavelengths have been used to compute the maps shown in Fig. 4. One can see that, depending on the wavelength, a bright spot appears above one or the other particle. Because the field amplitude of the nanowire mode is exponentially damped with the observation height, the grayscale does not allows one to visualize the propagation along the wires. Note that, to reach the two particles, the field of the nanowire mode has tunneled across an air-gap of 20 nm. In spite of the damping induced by the tunneling, the coupling between the wire and the particles remains efficient. Such a configuration could be of experimental interest for many applications since it achieves a single-particle excitation with the opportunity to switch from one particle to another by adjusting the incident wavelength.

The example discussed above not only illustrates the confinement of the plasmon field of gold nanowires (Fig. 1) in the near-field zone but also demonstrates that plasmon fields may used to transfer optical energy to subwavelength particles while avoiding direct illumination of the particles by the incident beam. The next section examines how a similar phenomenon, exploiting plasmon fields, allows one to bring a significant amount of power to the very end of a tetrahedral tip used as the light source of a SNOM.

4 Light Confinement at the Apex of a SNOM Tip

We now turn to the problem of light confinement at the probe of a SNOM. The SNOM probe acts as a source of light which is used to illuminate the object locally. In order to obtain a high spatial resolution, the influence of nanoscopic objects on the emission from the SNOM tip has to be detected. A resonant excitation of the SNOM probe can be exploited to enhance the contrast of the SNOM signal for imaging such small objects. Localized surface plasmons may provide such a resonant excitation at the apex of the SNOM

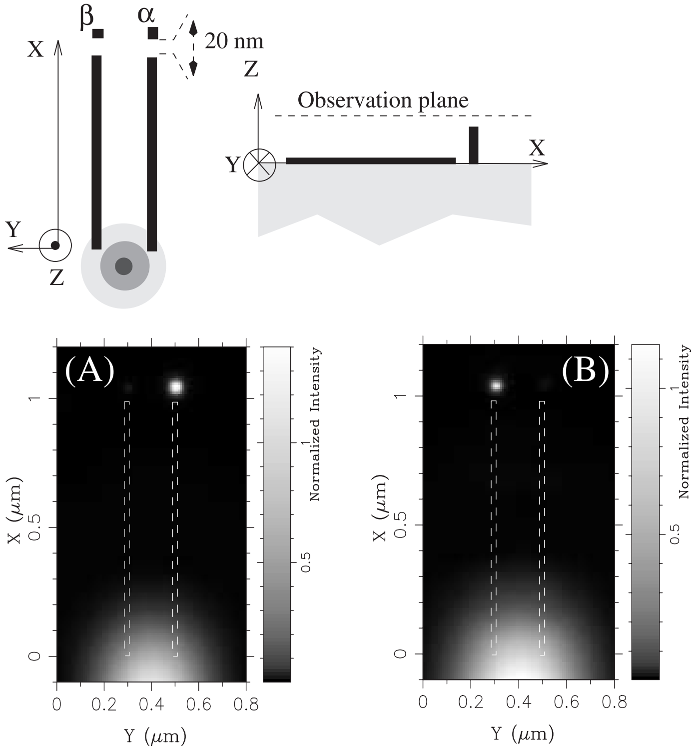

Fig. 4. Top and side views of a single-particle excitation setup and near-field maps calculated at 20 nm above the top of the isolated particles. **(A)** $\lambda = 730\,\text{nm}$, **(B)** $\lambda = 820\,\text{nm}$. The *dashed* lines in the maps show the position of the two nanowires used as waveguides

probe. A beam of light is usually incident within the body of the SNOM probe and should be confined to the nanoscopic dimensions of the light-emitting apex of the probe. Obtaining this confinement at the apex of the tip is crucial for achieving high resolution and is not feasible on the basis of classical far-field optical methods.

We shall focus our discussion on tetrahedral SNOM tips. Such tips were found to provide high-resolution optical images of small silver grains embedded in a flat surface of gold [15] at a resolution of 1–10 nm, which is usually not obtained when using other SNOM probes such as aperture probes. The high resolution of the SNOM image is a strong indication that a substantial amount of light emitted from the SNOM probe originates from a very localized tip exitation. In the case of these tetrahedral tips, it was proposed that surface plasmons may link the incident beam illuminating the tip to a confined excitation of the tip apex.

We propose here a model mechanism for an efficient transfer of electromagnetic energy to the apex of the tip, involving surface plasmons which are excited in the tetrahedral tip by the illuminating beam of light. First, a short description is given of the structure and the optical properties of a tetrahedral tip. The said model mechanism of light confinement relies on these properties.

4.1 Structure of a Tetrahedral Tip

The body of a tetrahedral tip consists of a glass prism with three faces and edges converging to a common corner as shown in Fig. 5. The prism is fabricated by a cleaving process similar to that used for the fabrication of glass knives. Such glass knives are used in ultramicrotomes to make thin sections of thickness 30 nm. The edges of such glass fragments are very sharp and are believed to have a radius of curvature in the 1 to 5 nm range. In the cleaving process, the angle between the edges K2 and K3 can be varied over a range of 30 to 180 degrees. Usually, this angle is adjusted to a value of 90 ± 5 degrees. The other angles, between the edges K1 and K2 and between the edges K1 and K3, are fixed to a value of about 90 degrees by the cleaving process. All faces of the corner are coated with a thin film of gold of thickness 50 nm. By a two-step evaporation process, the whole body of the tip is covered with gold except the edge K1, which is covered with less gold or no gold at all. Other metals such as silver or aluminum may be used instead of gold.

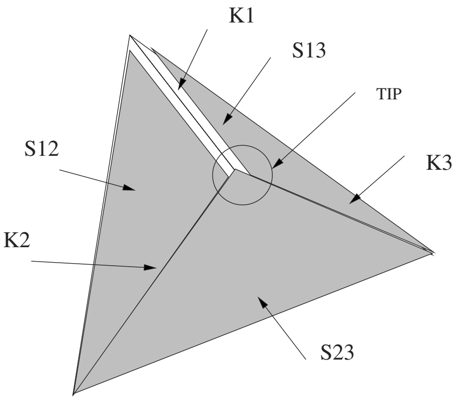

Fig. 5. Schematic view of a tetrahedral tip. The glass body of the tip is covered with a 50 nm thick film of gold. The edge K1 is covered with no metal or with less metal than the rest of the tip. The faces S12 and S13 are formed by two successive cleaving processes

4.2 Optical Properties of the Tetrahedral Tip

The optical properties of the tip were investigated. First, a wedge-type geometry was chosen as shown in Fig. 6, where a beam of light was directed perpendicularly into the wedge and light emitted from the edge K1 was detected [34]. This setup reminds us of a setup for measuring the transmission of light through a slit of subwavelength dimensions in a thin metal screen. The polarization of the incoming beam was adjusted to be either perpendicular or parallel to the edge K1. The intensity of the transmitted light was measured as a function of the wavelength and polarization of the incoming beam. The ratio $R = I_{\perp}/I_{\|}$ of the intensities $I_{\perp}$, for the perpendicular polarization, and $I_{\|}$, for the parallel polarization, was determined and plotted as a function of wavelength (λ) for a range between $\lambda = 540$ and $\lambda = 640\,\mathrm{nm}$ and for wedges with different metal coatings consisting of 50 nm of gold, silver, or aluminum, as shown in Fig. 7.

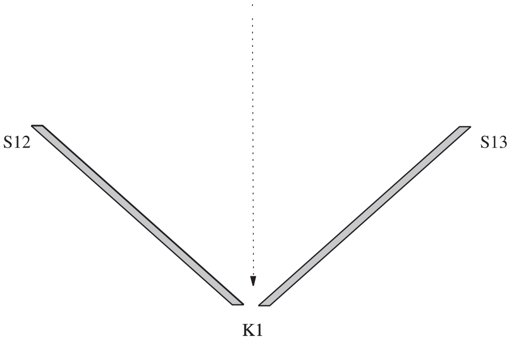

Fig. 6. Wedge configuration between the faces S12 and S13 of the tetrahedral tip. A beam of light is directed into this wedge from the inside of the tip and perpendicular to the edge K1

For aluminum, the value of R increases from 5 to 10 in this wavelength range. A value of $R > 1$ corresponds to the polarizing property of a thin slit in an infinitely conductive metal screen. The increase of R from a value of 5 at $\lambda = 540$ nm to 10 at $\lambda = 640$ nm corresponds to the $1/\lambda^3$ dependence of R for a thin slit in an infinitely conductive screen. *Novotny* et al. [32] calculated the transmission of a 40 nm wide slit at the apex of a glass wedge coated with aluminum, taking into account the dielectric properties of aluminum at $\lambda = 488$ nm. They obtained a value of $R = 10$ which is the same order of magnitude as our experimentally observed value (see Fig. 7).

For a gold coating, $R = 80$ is found for $\lambda = 640\,\mathrm{nm}$ and the value decreases to $R = 3$ at $\lambda = 540\,\mathrm{nm}$. This finding cannot be accounted for by the theory of light transmission through a narrow slit. The strong dependence of the ratio R on wavelength indicates that the phenomenon is related to the excitation of

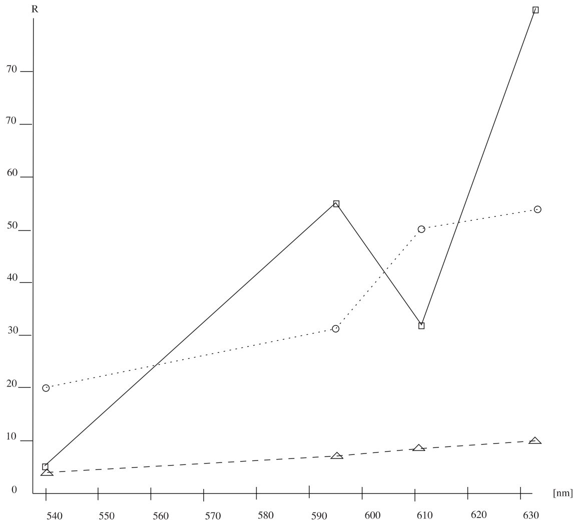

Fig. 7. Ratio R as a function of wavelength for three different metal coatings. *Squares:* 50 nm of gold. *Circles:* 50 nm of silver. *Triangles:* 100 nm of aluminum

surface plasmons on the thin metal film covering the glass wedge. Surface plasmons are known to be excited in the case of gold in the red spectral range by total internal reflection of a beam of light at an angle close to the critical angle, with the polarization perpendicular to the interface. We therefore assume that surface plasmons are excited on the metal films on both faces of the wedge by an incoming beam of p-polarized light having an angular range of 45 ± 3 degrees. Moreover, it may be expected that the intensity of light emission from the edge should be related to the decay length of surface plasmons on the metal faces, because this decay length should determine the range from which surface plasmons propagate towards the edge K1, where emission of light occurs. Indeed, the ratio R is found to scale approximately with the theoretically calculated decay length of surface plasmons on gold films of 600 nm at $\lambda = 540$ nm and of 8000 nm at $\lambda = 640$ nm.

The optical properties of the tip in a situation which corresponds very closely to the conditions of recording of the SNOM signal were investigated as follows. The tip was irradiated from the glass body of the tip at an angle close to the symmetry axis of the tip, which is inclined at an angle of 45 degrees with respect to the edge K1. Observation of light emission from the tip thus corresponds to the experiment above but with an inclined incidence of the incoming beam. In this case, for $\lambda = 635$ nm, $R = 0.2$, which is much smaller than 1. Moreover, in several experiments, a much stronger contrast was obtained in SNOM images if the polarization was chosen to be in the plane of incidence defined by the direction of the incident beam and by K1 [33]. In fact, when operating a SNOM with such a tip, one carefully chooses the polarization of the illuminating beam to be within this plane of incidence. The experimental observations thus raise the question of the origin of the different properties of the ratio R in the case of light emission from the edge K1 at normal incidence on one hand and in the case of light emission from the tip at oblique incidence on the other hand.

4.3 Surface Plasmons and Light Confinement in the Tetrahedral Tip

On the basis of the structure of the tetrahedral tip and its observed optical properties, we now discuss a hypothesis where surface plasmons may serve as a pathway for light confinement in the tetrahedral tip. At first sight, it is not obvious that surface plasmons which are excited by light might be useful for this purpose. Indeed, surface plasmons produced by total internal reflection on a thin film of gold supported by glass are excited at the gold–air interface. The evanescent electromagnetic surface wave associated with such a plasmon extends into the air to a distance from the gold–air interface on the order of the wavelength of the surface plasmon. This wavelength is larger than the wavelength of light in the glass. It is therefore not evident that confinement of the electromagnetic field to dimensions significantly smaller than the wavelength of the light can be achieved in the tetrahedral tip through the excitation of surface plasmons by optical means.

We now present a simple model which illustrates how the optical excitation of surface plasmons might achieve a fairly well localized field at the apex of a tetrahedral tip [35]. Consider the situation depicted in Fig. 6, where a beam of light is incident perpendicular to the edge K1. The incident beam may excite surface plasmons at the air–gold interfaces S12 and S13. Surface charges of opposite sign are induced on the gold–air interfaces at a wavefront of equal phase of the incoming beam. The surface plasmons on either side meet at the edge K1. A similar situation may also exist for an oblique incidence of the beam with respect to the edge K1 as illustrated in Fig. 8. This leads to a charge distribution at the edge K1 as depicted in Fig. 9. The electric near-field of such a charge distribution is expected to be strongly confined to the gap between the metal faces at the edge K1 similarly to the case of an the asynchronously excited double-wire transmission line described by Sommerfeld [36]. The decay of this localized field does not scale with the periodicity of the charge pattern but with the scale of charge separation and thus with the dimensions of the gap, which can be made much smaller than the wavelength of light. It is thus conceivable that the excitation of the edge propagates towards the tip, thus creating a local excitation of the tip.

This scheme agrees with the observation of efficient light emission from the edge K1 at normal incidence when the polarization is in the plane of incidence. However, it does not seem to agree with the observed properties of the light emission from the tip when the edge K1 is illuminated at oblique incidence, where the polarization in the plane of incidence is again the favourable

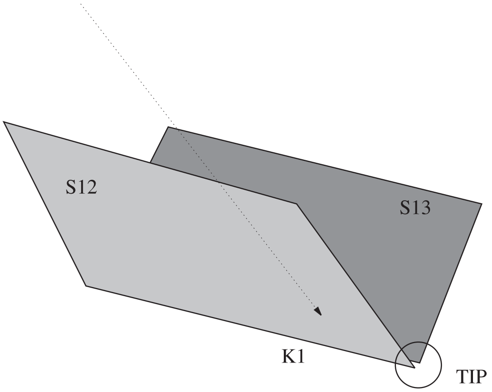

Fig. 8. Schematic view of a wedge with an obliquely incident beam

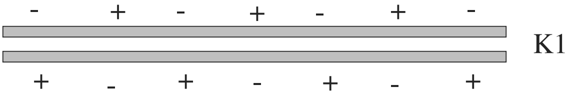

Fig. 9. Snapshot of the charge distribution at the edge K1 for an obliquely incident beam polarized perpendicular to the edge K1 (perpendicular to the plane of incidence defined by the direction of the incoming beam and the edge K1)

polarization. For this case of oblique incidence, however, surface plasmons can also be excited when the polarization of the incident beam is within the plane of incidence, as shown in Fig. 10. Indeed, in this case, there is also a component of the electric-field vector which is perpendicular to the metal films on the faces S12 and S13. Surface charges of the same sign would be induced on both gold–air interfaces at a wavefront of equal phase of the incoming beam. When they converged at the edge K1 they would therefore create no strongly localized electric field across the gap K1. We would thus expect no strong confinement of the electric field by these surface plasmons.

Another mechanism may, however, explain how surface plasmons can lead to a confined excitation at the tip apex in the case of oblique incidence and in plane polarization. Let us assume that the conditions for excitation of surface plasmons in the tetrahedral tip for oblique incidence of the beam at a certain height of the tip structure bear a relation to surface plasmon excitation of a symmetric layered structure consisting of a glass slab coated with a gold film of thickness 50 nm on both interfaces, as shown in Fig. 11. The thickness of the dielectric slab corresponds to the thickness of the crosssection through the dielectric body of the tetrahedral tip.

It is well known that not only surface plasmon modes exist which are localized at the metal–air interface, but that there exist also modes which are localized at the metal–dielectric interface. These modes normally cannot be excited by total internal reflection, because there is no phase matching to

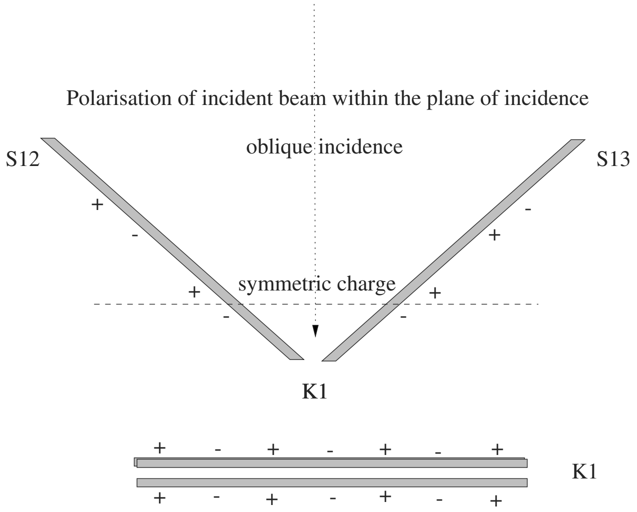

Fig. 10. Snapshot of the symmetric charge distribution at the edge K1 for an obliquely incident beam polarized in the plane of incidence

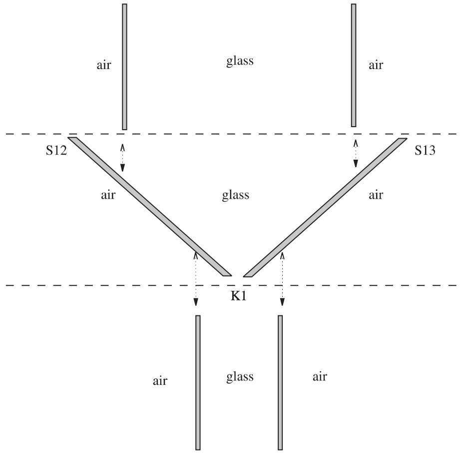

Fig. 11. Dispersion relations for a thin film of gold on a glass support, obtained using data from [29]. The *upper branch* corresponds to surface plasmons at the air–metal interface and the *lower branch* corresponds to surface plasmons at the glass–metal interface (below the line for light in glass, $\omega = kc/n$). The intersections between the *horizontal lines* and the dispersion relations indicate the conditions for surface plasmon excitation at $\lambda = 543\,\mathrm{nm}$ (*dot-dashed line*) and $\lambda = 633\,\mathrm{nm}$ (*dashed line*)

the incident beam. This is well known for a single gold film on a dielectric substrate, as illustrated by the dispersion relations for the two modes shown in Fig. 12. In the ω–$k_{||}$ space, only the mode at the air–gold interface overlaps the area which is bounded by the dispersion relations for bulk waves in air ($\omega = kc$) and in the dielectric ($\omega = kc/n$, where n is the index of refraction of the dielectric). These modes can be excited in the overlap region by a phase matching beam which is totally reflected at the dielectric–air interface. The modes at the glass–gold interface cannot be excited, because, for a given frequency, they involve $k_{||}$ values which cannot be sustained by the dielectric. However, the situation may be different for a layered structure. One might expect that the frequency of the surface plasmon modes located at the glass–gold interfaces of the slab would depend on the symmetry of the induced surface charges on the gold–dielectric interfaces. A symmetric charge distribution is expected to lead to charge repulsion and therefore to increase the plasmon frequency when the thickness of the dielectric slab is reduced. On the other hand, an antisymmetric charge distribution is expected to lead to an attraction of the charges and therefore to decrease the plasmon frequency. Increasing the frequency of the mode which is symmetric with respect to the charge distribution may shift the branch belonging to this mode in such way that it enters the region between the light lines in air ($\omega = kc$) and glass ($\omega = kc/n$) (see Fig. 12). It would be possible thereby to excite the internal modes with a beam of light incident from the glass. It would be thus conceivable that surface plasmons are excited at the internal interfaces of the tetrahedral tip and that the electromagnetic field does not penetrate to the

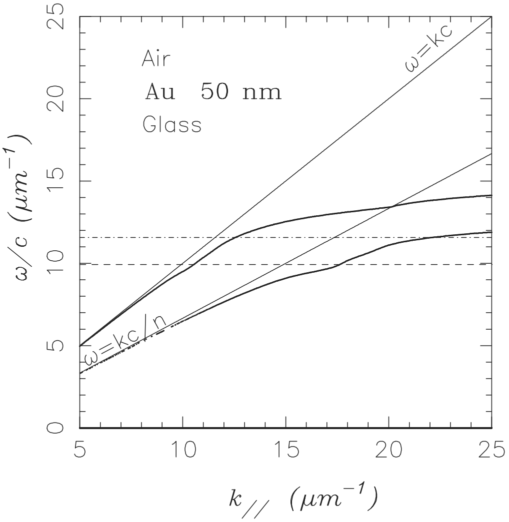

Fig. 12. Comparison of the wedge configuration with a metal-coated dielectric slab for two different cross sections of the wedge

outside of the tip, from which it is shielded by the gold layers. The symmetric surface plasmons could propagate along the internal interface of the edge K1 towards the tip apex, where they might produce a localized field. Of course, the detailed local field distribution at the tip apex cannot be explained by this simplified model. Let us note, however, that excitation of surface waves on the flat glass–metal interfaces, which are much less corrugated than the metal–air interfaces of the tetrahedral tip, implies a reduction of the radiative losses of surface plasmons due to roughness, and therefore less nonlocal background emission from the tip.

In order to assess whether excitation by light of the internal modes at the dielectric–metal interfaces might be possible, the dispersion relations of layered structures for different thickness of the dielectric slab were calculated numerically, following the method of [37]. The values of the dielectric function of gold were taken from [29]. A sequence of dispersion relations for a symmetric slab structure is shown in Fig. 13 for ten values of the glass thickness d from 25 to 500 nm. Starting with the dispersion relation for $d = 400$ nm (the case $d = 500$ nm will be discussed below), four surface plasmon modes can be recognized in the dispersion relation. The two lowest branches converge at high k to a common asymptotic value and can be identified with the symmetric and antisymmetric plasmon modes on the dielectric–metal interface. Two further branches, converging to a larger asymptotic value, correspond to the symmetric and antisymmetric surface plasmon modes on the metal–air interface. Three further branches, at higher energies, correspond not to surface plasmon modes but to guided-wave modes.

For values of d from 300 nm to 150 nm, the upper two plasmon branches do not change much, whereas a large change is observed for the lower two branches related to the metal–glass interfaces. One of the branches moves upward, whereas the other one moves downward. The upper one thus corresponds to the symmetric mode at the dielectric–metal interface, which is shifted to higher frequencies by the electrostatic repulsion, whereas the frequency of the lower, antisymmetric branch is decreased owing to electrostatic attraction. The upper two branches are not too much affected, because their mutual interaction is much weaker, as they are located on the outside at the metal–air interfaces. For values of d smaller than 150 nm, the separation of the two lower branches increases further. But, also, the upper two branches start to separate. The antisymmetric mode should be related here to a higher energy, as is known from the energy of the symmetric and antisymmetric branches of a single metal interface [38]. For small thicknesses d the branches of the symmetric modes at the outer, air–metal and the inner, glass–metal interfaces converge to an almost identical value. We therefore conclude that the dispersion relations of the inner and outer symmetric modes, which have been calculated here by neglecting the imaginary part of the dielectric function of gold, converge for small thickness of the dielectric layer to a practically identical value as soon as one takes finite-lifetime effects (a nonzero imagi-

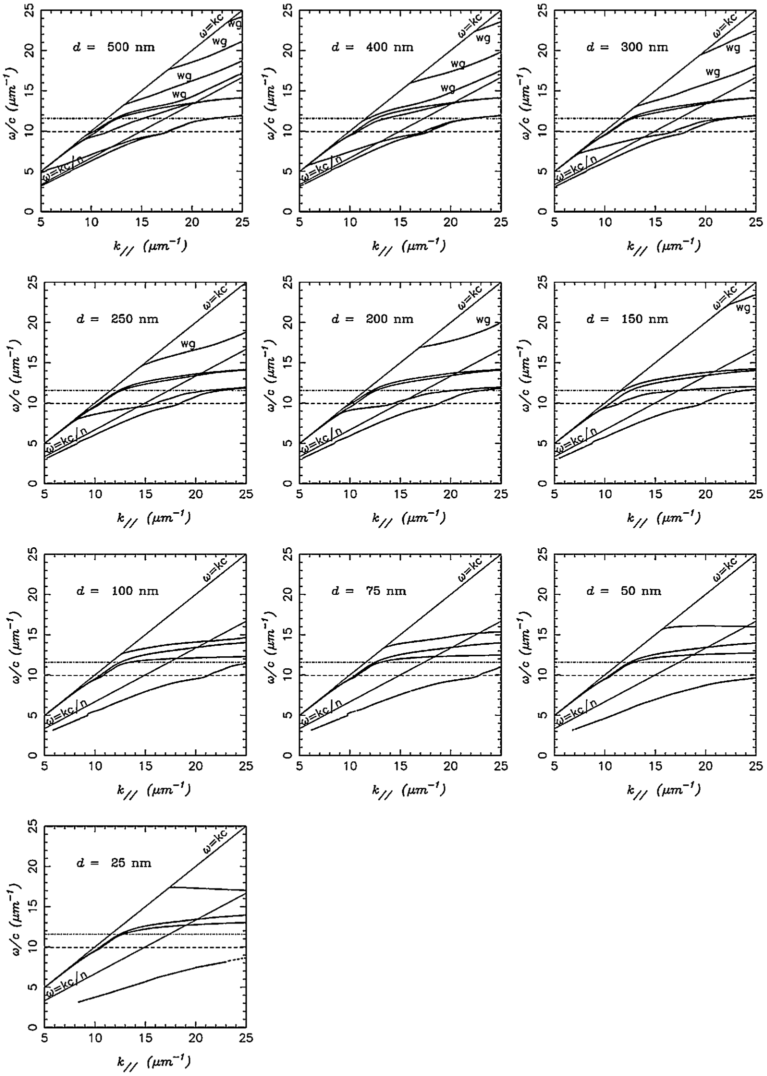

Fig. 13. Ten dispersion relations of TM modes for a metal-coated dielectric slab. The thickness d of the dielectric slab varies betweeen 5 nm and 500 nm while both metal coatings have a fixed thickness of 50 nm. The lines for light in air ($\omega = kc$) and glass ($\omega = kc/n$, where $n = 1.5$) are inserted for reference. Also, for convenience, the range of the ordinate ω/c extends from 0 to $25\mu\text{m}^{-1}$, although the computations dealt only with values of ω/c from π (i.e. $\lambda = 2\mu\text{m}$) to $25\mu\text{m}^{-1}$. This explains the truncation of the lowest branch of the interface modes at $\omega/c = \pi$. The branches labelled 'wg' are not interface modes but are waveguide modes, i.e volume modes of the dielectric slab, which disappear when $d < \pi c/\omega$. The intersections between the *horizontal lines* and the dispersion relations indicate the conditions for surface plasmon excitation at $\lambda = 543$ nm (*dot-dashed line*) and $\lambda = 633$ nm (*dashed line*)

nary part of the dielectric function of gold) into account. It is furthermore observed that the dispersion curve of the symmetric outer plasmon mode is practically not affected by the change in thickness of the dielectric layer.

We conclude that the branch of symmetric surface plasmon modes seems to be excitable by light under stable conditions for all d values smaller than $d = 400$ nm. The convergence of the inner symmetric mode to the rather constant symmetric mode on the outside implies that a symmetric mode excited at the outside may couple to an inner mode when the thickness d is small enough. We suggest that this coupling of an external surface plasmon mode to an internal one is a pathway in the tetrahedral tip which leads to a local excitation at the apex of the tip from within the dielectric body of the tip. The symmetric surface plasmon modes, which are essential for the proposed mechanism of light confinement, can be excited on the tetrahedral tip because the metal faces are not parallel to each other and because of the oblique incidence.

Some complications in this model turn up when the thickness d increases. As may be already seen in the case of $d = 500$ nm, the dispersion curves for the upper two branches of the modes on the air–gold interface separate again. This phenomenon is obviously related to an interaction of waveguide modes with the surface plasmon modes which becomes more and more important as the thickness of the dielectric layer increases further. We did not take this consideration further into account, since although these waveguide modes are typical of the layered system used to model the tip, they are not related to any physical feature at the apex of the tetrahedral tip. Conversely, new aspects appear in the three-dimensional configuration at the apex of the tip as compared with a parallel-layered medium. Accounting for such aspects requires time-consuming numerical modeling of three-dimensional tips. Of course, the proposed model is very simplified, and no information is obtained about the detailed local field distribution around the apex of the tip and thus about the local nature of tip excitation. The model mainly describes how energy might be transfered efficiently to the apex. We think, nevertheless, that the simplified model proposed here provides guidelines that will be useful before undertaking such computations on three-dimensional tips.

Acknowledgements

Stimulating discussions and/or collaborations with H. J. Maas, J. Heimel, A. Naber, H. Fuchs, C. Girard, F. R. Aussenegg, J. R. Krenn, A. Leitner, G. Schider, E. Bourillot, T. David, C. Chicanne, E. Devaux, J. P. Goudonnet, and Y. Lacroute are gratefully acknowledged. A. D. acknowledges the financial support of the Regional Council of Burgundy and U. C. F. acknowledges the financial support of the German Federal Ministery of Education and Research.

References

1. J. R. Krenn, W. Gotschy, D. Somitsch, A. Leitner, F. R. Aussenegg, Appl. Phys. A **61**, 541 (1995) 49
2. J. R. Krenn, R. Wolf, A. Leitner, F. R. Aussenegg, Opt. Commun. **137**, 46 (1997) 49
3. P. Dawson, F. de Fornel, J. P. Goudonnet, Phys. Rev. Lett. **72**, 2927 (1994) 49
4. I. Smolyaninov, D. L. Mazzoni, C. C. David, Phys. Rev. Lett. **77**, 3877 (1996) 49
5. A. V. Shchegrov, I. V. Novikov, A. A. Maradudin, Phys. Rev. Lett. **78**, 4269 (1997) 49
6. S. I. Bozhevolnyi, V. A. Markel, V. Coello, Phys. Rev. B **58**, 11441 (1998) 49
7. J. R. Krenn, A. Dereux, J. C. Weber, E. Bourillot, Y. Lacrouk, J. P. Goudonnet, G. Schider, W. Gotschy, A. Leitner, F. R. Aussenegg, C. Girard, Phys. Rev. Lett. **82**, 2590 (1999) 49
8. S. Grésillon, L. Aigouy, A. C. Baccara, J. C. Rivoal, X. Quelin, C. Desmarest, P. Gadenne, V. A. Shubin, A. K. Sarychev, V. M. Shalaev, Phys. Rev. Lett. **82**, 4520 (1999) 49
9. B. Hecht, H. Bielefeldt, L. Novotny, Y. Inonye, D. W. Pohl, Phys. Rev. Lett. **77**, 1889 (1996) 49
10. T. Klar, M. Perner, S. Grosse, G. von Plessen, W. Spirkl, J. Feldmann, Phys. Rev. Lett. **80**, 4249 (1998) 49
11. D. Courjon C. Bainier, Rep. Prog. Phys. **57**, 989 (1994) 49
12. U. C. Fischer, J. Opt. Soc. Am B **3**, 1239 (1986) 49
13. U. Fischer D. Pohl, Phys. Rev. Lett. **62**, 458 (1989) 49
14. M. Specht, J. D. Pedarnig, W. M. Heckl, T. W. Hänsch, Phys. Rev. Lett. **68**, 476 (1992) 49
15. J. Koglin, U. C. Fischer, H. Fuchs, Phys. Rev. B **55**, 249 (1997) 49, 57
16. S. I. Bozhevolnyi F. A. Pudonin, Phys. Rev. Lett. **78**, 2823 (1997) 49
17. J. R. Krenn *et al.*, Phys. Rev. B **60**, 5029 (1999) 49, 50
18. C. Girard, A. Dereux, C. Joachim, Europhys. Lett. **44**, 686 (1998) 50
19. C. Girard, A. Dereux, C. Joachim, Phys. Rev. E **59**, 6097 (1999) 50
20. J. C. Weeber *et al.*, Phys. Rev. B **60**, 9061 (1999) 50, 53
21. R. C. Reddick, R. J. Warmack, T. L. Ferrell, Phys. Rev. B **39**, 767 (1989) 50
22. C. Girard, A. Dereux, O. J. F. Martin, M. Devel, Phys. Rev. B **52**, 2889 (1995) 50
23. J. C. Weeber *et al.*, Phys. Rev. Lett. **77**, 5332 (1996) 50, 51
24. A. Dereux *et al.*, Ann. Phys. (Paris) **23**, C1 (1998) 50
25. C. Girard, A. Dereux, Rep. Prog. Phys. **59**, 657 (1996) 51, 53
26. P. Török, P. Varga, Z. Laczik, G. R. Booker, J. Opt. Soc. Am. A **12**, 325 (1995) 54
27. P. Török, P. Varga, Z. Laczik, G. R. Booker, J. Opt. Soc. Am. A **12**, 2136 (1995) 54
28. P. Török, P. Varga, Z. Laczik, G. R. Booker, J. Opt. Soc. Am. A **13**, 2232 (1996) 54
29. D. W. Lynch, W. R. Hunter, in *Handbook of Optical Constants of Solids*, E. D. Palik (Ed.) (Academic, New York 1985) Chap. II.1, p. 286 54, 63, 65

30. C. Bohren, D. Huffman, *Absorption and Scattering of Light by Small Particles* (Wiley, New York 1983) 54
31. U. Kreibig, M. Vollmer, *Optical Properties of Metal Clusters*, Springer Ser. Mater. Sci. **25**, (Springer, Berlin, Heidelberg 1995) 54
32. L. Novotny, D. W. Pohl, P. Regli, J. Opt. Soc. Am. A **11**, 1768 (1994) 59
33. J. Ferber, U. C. Fischer, N. Hagedorn, H. Fuchs, Appl. Phys. A **69**, 581 (1999) 60
34. U. C. Fischer, J. Koglin, A. Naber, A. Raschewski, R. Tiemann, H. Fuchs, *Near Field Optics and Scanning Near Field Optical Microscopy* in *Quantum Optics of Confined Systems* M. Ducloy, D. Bloch. (Eds.) NATO ASI Ser. E **314** (Kluwer, Dordrechet 1996) 59
35. U. C. Fischer, in *Scanning Probe Microscopy: Analytical Methods*, R. Wiesendanger (Ed.) (Springer, Berlin, Heidelberg 1998) 61
36. A. Sommerfeld, *Vorlesungen über theoretische Physik* (Harri Deutsch, Thun 1977), Vol. III Elektrodynamik 61
37. A. Dereux, J. P. Vigneron, P. Lambin, A. A. Lucas, Phys. Rev. B **38**, 5438 (1988) 65
38. K. L. Kliewer, R. Fuchs, *Theory of Dynamical Properties of Dielectric Surfaces* Adv. Chem. Phys. **27**, I. Prigogine (Ed.) (Wiley, New York 1974) 65

Spectroscopy of Gap Modes in Metal Particle–Surface Systems

Shinji Hayashi

Department of Electrical and Electronics Engineering, Kobe University,
Nada, Kobe 657-8501, Japan
`hayashi@eedept.kobe-u.ac.jp`

Abstract. We consider here a system with a metallic particle placed very near to a metallic surface and discuss the electromagnetic normal modes of the system. Based on electromagnetic calculations, neglecting the retardation effects, it is easy to predict the existence of so-called gap modes which are highly localized in the gap between the particle and the surface. The gap modes play important roles in various optical processes. We present the results of direct observation of the gap modes by reflection–absorption spectroscopy for Ag-island particles placed on an Al surface. We also describe the light emission from the gap modes as well as the excitation of surface plasmon polaritons mediated by the gap modes.

1 Introduction

It is well known that a metal surface can support surface plasmon polariton (SPP) modes [1,2], which are coupled modes of photons and plasmons. The SPP modes propagate along the surface and decay exponentially away from the surface. Since the SPP modes are nonradiative electromagnetic modes, they cannot be excited directly by incident photons. To excite them, an appropriate method, e.g. an attenuated-total-reflection (ATR) method, must be used. It is also well known that a fine metal particle can support localized surface plasmon (LSP) modes [3,4], which are plasma oscillations of free electrons confined in the particles. Since the electromagnetic fields associated with the LSP modes are radiative, the modes can be excited directly by incident photons and can be observed by ordinary absorption measurements.

In a system consisting of a fine metal particle placed very close to a metal surface, an electromagnetic interaction between the LSP and SPP modes is expected to occur. The interaction is expected to give rise to various interesting optical phenomena. Several authors [5,6,7] reported that the presence of metal particles can enhance the light emission from metal–insulator–metal tunnel junctions, suggesting that the interaction plays an important role. According to electromagnetic theories of a spherical particle placed close to a surface [8,9,10,11], there exist a special type of electromagnetic normal modes, the so-called ‘gap modes’, which are strongly localized in the space between the sphere and the surface. The gap modes were suggested to be the source of the light emission from the tunnel junctions. For light emission

S. Kawata (Ed.): Near-Field Optics and Surface Plasmon Polaritons,
Topics Appl. Phys. **81**, 71–95 (2001)

from a metal tip–surface system, i.e. a scanning tunneling microscope, the contribution of the gap modes excited by the tunnel current was also pointed out [12,13,14,15].

In scanning near-field optical microscopy (SNOM), several attempts have recently been made to use the interaction between a metal tip and a metal surface [16,17,18,19,20,21]. When an SPP mode is excited on a metallic surface by the ATR method, it is possible to modulate the intensity of the reflected light or generate scattered light by placing a sharpened metallic tip very close to the surface. Detection of the reflected or scattered light intensity while scanning the tip allows one to obtain images with a high lateral resolution. In theoretical treatments of the tip–surface system, the tip is often modeled by a sphere [18,19], since the exact shape of the tip is not well known. Therefore, a sphere–surface system provides an important model for discussing the performance of SNOM.

As mentioned above, metallic-particle–surface systems are encountered in many situations of near-field optics, although the roles played by the gap modes have not yet been fully explored. In this chapter, we shall focus on the fundamental aspects of the gap modes, in particular the spectroscopic aspects, and present recent experimental results which demonstrate the existence and importance of the gap modes. In Sect. 2, the characteristics of the gap modes are summarized on the basis of electromagnetic theory of a sphere placed close to a surface. The subsequent sections are devoted to the description of spectroscopic data. In Sect. 3, results of the absorption measurements intended to directly detect the gap mode between Ag island particles and an Al surface are presented. Sections 4 and 5 are devoted to the interaction of SPP modes on an Al surface with Ag nanoparticles. First, we discuss the light emission from the SPP modes caused by the presence of Ag nanoparticles (Sect. 4) and then discuss the excitation of SPP modes mediated by the Ag nanoparticles (Sect. 5). It will turn out that in both phenomena, the excitation of the gap modes plays a crucial role.

2 Characteristics of the Gap Modes

We first consider an isolated metal sphere with a dielectric function $\epsilon(\omega)$ embedded in a surrounding medium with a dielectric constant ϵ_{m}. If the radius of the sphere, R, is so small that the retardation effects of electromagnetic fields can be neglected, the resonant frequencies corresponding to the excitation of LSP are simply given by $\epsilon(\omega) = -\epsilon_{\mathrm{m}}(l+1)/l$ [3,4], where l is an integer ($l = 1, 2, \ldots$). The amplitude of the electric field outside the sphere decays as $r^{-(l+2)}$, where r is the distance from the center of the sphere. If the sphere is much smaller than the wavelength of the incident light, the dipole mode with $l = 1$ (the Fröhlich mode) is mainly excited. LSP resonances have been observed by absorption measurements for a variety of samples containing small metallic particles [4].

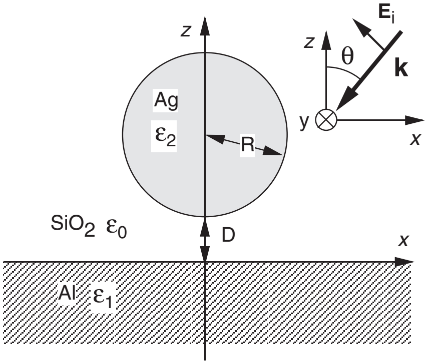

Fig. 1. A spherical particle of radius R placed at a distance D from a metallic surface. For numerical calculations, an Ag particle, Al surface and SiO_2 surrounding medium were assumed

A question then arises as to what happens when a metal sphere is brought into close proximity with a metal surface, as schematically shown in Fig. 1. A qualitative look at the problem can be taken by approximating the LSP mode as a dipole and considering its interaction with the image dipole induced inside the metal. It is easy to predict that the dipole–dipole interaction may greatly modify the LSP mode, i.e. the resonance frequency and the field distribution. Furthermore, because of the change in symmetry (the spherical symmetry for an isolated sphere changes into cylindrical symmetry for a sphere–surface system), new electromagnetic modes are expected to appear. These modes correspond to polarization modes parallel and perpendicular to the symmetry axis. The modification of the LSP mode will depend strongly on the distance of the sphere from the surface, D. If D is very small, the image dipole applies a spatially inhomogeneous field to the sphere and excites its quadrupole. This too causes an image field that further polarizes the sphere. The quadrupole resonance is also shifted and split by symmetry breaking and thus provides new resonances. A complete treatment of the problem should include all the multipoles of the sphere. A full set of the Maxwell equations should be solved with appropriate boundary conditions.

A rigorous electromagnetic theory of the sphere–surface system including retardation effects has been developed by *Takemori* et al. [22]. Electromagnetic theories neglecting retardation effects (the electrostatic approximation) were developed by *Rendell* et al. [8,9], *Ruppin* [10], and *Aravind* and *Metiu* [11]. Here, we assume that $D + 2R$ in Fig. 1 is smaller than the wavelength of light, so that we can neglect retardation. Under this assumption, the problem is reduced to solving Laplace's equation to obtain the scalar potentials in the surrounding medium, metal substrate and sphere. The mathematical procedure is not repeated here (see [8,9,10,11] for details), but can be summarized as follows: (1) The potentials are first expanded in spherical harmonics by using bispherical coordinates. (2) The unknown coefficients of the expansions are determined by imposing the boundary conditions. The conditions for the existence of nontrivial solutions for the coefficients give the frequencies of the electromagnetic normal modes. (3) Characteristics of the normal modes, such as the local field distribution and the optical response, can be calculated from the potentials found. Note that the results obtained within the electrostatic approximation depend only on the ratio D/R, not on the absolute values of R and D.

For illustrative purposes, results of numerical calculations performed by the author's group [23,24,25] for an Ag sphere placed above an Al surface are presented in Figs. 2 and 3. The surrounding medium is assumed to be SiO_2. For the dielectric functions ϵ_1 and ϵ_0, we used the literature values for Al [26] and SiO_2 [27], respectively. The dielectric function of the Ag particle,

(a) D=50nm λ=402nm (b) D=4.5nm λ=408nm

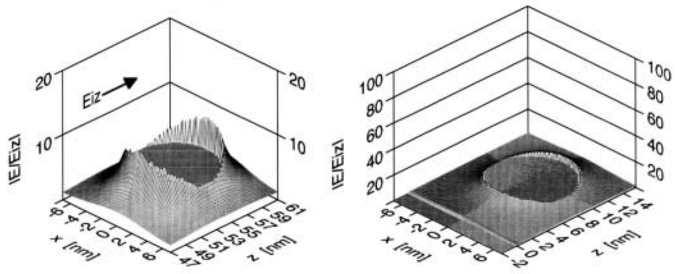

(c) D=0.9nm λ=454nm (d) D=0.3nm λ=520nm

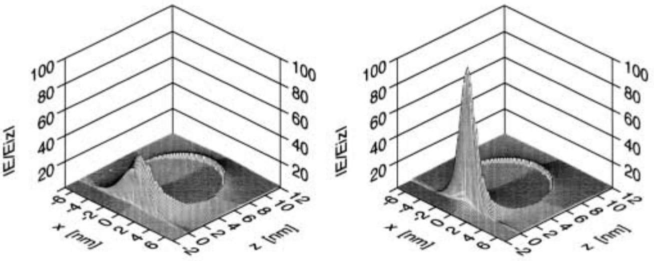

Fig. 2. Electric-field distributions generated by the z component of the incident field, E_{iz}. R was set to 4.5 nm. The center of the sphere is located at $(x, z) = (0\,\mathrm{nm}, D + 4.5\,\mathrm{nm})$ in the x–z plane. The surface of the Al metal is at $z = 0$. The absolute value of the electric field normalized to E_{iz}, $|E/E_{iz}|$, is plotted as a function of the position in the x–z plane. As the sphere–surface distance D decreases, the resonant wavelength varies. (**a**), (**b**), (**c**) and (**d**) correspond to $D = 50$, 4.5, 0.9, and 0.3 nm, respectively

ϵ_2, was calculated from the bulk value [28] by taking into account the size dependence of the imaginary part [4]. R was assumed to be 4.5 nm. The choices of the Ag particle–Al surface system and of the parameters were made in order to facilitate the discussion of the experiments described in Sects. 4 and 5. When a p-polarized plane wave is obliquely incident on the system, the electric field associated with it has two components, $E_{\mathrm{i}x}$ and $E_{\mathrm{i}z}$. The relative strength of these components varies depending on the angle of incidence. In order to see separately the effects of the components, we calculated separately the field distributions generated by them. Figs. 2 and 3 present electric-field distributions generated by $E_{\mathrm{i}z}$ and $E_{\mathrm{i}x}$, respectively. When s-polarized light is incident, the field has only one component, $E_{\mathrm{i}y}$. In this case, because of the symmetry of the system, the field distribution can be obtained by a 90° rotation (around the z axis) of the distribution generated by $E_{\mathrm{i}x}$.

Figure 2a shows the field distribution for an Ag sphere placed at $D = 50\,\mathrm{nm}$. The figure plots the absolute value of the local electric field normalized to the excitation field, $|E/E_{\mathrm{i}z}|$, as a function of the position in the x–z plane

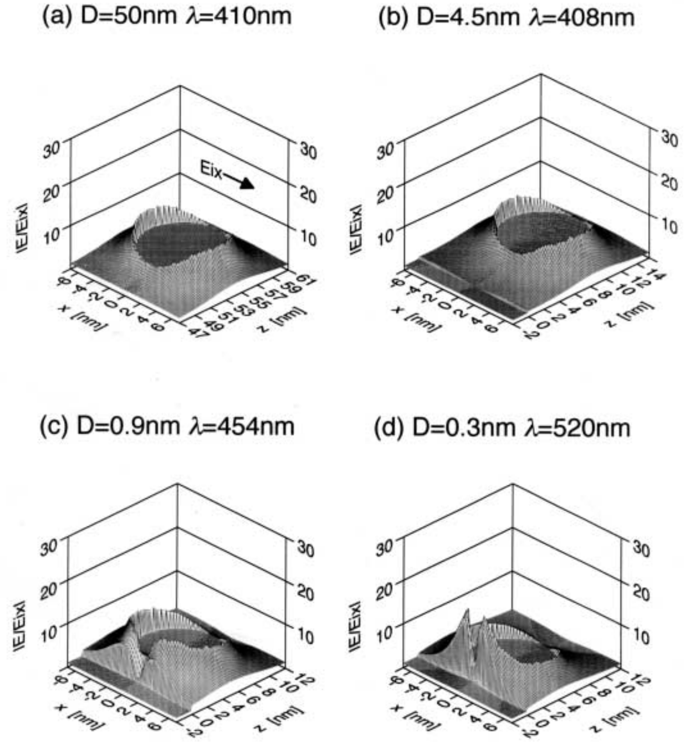
(a) D=50nm λ=410nm

(b) D=4.5nm λ=408nm

(c) D=0.9nm λ=454nm

(d) D=0.3nm λ=520nm

Fig. 3. Electric-field distributions generated by the x component of the incident field, $E_{\mathrm{i}x}$. The parameters used for the calculations are the same as those for Fig. 2

($y = 0$). The center of the sphere is located at (x, z)=(0 nm, 54.5 nm). In this case, the sphere is still very far from the surface, so that the LSP of the sphere is not modified and the resonant wavelength (402 nm) is identical to that of an isolated sphere in SiO_2. The electric field outside the sphere is enhanced around the top and bottom of the sphere. The maximum enhancement factor is $\sim$10. Figures 2b–d present results of a series of calculations obtained by varying the distance D. Figures 2b, 2c, and 2d correspond to $D = 4.5$, 0.9, and 0.3 nm ($D/R = 1.0$, 0.2, and 0.07), respectively. In each case, the wavelength was set at the resonance that gives the maximum field enhancement. In these figures, the Al surface is located at $z = 0$ nm and the scale of the z axis has been slightly changed from figure to figure. These figures demonstrate that as D decreases, the field becomes more and more localized at the gap between the particle and the surface. At the same time the field enhancement around the gap drastically increases, finally reaching a value $\sim$100 for $D = 0.3$ nm. The localization and enhancement of the electric field are caused by the resonant excitation of electromagnetic normal modes of the particle–surface system. Since the fields are strongly localized at the gap, the normal modes are called 'gap modes' [11]. The resonance wavelength was found to shift to longer wavelengths as D decreases.

Figures 3a–c show a similar behavior of the field distribution generated by $E_{\mathrm{i}x}$ (or $E_{\mathrm{i}y}$, if the x axis is changed to the y axis). When the sphere is far from the surface, the $E_{\mathrm{i}x}$ (or $E_{\mathrm{i}y}$) component generates an enhanced field at the right- and left-hand sides of the sphere (along the x axis or the y axis). As the sphere approaches the surface, the field again becomes more and more localized at the gap. However, the field pattern is considerably different from that generated by $E_{\mathrm{i}z}$ and shows two lobes at the right- and left-hand sides of the bottom of the sphere ($x = 0$ nm). The field enhancement factor is larger than that of an isolated sphere, but much smaller than in the case of $E_{\mathrm{i}z}$ excitation.

Results of numerical calculations have been reported so far for a variety of sphere–surface systems, including Ag sphere–Ag surface [11], Au sphere–Au surface [11] and Au sphere–Al surface [9] systems. Calculations have been performed also for dielectric particles [10,11] and dielectric surfaces [29]. From these results, together with those presented in Figs. 2 and 3, the characteristics of the electromagnetic normal modes of particle–surface systems, i.e. the gap modes, emerge and can be summarized as follows: (1) A particle–surface system can support a series of gap modes when the particle–surface distance is sufficiently small ($D/R < 1$). For a large particle–surface distance only the lowest-order mode is important, but for a small distance, higher-order modes come into play. (2) The resonant frequencies of the gap modes shift to lower frequencies as the particle–surface distance decreases. (3) As the particle–surface distance decreases, the electric field becomes more and more localized at the gap between the particle and the surface. (4) When the gap mode is excited, the intensity of the electric field is enhanced relative to that of the excitation field. The maximum enhancement factor is larger than that achieved with an isolated particle (LSP excitation) or a surface alone (SPP excitation) [11]. (5) The enhancement factor is larger for an excitation field perpendicular to the surface than for an excitation field parallel to the surface.

The characteristics summarized above may stimulate various applications of gap modes in near-field optics. A straightforward application is surface-enhanced spectroscopy, such as surface-enhanced Raman spectroscopy (SERS) and second-harmonic generation. However, it is of prime importance to provide spectroscopic evidence for the existence of gap modes. The following sections are devoted to the discussion of spectroscopic data which demonstrate the existence of gap modes.

3 Observation of Gap Modes for Ag Islands on an Al Surface

Absorption spectra revealing LSP resonances have been reported for various systems, such as metal colloids, island particles, and particles embedded in solid matrices. A few authors [30,31] measured spectra for particles placed on various substrates and attempted to clarify the effects of the substrate on the LSP resonances. As pointed out in Sect. 2, a system of metallic particles placed on a metallic substrate can support gap modes. However, to the author's knowledge, no systematic observation of gap modes has been reported so far. In this section, we present results of a systematic absorption measurement performed on Ag island particles placed above an Al surface and give direct evidence for the existence of gap modes.

3.1 Experimental Procedure

The sample prepared is schematically shown in Fig. 4. On half of the surface of a glass slide, a stack of thin films consisting of an Al thin film, an SiO_2 spacer layer, an Ag island film, and a CaF_2 film was prepared. On the remaining half of the glass slide, the same stack of films without the Al film was prepared. The Al, Ag, and CaF_2 films were deposited by a vacuum evaporation technique, while the SiO_2 film was deposited by an rf sputtering technique. The thicknesses of the films were monitored by a quartz microbalance. The thickness of the Al film was 50 nm. The thickness of the spacer layer, denoted by d, was varied from 3.2 to 13.0 nm. To obtain well-separated and round Ag island particles, an Ag island film with a mass thickness of 8 nm was first deposited and then annealed at 500°C in a high vacuum. After the deposition and annealing of the Ag film, the whole sample was coated with a 50 nm thick CaF_2 to prevent possible oxidation and degradation.

To obtain spectroscopic data, a conventional setup consisting of an Xe lamp, monochromator, chopper, Si photodiode, and lock-in amplifier was

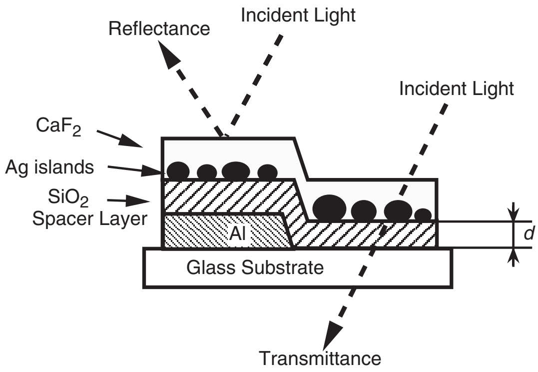

Fig. 4. Structure of the Ag island–Al surface samples prepared

used. For the part of the sample without the Al film, transmission spectra were measured, while for the part with the Al film, reflection spectra were measured. For both measurements the angle of incidence was fixed at 60° and the polarization of the incident light was set either to the s or the p polarization.

Figures 5a and 5b show plan view and cross-sectional transmission electron micrographs, respectively, of the sample. In the plan-view image, round Ag particles several tens of nanometers in diameter are seen. In the cross–sectional image, the particles appear to be flat rather than spherical. From both the plan view and the cross-sectional images, it turns out that the shape of the Ag island particles in these samples can be approximated by an ellipsoid of rotation. As mentioned in Sect. 2, the contribution of the gap modes becomes important when a particle is placed on a surface within a distance comparable to the diameter of the particle ($D/R < 1$). Since the thickness of the spacer layer is smaller than the particle diameter in the present samples, the observation of a gap mode is expected to be feasible.

3.2 Absorption Spectra

Figures 6a and 6b show the transmission and reflection spectra, respectively, obtained for the s polarization, and Figs. 7a and 7b those obtained for the p polarization. In Fig. 6a we see a transmission minimum (absorption peak) around 450 nm, whose position and depth are almost independent of the thickness of the spacer layer, d. In the reflection spectrum shown in Fig. 6b we see two minima (absorption peaks), one located around 400 nm and the other located in the 500–600 nm region. A remarkable feature observed is the red shift of the long-wavelength minimum as d decreases. The minimum around 400 nm is rather shallow for large values of d, but becomes more and more pronounced as d decreases. For the p-polarized incident light, the transmission spectra shown in Fig. 7a exhibit two minima whose position

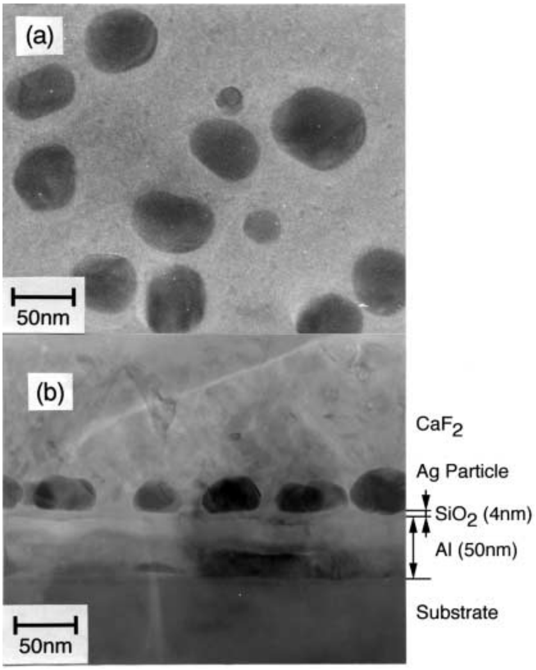

Fig. 5. Plan view (**a**) and cross-sectional (**b**) transmission electron micrographs of Ag island film

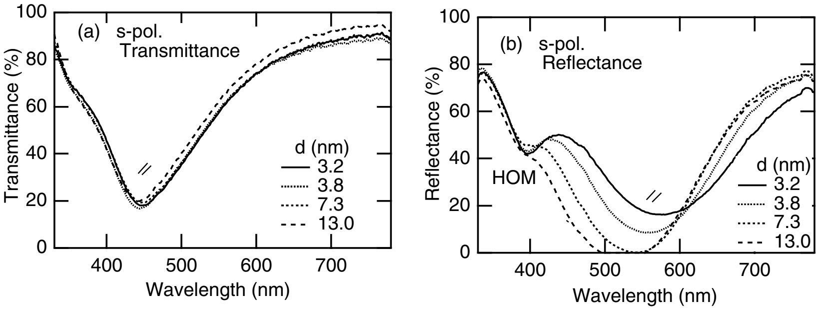

Fig. 6. Transmission (**a**) and reflection (**b**) spectra obtained for s-polarized incident light

and depth are almost independent of d. In the reflection spectra shown in Fig. 7b, three minima appear around 350, 400 and 500–600 nm. The minimum in the 500–600 nm region is again very sensitive to d and shows a red shift as d decreases. The minimum around 400 nm becomes pronounced for smaller values of d.

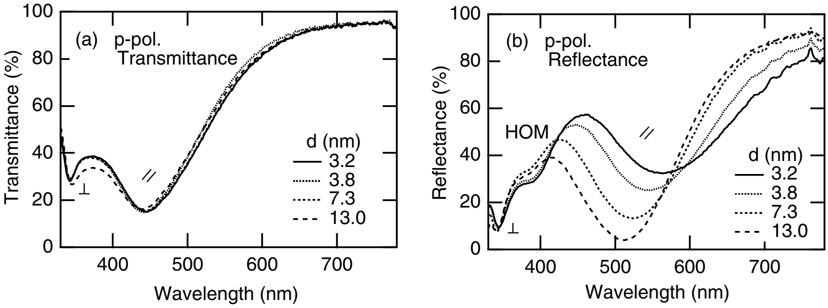

Fig. 7. Transmission (**a**) and reflection (**b**) spectra obtained for p-polarized incident light

The transmission minima seen in Figs. 6a and 7a are very similar to those previously reported for Ag island films [32,33]. They can be attributed to light absorption by LSP modes in Ag island particles. The polarization dependence of the spectra can be well explained by the ellipsoidal shape of the particles. As revealed by electron micrographs (Fig. 5), the present sample can be regarded as an assembly of ellipsoids of rotation with their long axes aligned parallel to the substrate and their short axes perpendicular to the substrate. For such a system, one absorption peak is predicted for s-polarized incident light, since the electric field associated with the s-polarization has only a component parallel to the substrate surface. The component can excite only the LSP mode oscillating parallel to the substrate surface (∥ mode). Therefore, the transmission minimum (absorption peak) appearing in Fig. 6a can be attributed to the ∥ mode. On the other hand, if the p-polarized light is obliquely incident (the angle of incidence was 60° in the present experiment), the electric field has two components, parallel and perpendicular to the substrate surface. These components can excite the LSP modes oscillating parallel and perpendicular to the substrate surface (∥ and ⊥ modes), resulting in two absorption peaks. The transmission minima at 450 and 360 nm can be assigned to the ∥ and ⊥ modes, respectively.

The reflection spectra presented in Figs. 6b and Figure 7b clearly indicate that the LSP modes of the Ag island particles are greatly influenced by the presence of the Al film. Remarkable features observed are the red shift of the reflection minimum in the 500–600 nm region and the appearance of the new minimum around 400 nm. As pointed out in Sect. 2, a red shift of the resonance with decreasing particle–surface distance is one of the most important characteristics of the gap modes. Taking into account the position and width of the minimum, we attribute the minimum appearing in the 500–600 nm region to the lowest-order gap mode originating from the ∥ mode. Numerical calculations performed by *Ruppin* [10] and *Aravind* and *Metiu* [11] predict that the resonance frequencies of the higher-order gap modes are higher than that of the lowest-order gap mode. From this prediction, together with the fact that the minimum becomes more and more pronounced as d decreases, we attribute the minimum appearing around 400 nm to the higher-order gap modes. Although the $\perp$ mode is also expected to shift to longer wavelengths as d decreases, no appreciable shift was observed in the present experiments. The reason for this is discussed later. The results presented in Figs. 6b and 7b provide direct evidence for the existence of gap modes.

Unfortunately, for an ellipsoidal particle placed close to a surface, a theoretical treatment as precise as that for a spherical particle has not been developed so far. Therefore it is difficult to further analyze the present results quantitatively. However, we have attempted to analyze the present results semiquantitatively within the framework of the dipole approximation [34]. We slightly extended the theory of *Ruppin* [10] for a sphere–surface system to an ellipsoid–surface system by introducing depolarization factors appropriate for an ellipsoid. In the theory the effects of the image dipole induced inside the substrate are taken into account. We calculated the shift of the $\|$ and $\perp$ modes as a function of the particle–surface distance. The amount of shift observed for the $\|$ mode could be well reproduced by the calculation. Furthermore, the shift of the $\perp$ mode was found to be very small, in good agreement with the experimental results. The difference in the behavior of the $\|$ and $\perp$ modes comes from the difference in the values of the depolarization factors governing the modes, as well as the difference in the strengths of the image fields generated by the image dipoles. In fact, the image field acting on the particle is a factor of two larger for the $\|$ mode, leading to a larger shift of the resonance frequency.

4 Light Emission from SPP Modes Mediated by Metallic Nanoparticles

The SPP modes on a flat metallic surface are not directly excited by light incident on the surface, because the component of the wave vector of the light parallel to the surface is smaller than that of the SPP modes and the requirement of conservation of parallel momentum is not satisfied. To excite the modes an appropriate coupler such as a prism, grating, or surface roughness could be used. However, the presence of metallic particles close to the surface changes the symmetry of the system and breaks the requirement of the conservation of parallel momentum. This results in a direct coupling between light and the SPP modes. This direct coupling can give rise to radiative decay of the SPP modes, i.e. light emission from the SPP modes, as well as to excitation of the SPP modes. In both phenomena, the gap modes are thought to play important roles, provided that the particles are placed very close to the surface. In this section, we describe experimental results on light emission and demonstrate the contribution of the gap modes.

4.1 Experimental Procedure

Spherical Ag nanoparticles embedded in SiO_2 films were prepared by an rf cosputtering technique (see [23,25,35] for details). Small pieces of Ag were placed on an SiO_2 target and were cosputtered in Ar gas. Figure 8 shows a typical high-resolution transmission electron microscope image of the Ag–SiO_2 film. In the figure, we can see dark patches corresponding to Ag particles. The Ag particles are spherical and well dispersed in the SiO_2 matrix. The average diameter determined from several images, was 5.6 nm, with a standard deviation of 2.1 nm. Figure 9 shows an absorption spectrum of the Ag–SiO_2 film. The absorption peak around 410 nm arises from the resonant excitation of the LSP mode in the Ag particles embedded in SiO_2. This absorption spectrum can be well reproduced by a theoretical calculation based on the Maxwell-Garnett effective dielectric function [25].

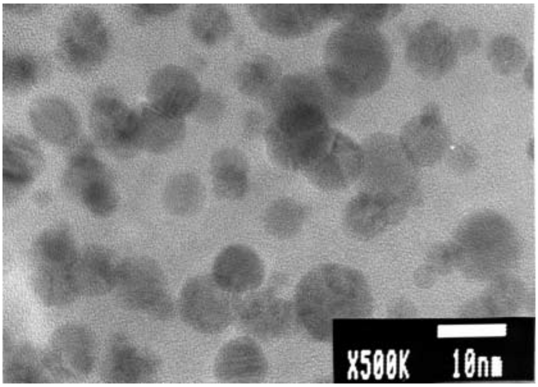

Fig. 8. Transmission electron micrograph of Ag nanoparticles embedded in an SiO_2 matrix prepared by an rf cosputtering method

A system of Ag particles placed on an Al surface was realized by preparing samples of the kind shown in Fig. 10a. First, Al films, 17 nm thick, were evaporated on glass substrates in a high vacuum. Spacer layers of SiO_2 were then deposited on the Al film by rf sputtering. Ag–SiO_2 films, 10 nm thick, were finally deposited on top of the spacer layer. In order to change the distance between the Al surface and the Ag particles, the thickness of the spacer layer *d* was varied between 0 and 9 nm. Hereafter, the samples are labeled by the thickness of the spacer layer. For example, *d*-3 indicates a sample with a spacer layer 3 nm thick. For comparison purposes, a sample whose overlayer did not contain Ag particles was also prepared, as shown in Fig. 10b.

In order to excite SPP modes on the Al–overlayer interface, we used an angle-scan ATR method, shown schematically in Figure 10c. The sample was pasted onto a right-angle glass prism (BK-7) with the aid of an

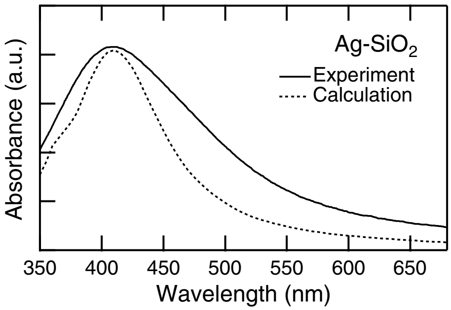

Fig. 9. Measured (*solid line*) and calculated (*broken line*) absorption spectra of the Ag–SiO$_2$ film [25]

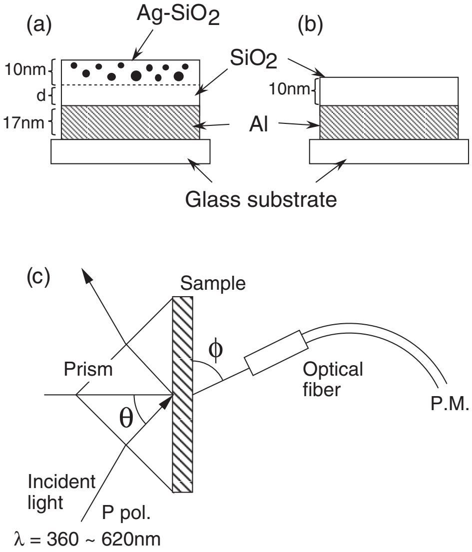

Fig. 10. (**a**), (**b**) Structures of the samples prepared. (**c**) Experimental arrangement for light emission measurements with SPP excitation. From [23]

index-matching oil, and the prism was mounted on a rotating stage. As a light source, an Xe lamp was used. The light monochromatized by a grating monochromator, was directed onto the sample through the prism. The illuminated spot was about $1 \times 1\,\mathrm{mm}^2$ in size. Since the SPP modes are transverse magnetic modes, the incident light was set to the p polarization. The intensity of the reflected light was measured as a function of the incidence angle θ. As shown in Fig. 10c, the light emitted from the sample was collected by an optical-fiber bundle that viewed the sample, and was guided to a photomultiplier. The aperture of the light collector was 2.5 mm in diameter. The distance between the aperture and the sample was 30 mm. We performed two types of measurements. In one type of measurement, the intensity of the emitted light was measured as a function of the incidence angle θ, fixing the observation angle ϕ at 90°. From this measurement we could confirm the excitation of SPPs, since the intensity had a maximum at an SPP excitation angle θ_{SPP}. In the other type of measurement, the light intensity was measured as a function of ϕ, while the incidence angle was fixed at θ_{SPP}. From this measurement, we obtained the angular pattern of the light emitted from the excited SPP. The above measurements were performed for various incident wavelengths, covering a range between 350 and 620 nm.

4.2 Light Emission Observed

Figure 11 shows typical ATR and θ-scan emission spectra obtained for sample *d*-0 and for a sample without Ag nanoparticles. The wavelength of the incident light was $\lambda = 520\,\text{nm}$. The ordinate in Fig. 11b represents the light intensity per unit solid angle normalized to the intensity of the incident light. The ATR spectra exhibit a dip in the reflectance due to the resonant excitation of SPP modes at the Al–overlayer interface. The presence of Ag nanoparticles in the overlayer causes a shift of the ATR dip to higher angles and makes

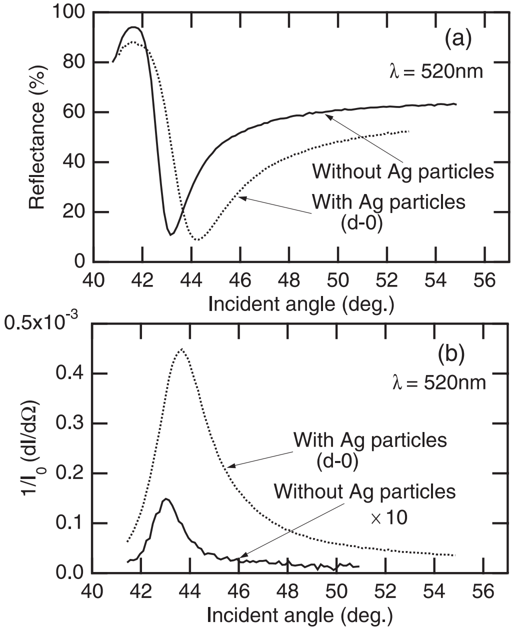

Fig. 11. (**a**) ATR spectra and (**b**) θ dependence of the emitted light intensity for sample *d*-0 and for a sample without Ag nanoparticles [23]. The emitted light was collected from the normal to the sample surface ($\phi = 0°$). The wavelength of the incident light was 520 nm

the dip broad. This is a consequence of the modification of the SPP dispersion curve, which has been studied in detail by the author's group [36]. In the emission spectra, we find a peak located at almost the same angle as the ATR dip. The coincidence of the peak and dip positions implies that the light emission is due to the radiative decay of the SPP modes towards the air side. The weak emission peak observed for the sample without Ag nanoparticles is attributed to the radiative decay of the SPP modes mediated by the surface roughness at the Al–SiO_2 interface. In the presence of the Ag nanoparticles, the intensity of the emitted light is greatly enhanced and is about one order of magnitude larger than the intensity without them.

Figure 12 shows the angular patterns of the emitted light. The result obtained for sample d-0 is shown in Fig. 12a, and the results obtained for samples d-3 and d-9 and the sample without Ag nanoparticles are shown in Fig. 12b. In the absence of the Ag nanoparticles, the angular pattern exhibits a lobe around $\phi = 10°$, in accordance with previous reports on nominally smooth (slightly rough) metallic surfaces. For a thick spacer layer (sample d-9), the angular pattern is almost the same as that for the sample without particles. As the spacer thickness d decreases, the lobe observed around 10° decreases and the two lobes around 30° and 150° grow. The intensities of

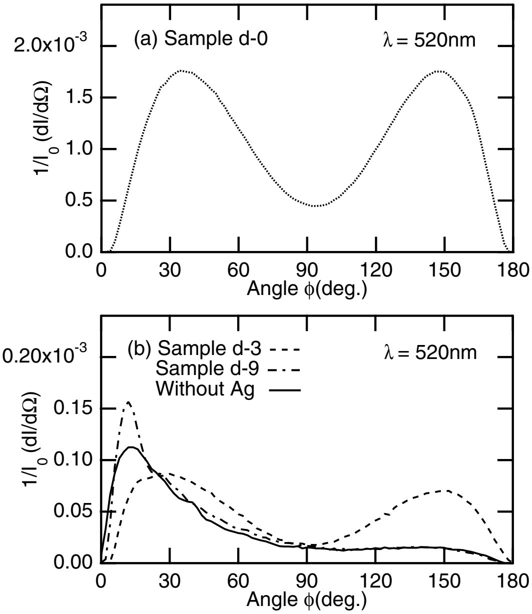

Fig. 12. Angular patterns of the emitted light under SPP excitation conditions for samples d-0 (*dotted line* in (**a**)), d-3 (*broken line* in (**b**)), and d-9 (*dash-dotted line* in (**b**)) and for the sample without Ag nanoparticles (*solid line* in (**b**)) [23]. The incident wavelength was 520 nm

the lobes increase drastically as d is decreased from 3 to 0 nm (note the change in the scale of the ordinate between Fig. 12a and Fig. 12b). The results presented in Fig. 12 demonstrate that Ag nanoparticles placed within a distance equal to their diameter (about 5 nm) from the Al surface strongly modify the intensity and angular pattern of the light emitted from the SPP modes.

In order to clarify the resonant behavior of the light emission mediated by the Ag nanoparticles, measurement of the angular pattern was performed while varying the incident wavelength in the range 350–650 nm. Figure 13 shows the λ dependence of the emitted light intensity integrated over ϕ. Sample d-9 emits light with almost the same intensity as for the sample without Ag nanoparticles. As d decreases from 3 to 0 nm, the intensity drastically increases. The most interesting feature in the figure is a pronounced peak observed around $\lambda = 520$ nm for sample d-0. We infer that a strong resonance exists in sample d-0 around $\lambda = 520$ nm.

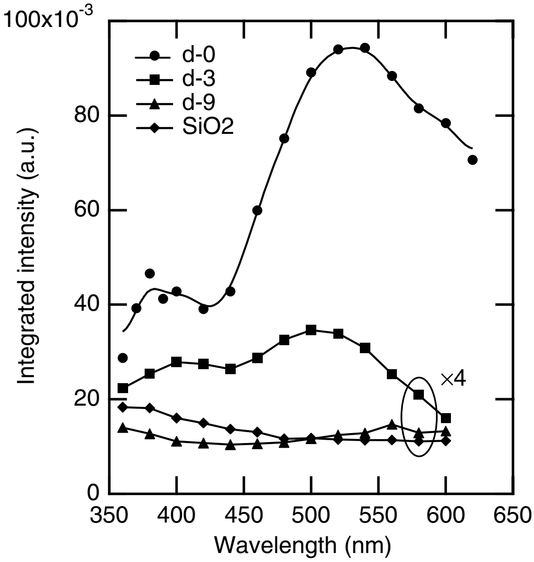

Fig. 13. Wavelength dependence of emitted light intensity under conditions of SPP excitation [23]. The intensity integrated from $\phi = 0$ to 180° is plotted

4.3 Contribution of the Gap Modes

For our samples, in particular those with thin spacer layers, the gap modes are believed to play an important role in the light emission processes. Since the resonance wavelength of the LSPs in isolated Ag particles in the SiO_2 matrix is 410 nm as can be seen in Fig. 9, the resonances of the gap modes are expected to lie at wavelengths longer than 410 nm. The appearance of the peak around 520 nm in Fig. 13 for sample d-0 strongly suggests contribution of gap modes.

The light emission from the SPP modes mediated by metallic particles is thought to arise from the following processes: (1) SPPs at the Al–overlayer interface are excited optically when the ATR method is used, (2) the electromagnetic fields associated with the SPPs then excite a gap mode of the Ag particle–Al surface system, (3) a surface current on the Al surface is induced upon excitation of the gap mode, and finally (4) the surface current emits light. On the basis of the above scenario, we performed electromagnetic calculations and attempted to theoretically reproduce the observed characteristics of the light emission (see [23] for details of the calculation). The mathematical procedures followed were similar to those described in Sect. 2 and [8,9,10,11]. As explained in Sect. 2, gap modes are excited effectively by the E_z component of the incident light. In the present situation, the E_z component of the field associated with the SPP mode is responsible for the excitation, and an electric-field distribution analogous to that shown in Fig. 2d is generated in the Ag particle–Al surface system. In fact, to obtain Figure 2 we used parameters appropriate for discussing the present experiment. In general, a large discontinuity in the electric field at an interface implies the induction of a large surface charge. When a gap mode is excited as in Fig. 2d, a very large field discontinuity and thus a large amount of surface charge are generated at the Al–SiO_2 interface just beneath the Ag particles. Since the electric field oscillates with a frequency ω, the surface charge also fluctuates with a frequency ω. The fluctuation of the surface charge can act as a radiation source, giving rise to light emission.

In order to calculate the characteristics of the emitted light, we followed the theoretical treatment of Kröger and Kretschmann [37], who introduced a surface current generated by surface roughness in the analysis of the radiative decay of SPPs. In their treatment, the radiation source was assumed to be the difference between the surface currents in the presence and absence of the roughness. In our calculation, we assumed the radiation source to be the difference between the surface currents in the presence and absence of the Ag particle. From a detailed analysis, it turns out that a surface current strongly localized beneath the Ag particle is generated and, among the components of the surface current J_x, J_y, and J_z, J_z contributes dominantly to the light emission [23]. The magnitude of J_z was found to depend strongly on D and λ. Figure 14 shows the wavelength dependence of the maximum value of J_z. In the calculation, R was set to 4.5 nm and the results obtained for $D = 3$ and 0.3 nm are presented in the figure. For $D = 0.3$ nm, we see a pronounced peak around 520 nm, which corresponds to the excitation of the gap mode. For $D = 3$ nm, the peak is very weak and is located around 420 nm, which is almost the same as the resonance wavelength of the LSPs in an isolated Ag particle in SiO_2. It should be noted that the features found in Fig. 14 agree very well with those of the experimental results shown in Fig. 13. The angular pattern of emitted light calculated from J_z also agrees very well with the experimental pattern shown in Fig. 12a. The qualitative agreement between the calculated and experimental results allows us finally, to conclude that the excitation of gap modes plays a crucial role in light emission from the Ag particle–Al surface system, in particular when the particle is placed very close to the surface ($d = 0$).

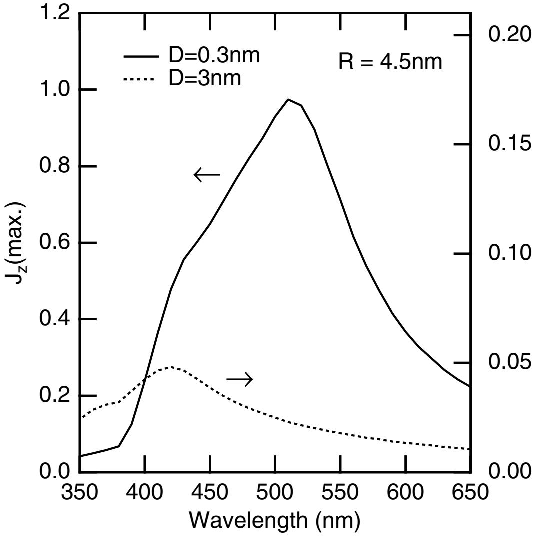

Fig. 14. Calculated wavelength dependence of z component of surface current J_z induced on the Al surface under conditions of SPP excitation [23]. The maximum value of J_z is plotted. The sphere radius was assumed to be $R = 4.5$ nm and the *solid* and *dashed lines* correspond to $D = 0.3$ and 3 nm, respectively

5 Excitation of SPPs Mediated by Metallic Nanoparticles

In Sect. 4, we demonstrated that the nonradiative SPP modes on a metallic surface can be converted to a radiation field (emitted light) with the aid of metallic nanoparticles. This is a consequence of the direct coupling between light and SPP modes allowed in the particle–surface system. Another interesting consequence of this direct coupling is the excitation of SPP modes without using coupling devices such as a prism or grating. In this section, we demonstrate the feasibility of the excitation of SPPs mediated by nanoparticles and again stress the contribution of the gap modes in the excitation processes.

The samples used in the experiments described here were the same as those described in the previous section. Samples *d*-0 (without spacer layer) and *d*-3 (3 nm spacer layer), and the sample not containing Ag particles were used. In order to confirm the excitation of SPP modes, we used the so-called reversed ATR (RATR) method [38], as shown schematically in Fig. 15. The sample was pasted onto a flat surface of a hemispherical prism (BK-7) with the aid of an index-matching oil (the glass substrate was in contact with the prism). Contrary to the standard ATR method, light was directed onto the sample surface from the opposite side of the prism. In this arrangement, if SPP modes are excited at the Al–overlayer interface, it should be possible to observe radiation coupled out through the prism. The decoupled SPP radiation should be observable in the form of a hollow light cone, as shown schematically in Fig. 15. This is because, for a fixed wavelength of incident light, the wave vectors of the excited SPP modes have a constant magnitude but various directions along the interface.

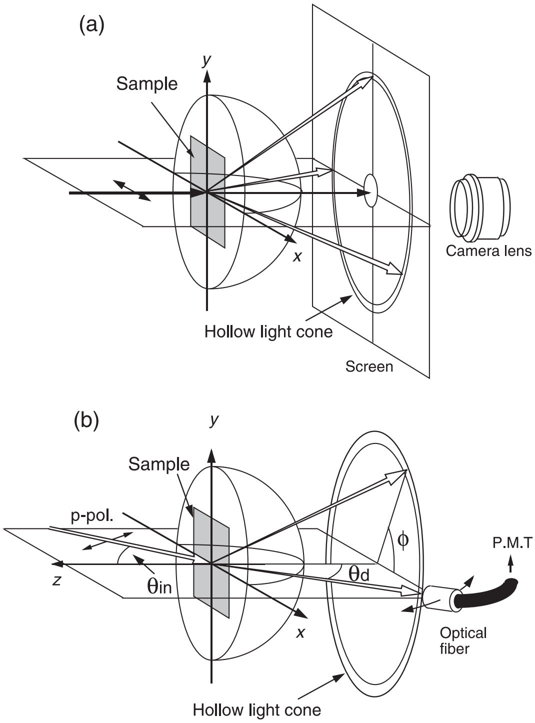

Fig. 15. RATR configurations. (**a**) A decoupled hollow light cone is projected on a screen and photographed. (**b**) The decoupled light is collected by an optical-fiber bundle and guided to a photomultiplier. The light intensity is measured as a function of the decoupling angle, θ_{d}, by scanning the head of the optical fiber

As shown in Fig. 15a, a simple observation of the SPP excitation was made by using a 488 nm beam from an Ar ion laser and taking a photograph of the decoupled light projected onto a screen (tracing paper) placed 5 cm behind the hemispherical prism. A typical photograph obtained for sample $d-0$ is reproduced in Fig. 16 [39]. At the center of the screen a hole 1 cm in diameter was made to allow the light beam transmitted through the sample–prism system to pass through. We can clearly see a light ring, which is a projection of the hollow light cone, demonstrating the excitation of the SPP modes. In the arrangement used to obtain Fig. 16, the laser beam was incident normal to the sample surface and the electric vector of the incident light was set parallel to the x direction in Fig. 15a. In this case, the intensity of the light has maxima in the x and $-x$ directions on the screen and decreases as one moves along the ring towards the y and $-y$ directions. When the incident electric vector was rotated, the angular pattern rotated simultaneously. We found that the light rings become very weak as the particle–surface distance increases (samples with spacer layers) and become rather difficult to see with the naked eye or to photograph clearly.

In order to be able to discuss the SPP excitation more quantitatively, we attempted to measure the intensity of the decoupled light as a function of the decoupling angle, θ_{d}, in the horizontal plane (x–z plane), as shown schematically in Fig. 15b. The light from an Xe lamp, monochromatized by a monochromator, was used. The p-polarized light was incident on the sample at an angle of 30°. The decoupled light was collected by an optical-fiber bundle with an aperture 2 mm in diameter and guided to a photomultiplier. In Fig. 17, the RATR spectra so obtained are compared with ATR spectra obtained in a standard Kretschmann configuration. The wavelength of the incident light was 500 nm. In the ATR measurements, a 90° prism with the same refractive index as the hemispherical prism of the RATR measurements was used. All the samples show ATR dips corresponding to the excitation of SPP modes at the Al–overlayer interface. The position and width of the dip

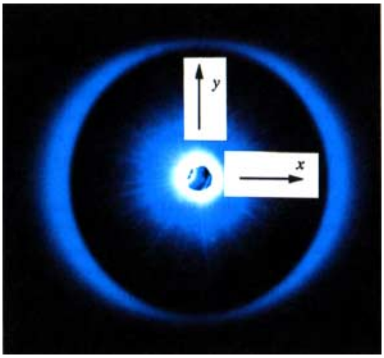

Fig. 16. Photograph of the light ring for sample d-0 [39]

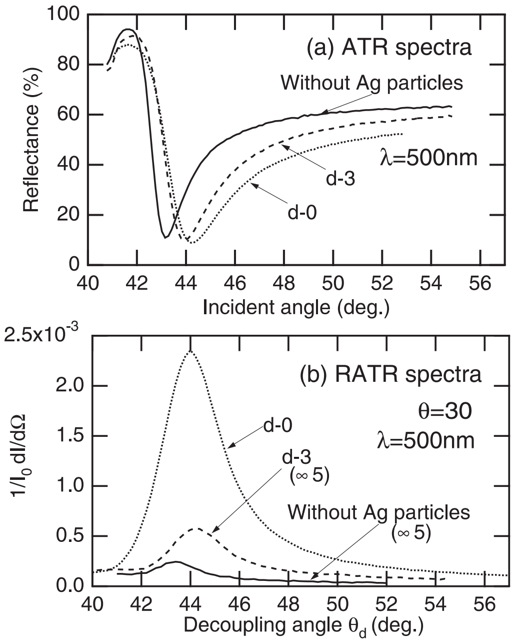

Fig. 17. (**a**) ATR spectra and (**b**) RATR spectra obtained for samples with (*d*-0 and *d*-3) and without Ag nanoparticles [24]. The incidence wavelength was 500 nm. For RATR measurements, the incident angle was set to $\theta = 30^\circ$

depend on the nature of the overlayer. In the RATR spectra we can see peaks located at almost the same angles as the corresponding ATR dips. The coincidence between the peak positions in the RATR spectra and the dip positions in the ATR spectra confirms that the decoupled light comes from SPP modes excited on Al–overlayer interfaces. The weak peak seen for the sample without Ag nanoparticles is mainly due to SPP excitation mediated by the surface roughness. The presence of Ag nanoparticles very close to the Al surface (*d*-0) causes a dramatic increase in the intensity of the decoupled-light, thus demonstrating the effectiveness of the SPP excitation mediated by the Ag nanoparticles. However, the decoupled light intensity decreases rapidly as the particle–surface distance (spacer layer thickness) increases, and reaches that of the roughness-mediated SPP excitation for sample *d*-3.

Similar measurements of the decoupled-light intensity were performed by varying the wavelength of incident light. In Fig. 18 the maximum intensity in the RATR spectra is plotted as a function of the wavelength. Sample *d*-0 shows a pronounced peak around 520 nm, while the other samples show very low intensities. It is interesting to note that the results presented in this figure are very similar to those presented in Fig. 13. This suggests that although the processes studied are different, one being the conversion of SPP modes into light and the other being the conversion of light into SPP modes, the

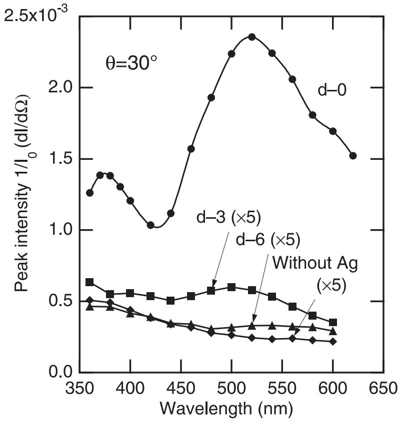

Fig. 18. Dependence of the peak intensity in RATR spectra on the incident wavelength [24]. The incidence angle was $\theta = 30°$

underlying mechanism is the same, i.e. the contribution of the gap modes. In order to confirm this idea, we performed electromagnetic calculations similar to those described in Sect. 4 We found again that the surface current induced beneath an Ag particle upon excitation of a gap mode is responsible for SPP excitation.

6 Concluding Remarks

In this chapter, we have focused on discussion of the gap modes that exist in a system of a metallic particle placed very near to a metallic surface. After the characteristics of the gap modes predicted from electromagnetic theories were summarized, results of spectroscopic measurements, which demonstrate the existence and importance of these modes, were presented. The gap modes play important roles in various optical phenomena when the distance of the particle from the surface is smaller than the particle radius. The electric fields associated with the gap modes are strongly localized at the particle–surface gap and very much enhanced relative to the excitation field. The resonance frequencies depend strongly on the distance of the particle from the surface.

As mentioned at the beginning of this chapter, the sphere–surface system is an important model for discussing the performance of SNOM. In a metal tip–metal surface system, strong resonances due to the excitation of gap modes are expected to occur, provided that the tip–surface distance is sufficiently small. The resonance wavelength depends strongly on this distance. Although the high spatial resolution of SNOM images has already been demonstrated for metal tip–metal surface systems [16,17,18,19,20,21], experiments have usually been performed by using light of a single wavelength, and the resonant behavior depending on the tip–surface distance seems to have been ignored so far. Further optimization of the performance of SNOM may be achieved by appropriately choosing the light wavelength, i.e. by tuning the wavelength to the resonance wavelength of the tip–surface system.

Under conditions of resonant excitation of the gap modes, strong localization and strong enhancement of electromagnetic field are realized. The field enhancement factor is much larger than that achieved by excitation of LSPs in a single sphere or by SPP excitation on a flat surface [11]. Gap mode excitation thus provides a new way to achieve enhanced spectroscopy with a high spatial resolution. The enhancement of various optical phenomena, such as Raman scattering, luminescence, second-harmonic generation, etc. is possible. To the author's knowledge, no systematic observation of such enhancement upon gap mode excitation has been reported so far. A systematic observation of the enhancement while the particle–surface distance is varied may be of great interest.

The discussions of this chapter were limited to a metal sphere placed above a metal substrate. It should be noted here that field localization and enhancement can be expected even when the metal sphere and/or the metal substrate are replaced by a dielectric sphere and/or a dielectric substrate, although the degree of localization and enhancement is smaller than that for a metal sphere–metal surface system [29]. The resonant wavelength in systems containing a dielectric sphere and substrate does not change very much as a function of the sphere–surface distance.

The discussions of this chapter were based on the electrostatic approximation, which is valid when $D + 2R$ is smaller than the wavelength of light. When the radius of the sphere is comparable to or larger than the wavelength of light, it is well known that so-called Mie resonances or morphological resonances become important [40]. Theoretical analyses [41,42,43] suggest that the Mie resonances are modified significantly when the sphere is placed on a substrate. Futhermore, the scattering and extinction of evanescent waves by a sphere, in particular the polarization characteristics, are predicted to be very different from ordinary Mie scattering of plane waves. However, no systematic experimental observation of substrate effects or the scattering of evanescent waves has been reported so far. These topics are outside the scope of the present chapter, but may be of great importance for physical discussions of a variety of particle–surface systems encountered in near-field optics, in particularly SNOM systems. Further extensive experimental and theoretical work is still required to fully explore the interesting optical characteristics of particle–surface systems and achieve fruitful applications.

References

1. H. Reather, *Surface Plasmons on Smoth and Rough Surfaces and on Grating*, Springer Tracts Mod. Phys. **111** (Springer, Berlin, Heidelberg 1988) 71
2. V. M. Agranovich, D. L. Mills (Eds.), *Surface Polaritons, Modern Problems in Condensed Matter Sciences* (North-Holland, Amsterdam 1982) 71
3. R. Ruppin, *Electromagnetic Surface Modes*, A. D. Boardman (Ed.) (Wiley, Chichester 1982) Chap 9, pp. 345-398 71, 72
4. U. Kreibig, M. Vollmer, *Optical Properties of Metal Clusters*, Springer Ser. Mater. Sci. **25** (Springer, Berlin, Heidelberg 1995) 71, 72, 75
5. S. L. McCarthy, J. Lambe, Appl. Phys. Lett. **33**, 858 (1978) 71
6. A. Adams, J. C. Wyss, P. K. Hansma, Phys. Rev. Lett. **42**, 912 (1979) 71
7. A. Adams, P. K. Hansma, Phys. Rev. B **23**, 3587 (1981) 71
8. R. W. Rendell, D. J. Scalapino, B. Mühlschlegel, Phys. Rev. Lett. **41**, 1746 (1978) 71, 73, 87
9. R. W. Rendell, D. J. Scalapino, Phys. Rev. B **24**, 3276 (1981) 71, 73, 76, 87
10. R. Ruppin, Surf. Sci. **127**, 108 (1983) 71, 73, 76, 80, 81, 87
11. P. K. Aravind, H. Metiu, Surf. Sci. **124**, 506 (1983) 71, 73, 76, 77, 80, 87, 93
12. J. K. Gimzewski, B. Reihl, J. H. Coombs, R. R. Schlitter, Z. Phys. B **72**, 497 (1988) 72
13. R. Berndt, J. K. Gimzewski, P. Johansson, Phys. Rev. Lett. **67**, 3796 (1991) 72
14. P. Johansson, R. Monreal, P. Appel, Phys. Rev. B **42**, 9210 (1990) 72
15. P. Johansson, R. Monreal, Z. Phys. B **84**, 269 (1991) 72
16. W. Denk, D. W. Pohl, J. Vac. Sci. Technol. B **9**, 510 (1991) 72, 92
17. M. Specht, J. D. Pedarnig, W. M. Heckel, T. W. Hänsch, Phys. Rev. Lett. **68**, 476 (1992) 72, 92
18. A. Madrazo, M. Neito-Vesperinas, N. Garcia, Phys. Rev. B **53**, 3654 (1996) 72, 92
19. M. Neito-Vesperinas, A. Madrazo, *Photons and Local Probes*, O. Mari, R. Möller (Eds.) (Kluwer Academic, Dordrecht 1995) p. 35 72, 92
20. Y. Inouye, S. Kawata, Opt. Commun. **134**, 31 (1997) 72, 92
21. T. Sugiura, T. Okada, Y. Inoue, O. Nakamura, S. Kawata, Opt. Lett. **22**, 1663 (1997) 72, 92
22. T. Takemori, M. Inoue, K. Ohtaka, J. Phys. Soc. Jpn. **56**, 1587 (1987) 73
23. T. Kume, S. Hayashi, K. Yamamoto, Phys. Rev. B **55**, 4774 (1997) 74, 82, 83, 84, 85, 86, 87, 88
24. T. Kume, S. Hayashi, K. Yamamoto, Mater. Sci. Eng. A **217/218**, 171 (1996) 74, 91, 92
25. T. Kume, Excitation of Surface Plasmon Polaritons and its Application to an Organic Solar Cell, Ph. D. Thesis, Graduate School of Science and Technology, Kobe University (1996) 74, 82, 83
26. D. Y. Smith, E. Shiles, M. Inokuti, *Handbook of Optical Constants of Solids*, E. D. Palik (Ed.) (Academic, Orlando 1985) p. 398 74
27. H. R. Philipp, *Handbook of Optical Constants of Solids*, E. D. Palik (Ed.) (Academic, Orlando 1985) p. 749 74
28. D. W. Lynch, W. R. Hunter, *Handbook of Optical Constants of Solids*, E. D. Palik (Ed.) (Academic, Orlando 1985) p. 350 75
29. T. Okamoto, I. Yamaguchi, Opt. Rev. **6**, 211 (1999) 76, 93

30. P. Royer, J. P. Goudonnet, R. J. Warmack, T. L. Ferrell, Phys. Rev. B **35**, 3753 (1987) 77
31. G. Bader, P. V. Ashrit, F. E. Girouard, V. Truong, J. Appl. Phys. **68**, 1820 (1990) 77
32. S. Yoshida, T. Yamaguchi, A. Kinbara, J. Opt. Soc. Am. **61**, 62 (1971) 80
33. S. Yoshida, T. Yamaguchi, A. Kinbara, J. Opt. Soc. Am. **62**, 1415 (1972) 80
34. H. Kurokawa, S. Hayashi, Technical Digest 5th Int. Conf. Near Field Optics and Related Techniques (1998) p. 379 81
35. M. Fujii, T. Nagareda, S. Hayashi, K. Yamamoto, Phys. Rev. B **44**, 6243 (1991) 82
36. T. Kume, N. Nakagawa, S. Hayashi, K. Yamamoto, Solid State Commun. **93**, 171 (1995) 85
37. E. Kröger, E. Kretschmann, Z. Phys. **237**, 1 (1970) 87
38. S. Hayashi, Surf. Sci. **158**, 229 (1985) 89
39. S. Hayashi, T. Kume, T. Amano, K. Yamamoto, Jpn. J. Appl. Phys. **35**, L331 (1996) 90
40. G. F. Bohren, D. R. Huffman, *Absorption and Scattering of Light by Small Particles* (Wiley, New York 1983) 93
41. H. Chew, D. S. Wang, M. Kerker, Appl. Opt. **18**, 2679 (1979) 93
42. D. Barshiesi, P. M. Duffieux, J. Mod. Opt. **40**, 1239 (1993) 93
43. R. Wannemacher, A. Pack, M. Quinten, Appl. Phys. B **68**, 225 (1999) 93

Near-Field Spectral Analysis of Metallic Beads

Takayuki Okamoto

Optical Engineering Laboratory, RIKEN,
Wako, Saitama 351-0198, Japan
`okamoto@optsun.riken.go.jp`

Abstract. The scattering and absorption properties of metal particles smaller than the wavelength are described. In particular, the surface plasmon resonance in gold and silver nanoparticles is mentioned. In Sec. 1 the dielectric function of noble metals, including the size effect is described. In Sec. 2 the scattering problem for a small metal sphere is solved using the static approximation and the exact Mie theory. In particular, the details of the near-field of the sphere are mentioned. Spectra of scattering, absorption, and near-field scattering cross sections are plotted. In Sec. 3 the scattering by ellipsoids is described. In Sec. 4 the scattering by coated spheres and metal shell particles are described. In Sec. 5 and 6 the scattering by a sphere above the substrate and two adjacent identical spheres is described. In the last section an optical sensor is mentioned as an application of the surface plasmon resonance in gold nanoparticles.

1 Dielectric Function of Metals

The dielectric constant of a metal is given by the sum of a contribution from the free electrons of the metal and a contribution from the interband transitions. The contribution from the free electrons ε_{f} is given by the Drude free-electron model.

1.1 Drude Free Electron Model

This model is similar to the Lorentz harmonic-oscillator model, but the spring constant is zero. The equation of motion of a free electron is

$$m_{\mathrm{e}}\frac{\partial^2 \boldsymbol{r}}{\partial t^2} + m_{\mathrm{e}}\Gamma\frac{\partial \boldsymbol{r}}{\partial t} = e\boldsymbol{E}_0\mathrm{e}^{-\mathrm{i}\omega t}\,, \tag{1}$$

where m_{e} is the effective mass of the electron, e is the charge of the electron, $\boldsymbol{E} = \boldsymbol{E}_0\mathrm{e}^{-\mathrm{i}\omega t}$ is the external electric field, and Γ is the damping constant. Solving (1) gives the displacement $\boldsymbol{r}$ of the electron from its mean position. The dipole moment is given by $\boldsymbol{p} = e\boldsymbol{r}$. Denoting the number of free electrons per unit volume by n, the polarization is $\boldsymbol{P} = n\boldsymbol{p}$. If we assume that the medium is isotropic ($\boldsymbol{P} \parallel \boldsymbol{E}$), the dielectric function $\varepsilon_{\mathrm{f}}(\omega)$ is

$$\varepsilon_{\mathrm{f}}(\omega) = 1 + |\boldsymbol{P}|/(\varepsilon_0|\boldsymbol{E}|)\,, \tag{2}$$

S. Kawata (Ed.): Near-Field Optics and Surface Plasmon Polaritons,
Topics Appl. Phys. **81**, 97–123 (2001)

where ε_0 is the dielectric constant of a vacuum. From (1) and (2), we obtain

$$\varepsilon_{\mathrm{f}}(\omega) = 1 - \frac{\omega_{\mathrm{p}}^2}{\omega^2 + \mathrm{i}\Gamma\omega} = 1 - \frac{\omega_{\mathrm{p}}^2}{\omega^2 + \Gamma^2} + \mathrm{i}\frac{\omega_{\mathrm{p}}^2 \Gamma}{\omega(\omega^2 + \Gamma^2)}\,, \tag{3}$$

where ω_{p} is the Drude, or volume plasma, frequency:

$$\omega_{\mathrm{p}} = \left(\frac{ne^2}{\varepsilon_0 m_{\mathrm{e}}}\right)^{1/2}. \tag{4}$$

The damping constant Γ is related to the electron mean free path l and the Fermi velocity v_{F} and is given by

$$\Gamma = v_{\mathrm{F}}/l\,. \tag{5}$$

1.2 Interband Transitions

In real metals, besides the contribution of the free electrons, we have to consider the effects of interband transitions. For alkali metals, such as sodium and potassium, interband transitions do not affect the dielectric function in the visible range, because the energy of the band gap is large. However, we shall not discuss alkali metals further, because they are unstable in air. For the noble metals such as copper, silver, and gold, we cannot ignore the influence of interband transitions in the visible range. For copper, silver, and gold, the interband transitions are 3d → 4sp, 4d → 5sp, and 5d → 6sp, respectively, and the free electrons are in the 4s, 5s, and 6s states, respectively. For copper and gold the absorption edge due to interband transitions is in the visible range, so that, these metals are colored. For silver, although the absorption edge is in the ultraviolet, it affects the dielectric constant in the visible range very much. The dielectric constant of a real metal is given by the sum of the contribution fo the free electrone $\varepsilon_{\mathrm{f}}(\omega)$ and the contribution of the interband transitions $\varepsilon_{\mathrm{ib}}(\omega)$:

$$\varepsilon(\omega) = \varepsilon_{\mathrm{f}}(\omega) + \varepsilon_{\mathrm{ib}}(\omega) = 1 - \frac{\omega_{\mathrm{p}}^2}{\omega^2 + \mathrm{i}\Gamma\omega} + \varepsilon_{\mathrm{ib}}(\omega)\,. \tag{6}$$

1.3 Size Effect

The above discussion applies to bulk metals. If the dimension of the metal is decrease, i. e. we have small particles, the dielectric constant deviates from that for the bulk metal. When the size of the particle becomes smaller than the mean free path of the free electrons, the electrons collide with the boundary of the particle. If this effect is included, the damping constant is given by

$$\Gamma = \Gamma_{\mathrm{bulk}} + Av_{\mathrm{F}}/r_1\,. \tag{7}$$

where Γ_{bulk} is the damping constant for the bulk, r_1 is the radius of the particle, and A is a constant. The value of A depends on the particle shape and the theory used and is usually around unity. Using the experimentally obtained dielectric constant $\varepsilon_{\mathrm{exp}}(\omega)$, the dielectric constant including the size effect is given by

$$\varepsilon(\omega) = \varepsilon_{\mathrm{exp}}(\omega) + \frac{\omega_{\mathrm{p}}^2}{\omega^2 + \mathrm{i}\Gamma_{\mathrm{bulk}}\omega} - \frac{\omega_{\mathrm{p}}^2}{\omega^2 + \mathrm{i}\Gamma\omega} \,. \tag{8}$$

The plasma frequency ω_{p} and the damping constant Γ are obtained by fitting the following functions, which are valid for $\omega \gg \Gamma_{\mathrm{bulk}}$, to the experimentally obtained dielectric function in the near infrared region, where the influence of the interband transitions can be ignored:

$$\mathrm{Re}[\varepsilon_1(\omega)] \simeq 1 - \frac{\omega_{\mathrm{p}}^2}{\omega^2} \,, \quad \mathrm{Im}[\varepsilon_2(\omega)] \simeq \frac{\omega_{\mathrm{p}}^2}{\omega^3}\Gamma_{\mathrm{bulk}} \,. \tag{9}$$

Table 1 shows the plasma frequency, the damping constants, and the Fermi velocity for copper, silver, and gold. Figures 1 and 2 show the dielectric

Table 1. Plasma frequency, relaxation constant, and Fermi velocity of copper, silver, and gold

	Copper	Silver	Gold
$\omega_{\mathrm{p}}(10^{15}\ \mathrm{s}^{-1})$ [1]	13.4	14.0	13.8
$\tau = 1/\Gamma_{\mathrm{bulk}}\ (10^{-15}\mathrm{s})$ [1]	6.9	31	9.3
$v_{\mathrm{F}}\ (10^8\ \mathrm{cm/s})$ [2]	1.57	1.39	1.39

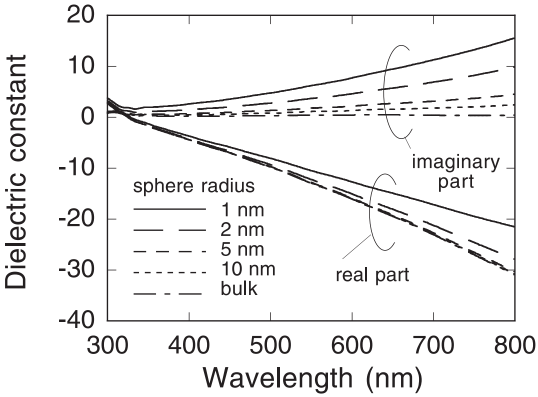

Fig. 1. Dielectric function of silver including size effect

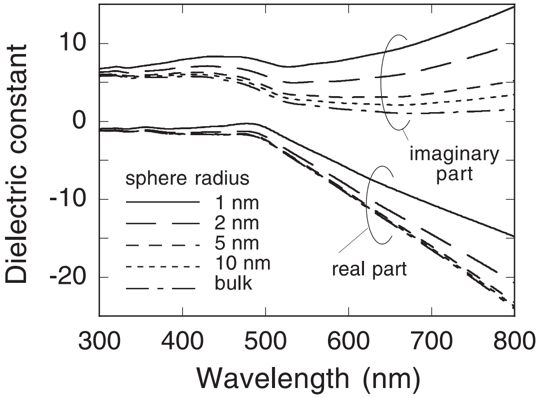

Fig. 2. Dielectric function of gold including size effect

functions of silver and gold calculated using (8). We have used the bulk dielectric functions of these metals obtained by *Johnson* and *Christy* [1] and $A = 1$. These calculated values will be used hereafter.

2 Scattering by a Small Metal Sphere

The scattering problem for an arbitrary sphere has been solved exactly by *Mie* [3]. However, the quasi-static approximation is more appropriate if one wishes to obtain a clear physical insight. This approximation can be employed when the diameter is much smaller than the wavelength.

2.1 Quasi-Static Approximation

'Quasi-static' implies that spatially the field is static, i. e. no retardation effects, but temporally it oscillates according to $\mathrm{e}^{-\mathrm{i}\omega t}$. The range of the validity of the electrostatic solution is discussed in *Kerker's* book [4]. In this approximation the potential Φ satisfies Laplace's equation ($\nabla^2\Phi = 0$). The equation in spherical polar coordinates is

$$\frac{1}{r^2}\frac{\partial}{\partial r}\left(r^2\frac{\partial \Phi}{\partial r}\right) + \frac{1}{r^2\sin\theta}\frac{\partial}{\partial\theta}\left(\sin\theta\frac{\partial\Phi}{\partial\theta}\right) + \frac{1}{r^2\sin^2\theta}\frac{\partial^2\Phi}{\partial\phi^2} = 0\,. \tag{10}$$

The general solution of this equation is given by

$$\Phi = \sum_{n=0}^{\infty}\sum_{m=0}^{n}\left(a_{nm}r^n + \frac{b_{nm}}{r^{n+1}}\right)P_n^m(\cos\theta)\mathrm{e}^{\mathrm{i}m\phi}\,. \tag{11}$$

The potential inside the sphere Φ_1 and that outside the sphere $\Phi_2 = \Phi_\mathrm{s} + \Phi_0$ must satisfy the boundary conditions at the surface of the sphere, where

$\mathit{\Phi}_0 = -E_0 z = -E_0 r P_1^0(\cos\theta)$ is the external potential and $\mathit{\Phi}_\mathrm{s}$ is the scattering potential. The continuity of the electric field gives

$$\left.\frac{\partial \mathit{\Phi}_1}{\partial \theta}\right|_{r=r_1} = \left.\frac{\partial \mathit{\Phi}_2}{\partial \theta}\right|_{r=r_1}, \tag{12}$$

and the continuity of the electric displacement gives

$$\varepsilon_1 \left.\frac{\partial \mathit{\Phi}_1}{\partial r}\right|_{r=r_1} = \varepsilon_2 \left.\frac{\partial \mathit{\Phi}_2}{\partial r}\right|_{r=r_1}, \tag{13}$$

where r_1 is the sphere radius, and ε_1 and ε_2 are the dielectric constants of the sphere and the ambient, respectively. Using these equations and the orthogonality of the associated Legendre functions, the potential inside the sphere is obtained as

$$\mathit{\Phi}_1 = -\frac{3\varepsilon_2}{\varepsilon_1 + 2\varepsilon_2} E_0 r \cos\theta\,. \tag{14}$$

The potential outside the sphere is

$$\mathit{\Phi}_2 = -E_0 r \cos\theta + \frac{\varepsilon_1 - \varepsilon_2}{\varepsilon_1 + 2\varepsilon_2} r_1^3 E_0 \frac{\cos\theta}{r^2}\,. \tag{15}$$

The electric field is given by $\boldsymbol{E} = -\boldsymbol{\nabla}\mathit{\Phi}$:

$$\boldsymbol{E}_1 = \frac{3\varepsilon_2}{\varepsilon_1 + 2\varepsilon_2}(E_0 \cos\theta\,\boldsymbol{e}_r - E_0 \sin\theta\,\boldsymbol{e}_\theta) = \frac{3\varepsilon_2}{\varepsilon_1 + 2\varepsilon_2} E_0 \boldsymbol{e}_z\,, \tag{16}$$

$$\begin{aligned}\boldsymbol{E}_2 &= E_0 r \cos\theta\,\boldsymbol{e}_r - E_0 r \sin\theta\,\boldsymbol{e}_\theta + \frac{\varepsilon_1 - \varepsilon_2}{\varepsilon_1 + 2\varepsilon_2}\frac{r_1^3}{r^3} E_0 (2\cos\theta\,\boldsymbol{e}_r + \sin\theta\,\boldsymbol{e}_\theta) \\ &= E_0 \boldsymbol{e}_z + \frac{\varepsilon_1 - \varepsilon_2}{\varepsilon_1 + 2\varepsilon_2}\frac{r_1^3}{r^3} E_0 (2\cos\theta\,\boldsymbol{e}_r + \sin\theta\,\boldsymbol{e}_\theta)\,,\end{aligned} \tag{17}$$

where $\boldsymbol{e}_z$, $\boldsymbol{e}_r$, and $\boldsymbol{e}_\theta$ are unit vectors. The induced scattering field outside the sphere, expressed by the second term in (17), is identical to the field of a dipole of moment $\boldsymbol{p}$, given by the following equation, placed at the center of the sphere:

$$\boldsymbol{p} = \varepsilon_2 \alpha E_0\,, \tag{18}$$

where

$$\alpha = 4\pi r_1^3 \frac{\varepsilon_1 - \varepsilon_2}{\varepsilon_1 + 2\varepsilon_2}\,. \tag{19}$$

Thus, the polarizability of this sphere is given by α as defined above.

2.2 Field Induced by Oscillating Dipole

In the above discussion we have ignored time dependence of the external field $\boldsymbol{E}_0$. In actual, however, the field oscillates according to $\mathrm{e}^{-\mathrm{i}\omega t}$. It is well known that oscillating dipoles radiate (dipole radiation). The field of an oscillating dipole is given by [5]

$$\boldsymbol{E} = \frac{1}{4\pi\varepsilon_2}\left(-\frac{\boldsymbol{p}(t_0)}{r^3} + \frac{3\boldsymbol{r}[\boldsymbol{r}\cdot\boldsymbol{p}(t_0)]}{r^5} + \frac{\mathrm{i}k\boldsymbol{p}(t_0)}{r^2} - \frac{3\mathrm{i}k\boldsymbol{r}[\boldsymbol{r}\cdot\boldsymbol{p}(t_0)]}{r^4} \right. \\ \left. -\frac{k^2}{r^3}\boldsymbol{r}\times[\boldsymbol{r}\times\boldsymbol{p}(t_0)]\right), \tag{20}$$

where $t_0 = t - kr/\omega$ and k is the wave vector in the ambient. The magnetic field is given by [5]

$$\boldsymbol{H} = -\frac{\mathrm{i}\omega}{4\pi}\left(\frac{1}{r^2} - \frac{\mathrm{i}k}{r}\right)\boldsymbol{r}\times\boldsymbol{p}(t_0)\,. \tag{21}$$

The first two terms in (20) are called the *static field* and are the scattering field discussed above. The next two terms, called the *induction field*, are the field induced by the current due to the dipole oscillation. The last term is called the *radiation field*. These three fields decay as r^{-3}, r^{-2}, and r^{-1}, respectively. Among them, only the radiation field propagates to infinite distance, and therefore is the far-field component; the other two are the near-field components. Developing (20), we obtain

$$\boldsymbol{E} = \frac{p\mathrm{e}^{\mathrm{i}kr}}{4\pi\varepsilon_2}\left[\left(\frac{2}{r^3} - \frac{2\mathrm{i}k}{r^2}\right)\cos\theta\,\boldsymbol{e}_r + \left(\frac{1}{r^3} - \frac{\mathrm{i}k}{r^2} - \frac{k^2}{r}\right)\sin\theta\,\boldsymbol{e}_\theta\right], \tag{22}$$

$$\boldsymbol{H} = -\frac{\mathrm{i}\omega p\mathrm{e}^{\mathrm{i}kr}}{4\pi}\left(\frac{1}{r^2} - \frac{\mathrm{i}k}{r}\right)\sin\theta\,\boldsymbol{e}_\phi\,. \tag{23}$$

From (22), E_θ becomes zero but E_r has its maximum on the z axis and vice versa on the x axis. In the region $r \ll 1/k = 0.16\lambda$, the static field is dominant and

$$|\boldsymbol{E}| \propto \left(\frac{r_1}{r}\right)^3. \tag{24}$$

Note that the field profile along the x or y axis does not depend on the radius of the sphere but depends on the distance from the center of the sphere. The radius affects only the amplitude of the field. However, when we take the origin of the distance on the surface of the sphere, the situation changes. Denoting the distance from the sphere surface by R, we obtain

$$|\boldsymbol{E}| \propto \left(\frac{r_1}{r_1 + R}\right)^3. \tag{25}$$

We can try to fit this function with an exponential function of decay length R', i.e. $\exp(-R/R')$. We obtain $R' = 0.49r_1$ for the fitting region $0 \leq R \leq r_1$, and $R' = 0.63r_1$ for $0 \leq R \leq 2r_1$. Hence, when the static field is approximated by an exponential function penetrating from the surface of the sphere, its decay length is proportional to the radius of the sphere.

2.3 Scattering Cross Section

The time average of the energy flow is expressed by the real part of the Poynting vector:

$$\bar{\boldsymbol{S}} = \frac{1}{2}\mathrm{Re}(\boldsymbol{E} \times \boldsymbol{H}^*) = \frac{1}{2}\mathrm{Re}(E_\theta H_\phi^* \boldsymbol{e}_r - E_r H_\phi^* \boldsymbol{e}_\theta)\,. \tag{26}$$

The total radiation power is

$$W = \int_0^{2\pi}\int_0^{\pi} |\bar{S}| r^2 \sin\theta \,\mathrm{d}\theta \,\mathrm{d}\phi = \frac{\omega k^3 |\boldsymbol{p}|^2}{12\pi\varepsilon_2} = \frac{\omega k^3 \varepsilon_2}{12\pi}|\alpha|^2 E_0^2\,. \tag{27}$$

As the energy density of the external field $\bar{S}_0$ is

$$\bar{S}_0 = \frac{\omega\varepsilon_2}{2k}E_0^2\,, \tag{28}$$

the scattering cross section C_{sca} is given by

$$C_{\mathrm{sca}} = \frac{W}{\bar{S}_0} = \frac{k^4}{6\pi}|\alpha|^2\,. \tag{29}$$

The absorption cross section is given by

$$C_{\mathrm{abs}} = k\,\mathrm{Im}(\alpha)\,. \tag{30}$$

In the above we have calculated the scattering cross section from the real energy flow. In the near field there is no energy flow outward but a very large electric field. Here we pay attention to the near-field components. We define the generalized scattering cross section by integration of the intensity of the electric field on the surface of a sphere of radius r concentric with the spherical particle:

$$\begin{aligned} C(r) &= \int_0^{2\pi}\int_0^{\pi} |\boldsymbol{E}|^2 r^2 \sin\theta \,\mathrm{d}\theta \,\mathrm{d}\phi = C_\theta(r) + C_r(r) \\ &= \frac{\alpha^2}{6\pi}\left(\frac{3}{r^4} + \frac{k^2}{r^2} + k^4\right), \end{aligned} \tag{31}$$

where

$$C_\theta(r) = \frac{\alpha^2}{6\pi}\left(\frac{1}{r^4} - \frac{k^2}{r^2} + k^4\right), \quad C_r(r) = \frac{\alpha^2}{6\pi}\left(\frac{2}{r^4} + \frac{2k^2}{r^2}\right). \tag{32}$$

In addition, if we define the near-field scattering cross section as the generalized scattering cross section on the sphere surface,

$$C_{\mathrm{nf}} = C(r_1) = \frac{\alpha^2}{6\pi}\left(\frac{3}{r_1^4} + \frac{k^2}{r_1^2} + k^4\right)\,. \tag{33}$$

2.4 Mie's Theory

When the size of the sphere becomes large compared with the wavelength, we cannot ignore the retardation effect. In this case we have to use *Mie*'s theory [3], where the Maxwell's equations are solved analytically without approximations. Arbitrary vector fields can be expressed by the vector spherical harmonics given by

$$\begin{aligned}\boldsymbol{M}_{\left\{\substack{\mathrm{e}\\ \mathrm{o}}\right\}mn} = & \frac{m}{\sin\theta}\left\{\begin{matrix}-\sin m\phi\,, \\ \cos m\phi\end{matrix}\right\} P_n^m(\cos\theta) z_n(r)\boldsymbol{e}_\theta \\ & -\left\{\begin{matrix}\cos m\phi \\ \sin m\phi\end{matrix}\right\}\frac{\mathrm{d}P_n^m(\cos\theta)}{\mathrm{d}\theta} z_n(r)\boldsymbol{e}_\phi \end{aligned} \tag{34}$$

$$\begin{aligned}\boldsymbol{N}_{\left\{\substack{\mathrm{e}\\ \mathrm{o}}\right\}mn} = & \frac{z_n(r)}{r}\left\{\begin{matrix}\cos m\phi \\ \sin m\phi\end{matrix}\right\} n(n+1) P_n^m(\cos\theta)\boldsymbol{e}_r \\ & +\left\{\begin{matrix}\cos m\phi \\ \sin m\phi\end{matrix}\right\}\frac{\mathrm{d}P_n^m(\cos\theta)}{\mathrm{d}\theta}\frac{1}{r}\frac{\mathrm{d}}{\mathrm{d}r}[r z_n(r)]\boldsymbol{e}_\theta \\ & +m\left\{\begin{matrix}-\sin m\phi \\ \cos m\phi\end{matrix}\right\}\frac{P_n^m(\cos\theta)}{\sin\theta}\frac{1}{r}\frac{\mathrm{d}}{\mathrm{d}r}[r z_n(r)]\boldsymbol{e}_\phi\,. \end{aligned} \tag{35}$$

The function $z_n(r)$ is a linear combination of the spherical Bessel functions $j_n(r)$ and $y_n(r)$:

$$j_n(r) = \sqrt{\frac{\pi}{2r}} J_{n+1/2}(r)\,, \quad y_n(r) = \sqrt{\frac{\pi}{2r}} Y_{n+1/2}(r)\,, \tag{36}$$

where J_ν and Y_ν are the Bessel functions of the first and second kind, respectively. The scattering fields $\boldsymbol{E}_\mathrm{s}$ and $\boldsymbol{H}_\mathrm{s}$ can be expressed by vector spherical harmonics:

$$\boldsymbol{E}_\mathrm{s} = \sum_{n=1}^{\infty} \mathrm{i}^n \frac{2n+1}{n(n+1)} E_0 (\mathrm{i} a_n \boldsymbol{N}_{\mathrm{e}1n}^{(3)} - b_n \boldsymbol{M}_{\mathrm{o}1n}^{(3)})\,, \tag{37}$$

$$\boldsymbol{H}_\mathrm{s} = \frac{k}{\omega\mu}\sum_{n=1}^{\infty} \mathrm{i}^n \frac{2n+1}{n(n+1)} E_0 (\mathrm{i} b_n \boldsymbol{N}_{\mathrm{o}1n}^{(3)} - a_n \boldsymbol{M}_{\mathrm{e}1n}^{(3)})\,, \tag{38}$$

where the superscript '(3)' of the spherical harmonics implies $z_n = j_n + \mathrm{i} y_n$. The coefficients a_n and b_n are obtained by solving the boundary conditions on the surface of the sphere and are given by

$$a_n = \frac{m\psi_n(mx)\psi_n'(x) - \psi_n(x)\psi_n'(mx)}{m\psi_n(mx)\xi_n'(x) - \xi_n(x)\psi_n'(mx)}\,, \tag{39}$$

$$b_n = \frac{\psi_n(mx)\psi_n'(x) - m\psi_n(x)\psi_n'(mx)}{\psi_n(mx)\xi_n'(x) - m\xi_n(x)\psi_n'(mx)}\,, \tag{40}$$

where x is the size parameter $x = kr_1$, $m = (\varepsilon_1/\varepsilon_2)^{1/2}$, and

$$\psi_n(r) = rj_n(r)\,, \quad \xi_n(r) = r[j_n(r) - iy_n(r)]\,. \tag{41}$$

The scattering cross section and the extinction cross section are

$$C_{\mathrm{sca}} = \pi r_1^2 Q_{\mathrm{sca}} = \frac{2\pi}{k^2}\sum_{n=1}^{\infty}(2n+1)(|a_n|^2 + |b_n|^2)\,, \tag{42}$$

$$C_{\mathrm{ext}} = \pi r_1^2 Q_{\mathrm{ext}} = \frac{2\pi}{k^2}\sum_{n=1}^{\infty}(2n+1)\mathrm{Re}(a_n + b_n)\,. \tag{43}$$

The absorption cross section is

$$C_{\mathrm{abs}} = C_{\mathrm{ext}} - C_{\mathrm{sca}}\,. \tag{44}$$

The near-field scattering cross section C_{nf} is given by [6]

$$\begin{aligned} C_{\mathrm{nf}} &= \pi r_1^2 Q_{\mathrm{nf}} \\ &= 2\pi r_1^2 \sum_{n=1}^{\infty}\Big\{|a_n|^2[(n+1)|h_{n-1}^{(2)}(x)|^2 + n|h_{n+1}^{(2)}(x)|^2] \\ &\qquad + (2n+1)|b_n|^2|h_n^{(2)}(x)|^2\Big\} \end{aligned} \tag{45}$$

where $h_n^{(2)} = j_n - \mathrm{i}y_n$. The radial component of the near-field scattering cross section is given by [6]

$$C_{\mathrm{r}} = \pi r_1^2 Q_{\mathrm{r}} = \frac{2\pi}{k^2}\sum_{n=1}^{\infty}(2n+1)(n+1)n|a_n|^2|h_n^{(2)}(x)|^2\,. \tag{46}$$

2.5 Spectra of Cross Sections

Figure 3 shows the spectra of the scattering cross sections of gold spheres of various radii. To clarify the size effect and the retardation effect, the scattering cross section has been normalized by r_1^6 because the scattering cross section C_{sca} is proportional to r_1^6, as described by (29). The peaks appearing between 500 nm and 600 nm are caused by the surface plasmon resonance, sometimes called the local plasmon resonance, in the gold sphere. At the peak wavelength, which is sometimes called the Fröhlich wavelength [7], the real part of the denominator of the polarizability, i. e. $\mathrm{Re}(\varepsilon_1 + 2\varepsilon_2)$, is zero. The low peak height for small spheres is caused by the size effect, where the imaginary part of the dielectric constant is relatively large (see Fig. 2). The low and broadened peak for a 100 nm radius sphere is caused by the retardation effect. Figure 4 shows the absorption cross section of gold spheres in air. The cross sections are normalized by the volume of the sphere for the same reason as for the scattering cross section. The spectra are similar to those of

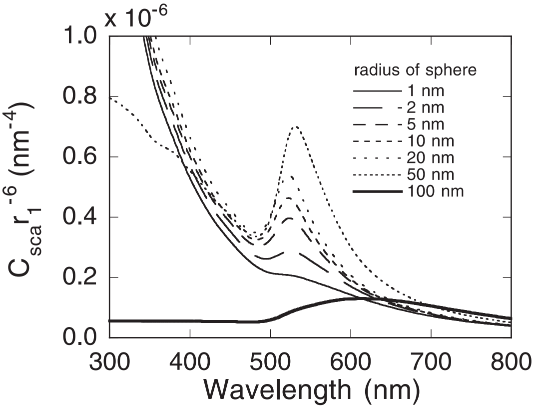

Fig. 3. Scattering cross section of a gold sphere in air normalized by r_1^6

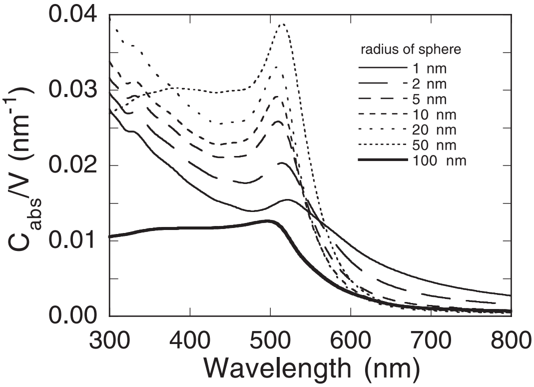

Fig. 4. Absorption cross section of a gold sphere in air normalized by its volume

the scattering cross section but the absorption due to interband transition appearing below a wavelength of 500 nm is more pronounced. Figure 5 shows the near-field scattering efficiencies of gold spheres in air. The near-field scattering efficiency is much larger than the far-field scattering efficiency. For example, the peak of the near-field scattering efficiency for a sphere of 50 nm radius is $Q_{\mathrm{nf}}(\lambda = 537\,\mathrm{nm}) = 41.1$, which is 30 times larger than the far-field scattering efficiency, $Q_{\mathrm{sca}}(\lambda = 531\,\mathrm{nm}) = 1.39$. In contrast to the spectra for the absorption cross section, the interband transitions suppress the scattering efficiency in the wavelength region below a wavelength of 500 nm. This causes a shift of the peak wavelength of the near-field scattering efficiency from the peak wavelength of the absorption efficiency. The spectra of the radial component of the near-field scattering efficiency (not shown here) have almost the same shape but the amplitude is reduced by a factor of 2/3.

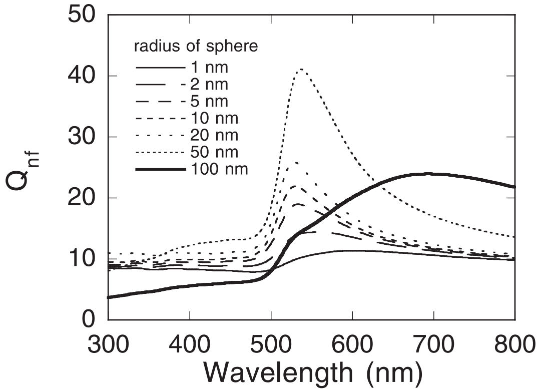

Fig. 5. Near-field scattering efficiency of a gold sphere in air

Figures 6, 7, and 8 show the scattering cross section, the absorption cross section, and the near-field cross section for silver spheres in air. The peaks around 350 nm wavelength are caused by the surface plasmon resonance. These cross sections are one order of magnitude larger than those for gold spheres. For silver, the profile of the peaks is not affected by interband transitions. While for gold spheres the highest peak is given by a 50 nm radius sphere, for silver it is given by spheres of 10 or 20 nm radius. This is because of the shorter Fröhlich wavelength than for gold spheres. The retardation effect is more pronounced at shorter wavelengths.

The scattering and absorption cross sections also depend on the dielectric constant of the ambient. Figure 9 shows the dependence of the absorption efficiency of a gold sphere of 20 nm diameter on the refractive index of the ambient. The absorption efficiency increases, and the resonance, or Fröhlich,

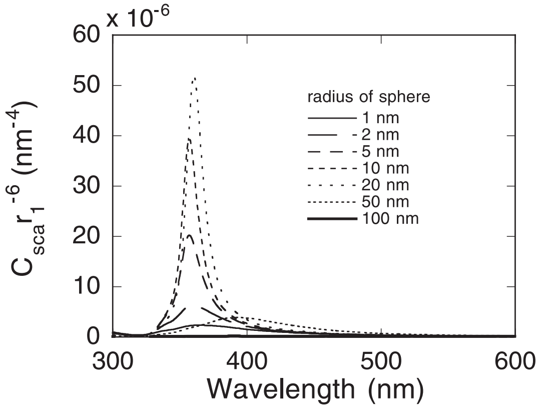

Fig. 6. Scattering cross section of a silver sphere in air normalized by r_1^6

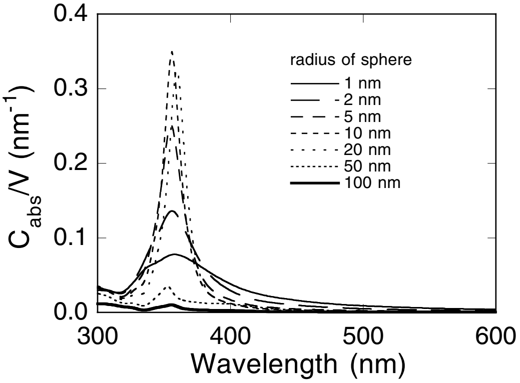

Fig. 7. Absorption cross section of a silver sphere in air normalized by its volume

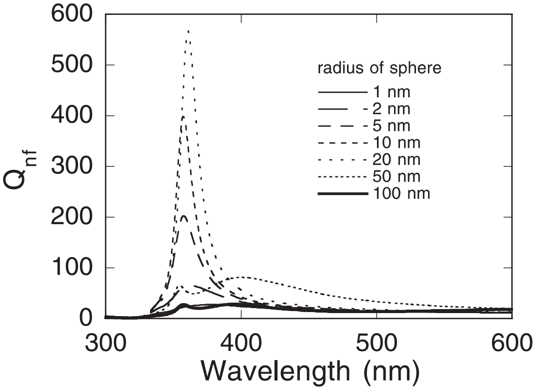

Fig. 8. Near-field scattering efficiency of a silver sphere in air

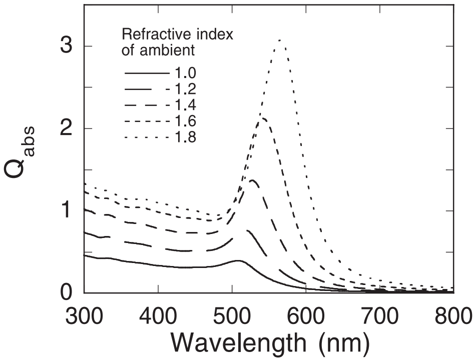

Fig. 9. Absorption efficiency of a 20 nm gold sphere for ambients of various refractive index

wavelength becomes longer as the refractive index of the ambient increases. The other cross sections show a similar dependence.

3 Scattering by Ellipsoids

Here we consider scattering by an ellipsoid whose surface is expressed by

$$\frac{x^2}{a^2}+\frac{y^2}{b^2}+\frac{z^2}{c^2}=1\,, \quad a>b>c\,. \tag{47}$$

When the size of the ellipsoid is much smaller than the wavelength ($a, b, c \ll \lambda$), the quasi-static approximation can be employed, as in the scattering problem for a sphere. By solving Laplace's equation with appropriate boundary conditions in ellipsoidal coordinates, the scattering potential can be obtained. Then, applying the far-field approximation, we obtain the polarizability of the ellipsoid for an external field parallel to the z axis: [8]:

$$\alpha_3 = 4\pi abc\frac{\varepsilon_1-\varepsilon_2}{3\varepsilon_2+3L_3(\varepsilon_1-\varepsilon_2)}\,, \tag{48}$$

where

$$\begin{aligned} L_3 &= \int_0^\infty \frac{\mathrm{d}s}{(s+c^2)f(s)}\,, \\ f(s) &= [(s+a^2)(s+b^2)(s+c^2)]^{1/2}\,. \end{aligned} \tag{49}$$

L_3 is called the geometric factor. When the external field is parallel to the x or y axis, L_3 is replaced by

$$L_1 = \int_0^\infty \frac{ds}{(s+a^2)f(s)}\,, \quad \text{or} \quad L_2 = \int_0^\infty \frac{ds}{(s+b^2)f(s)}\,, \tag{50}$$

respectively. If the ellipsoid is a spheroid, the geometric factor can be obtained analytically. For a prolate spheroid

$$L_1 = \frac{1-e^2}{e^2}\left(-1+\frac{1}{2}\ln\frac{1+e}{1-e}\right), \quad e^2 = 1-\frac{b^2}{a^2}\,, \tag{51}$$

$$L_2 = L_3 = (1-L_1)/2\,. \tag{52}$$

and for an oblate spheroid

$$L_1 = L_2 = \frac{g(e)}{2e^2}\left[\frac{\pi}{2}-\tan^{-1}g(e)\right]-\frac{g^2(e)}{2}\,, \tag{53}$$

$$\begin{aligned} g(e) &= \left(\frac{1-e^2}{e^2}\right), \quad e^2 = 1-\frac{c^2}{a^2}\,, \\ L_3 &= 1-2L_1\,. \end{aligned} \tag{54}$$

Figures 10 and 11 show the absorption cross sections of various gold spheroids in air normalized by their volumes. The dielectric constant used was that for a 20 nm sphere. In Fig. 10 the external field is parallel to the symmetry axis, and in Fig. 11 it is perpendicular to this axis. When the field is parallel to the symmetry axis, the more prolate the spheroid, the larger the absorption cross section becomes. On the other hand, when the external field is perpendicular to the axis, the more oblate the spheroid, the larger the absorption cross section becomes. In a prolate spheroid, the scattering field at both ends of the spheroid becomes very large. Using this property, *Wessel* [9] has proposed a near-field optical microscope for observing enhanced nonlinear phenomena, such as Raman scattering, two-photon phenomena, and second-harmonic generation.

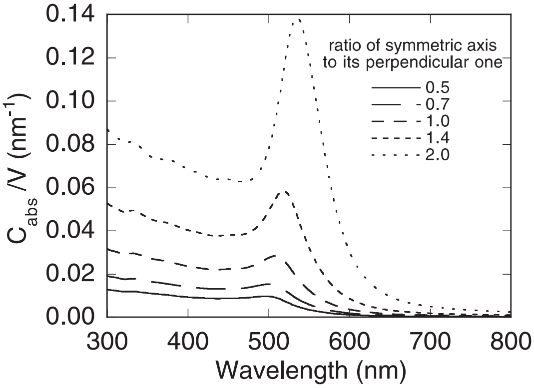

Fig. 10. Absorption cross section of a gold spheroid in air normalized by its volume. The external field is parallel to the symmetry axis of the spheroid

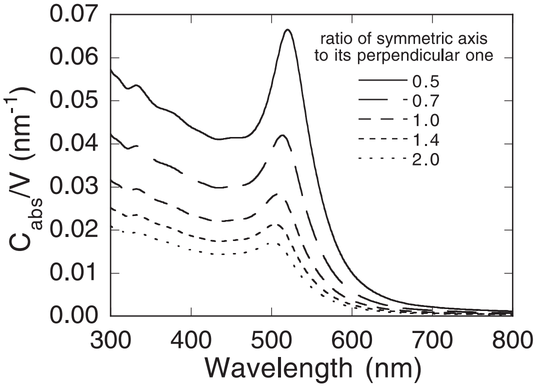

Fig. 11. Absorption cross section of a gold spheroid in air normalized by its volume. The external field is perpendicular to the symmetry axis of the spheroid

Asano and *Yamamoto* [10] have solved the scattering problem for large spheroids including the retardation effect. Using this solution, *Barber* et al. [11] have calculated the surface intensities on large silver spheroids.

4 Scattering by a Coated Sphere and by a Metal Shell

Here we consider scattering by a metal sphere coated with a dielectric and by a dielectric sphere coated with a metal, i. e. a spherical metal shell. We assume that the radii of the core and the shell are r_1 and r_2, and the dielectric constants of the core, the shell, and the ambient are ε_1, ε_2, and ε_3, respectively. Using the quasi-static approximation, the polarizability of the coated sphere is given by [12]

$$\alpha = 4\pi r_2^3 \left(\frac{\varepsilon_2 \varepsilon_{\mathrm{a}} - \varepsilon_3 \varepsilon_{\mathrm{b}}}{\varepsilon_2 \varepsilon_{\mathrm{a}} + 2\varepsilon_3 \varepsilon_{\mathrm{b}}} \right), \tag{55}$$

where

$$\varepsilon_{\mathrm{a}} = \varepsilon_1 (3 - 2P) + 2\varepsilon_2 P \,, \quad \varepsilon_{\mathrm{b}} = \varepsilon_1 P + \varepsilon_2 (3 - P) \,,$$
$$P = 1 - (r_1/r_2)^3 \,.$$

Using this polarizability α, (29), and (30), the scattering cross section C_{sca} and the absorption cross section C_{abs} of the particle can be obtained.

The scattering problem for a coated sphere including the retardation effect is easily solved by determining the coefficients in (37) so as to satisfy the boundary conditions at the two surfaces of the shell and the core[8]:

$$a_n = \frac{\psi_n(y)[\psi_n'(m_2 y) - A_n \chi_n'(m_2 y)] - m_2 \psi_n'(y)[\psi_n(m_2 y) - A_n \chi_n(m_2 y)]}{\xi(y)[\psi_n'(m_2 y) - A_n \chi_n'(m_2 y)] - m_2 \xi_n'(y)[\psi_n(m_2 y) - A_n \chi_n(m_2 y)]} \tag{56}$$

$$b_n = \frac{m_2 \psi_n(y)[\psi_n'(m_2 y) - B_n \chi_n'(m_2 y)] - \psi_n'(y)[\psi_n(m_2 y) - B_n \chi_n(m_2 y)]}{m_2 \xi_n(y)[\psi_n'(m_2 y) - B_n \chi_n'(m_2 y)] - \xi_n'(y)[\psi_n(m_2 y) - B_n \chi_n(m_2 y)]}, \tag{57}$$

$$A_n = \frac{m_2 \psi_n(m_2 x) \psi_n'(m_1 x) - m_1 \psi_n'(m_2 x) \psi_n(m_1 x)}{m_2 \xi_n(m_2 x) \psi_n'(m_1 x) - m_1 \xi_n'(m_2 x) \psi_n(m_1 x)}, \tag{58}$$

$$B_n = \frac{m_2 \psi_n(m_1 x) \psi_n'(m_2 x) - m_1 \psi_n(m_2 x) \psi_n'(m_1 x)}{m_2 \xi_n'(m_2 x) \psi_n(m_1 x) - m_1 \psi_n'(m_1 x) \xi_n(m_2 x)}, \tag{59}$$

where $x = kr_1$, $y = kr_2$, $m_1 = (\varepsilon_1/\varepsilon_3)^{1/2}$, $m_2 = (\varepsilon_2/\varepsilon_3)^{1/2}$, and $\chi_n(z) = -zy_n(z)$. Using these coefficients a_n and b_n and (42)-(45), we can calculate C_{sca}, C_{abs}, and C_{nf}.

Figure 12 shows the dependences of the absorption cross section of a silica-coated gold sphere in air on the thickness of the coating. As the thickness

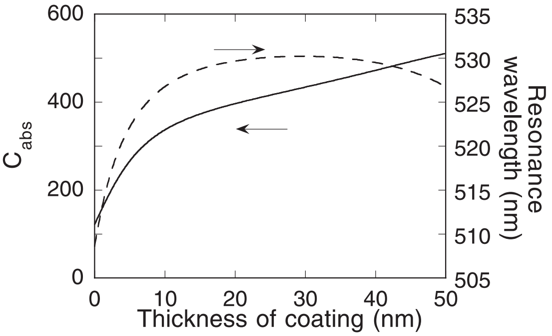

Fig. 12. Absorption cross section of a 20 nm gold particle coated with silica of various thicknesses in air

of the coating increases, the peak height becomes larger and the resonance wavelength becomes longer. These dependences are similar to those in Fig. 9. For the coated sphere, however, the dependences of the peak tend to saturate for thick silica coatings. This is caused by the fact that the range of the near-field radiation from the sphere is of the order of the radius of the sphere. The lens effect of the silica coating appears in the region of thicker coatings. Of course, if the dielectric constant of the coating is smaller than that of the ambient, the dependences of the peak height and the resonance wavelength are inverted.

Figure 13 shows the absorption efficiency of spherical metal shell particles in air. The shell and core materials are gold and silica, respectively. In the calculation of the dielectric constant of the gold shell, we considered the size effect, replacing the radius r_1 in (7) by the shell thickness $r_2 - r_1$. Although

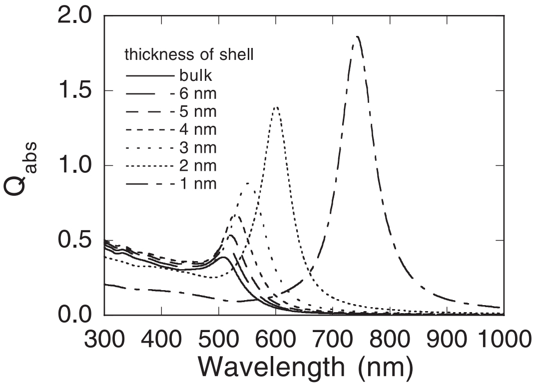

Fig. 13. Absorption efficiency of a spherical gold shell whose outer diameter is 20 nm and shell thickness is varied. The core and ambient are silica and air, respectively

the outer diameter is fixed at 20 nm, the peak height and the resonance wavelength depend sensitively on the shell thickness.

Several methods for making metal shell particles have been proposed [13,14,15,16].

5 Sphere above Substrate

In this section we the consider the scattering problem of a small sphere above a substrate with a flat surface. There are no analytic solutions corresponding to Mie's scattering formula. The simplest method to solve this problem uses the dipole approximation, where a dipole is generated at the center of the sphere and an image dipole is induced in the substrate. In the quasi-static approximation, this problem has been solved by *Aravind* and *Metiu* [17] and *Wind* et al. [19]. As *Aravind* and *Metiu* use bispherical coordinates [18], we cannot set the distance between the sphere and the substrate to zero. On the other hand, the method of *Wind* et al. is free from this restriction because it employs spherical polar coordinates. Even a system where the sphere is truncated by the substrate can be treated in the calculation. Moreover, the polarizability of the sphere can be calculated easily. However, as the distance between the sphere and the substrate becomes smaller, the number of the terms needed in the calculation becomes large. This disadvantage is also present in the method of *Aravind* and *Metiu* and is significant for metallic substrates. Here we introduce the method of *Wind* et al. briefly. In a sphere placed in a homogeneous field only a dipole is excited. If a substrate exists, we have to take account of multipoles. Using a reduced distance r that is normalized by the radius of the sphere r, the reduced potential $\mathit{\Psi} = -\mathit{\Phi}/(E_0 r_1)$, where $\mathit{\Phi}$ is the potential, in the ambient is

$$\begin{aligned}\mathit{\Psi}_1 = {} & r\cos\theta\cos\theta_0 + r\sin\theta\sin\theta_0\cos\phi \\ & + \sum_{j=1}^{\infty} r^{-j-1}[A_{1j}P_j^0(\cos\theta) + B_{1j}P_j^1(\cos\theta)\cos\phi] \\ & + \sum_{j=1}^{\infty}[A'_{1j}V_j^0(r,\cos\theta) + B'_{1j}V_j^1(r,\cos\theta)\cos\phi]\,, \end{aligned} \tag{60}$$

where

$$\begin{aligned}V_j^m(r,\cos\theta) = {} & (r^2 - 4rr_0\cos\theta + 4r_0^2)^{-(j+1)/2} \\ & \times P_j^m[(r\cos\theta - 2r_0)(r^2 - 4rr_0\cos\theta + 4r_0^2)^{-1/2}]\,, \end{aligned} \tag{61}$$

Here θ_0 is the angle of the direction at the external field, $r_0 = D/r_1$, r_1 and D is the distance between the center of the sphere and the surface of the substrate. In the substrate, the reduced potential $\mathit{\Psi}_2$ is

$$\mathit{\Psi}_2 = \mathit{\Psi}'_2 + \alpha r\cos\theta\cos\theta_0 + \beta r\sin\theta\sin\theta_0\cos\phi$$

$$+\sum_{j=1}^{\infty} r^{-j-1}\left[A_{2j}P_j^0(\cos\theta) + B_{2j}P_j^1(\cos\theta)\cos\phi\right], \tag{62}$$

and inside the sphere the reduced potential Ψ_3 is

$$\Psi_3 = \Psi_3' + \sum_{j=1}^{\infty} r^j \left[A_{3j}P_j^0(\cos\theta) + B_{3j}P_j^1(\cos\theta)\cos\phi\right], \tag{63}$$

where Ψ_2' and Ψ_3' are constants. Using the boundary conditions at the surface of the substrate ($r\cos\theta = r_0$) and at the surface of the sphere ($r = 1$) and the orthogonality of the associated Legendre functions, we obtain

$$\sum_{j=1}^{\infty}\left(\delta_{kj} + \frac{(\varepsilon_2 - \varepsilon_1)k(\varepsilon_1 - \varepsilon_3)}{(\varepsilon_2 + \varepsilon_1)[(k+1)\varepsilon_1 + k\varepsilon_3]}\frac{(k+j)!}{k!j!(2r_0)^{k+j+1}}\right)A_{1j}$$
$$= \frac{\varepsilon_1 - \varepsilon_3}{2\varepsilon_1 + \varepsilon_3}\cos\theta_0\delta_{k1}\,, \tag{64}$$

$$\sum_{j=1}^{\infty}\left(\delta_{kj} + \frac{(\varepsilon_2 - \varepsilon_1)k(\varepsilon_1 - \varepsilon_3)}{(\varepsilon_2 + \varepsilon_1)[(k+1)\varepsilon_1 + k\varepsilon_3]}\frac{(k+j)!}{(k+1)!(j-1)!(2r_0)^{k+j+1}}\right)B_{1j}$$
$$= \frac{\varepsilon_1 - \varepsilon_3}{2\varepsilon_1 + \varepsilon_3}\sin\theta_0\delta_{k1}\,, \tag{65}$$

where δ_{jk} is the Kronecker delta, and ε_1, ε_2, and ε_3 are the dielectric constants of the ambient, the substrate, and the sphere, respectively. By solving these linear equations, A_{1j} and B_{1j} are obtained. The coefficients A_{11} and B_{11} determine the polarizabilities of the sphere:

$$\alpha_{\parallel} = -4\pi\varepsilon_1 R^3 B_{11}/\sin\theta\,, \tag{66}$$

$$\alpha_{\perp} = -4\pi\varepsilon_1 R^3 A_{11}/\cos\theta\,. \tag{67}$$

The scattering cross section C_{sca} and the absorption cross section C_{abs} can be calculated using (29) and (30).

Figure 14 shows the absorption efficiency of a 20 nm gold sphere above a silica substrate for an incident field perpendicular to the surface of the substrate. The ambient is air. Even when the sphere contacts the surface, the absorption efficiency is not much modified. Needless to say, the influence of the substrate depends on the difference between the dielectric constants of the substrate and the ambient. When the incident field is parallel to the surface of the substrate, the substrate affects the cross section (not shown here) less.

In contrast to dielectric substrates, the substrate effect is much more pronounced for metallic substrates. Figure 15 shows the absorption efficiency of a gold sphere above a gold substrate for an external field perpendicular to the surface of the substrate. The peak height becomes higher and the

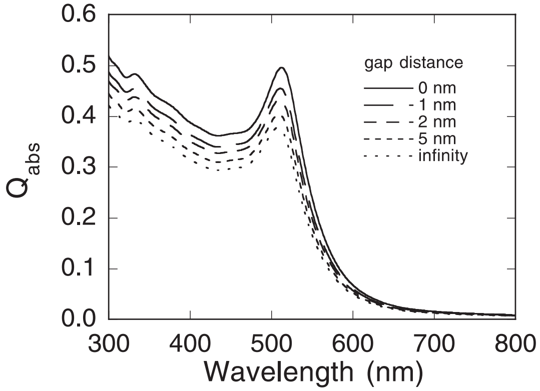

Fig. 14. Absorption efficiency of a gold sphere above a silica substrate. The diameter of the sphere is 20 nm and the ambient is air. The external field is perpendicular to the surface of the substrate

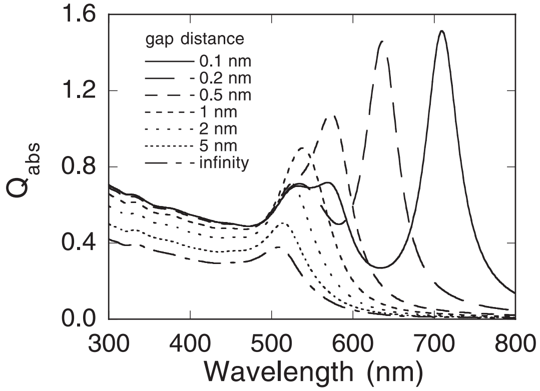

Fig. 15. Absorption efficiency of a gold sphere above a gold substrate. The diameter of the sphere is 20 nm and the ambient is air. The external field is perpendicular to the surface of the substrate

resonance wavelength becomes longer as the gap between the sphere and the substrate decreases. Moreover, for smaller gaps, the peak is split into two or three owing to multipoles. When the sphere contacts the substrate, the solution does not converge even if 100 terms are considered. When the external field is parallel to the substrate surface, on the other hand, the substrate effect is very small, as shown in Fig. 16.

The characteristic property of this system is the much enhanced field between the sphere and the substrate. Figure 17 shows a contour plot of the cross-sectional distribution of the calculated scattered intensity around a gold sphere on a BK7 glass substrate ($n_d = 1.516$) in the plane of incidence, i. e. the xy plane [20]. It is assumed here that a p-polarized plane wave (wave-

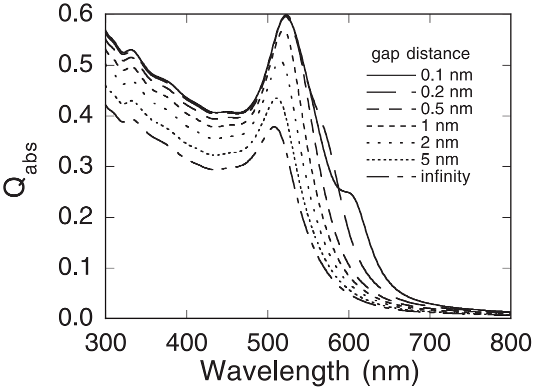

Fig. 16. Absorption efficiency of a gold sphere above a gold substrate. The diameter of the sphere is 20 nm and the ambient is air. The external field is parallel to the surface of the substrate

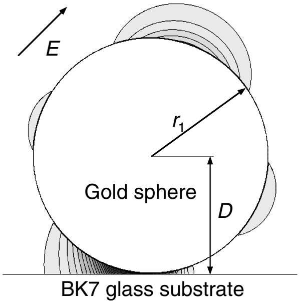

Fig. 17. Cross-sectional intensity distribution of the scattered local field around a gold sphere on a BK7 glass substrate. The ratio of the gap to the radius is 0.01. A p-polarized field with 548 nm wavelength is incident at 45 degrees. The maximum intensity is 79 times higher than the intensity of the incident field [20]

length $\lambda = 548\,\text{nm}$, intensity $I_0 = 1.0$) illuminates the sphere at a 45 degree incidence angle, the ratio of the gap to the sphere radius is 0.01, and the size effect in the gold sphere can be ignored. The dark regions correspond to the high-intensity areas. The intensity in the gap between the sphere and the substrate is much enhanced. The maximum intensity in the gap is 79 times larger than that of the incident field and is polarized almost perpendicularly. The corresponding value for s-polarized incidence is only 1.9. The field-enhanced area is very localized and its diameter on the substrate is less than one-fifth of the sphere diameter.

Figure 18 shows the dependence of the intensity on the gap width, calculated at the top and bottom of the sphere and at a point on the substrate surface just below the center of the sphere [20]. At the top of the sphere the intensity is almost independent of the gap distance and is low. The intensity

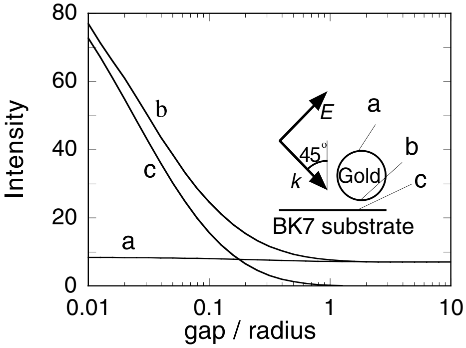

Fig. 18. Intensity of the scattered local field as a function of the gap width, calculated (**a**) at the top of the sphere, (**b**) at the bottom of the sphere, and (**c**) on the surface of the substrate just below the center of the sphere [20]

in the gap increases as the gap width decreases. This result predicts that the intensity in the gap becomes infinite when the gap width becomes infinitely small.

Figure 19 shows the dependence of the scattered intensity on the incident wavelength, calculated on the substrate just below the center of the sphere [20]. Three substrates are assumed: an LaSFn17 glass (Sumita Optical Glass, $n_\mathrm{d} = 1.883$), a BK7 glass, and air, i. e. no substrate. The resonance wavelengths are 552 nm, 548 nm, and 542 nm for LaSFn17, BK7, and air, respectively. Though the dependence of the resonance wavelength on the refractive index of the substrate is not notable, the intensity at the resonance depends highly on the refractive index. The higher the refractive index

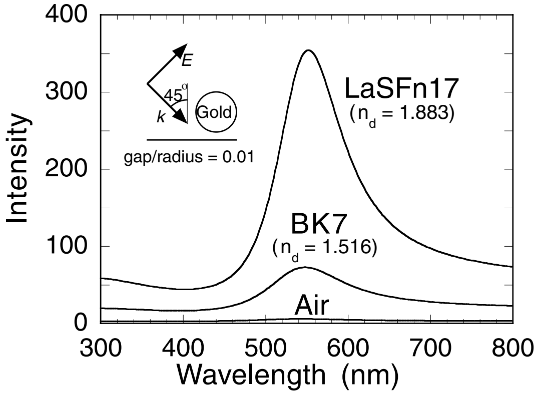

Fig. 19. Intensity of the scattered local field as a function of the incident wavelength, calculated on the surface of the substrate just below the center of the sphere for an LaSFn17 glass substrate ($n_\mathrm{d} = 1.883$), a BK7 substrate, and air, i. e. no substrate. The other parameters are the same as in Fig. 17 [20]

of the substrate, the larger the intensity of the peak becomes. An LaSFn17 substrate $0.01r_1$ from the sphere enhances the intensity by a factor of 60 compared with the intensity for the isolated sphere.

6 Scattering by Multiparticles

For two identical spheres *Levine* and *McQuarrie* [21] first solved the problem in the static approximation using bispherical coordinates. In this paper, however, the sphere was assumed to be a perfect conductor. Using a similar method, *Goyette* and *Navon* [22] obtained a solution for dielectric spheres. However, these workers used a perturbation expansion. Then *Aravind* et al. [23] solved this problem exactly. The solution is also obtainable from (64) and (65) by putting $(\varepsilon_2 - \varepsilon_1)/(\varepsilon_2 + \varepsilon_1) = 1$ for the case of an external field parallel to the axis connecting the centers of the spheres, and by putting $(\varepsilon_2 - \varepsilon_1)/(\varepsilon_2 + \varepsilon_1) = -1$ for the case of a field perpendicular to the axis [19]. The general solutions including the retardation effect are discussed by *Fuller* [24] and references therein.

For multiparticles, we have to consider a fourth field, that is, the field scattered by the other spheres, in addition to the fields acting in the case of an isolated sphere. The problem is generally solved self-consistently, considering the above fields. *Clippe* et al. [25] solved the problem of multispheres using a Hamiltonian. However, these workers considered only dipole moments. *Gerady* and *Ausloos* [26,27,28] have solved this problem, including multipoles.

7 Optical Sensors Using Gold Colloid Monolayers

As an application of the spectral analysis of small metal spheres, a local plasmon sensor has been proposed using gold colloid monolayers deposited on glass substrates [29]. This sensor uses a property of the absorption peak of gold spheres that is due to the local plasmon resonance. The peak wavelength and the peak absorbance depend sensitively on the dielectric constant of the ambient near the particles. In the gold colloid monolayer colloidal gold particles a few tens of nanometers in diameter are immobilized on a glass slide using a functional organic coupling agent [30,31,32,33,34].

This sensor intrinsically measures the refractive index of a sample surrounding the gold particles. It can also detect the thickness of a film coated on the gold particles. This sensor has several advantages in comparison with conventional surface plasmon resonance (SPR) sensors [35]. It requires no glass prism to provide an attenuated-total-reflection geometry. The colloidal monolayer can be deposited on an inner surface such as a capillary wall because there is no use of vacuum deposition that requires open surfaces. Furthermore, theoretically, the sensor could consist of only one nanoparticle.

This could greatly reduce the dimensions of the sensor and the required sample size. For these reasons this sensor may be applied in wider fields where a conventional SPR sensor cannot be used.

Figure 20 shows a scanning electron micrograph of a gold colloid monolayer deposited on a glass surface using a coupling agent, 3-aminopropyltrimethoxysilane [29]. The gold particles are immobilized uniformly and are isolated from each other. The mean diameter of the deposited particles is 20.2 nm. The immobilized gold particles were not washed off by ultrasonic cleaning, even in organic solvents (methanol and ethanol). The density of the particles was roughly 370 particles per square micron.

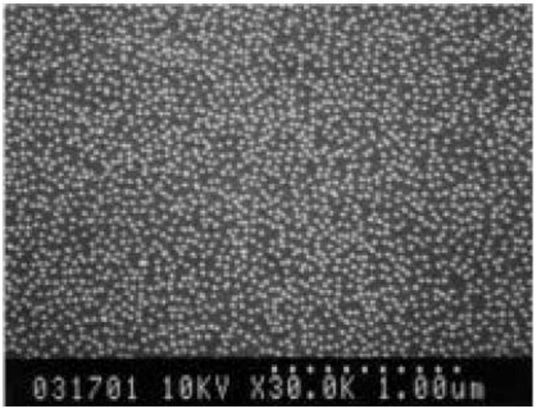

Fig. 20. Scanning electron micrograph of a 20.2 nm gold colloid monolayer [29]

Figure 21 shows typical absorption spectra of a 20.2 nm gold colloid monolayer immersed in several kinds of liquid samples, namely methanol, ethanol, water, glycerol, and diiodemethane [29]. The indices of refraction of these liquids at a wavelength of 589.3 nm are also shown in Fig. 21. The peak absorbance increases and the resonance wavelength becomes longer as the refractive index of the sample liquid increases.

For biosensors, especially for affinity sensors, changes in the thickness or in the refractive index of the film sample at the sensor surface must be sensitively detected. To investigate this sensitivity, poly (methyl methacrylate) (PMMA) films with several thicknesses were deposited on a gold colloid monolayer. The refractive index of PMMA is 1.496 at a wavelength of 520 nm. Figure 22 shows the measured absorption spectra for the various thicknesses of PMMA used [29]. Both the resonance wavelength and the peak absorbance increase as the thickness increases. Figure 23 summarizes the dependences of the peak absorbance and the resonance wavelength on the thickness of the PMMA [29]. The peak absorbance is normalized by the absorbance without a coating. Single exponential functions fitted to the experimental values are

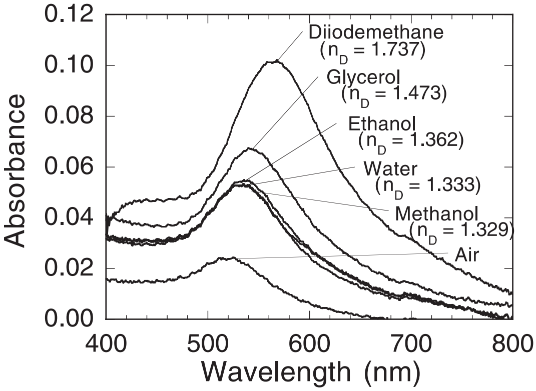

Fig. 21. Measured absorption spectra of a 20.2 nm gold colloid monolayer immersed in liquid samples of various refractive indices

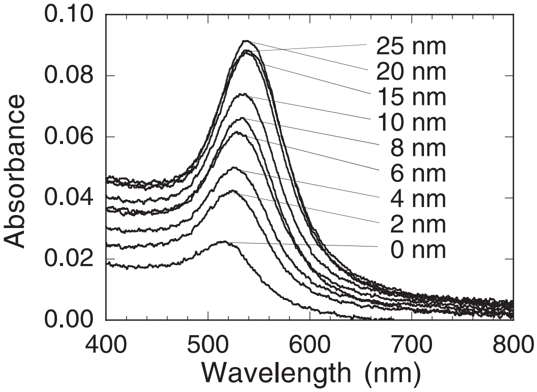

Fig. 22. Measured absorption spectra of a 13.9 nm gold colloid monolayer coated with a PMMA film of various thicknesses

also shown in the figure. The peak absorbance and the resonance wavelength depend sensitively on the thickness of the film samples for thicknesses less than ~ 10 nm and saturated for thicker film. The maximum sensitivities of the resonance wavelength to the film thickness, i. e. the slopes of the fitted curves in Fig. 23 at zero thickness, are 5.7 and 3.6 for 13.9 and 20.2 nm particles, respectively. The decay thicknesses for the resonant wavelength, at which the slopes become $1/e$, are 4.8 nm and 6.3 nm for 13.9 and 20.2 nm particles, respectively. The decay thicknesses for the peak absorbance are 6.0 nm and 6.6 nm for 13.9 and 20.2 nm particles, respectively. These values are comparable to the dimensions of biological samples such as antibody or antigen proteins.

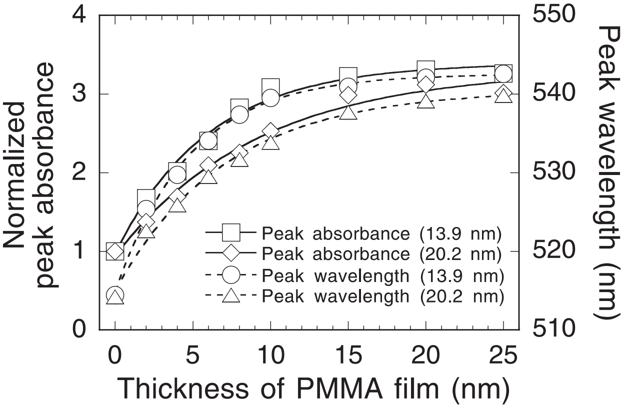

Fig. 23. Peak absorbance and resonance wavelength as a function of the thickness of the coated PMMA film for a 13.9 and a 20.2 nm gold colloid monolayer. The *solid* and *dashed curves* show the fitted single exponential functions [29]

References

1. P. B. Johnson, R. W. Christy, Optical constants of the noble metals, Phys. Rev. B **6**, 4370–4379 (1972) 99, 100
2. C. Kittel, *Introduction to Solid State Physics* (Wiley, NewYork, 1976). 99
3. G. Mie, Beiträge zur Optik trüber Medien, speziell kolloidaler Metallösungen. Ann. Phys. (Leipzig) **25**, 377–445 (1908) 100, 104
4. M. Kerker, The Scattering of Light and Other Electromagnetic Radiation. (Academic, New York 1969) p. 84 100
5. J. A. Stratton, Electromagnetic Theory (McGraw-Hill, NewYork 1941) 102
6. B. J. Messinger, K. U. Ravon, R. K. Chang, P. W. Barber, Local Field at the Surface of Noble-Metal Microspheres, Phys. Rev. B **24**, 649–657 (1981) 105
7. H. Fröhlich, *Theory of Dielectrics* (Oxford Univ. Press, London 1949) 105
8. C. F. Bohren, D. R. Huffman, Absorption and Scattering of Light by Small Particles. (Wiley, New York 1983) 109, 111
9. J. Wessel, Surface-enhanced optical microscopy, J. Opt. Soc. Am. B **2**, 1538–1540 (1985) 110
10. S. Asano , G. Yamamoto, Light scattering by a spheroidal particle, Appl. Opt. **14**, 29–49 (1975) 111
11. P. W. Barber, R. K. Chang, H. Massoudi, Surface-enhanced electric intensitied on large silver spheroids, Phys. Rev. Lett. **50**, 997–1000 (1983) 111
12. A. E. Neeves, M. H. Birnboim, Composite structure for the enhancemeent of nonlinear-optical susceeptibility, J. Opt. Soc. Am. B **6**, 787–796 (1989) 111
13. H. S. Zhou, T. Wada, H. Sasabe, H. Komiyama, Synthesis and optical properties of nanocomposite silver–polydiacetylene, Synth. Met. **81**, 129–132 (1996) 113
14. H. S. Zhou, I. Homma, H. Komiyama, J. W. Haus, Controlled synthesis and quantum-size effect in gold-coated nanoparticles, Phys. Rev. B **50**, 12052–12056 (1994) 113
15. R. D. Averitt, D. Sarkar, N. J. Halas, Plasmon resonance shifts of Au-coated Au_2S nanosheells: Insight into multicomponent nanoparticle growth, Phys. Rev. Lett. **78**, 4217–4220 (1997) 113

16. S. J. Oldenburg, R. D. Averitt, S. L. Westcott, N. J. Halas, Nanoengineering of optical resonances. Phys. Lett. **288**, 243–247 (1998) 113
17. P. K. Aravind, H. Metiu, The effects of the interaction between resonances in the electromagnetic response of a sphere-plane structure; applications to surface enhanced spectroscopy, Surf. Sci. **124**, 506–528 (1983) 113
18. P. Moon, D. E. Spencer, *Field Theory Handbook* (Springer, Berlin, Heidelberg 1961) p. 110. 113
19. M. M. Wind, J. Vlieger, D. Bedeaux, The polarizability of a truncated sphere on a substrate I, Physica **A** **141**, 33–57 (1987) 113, 118
20. T. Okamoto, I. Yamaguchi, Field enhancement by a metallic sphere on dielectric substrates, Opt. Rev. **6**, 211–214 (1999) 115, 116, 117
21. H. B. Levine, D. A. McQuarrie, Dielectric constant of simple gases, J. Chem. Phys. **49**, 4181–4187 (1968) 118
22. A. Goyette, A. Navon. Two dielectric spheres in an electric field, Phys. Rev. B **13** 4320–4327 (1976) 118
23. P. K. Aravind, A. Nitzan, H. Metiu, The interaction between electromagnetic resonances and its role in spectroscopic studies of molecules adsorbed on colloidal particles or metal spheres, Surf. Sci. **110**, 189–204 (1981) 118
24. K. A. Fuller, Optical resonances and two-sphere systems, Appl. Opt. **30**, 4716–4731 (1991) 118
25. P. Clippe, R. Evard, A. A. Lucas, Aggregation effect on the infrared absorption spectrum of small ionic crystals, Phys. Rev. **14**, 1715–1721 (1976) 118
26. J. M. Gerady, M. Ausloos, Absorption spectrum of clusters of spheres from the general solution of Maxwell's equations: The long-wavelength limit, Phys. Rev. B **22**, 4950–4959 (1980) 118
27. J. M. Gerady, M. Ausloos, Absorption spectrum of clusters of spheres from the general solution of Maxwell's equations, II: Optical properties of aggregated metal spheres, Phys. Rev. B **25**, 4204–4229 (1982) 118
28. J. M. Gerady, M. Ausloos, Absorption spectrum of clusters of spheres from the general solution of Maxwell's equations, IV: Proximity, bulk, surface, and shadow effects (in binary clusters), Phys. Rev. B **27**, 6446–6463 (1983) 118
29. T. Okamoto, I. Yamaguchi, T. Kobayashi, Local plasmon sensor with gold colloid monolayers deposited upon glass substrates, Opt. Lett. **25**, 372–374 (2000) 118, 119, 121
30. A. Doron, E. Katz, I. Willner, Organization of Au colloids as monolayer films onto ITO glass surfaces: Application of metal colloid films as base interfaces to construct redox-active monolayers, Langmuir **11**, 1313–1317 (1995) 118
31. R. G. Freeman, K. C. Grabar, K. J. Allison, R. M. Bright, J. A. Davis, A. P. Guthrie, M. B. Hommer, M. A. Jackson, P. C. Smith, D. G. Walter, M. J. Natan, Self-assemble metal colloid monolayers: An approach to SERS substrates, Science **267**, 1629–1632 (1995) 118
32. K. C. Grabar, P. C. Smith, M. D. Musick, J. A. Davis, D. G. Walter, M. A. Jackson, A. P. Guthrie, M. J. J. Natan, Am. Chem. Soc. **118**, 1148–1153 (1996) 118
33. G. Schmid, St. Peschel, Th. Sawitowski, Two-dimensional arrangements of gold clusters and gold colloids on various surfaces, Z. anorg. allg. Chem. **623**, 719–723 (1997) 118
34. T. Sato, D. G. Hasko, H. Ahmed, Nanoscale colloidal particles: Monolayer organization and patterningm J. Vac. Sci. Technol. B **15**, 45–48 (1997) 118

35. S. S. Yee, *Surface Plasmon Resonance (SPR) Optical Sensors, Current Technology and Applications,* Sens. Actuators B **54**, Nos. 1–2 (1999) 118

Forces in Optical Near-Fields

Lukas Novotny

The Institute of Optics, University of Rochester
Rochester, NY 14527, USA
`novotny@optics.rochester.edu`

Abstract. In this article we use classical electrodynamics to derive the conservation law for linear momentum in an optical field. The net force exerted on an arbitrary object is determined by Maxwell's stress tensor. It is shown that in the limiting case of an infinitely extended object, the formalism renders the known expressions for radiation pressure. Similarly, in the small object limit, we obtain the familiar expressions for gradient and scattering forces. The theory is applied to calculate the trapping forces near a laser-illuminated metal tip.

1 Introduction

As early as 1619 Johannes Kepler suggested that the mechanical effect of light might be responsible for the deflection of the tails of comets entering our solar system. The classical Maxwell theory showed in 1873 that the radiation field carries with it momentum and that 'light pressure' is exerted on illuminated objects. In 1905 Einstein introduced the concept of the photon and showed that energy transfer between light and matter occurs in discrete quanta. Momentum and energy conservation was found to be of great importance in microscopic events. The discrete momentum transfer between photons (X-rays) and other particles (electrons) was experimentally demonstrated by Compton in 1925 and the recoil momentum transferred from photons to atoms was observed by *Frisch* in 1933 [1]. Important studies of the action of photons on neutral atoms were made in the 1970s by Letokhov and other researchers in the former USSR and in Ashkin's group at Bell Laboratories, USA. The latter group proposed, the bending and focusing of atomic beams and the trapping of atoms in focused laser beams. Later work by Ashkin and coworkers led to the development of 'optical tweezers'. These devices allow one to optically trap and manipulate macroscopic particles and living cells with typical sizes in the range of 0.1–10μm [2,3]. Milliwatts of laser power produce piconewtons of force. Owing to the high field gradients of evanescent waves, strong forces are to be expected in optical near fields. A recent discussion is given in [4].

The idea that an object might cool through its interaction with the radiation field had already been suggested in 1929 by *Pringsheim* [5]. However, the first proposal to cool atoms in counter-propagating laser beams was made by *Hänsch* and *Schawlow* in 1975 [6]. This proposal was the starting point for a series of exciting experiments which led to the 1997 Nobel Prize in physics.

S. Kawata (Ed.): Near-Field Optics and Surface Plasmon Polaritons,
Topics Appl. Phys. **81**, 123–141 (2001)

The mechanical force in laser trapping and cooling experiments can be understood on a semiclassical basis, where the electromagnetic field is treated classically and the particle being trapped is treated as a quantized two-level system [7]. However, the quantum theory of photons must be used for the correct interpretation of the results [8]. Furthermore, the photon concept asserts that there are quanta of energy and momentum transfer between the radiation field and the atom.

2 Theory

The general law for forces in electromagnetic fields is based on the conservation law for linear momentum. We therefore derive this conservation law in the following. Later we shall discuss two different limits, the dipolar limit and the limit of a planar interface. For simplicity, we consider Maxwell's equations in vacuum. In this case we have $\boldsymbol{D} = \varepsilon_o \boldsymbol{E}$ and $\boldsymbol{B} = \mu_0 \boldsymbol{H}$. Later we shall relax this constraint. The conservation law for linear momentum is entirely a consequence of Maxwell's equations,

$$\nabla \times \boldsymbol{E}(\boldsymbol{r},t) = -\frac{\partial \boldsymbol{B}(\boldsymbol{r},t)}{\partial t} \,, \tag{1}$$

$$\nabla \times \boldsymbol{B}(\boldsymbol{r},t) = \frac{1}{c^2}\frac{\partial \boldsymbol{E}(\boldsymbol{r},t)}{\partial t} \, + \, \mu_0 \boldsymbol{j}(\boldsymbol{r},t) \,, \tag{2}$$

$$\nabla \cdot \boldsymbol{E}(\boldsymbol{r},t) = \frac{1}{\varepsilon_0}\rho(\boldsymbol{r},t) \,, \tag{3}$$

$$\nabla \cdot \boldsymbol{B}(\boldsymbol{r},t) = \boldsymbol{0} \,, \tag{4}$$

and of the force law

$$\begin{aligned}\boldsymbol{F}(\boldsymbol{r},t) &= q\left[\boldsymbol{E}(\boldsymbol{r},t) \, + \, \boldsymbol{v}(\boldsymbol{r},t) \times \boldsymbol{B}(\boldsymbol{r},t)\right] \\ &= \int_V \left[\rho(\boldsymbol{r},t)\boldsymbol{E}(\boldsymbol{r},t) \, + \, \boldsymbol{j}(\boldsymbol{r},t) \times \boldsymbol{B}(\boldsymbol{r},t)\right] dV \,.\end{aligned} \tag{5}$$

The first expression applies to a single charge q moving with velocity $\boldsymbol{v}$, and the second expression to a distribution of charges and currents satisfying the charge conservation law

$$\nabla \cdot \boldsymbol{j}(\boldsymbol{r},t) \, + \, \frac{\partial \rho(\boldsymbol{r},t)}{\partial t} \; = \; 0 \,, \tag{6}$$

which is a direct consequence of Maxwell's equations. The force law connects the electromagnetic world with the mechanical one. The two terms in the first expression are basically definitions of the electric and magnetic fields.

If we operate on Maxwell's first equation by $\times\varepsilon_0\boldsymbol{E}$ and on the second equation by $\times\mu_0\boldsymbol{H}$, and then add the two resulting equations we obtain

$$\varepsilon_0(\nabla\times\boldsymbol{E})\times\boldsymbol{E}+\mu_0(\nabla\times\boldsymbol{H})\times\boldsymbol{H}=\boldsymbol{j}\times\boldsymbol{B}-\frac{1}{c^2}\left(\frac{\partial\boldsymbol{H}}{\partial t}\times\boldsymbol{E}\right)+\frac{1}{c^2}\left[\frac{\partial\boldsymbol{E}}{\partial t}\times\mathbf{H}\right].\qquad(7)$$

We have omitted the arguments $(\boldsymbol{r},t)$ for the various fields and have used $\varepsilon_0\mu_0=1/c^2$. The last two expressions in (7) can be combined to give $(1/c^2)\,\mathrm{d}/\mathrm{d}t\;[\boldsymbol{E}\times\boldsymbol{H}]$. For the first expression in (7) we can write

$$\begin{aligned}\varepsilon_0(\nabla\times\boldsymbol{E})\times\boldsymbol{E}\;&=\\ &\varepsilon_0\begin{bmatrix}\partial/\partial x\,(E_x^2-E^2/2) & +\,\partial/\partial y\,(E_xE_y) & +\,\partial/\partial z\,(E_xE_z)\\ \partial/\partial x\,(E_xE_y) & +\,\partial/\partial y\,(E_y^2-E^2/2) & +\,\partial/\partial z\,(E_yE_z)\\ \partial/\partial x\,(E_xE_z) & +\,\partial/\partial y\,(E_yE_z) & +\,\partial/\partial z\,(E_z^2-E^2/2)\end{bmatrix}-\varepsilon_0\,\boldsymbol{E}\,\nabla\cdot\boldsymbol{E}\\ &=\;\nabla\cdot[\varepsilon_0\boldsymbol{E}\boldsymbol{E}\;-\;(\varepsilon_0/2)E^2\,\mathsf{I}]-\rho\boldsymbol{E}\;.\end{aligned}\qquad(8)$$

where (3) has been used in the last step. The notation $\boldsymbol{E}\boldsymbol{E}$ denotes the outer product, $E^2=E_x^2+E_y^2+E_z^2$ is the electric field strength, and I denotes the unit tensor. A similar expression can be derived for $\mu_0(\nabla\times\boldsymbol{H})\times\boldsymbol{H}$. Using these two expressions in (7) we obtain

$$\nabla\cdot\left[\varepsilon_0\boldsymbol{E}\boldsymbol{E}-\mu_0\boldsymbol{H}\boldsymbol{H}-\frac{1}{2}\,(\varepsilon_0E^2+\mu_0H^2)\,\mathsf{I}\right]=\frac{\mathrm{d}}{\mathrm{d}t}\frac{1}{c^2}[\boldsymbol{E}\times\boldsymbol{H}]+\rho\,\boldsymbol{E}+\boldsymbol{j}\times\boldsymbol{B}\,.\qquad(9)$$

The expression in square brackets on the left-hand side is called Maxwell's stress tensor in vacuum, usually denoted by T. In cartesian components it reads

$$\begin{aligned}\mathsf{T}\;&=\;\varepsilon_0\boldsymbol{E}\boldsymbol{E}-\mu_0\boldsymbol{H}\boldsymbol{H}\;-\;\frac{1}{2}\,(\varepsilon_0E^2+\mu_0H^2)\,\mathsf{I}\;=\\ &\begin{bmatrix}\varepsilon_o(E_x^2-E^2/2)\,+\,\mu_o(H_x^2-H^2/2) & \varepsilon_oE_xE_y\,+\,\mu_oH_xH_y & \varepsilon_oE_xE_z\,+\,\mu_oH_xH_z\\ \varepsilon_oE_xE_y\,+\,\mu_oH_xH_y & \varepsilon_o(E_y^2-E^2/2)\,+\,\mu_o(H_y^2-H^2/2) & \varepsilon_oE_yE_z\,+\,\mu_oH_yH_z\\ \varepsilon_oE_xE_z\,+\,\mu_oH_xH_z & \varepsilon_oE_yE_z\,+\,\mu_oH_yH_z & \varepsilon_o(E_z^2-E^2/2)\,+\,\mu_o(H_z^2-H^2/2)\end{bmatrix}.\end{aligned}\qquad(10)$$

After integration of (9) over an arbitrary volume V which contains all sources ρ and $\boldsymbol{j}$ we obtain

$$\int_V\nabla\cdot\mathsf{T}\,\mathrm{d}V\;=\;\frac{\mathrm{d}}{\mathrm{d}t}\frac{1}{c^2}\int_V(\boldsymbol{E}\times\boldsymbol{H})\,\mathrm{d}V\;+\;\int_V(\rho\,\boldsymbol{E}\;+\;\boldsymbol{j}\times\boldsymbol{B})\,\mathrm{d}V\;.\qquad(11)$$

The last term can be recognized as the mechanical force (see (5)). The volume integral on the left can be transformed to a surface integral using Gauss's integration law

$$\int_V \nabla \cdot \mathsf{T}\, \mathrm{d}V \;=\; \int_{\partial V} \mathsf{T} \cdot \boldsymbol{n}\, \mathrm{d}a \;. \tag{12}$$

Here ∂V denotes the surface of V, $\boldsymbol{n}$ the unit vector perpendicular to the surface, and da an infinitesimal surface element. We then finally arrive at the conservation law for linear momentum,

$$\int_{\partial V} \mathsf{T}(\boldsymbol{r},t) \cdot \boldsymbol{n}(\boldsymbol{r})\, \mathrm{d}a \;=\; \frac{\mathrm{d}}{\mathrm{d}t}\left[\boldsymbol{G}_{field}(\boldsymbol{r},t) \,+\, \boldsymbol{G}_{mech}(\boldsymbol{r},t)\right] . \tag{13}$$

where $\boldsymbol{G}_{mech}$ and $\boldsymbol{G}_{field}$ denote the mechanical momentum and the field momentum, respectively. In (13) we have used Newton's expression for the mechanical force $\boldsymbol{F} = d/dt\boldsymbol{G}_{mech}$ and the definition of the field momentum

$$\boldsymbol{G}_{field} \;=\; \frac{1}{c^2}\int_V [\boldsymbol{E} \times \boldsymbol{H}]\, \mathrm{d}V \;. \tag{14}$$

This is the momentum carried by the electromagnetic field within the volume V. It is created by the dynamic terms in Maxwell's curl equations, i.e. by the terms containing the time derivatives. The field momentum is zero when it is averaged over one oscillation period, and the average force becomes

$$\langle \boldsymbol{F} \rangle \;=\; \int_{\partial V} \langle \mathsf{T}(\boldsymbol{r},t) \rangle \cdot \boldsymbol{n}(\boldsymbol{r})\;\mathrm{d}a \;, \tag{15}$$

with $\langle 3 - pointellipsis \rangle$ denoting a time average. Equation (15) is of general validity. It allows one to calculate the mechanical force acting on an arbitrary body within the closed surface ∂V. The force is entirely determined by the electric and magnetic fields on the surface ∂V Fig. 1. It is interesting to note that no material properties enter into the expression for the force; the entire information is contained in the electromagnetic field. The only material constraint is that the body is rigid. If the body deforms when it is subjected to an electromagnetic field we have to include electro- and magnetostrictive forces. Since the enclosing surface is arbitrary, the same results are obtained whether the fields are evaluated at the surface of the body or in the far field. It is important to note that the fields used to calculate the force are the self-consistent fields of the problem, which means that they are a superposition of the incident and the scattered fields. Therefore, prior to calculating the force, one has to solve for the electromagnetic fields. If the object B is surrounded by a medium which can be represented accurately enough by a dielectric constant ε and magnetic susceptibility μ the mechanical force can be calculated in the same way if we replace Maxwell's stress tensor (10) by

$$\mathsf{T} \;=\; \varepsilon_0\varepsilon \boldsymbol{E}\boldsymbol{E} \,-\, \mu_0\mu \boldsymbol{H}\boldsymbol{H} \,-\, \frac{1}{2}\,(\varepsilon_0\varepsilon E^2 \,+\, \mu_0\mu H^2)\mathsf{I} \;. \tag{16}$$

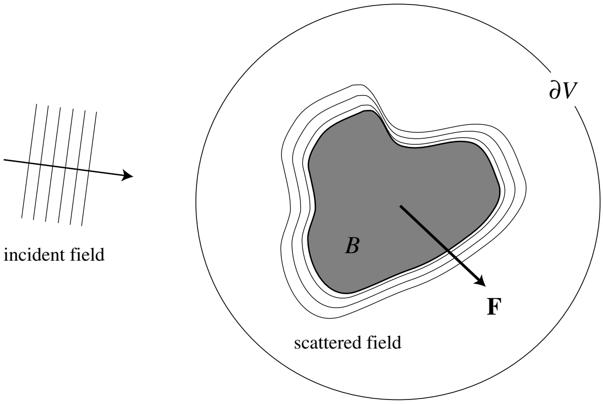

Fig. 1. The mechanical force $\boldsymbol{F}$ acting on the object B is entirely determined by the electric and magnetic fields at an arbitrary surface ∂V enclosing B

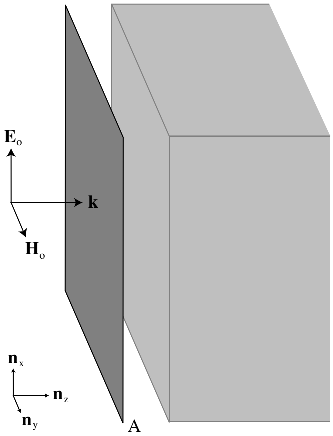

Fig. 2. Configuration used to derive the radiation pressure

2.1 Radiation Pressure

In this subsection we consider the radiation pressure on a medium with an infinitely extended planar interface as shown in Fig. 2. The medium is irradiated by a monochromatic plane wave at normal incidence to the interface. Depending on the material properties of the medium, part of the incident field is reflected at the interface. Introducing the complex reflection coefficient R, the electric field outside the medium can be written as the superposition of two counter propagating plane waves

$$\boldsymbol{E}(\boldsymbol{r},t) \;=\; E_0 \,\mathrm{Re}\left[(\mathrm{e}^{\mathrm{i}kz} \,+\, R\,\mathrm{e}^{-\mathrm{i}kz})\,\mathrm{e}^{-\mathrm{i}\omega t}\right]\,\boldsymbol{n}_x \;. \tag{17}$$

Using Maxwell's curl equation (1), we find for the magnetic field

$$\boldsymbol{H}(\boldsymbol{r},t) \;=\; \sqrt{\varepsilon_0/\mu_0}\;E_0 \,\mathrm{Re}\left[(\mathrm{e}^{\mathrm{i}kz} \,-\, R\,\mathrm{e}^{-\mathrm{i}kz})\,\mathrm{e}^{-\mathrm{i}\omega t}\right]\,\boldsymbol{n}_y \;. \tag{18}$$

To calculate the radiation pressure P we integrate Maxwell's stress tensor on an infinite planar surface A parallel to the interface as shown in Fig. 2. The radiation pressure can be calculated by using (15) as

$$P\,\boldsymbol{n}_z \;=\; \frac{1}{A}\int_A \langle \mathsf{T}(\boldsymbol{r},t)\rangle \cdot \boldsymbol{n}_z \,\mathrm{d}a\;. \tag{19}$$

We do not need to consider a closed surface ∂V, since we are interested in the pressure exerted on the interface of the medium and not in the mechanical force acting on the medium. Using the fields given in (17) and (18), we find that the first two terms in Maxwell's stress tensor (10) give no contribution to the radiation pressure. The third term yields

$$\langle \mathsf{T}(\boldsymbol{r},t)\rangle \cdot \boldsymbol{n}_z \;=\; -\frac{1}{2}\,\langle \varepsilon_0 E^2 + \mu_0 H^2\rangle\, \boldsymbol{n}_z \;=\; \frac{\varepsilon_0}{2}\,E_0^2\,(1+|R|^2)\,\boldsymbol{n}_z\;. \tag{20}$$

Using the definition of the intensity of a plane wave $I_0 = (\varepsilon_0/2)c\,E_0^2$, c being the vacuum speed of light, we can express the radiation pressure as

$$P \;=\; \frac{I_0}{c}\,(1\,+\,|R|^2)\;. \tag{21}$$

For a perfectly absorbing medium we have $R=0$, whereas for a perfectly reflecting medium $R=1$. Therefore, the radiation pressure on a perfectly reflecting medium is twice as high as that on a perfectly absorbing medium.

2.2 Dipole Approximation

Let us consider two oppositely charged particles with masses m_1, m_2, separated by a tiny distance $|\boldsymbol{s}|$, and illuminated by an arbitrary electromagnetic field $\boldsymbol{E}$, $\boldsymbol{B}$, as shown in Fig. 3. In the nonrelativistic limit, the equation of motion for each particle follows from (5) if we set $\boldsymbol{F}$ equal to $m_1\ddot{\boldsymbol{r}}_1$ and $m_2\ddot{\boldsymbol{r}}_2$, respectively. The dots denote differentiation with respect to time. Since the particles are bound to each other, we have to consider their binding energy U. Including this contribution, the equation of motion for the two particles reads

$$m_1\,\ddot{\boldsymbol{r}}_1 = \;\; q\,[\boldsymbol{E}(\boldsymbol{r}_1,t)\;+\;\dot{\boldsymbol{r}}_1\times\boldsymbol{B}(\boldsymbol{r}_1,t)]\;-\;\nabla U(\boldsymbol{r}_1,t)\;, \tag{22}$$

$$m_2\,\ddot{\boldsymbol{r}}_2 = -q\,[\boldsymbol{E}(\boldsymbol{r}_2,t)\;+\;\dot{\boldsymbol{r}}_2\times\boldsymbol{B}(\boldsymbol{r}_2,t)]\;+\;\nabla U(\boldsymbol{r}_2,t)\;. \tag{23}$$

The two particles constitute a two body problem which is most conveniently solved by introducing the center of mass coordinate

$$\boldsymbol{r} \;=\; \frac{m_1}{m_1+m_2}\,\boldsymbol{r}_1 \;+\; \frac{m_2}{m_1+m_2}\,\boldsymbol{r}_2\;. \tag{24}$$

Expressing the problem in terms of $\boldsymbol{r}$ allows us to separate the internal motion of the two particles from the center-of-mass motion. The electric field at the

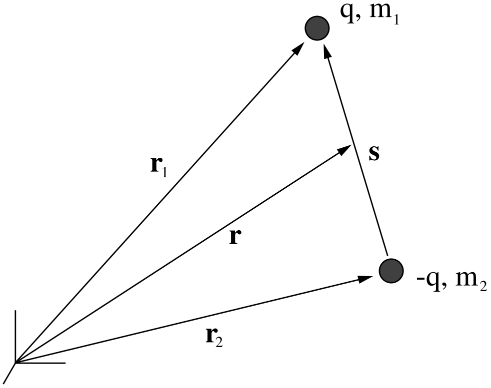

Fig. 3. Graphical representation of the symbols used to derive the mechanical force in the dipolar limit; $\boldsymbol{r}$ denotes the center-of-mass coordinate. The two particles are bound to each other by the potential U

positions of the two particles can be represented by a Taylor expansion [9]:

$$\begin{aligned}\boldsymbol{E}(\boldsymbol{r}_1) = \sum_{n=0}^{\infty} \frac{1}{n!}\Big[(\boldsymbol{r}_1-\boldsymbol{r})\cdot\nabla\Big]^n \boldsymbol{E}(\boldsymbol{r}) &= \boldsymbol{E}(\boldsymbol{r}) + (\boldsymbol{r}_1-\boldsymbol{r})\cdot\nabla\boldsymbol{E}(\boldsymbol{r}) + \ldots,\\ \boldsymbol{E}(\boldsymbol{r}_2) = \sum_{n=0}^{\infty} \frac{1}{n!}\Big[(\boldsymbol{r}-\boldsymbol{r}_2)\cdot\nabla\Big]^n \boldsymbol{E}(\boldsymbol{r}) &= \boldsymbol{E}(\boldsymbol{r}) - (\boldsymbol{r}_2-\boldsymbol{r})\cdot\nabla\boldsymbol{E}(\boldsymbol{r}) + \ldots.\end{aligned} \tag{25}$$

A similar expansion can be found for $\boldsymbol{B}(\boldsymbol{r}_1)$ and $\boldsymbol{B}(\boldsymbol{r}_2)$. For $|\boldsymbol{s}| \ll \lambda$, λ being the wavelength of the radiation field, the expansions can be truncated after the second term (dipole approximation). A straightforward calculation using 22–25 and the definition of the dipole moment

$$\boldsymbol{p} = q\,\boldsymbol{s}\,, \tag{26}$$

where $\boldsymbol{s} = \boldsymbol{r}_1 - \boldsymbol{r}_2$ leads to [8]

$$\begin{aligned}\boldsymbol{F} &= (m_1 + m_2)\,\ddot{\boldsymbol{r}}\\ &= (\boldsymbol{p}\cdot\nabla)\,\boldsymbol{E} \;+\; \dot{\boldsymbol{p}}\times\boldsymbol{B} \;+\; \ddot{\boldsymbol{r}}\times(\boldsymbol{p}\cdot\nabla)\,\boldsymbol{B}\;.\end{aligned} \tag{27}$$

Here, we have omitted the arguments $(\boldsymbol{r}, t)$ for clarity. The brackets in $(\boldsymbol{p}\cdot\nabla)\,\boldsymbol{E}$ indicate that the inner product $\boldsymbol{p}\cdot\nabla = (p_x, p_y, p_z)\cdot(\partial/\partial x, \partial/\partial y, \partial/\partial z)$ has to be evaluated prior to operating on $\boldsymbol{E}$. Equation (27) is the central equation of this subsection. It gives the mechanical force exerted by the electromagnetic field on the two particles represented by the dipole moment $\boldsymbol{p}$. The force consists of three terms: the first originates from the inhomogeneous electric field, the second is the familiar Lorentz force, and the third is due to movement in the inhomogeneous magnetic field. Usually, the third term is much smaller than the other two terms and it will be omitted in the following discussion. It is interesting to note that the fields appearing in (27) correspond to the exciting field. It is assumed that the system represented by the dipole does not change the fields. This is different from the general formalism based on Maxwell's stress tensor, where the self-consistent fields are considered.

A quantized two-level system, such as an atom with transitions restricted to two states is well described by a dipole. The same is true for a macroscopic particle with dimensions much smaller than the wavelength of the illuminating light (a Rayleigh particle). For simplicity, we shall refer to the system represented by the dipole as a particle. Let us consider a particle irradiated by an arbitrary monochromatic electromagnetic wave with angular frequency ω. In this case the fields can be written as

$$\begin{aligned}\boldsymbol{E}(\boldsymbol{r},t) &= \mathrm{Re}\Big[\boldsymbol{E}(\boldsymbol{r})\,\mathrm{e}^{-\mathrm{i}\omega t}\Big]\\ \boldsymbol{B}(\boldsymbol{r},t) &= \mathrm{Re}\Big[\boldsymbol{B}(\boldsymbol{r})\,\mathrm{e}^{-\mathrm{i}\omega t}\Big]\ ,\end{aligned} \tag{28}$$

and the dipole moment as

$$\boldsymbol{p}(t) \;=\; \mathrm{Re}\Big(\boldsymbol{p}\,\mathrm{e}^{-\mathrm{i}\omega t}\Big)\ . \tag{29}$$

The fields and dipole moment can be represented by their complex amplitudes $\boldsymbol{E}(\boldsymbol{r}), \boldsymbol{B}(\boldsymbol{r}), \boldsymbol{p}$. In what follows we shall use $\boldsymbol{E}, \boldsymbol{B}, \boldsymbol{p}$ to refer to the complex amplitudes. We assume that the particle has no static dipole moment. In this case, to first order, the induced dipole moment is proportional to the electric field at the particle's position $\boldsymbol{r} = \boldsymbol{r}_0$

$$\boldsymbol{p} \;=\; \alpha(\omega)\,\mathbf{E}(\boldsymbol{r}_0)\ , \tag{30}$$

α denotes the polarizability of the particle. Its form depends on the nature of the particle (two-level system, Rayleigh particle, ...). In the time average, (27) reads

$$\langle \boldsymbol{F}\rangle \;=\; \frac{1}{2}\mathrm{Re}\left[(\boldsymbol{p}^{*}\!\cdot\nabla)\,\boldsymbol{E} \;-\; \mathrm{i}\omega\,(\boldsymbol{p}^{*}\!\times\boldsymbol{B})\right]\ , \tag{31}$$

where we have dropped the third term as discussed before. If we replace the dipole moment by its expression in Eq. 30 and split the polarizability into its real part α' and imaginary part α'', we find after some rearrangement,

$$\langle \boldsymbol{F}\rangle = (\alpha'/2)\,\nabla E^2 \;+\; \omega\,\alpha''\,(\boldsymbol{E}\times\boldsymbol{B}) \tag{32}$$

$$= -\nabla V_{\mathrm{pot}} \;+\; (\alpha''\,\omega/\varepsilon_0)\,\boldsymbol{g}_{\mathrm{field}}\ , \tag{33}$$

where $\boldsymbol{g}_{\mathrm{field}}$ denotes the density of the field momentum (see (14)) and V_{pot} the potential energy of the induced dipole moment. We find that two different terms determine the mechanical force: the first is denoted as the dipole force (or gradient force) and the second one as the scattering force. The dipole force originates from field inhomogeneities. It is proportional to the dispersive part (real part) of the complex polarizability. On the other hand, the scattering force is proportional to the field strength (Poynting vector) and to the dissipative part (imaginary part) of the complex polarizability. The scattering force may also be regarded as a consequence of the momentum delivered by the scattered photons to the particle. For a lossless particle there is no momentum transfer from the radiation field to the particle, and the scattering force is zero. Polarizable particles are accelerated by the dipole force towards extrema of the radiation field. Therefore, a tightly focused laser beam can trap a particle in all dimensions at its focus. However, the scattering force pushes the particle in the direction of propagation and if the focus of the trapping laser is not tight enough, the particle may be pushed out of the focus.

In atom manipulation experiments the scattering force is used to cool atoms down to extremely low temperatures, thereby bringing them almost to rest. Under ambient conditions, atoms and molecules move at speeds of about 1000 m/s in random directions. Even at temperatures as low as −270°C, the speeds are on the order of 100 m/s. Only for temperatures close to absolute zero (−273°C) does the motion of atoms slow down significantly. The initial idea for slowing down the motion of atoms was based on the Doppler effect. It was first proposed by *Hänsch* and *Schawlow* in 1975 [6]. Neutral atoms are irradiated by pairs of counter propagating laser beams. If an atom moves against the propagation direction of one of the laser beams, the frequency as seen from the atom will shift towards higher frequencies (blue shift) according to the Doppler effect. On the other hand, an atom moving in the direction of propagation of the beam will experience a shift towards lower frequencies (red shift). If the laser frequency is tuned slightly below a resonance transition, an atom will predominantly absorb a photon when it moves against the propagation of the beam. The absorption process slows the atom down, according to momentum conservation. Once the atom is excited, it will eventually reemit its excitation energy by spontaneous emission, which is a random process and does not favor any particular direction.

Thus, averaged over many absorption/emission cycles, an atom moving towards the laser will lose velocity and effectively cool. To slow the atom down in all dimensions, one requires six laser beams opposed in pairs and arranged in three directions at right angles to each other. Whichever direction the atom tries to move it will be met by photons of the right energy and pushed back into the area where the six laser beams intersect. The movement of the atoms in the intersection region is similar to the movement in a hypothetical viscous medium (optical molasses). It can be calculated that two-level atoms cannot be cooled below a certain temperature, called the Doppler limit [8]. For sodium atoms the limiting temperature is 240 μK corresponding to speeds of 30 cm/s. However, it was found experimentally that much lower temperatures could be attained. After surpassing another limit, the so-called recoil limit, which states that the speed of an atom cannot be less than that imparted by a single photon recoil, temperatures as low as 0.18 μK have been generated for helium atoms. Under these conditions the helium atoms move at speeds of only 2 cm/s. So far, the atoms have been slowed down, but not captured. An optical atom trap is needed to prevent the atoms from falling out of the optical molasses owing to gravity. An initial trapping scheme based on the dipole force allowed one to grip the atoms at the focal point of a tightly focused beam [10]. Unfortunately, the optical dipole trap was not strong enough for most applications, and a new three-dimensional trap based on the scattering force has been developed. This kind of trap is now called the magneto-optic trap. Its restoring force comes from a combination of oppositely directed circularly polarized laser beams and a weak, varying, inhomogeneous magnetic field with a minimum in the intersection region of the laser beams. The magnetic field strength increases with distance from the trap center and gives rise to a force towards the trap center. For more detailed descriptions on laser cooling and trapping experiments, the reader is referred to [11,12,13].

In principle, any macroscopic object can be regarded as being composed of individual dipolar subunits. The self-consistent solution for the electric and magnetic fields generated by these dipoles is [14,15]

$$\begin{aligned} \boldsymbol{E}(\boldsymbol{r}) &= \boldsymbol{E}_0(\boldsymbol{r}) \;+\; \omega^2 \mu_0 \sum_{n=1}^{N} \mathsf{G}(\boldsymbol{r}, \boldsymbol{r}_n) \cdot \boldsymbol{p}_n , \\ \boldsymbol{H}(\boldsymbol{r}) &= \boldsymbol{H}_0(\boldsymbol{r}) \;-\; \mathrm{i}\omega \sum_{n=1}^{N} \left[\nabla \times \mathsf{G}(\boldsymbol{r}, \boldsymbol{r}_n) \right] \cdot \boldsymbol{p}_n \qquad \boldsymbol{r} \neq \boldsymbol{r}_n \;, \end{aligned} \tag{34}$$

where we have used the complex representation of time-harmonic fields. G denotes the dyadic Green's function, $\boldsymbol{p}_n$ the electric dipole moment at $\boldsymbol{r} = \boldsymbol{r}_n$, and $\boldsymbol{E}_0$, $\boldsymbol{H}_0$ the exciting field. The system is assumed to consist of N individual dipoles. To first order, the dipole moment $\boldsymbol{p}_n$ is

$$\boldsymbol{p}_n = \alpha_n(\omega)\, \boldsymbol{E}(\boldsymbol{r}_n) \; . \tag{35}$$

Combining (34) and (35), we obtain implicit equations for the fields $\boldsymbol{E}$ and $\boldsymbol{H}$ which can be solved by matrix inversion techniques. Figure 4 illustrates how a laser illuminated tip is subdivided into dipolar subunits. Near the end of the tip, the field is dominated by the faremost dipole. In principle, the mechanical force acting on an arbitrary object made of single dipolar subunits can be determined by using (33) in combination with (34) and (35). However, if we require that the object does not deform under the influence of the electromagnetic field, the internal forces must cancel and the mechanical force is entirely determined by the fields outside the object. In this case, the mechanical force can be determined by solving for the fields outside the object and evaluating Maxwell's stress tensor according to (10) and (15).

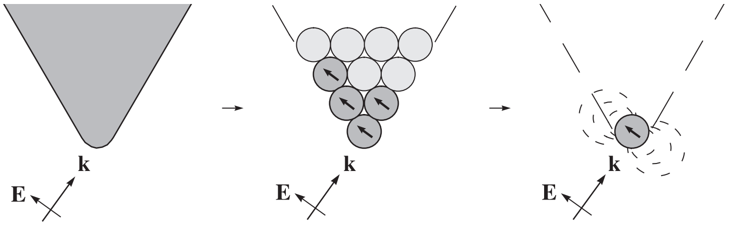

Fig. 4. Illustration of the coupled-dipole approach. A macroscopic object is subdivided into individual, microscopic dipolar subunits. Each dipole moment can be calculated self-consistently by using the Green's function formalism. In a rough approximation, the field in front of a metal tip can be replaced by the field of a single dipole. However, the parameters of the polarizability have to be deduced from a rigorous calculation

3 Trapping by a Laser-Illuminated Metal Tip

As an application of the theory outlined above, we consider a sharp, laser-illuminated gold tip. This configuration has been proposed for the trapping of nanometric particles and biomolecules in aqueous environments [19]. The resulting electric-field distribution for this geometry is strongly polarization-dependent, as shown in Fig. 5. The figure shows the electric field intensity E^2 near the end of the gold tip (5 nm tip radius) for two different monochromatic plane-wave excitations. The wavelength of the illuminating light is $\lambda = 810$ nm (Ti:sapphire laser), which does not match the surface plasmon resonance. The dielectric constants of the tip and water were taken to be $\varepsilon = -24.9 + 1.57\mathrm{i}$ and $\varepsilon = 1.77$, respectively. In Fig. 5a, a plane wave is incident from the bottom, with the polarization perpendicular to the tip axis, whereas in Fig. 5b the tip is illuminated from the side, with the polarization parallel to the tip axis. A striking difference is seen for the two different polarizations: in Fig. 5b, the intensity at the end of the tip is ≈ 3000 times stronger than the illumination intensity, whereas no enhancement beneath the tip exists in Fig. 5a. This result suggests that it is crucial to have a large component of the excitation field along the axial direction to obtain a high field enhancement. Calculations for platinum and tungsten tips show lower enhancements, whereas the field beneath a dielectric tip is reduced compared with the excitation field.

Figure 6 shows the calculated induced surface charge density for the two situations shown in Figs. 5a,b. The incident light drives the free electrons in the metal along the direction of polarization. While the charge density is zero inside the metal at any instant of time ($\nabla \cdot \boldsymbol{E} = 0$), charges accumulate on the surface of the metal. When the incident polarization is perpendicular to the tip axis (Fig. 5a), diametrically opposite points on the tip surface have opposite charges. As a consequence, the end of the tip remains uncharged. On the other hand, when the incident polarization is parallel to the tip axis (Fig. 5b),

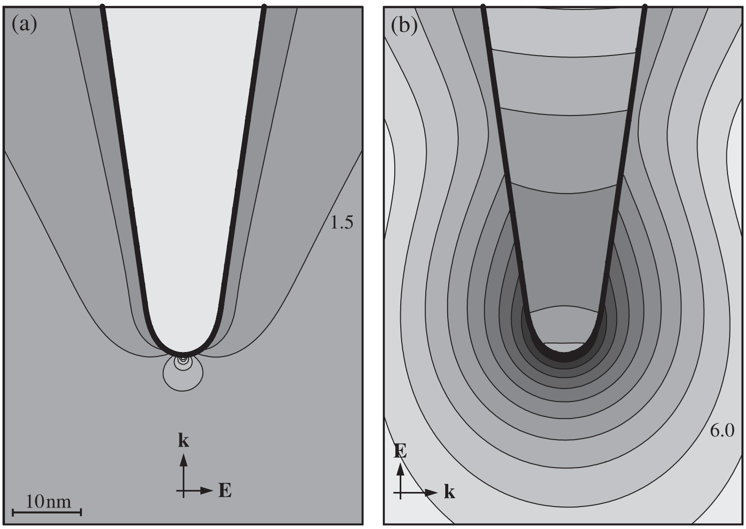

Fig. 5. Near field of a gold tip in water illuminated by two different monochromatic waves at $\lambda = 810$ nm. The direction and polarization of the incident wave are indicated by the $\boldsymbol{k}$ and $\boldsymbol{E}$ vectors. The figures show contours of E^2 (factor of 2 between successive lines). The scaling is given by the numbers in the figures (multiples of the exciting field). No enhancement at the tip in (**a**); enhancement of ≈3000 in (**b**). The field in (**b**) is almost rotationally symmetric in the vicinity of the tip

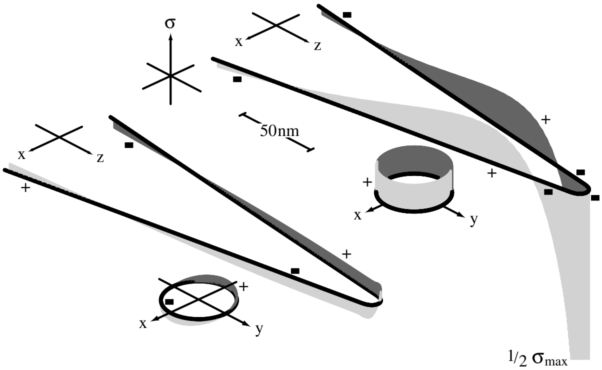

Fig. 6. Induced surface charge density corresponding to Fig. 5a (*left*) and Fig. 5b (*right*). The surface charges form a standing wave in each case. In Fig. 5a, the surface charge wave has a node at the end of the tip, whereas in Fig. 5b there is a large surface charge accumulation at the end, responsible for the field enhancement

the induced surface charge density is rotationally symmetric and has its highest amplitude at the end of the tip. In both cases the surface charges form an oscillating standing wave (surface plasmons) with wavelengths shorter than the wavelength of the illuminating light. While the field enhancement has been calculated in the electrostatic limit [18], the presence of surface plasmons indicates that it is essential to include retardation in the analysis.

With the field distribution around the tip determined, the gradient force for a Rayleigh particle can be easily calculated from

$$\boldsymbol{F} = (\alpha/2)\,\nabla E^2\,, \tag{36}$$

where α is the polarizability of the particle. The particle tends to move to the higher-intensity region, where its induced dipole has a lower potential energy. The assumptions inherent in (36) are that the external field is homogeneous across the particle and that the particle does not alter the field $\boldsymbol{E}$ in (36). These assumptions however, do not hold for a nanometric particle close to the tip as shown in Fig. 7. The intensity contours are distorted around a dielectric sphere ($\varepsilon = 2.5$, 10 nm diameter), and the field inside the sphere is highly inhomogeneous.

Nevertheless, in order to be able to follow the underlying physics without elaborate computations, we shall represent both the tip and the particle

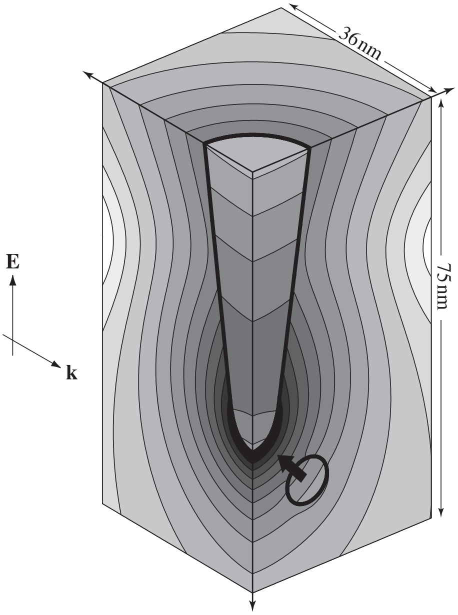

Fig. 7. Perturbation of the near field by a particle being trapped ($\varepsilon = 2.5$, 10 nm diameter). The field inside the particle is highly inhomogeneous, requiring rigorous calculation of the trapping force. The *arrow* indicates the direction of the trapping force. Same scaling as in Fig. 5b

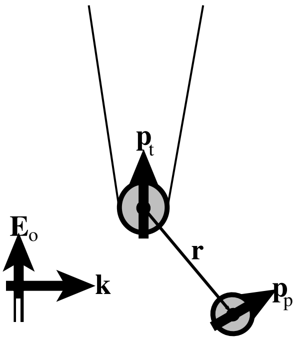

Fig. 8. Trapping of a particle by a laser illuminated metal tip. The tip is illuminated by a plane wave polarized along the tip axis. Both tip and particle are represented by dipoles

by point dipoles. The error of this approximation can then be estimated by comparison with the exact solutions of [19]. The situation that we are going to analyze is shown in Fig. 8. The sharply pointed metal tip is illuminated by a plane wave at right angles, such that the polarization is parallel to the tip axis. The factor f of enhancement of the electric field intensity in front of the tip is determined by the material properties, the sharpness and shape of the tip, and the wavelength of the illuminating field [16,17,18]. We denote the dipoles corresponding to the tip and particle by $\boldsymbol{p}_t$ and $\boldsymbol{p}_p$, respectively. Without loss of generality, the tip dipole is chosen to be located at the origin of the coordinate system. To further simplify the situation, we assume that the coupling between the tip and the particle can be neglected. In this picture, the incident field $\boldsymbol{E}_0$, $\boldsymbol{H}_0$ excites a dipole moment $\boldsymbol{p}_{\mathrm{t}}$ in the tip, and the fields generated by $\boldsymbol{p}_{\mathrm{t}}$ induce a dipole moment $\boldsymbol{p}_{\mathrm{p}}$ in the particle. The dielectric constants of the particle and the environment are $\varepsilon_{\mathrm{p}}(\omega)$ and $\varepsilon_{\mathrm{s}}(\omega)$, respectively. The polarizability of the particle in the nonretarded regime can be calculated as

$$\alpha_{\mathrm{p}}(\omega) \;=\; 3\,\varepsilon_0\,\varepsilon_{\mathrm{s}}(\omega)\,\Delta\,V_{\mathrm{p}}\,\frac{\varepsilon_{\mathrm{p}}(\omega)-\varepsilon_{\mathrm{s}}(\omega)}{\varepsilon_{\mathrm{p}}(\omega)+2\,\varepsilon_{\mathrm{s}}(\omega)}\;, \tag{37}$$

where $\Delta\,V_{\mathrm{p}}$ is the particle volume.

According to the coupled-dipole formalism, any object can be subdivided into dipolar subunits. In a metal, these units have to be chosen so densely that the field at the tip cannot be attributed to the closest dipole alone. Consequently, a metal tip cannot be approximated by a single polarizable sphere, as is often done for dielectric tips [20]. However, rigorous calculations show that the spatial distribution of the field close to a metal tip is similar to the field of a vertical dipole. The dipole moment $\boldsymbol{p}_{\mathrm{t}}$ can be expressed in terms of the computationally determined enhancement factor f of the electric field intensity as

$$\boldsymbol{E}(x{=}0, y{=}0, z{=}a_{\mathrm{t}}) \;=\; \frac{2\;\boldsymbol{p}_t}{4\pi\varepsilon_0\varepsilon_{\mathrm{s}}\,a_{\mathrm{t}}^3} \;\equiv\; \sqrt{f}\,\boldsymbol{E}_0\;, \tag{38}$$

where a_{t} denotes the tip radius and $(x, y, z) = (0, 0, a_{\mathrm{t}})$ are the coordinates of the end of the tip. In this equation, we have considered only the near field of the dipole, since $k\,a_{\mathrm{t}} \ll 1$. Thus, we find for the tip dipole that $\boldsymbol{p}_{\mathrm{t}} = 2\pi\varepsilon_0\varepsilon_{\mathrm{s}}\,a_{\mathrm{t}}^3\sqrt{f}\,\boldsymbol{E}_0$. To determine the mechanical force on the particle in the vicinity of the tip, we have to evaluate (33). Since we consider tip–particle distances d for which $kd \ll 1$ we can neglect retardation effects and consider quasi-static fields. We can also neglect the scattering force (the second term in (33)) because of the small particle size and because there is no radiation pressure associated with the near–fields. In this case we have

$$\langle\boldsymbol{F}\rangle \;=\; (\alpha'_{\mathrm{p}}/2)\,\nabla E^2(\boldsymbol{r})\;. \tag{39}$$

The electric field in this equation corresponds to the field generated by the tip dipole $\boldsymbol{p}_{\mathrm{t}}$ evaluated at the particle's position $\boldsymbol{r}$. Its square amplitude is

$$E^2(\boldsymbol{r}) \;=\; \frac{|\boldsymbol{p}_{\mathrm{t}}|^2}{(4\pi\varepsilon_0\varepsilon_{\mathrm{s}})^2}\,\frac{1\,+\,3\,(z/r)^2}{r^6}\;, \tag{40}$$

where $r = |\boldsymbol{r}|$ is the tip–particle distance and $z = \boldsymbol{r}\cdot\boldsymbol{n}_z$ is the projection of $\boldsymbol{r}$ on the tip axis, $\boldsymbol{n}_z$ being the unit vector along the tip axis. A comparison of the retarded fields of a single dipole and the fields of the rigorous solution for a

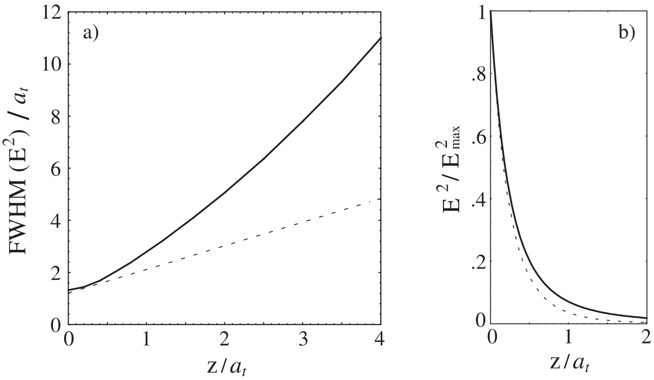

Fig. 9. Comparison of the nonretarded fields of a single dipole (*dotted curves*) and the rigorous solution for a laser-illuminated metal tip (*solid curves*). (**a**) Lateral spread of the field (perpendicular to tip axis) as a function of the distance z from the end of the tip. (**b**) Decay of the field along the tip axis. Normalization by the tip radius $a_{\mathrm{t}} = 5\,\mathrm{nm}$ has been applied

laser-illuminated metal tip is shown in Fig. 9. Combining (38)–(40) we find for the mechanical trapping force

$$\langle \boldsymbol{F} \rangle \;=\; -(3/4)\, a_{\mathrm{t}}^{6}\, f\, E_0^2\, \alpha_{\mathrm{p}}' \,\frac{1}{r^6} \left[\rho\,(1 + 4\,z^2/r^2)\boldsymbol{n}_\rho \;+\; 4\,z^3/r^2\,\boldsymbol{n}_z \right] \,, \tag{41}$$

$\boldsymbol{n}_\rho$ being the unit vector in the radial direction perpendicular to the tip axis, and $\rho = \boldsymbol{r}\cdot\boldsymbol{n}_\rho$. The minus sign indicates that the force is directed towards the tip. We find that $\langle \boldsymbol{F} \rangle$ is proportional to the enhancement factor f, the intensity of the illuminating light $I_0 = (1/2)\sqrt{\varepsilon_0\,\varepsilon_{\mathrm{s}}/\mu_0}\,E_0^2$, the real part of the particle polarizability α_{p}', and the sixth power of the tip radius a_{t}. It has to be kept in mind, that f and a_{t} are not independent parameters; their relationship can be determined by rigorous calculations only.

In the next step we calculate the trapping potential

$$V_{\mathrm{pot}}(\boldsymbol{r}) \;=\; -\int_{\infty}^{\boldsymbol{r}} \langle \boldsymbol{F}(\boldsymbol{r}') \rangle \,\mathrm{d}\boldsymbol{r}' \,, \tag{42}$$

which corresponds to the potential energy of the particle in the field of the tip dipole. The integration path from $\boldsymbol{r}$ to ∞ is arbitrary because $\boldsymbol{F}$ is a conservative vector field. After carrying out the integration, we find

$$V_{\mathrm{pot}}(\boldsymbol{r}) \;=\; -a_{\mathrm{t}}^{6}\, f\, E_0^2\, \alpha_{\mathrm{p}}' \,\frac{1 + 3\,z^2/r^2}{8r^6} \;. \tag{43}$$

The maximum value of V_{pot} is reached exactly in front of the tip ($z = a_{\mathrm{t}} + a_{\mathrm{p}}$). Figure 10 shows $V_{\mathrm{pot}}(\boldsymbol{r}_{\mathrm{p}})$ along the tip axis and along a transverse axis immediately in front of the tip. An enhancement factor of $f = 3000$ is assumed,

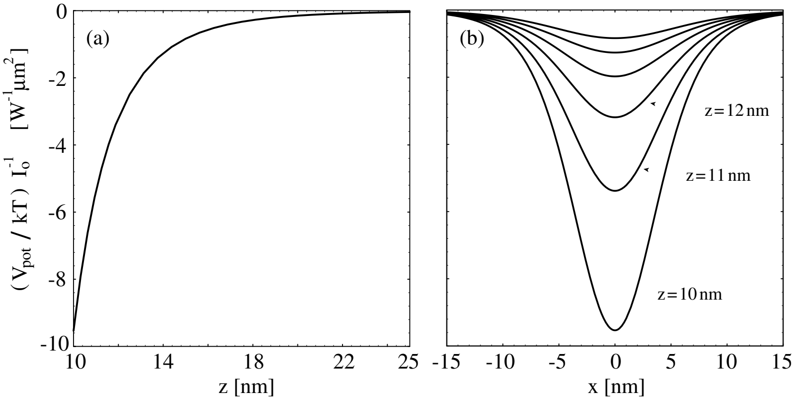

Fig. 10. Trapping potential V_{pot} along the tip axis (**a**) and along a transverse direction at $z \;=\; a_{\mathrm{t}} + a_{\mathrm{p}}$ (**b**) beneath the tip. An enhancement factor of $f = 3000$ is assumed. The radii of the tip and the particle are $a_{\mathrm{t}} = a_{\mathrm{p}} = 5\,\mathrm{nm}$. The dielectric constants of the particle and the environment are $\varepsilon_{\mathrm{p}} = 2.5$ (biomolecule) and $\varepsilon_{\mathrm{s}} = 1.77$ (water), respectively. Normalization by $k_{\mathrm{B}}T$ and by the incident intensity I_0 have been applied

and the radii of both the tip and the particle are chosen as $a_\mathrm{t} = a_\mathrm{p} = 5\,\mathrm{nm}$. The dielectric constants of the particle and the environment are $\varepsilon_\mathrm{p} = 2.5$ (biomolecule) and $\varepsilon_\mathrm{s} = 1.77$ (water), respectively. Since in aqueous environments the trapping forces compete with Brownian motion, the potential in Fig. 10 is normalized by $k_\mathrm{B}T$ (where k_B is the Boltzmann constant and $T = 300\,\mathrm{K}$). Additionally, the curves are scaled with the incident intensity I_0. To obtain a trapping potential which is just equal to $k_\mathrm{B}T$ at room temperature, an intensity of $I_0 \approx 100\,\mathrm{mW/\mu m^2}$ is required. It should be noted that the present calculation is a rough approximation. Comparison with the rigorous treatment in [19] shows that the present results are off by a factor ≈ 2–3. However, the general shape of the trapping potential is in accordance with [19].

Let us assume for the following that a sufficient condition for trapping is $V_\mathrm{pot} > k_\mathrm{B}T$. We can then calculate the intensity required to trap a particle of a given size. Using the expression (37) for the particle polarizability and evaluating (43) at $\boldsymbol{r} = (a_\mathrm{t} + a_\mathrm{p})\boldsymbol{n}_z$, we find

$$I_0 > \frac{kTc}{4\pi\sqrt{\varepsilon_\mathrm{s}}}\,\mathrm{Re}\left(\frac{\varepsilon_\mathrm{p} + 2\,\varepsilon_\mathrm{s}}{\varepsilon_\mathrm{p} - \varepsilon_\mathrm{s}}\right)\frac{(a_\mathrm{t} + a_\mathrm{p})^6}{f\,a_\mathrm{t}^6\,a_\mathrm{p}^3}\ . \tag{44}$$

The curve for which the equality holds is shown in Fig. 11. The same parameters as above have been used. The minimum in the curve indicates that the incident intensity and the tip radius can be adjusted to selectively trap particles with sizes in a limited range. Particles that are too small are not trapped, because their polarizability is too small. On the other hand, for particles that are too big the minimum separation between the tip and the particle $(a_\mathrm{t} + a_\mathrm{p})$ becomes too large. For the parameters used here the optimum particle size is $a_\mathrm{p} \approx 5\,\mathrm{nm}$. However, since the trapping fields decay more slowly the larger the tip radius is, it can be expected that for larger tip sizes the optimum particle size becomes larger. As a rule of thumb, the particle size should be in the region of the tip size. Finally, it should be noted

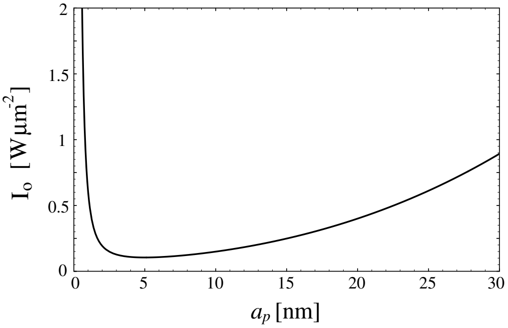

Fig. 11. Minimum trapping intensity I_0 as a function of the particle radius a_p. An enhancement factor of $f = 3000$ is assumed and the tip radius is $a_t = 5\,\mathrm{nm}$. The dielectric constants of the particle and the environment are $\varepsilon_\mathrm{p} = 2.5$ (biomolecule) and $\varepsilon_\mathrm{s} = 1.77$ (water), respectively

that instead of calculating first the trapping force, we could have determined the potential $V_{\mathrm{pot}}(\boldsymbol{r})$ more easily by considering the interaction energy of the particle in the dipole approximation. If $\boldsymbol{E}$ is the field of the tip dipole $\boldsymbol{p}_{\mathrm{t}}$ it is easy to show that

$$V_{\mathrm{pot}}(\boldsymbol{r}) \;=\; -\boldsymbol{p}_p \cdot \boldsymbol{E}(\boldsymbol{r}) \;=\; -(\alpha'_{\mathrm{p}}/2)\, E^2(\boldsymbol{r}) \;, \tag{45}$$

leads to the same result as (43).

In conclusion, we have outlined a general formalism to calculate the forces on arbitrary objects in electromagnetic fields. The formalism is independent of the material properties of the object being trapped and therefore has general validity. The optical properties of the object enter the formalism indirectly through the solution for the electromagnetic fields. On the basis of a simple model we have shown that moderate laser powers are needed to trap a nanoparticle at the end of a gold tip in an aqueous environment. Preliminary experimental results have shown that the formation of eddy currents in the aqueous environment has an effect on the trapping scheme. These eddy currents are generated by laser heating of the metal tip. Although the temperature increase for the required laser powers is small, it will be necessary to perform near-field trapping experiments under favorable conditions (air, vacuum). This will lead to a better understanding of the underlying parameters.

References

1. R. Frisch, Experimenteller Nachweis des Einsteinischen Strahlungsrückstosses. Z. Phys. **86**, 42 (1933) 123
2. A. Ashkin, Optical trapping and manipulation of neutral particles using lasers, Proc. Natl. Acad. Sci. USA **94**, 4853 (1987) 123
3. K. Svoboda, S. M. Block, Biological Applications of Optical Forces, Ann. Rev. Biophys. Biomol. Struct. **23**, 247 (1994) 123
4. D. W. Pohl, in *Forces in Scanning Probe Methods* of NATO Advanced Study Institute, Series E **286**, H.-J. Güntherodt, D. Anselmetti, E. Meyer (Eds.) (Kluwer, Dordrecht 1995) p. 235 123
5. B. Pringsheim, Zwei Bemerkungen über den Unterschied von Lumineszenz- und Temperaturstrahlung, Z. Phys. **57**, 739 (1929) 123
6. Hänsch T. W., A. L. Schawlow, Cooling of gases by laser radiation, Opt. Commun. **13**, 68 (1975) 123, 131
7. Y. Shimizu, H. Sasada, Mechanical force in laser cooling and trapping, Am. J. Phys. **66**, 960 (1998) 124
8. S. Stenholm, The semiclassical theory of laser cooling, Rev. Mod. Phys. **58**, 699 (1986) 124, 129, 131
9. G. Arfken, *Mathematical Methods for Physicists* (3rd ed.) (Academic Press, New York 1985) 129
10. S. Chu, J. E. Bjorkholm, A. Ashkin, A. Cable, Experimental observation of optically trapped atoms, Phys. Rev. Lett. **57**, 314 (1986) 132

11. C. N. Cohen-Tannoudji, W. D. Phillips, New mechanisms for laser cooling, Physics Today **10**, 33 (1990) 132
12. S. Chu, Laser trapping of neutral particles, Scientific Am. **2**, 71 (1992) 132
13. G. B. Lubkin, Experimenters cool Helium below single-photon recoil limit in three dimensions, Physics Today **1**, 22 (1996) 132
14. O. J. F. Martin, A. Dereux, C. Girard, Iterative scheme for computing exactly the total field propagating in dielectric structures of arbitrary shape, J. Opt. Soc. Am. A **11**, 1073 (1994) 132
15. L. Novotny, Allowed and forbidden light in near-field optics II. Interacting dipolar particles, J. Opt. Soc. Am. A **14**, 105 (1997) 132
16. L. Novotny, E. J. Sanchez, X. S. Xie, Near-field optical imaging using metal tips illuminated by higher-order Hermite-Gaussian beams, Ultramicroscopy **71**, 21 (1998) 136
17. O. J. F. Martin, C. Girard, Controlling and tuning strong optical field gradients at a local probe microscope tip apex, Appl. Phys. Lett. **70**, 705 (1997) 136
18. W. Denk, D. W. Pohl, Near-field optics: Microscopy with nanometer-size fields, J. Vac. Sci. and Technol. B **9**, 510 (1991) 135, 136
19. L. Novotny, R. X. Bian, X. S. Xie, Theory of nanometric optical tweezers, Phys. Rev. Lett. **79**, 645 (1997) 133, 136, 139
20. D. V. Labeke, D. Barchiesi, Theoretical problems in scanning near-field optical microscopy, in *Near-Field Optics* D. W. Pohl, D. Courjon (Eds.) Vol. 242, NATO Advanced Study Institute, Series E, (Kluwer, Academic 1993) p. 157 136

Laser Trapping of a Metallic Probe for Near Field Microscopy

Tadao Sugiura

Department of Applied Physics, Osaka University
Suita, Osaka 565-0871, Japan
sugiura@ap.eng.osaka-u.ac.jp

Abstract. A metallic particle is an ideal scattering probe in near-field microscopy. The Laser trapping technique, which enables us to capture a microscopic object using radiation pressure force, has been applied to trap a nanometer-sized metallic particle and to scan the particle over a sample surface as a near-field probe. In this section the mechanism and experimental verification of three-dimensional laser trapping of a metallic particle are explained. The trapping force on a gold particle is greater than that on a glass particle when these particles are sufficiently small compared to the wavelength of light. Also the development of laser trapping NSOM is described. Observed images on various samples using 40 nm diameter gold particles are shown.

1 Introduction

Micrometer-sized particle can be trapped by the radiation pressure exerted by laser light focused with a microscope objective. This phenomenon has been utilized for manipulation of small objects such as biological cells under an optical microscope. This technique is known as optical tweezers or laser trapping, and was first demonstrated by *Ashkin* et al.in 1986 [1,2].

For near-field microscopy, the technique can be applied to hold a small particle on a sample surface so that it can ba used as a near-field probe and to scan the particle over the surface for near-field imaging [3]. This near-field microscope is one of the derivatives of the scattering-probe configuration [4]. It is called a laser-trapping near-field scanni ng optical microscope (laser-trapping NSOM). The laser-trapping NSOM has the following advantages. (1) The spring constant for holding a probe particle is so weak, typically several mN/m, that the probe particle rarely damages the sample. (2) It is possible to scan the particle while it touches to the sample surface. Therefore distance regulation between the particle and the sample surface is not necessary. (3) A metallic particle can be used as a near-field probe [5,6,7]. Because of the greater scattering efficiency of a metallic particle compared with a dielectric one, a metallic particle enables us to abtain a large amount of scattered light scattered from a near-field probe.

In this chapter we discuss the laser trapping of a metallic particle which has a radius of several tens of nanometers for near-field microscopy. First, general explanations of laser trapping will be presented, and then the mechanism

S. Kawata (Ed.): Near-Field Optics and Surface Plasmon Polaritons,
Topics Appl. Phys. **81**, pp. 143–161, 2001.

of trapping of metallic particles will be explained. Afterwards, the scattering properties of a metallic particle will be described. Finally, near-field images obtained with a laser-trapping NSOM will be presented.

2 Mechanism of Laser Trapping

The radiation pressure force is generated as a result of momentum changes of photons in light scattering. Figure. 1a shows a schematic diagram of the generation of the radiation force on a particle. The momentum of the photon, $\boldsymbol{p}$, before incidence on the particle changes to $\boldsymbol{p}'$ in the scattering process. The momentum change $\boldsymbol{p}' - \boldsymbol{p}$ causes the radiation pressure force $\boldsymbol{f}$ to act on the particle as shown in Fig. 1a owing to conservation of momentum.

When a strongly converging laser beam is directed onto the particle, radiation force generated on the particle becomes like the force shown in the Fig. 1b. In the figure, the particle is assumed to be larger than the spot size of the laser beam and to have a higher refractive index than that of the surroundings. The ray depicted by A–A' in Fig. 1b generates a radiation force $\boldsymbol{f}_\mathrm{A}$ on the particle as shown in the figure. Other rays generate radiation forces on the particle in the same manner. The net radiation force on the particle is given by the summation of the forces induced by all rays hitting the particle. The net radiation force is the force $\boldsymbol{F}$ shown in the figure. This force pulls the particle into the laser beam spot, even if the particle is located at beneath the spot. A particle which has a higher refractive index than the surroundings can be trapped in three dimensions.

If the particle has a lower refractive index than the surroundings, the particle is very weakly trapped, because the particle is pushed away from the laser beam. Also, a metallic particle which has a size of the order of a micrometer is barely trapped in three dimensions, because of the reflection at the surface of thee metal. For lower-refractive index particles and metallic particles three-dimensional laser trapping was demonstrated by *Sasaki* et al. [8].

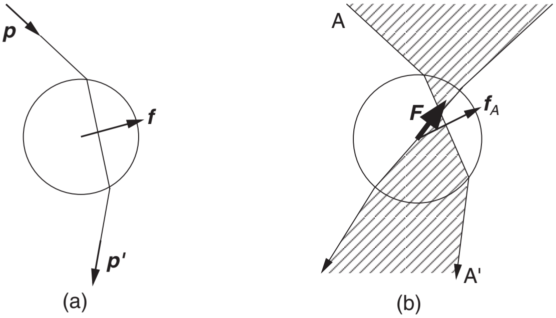

Fig. 1. Schematic illustration of laser trapping. **(a)** Radiation force exerted on a particle by scattering. **(b)** The radiation force of a converging laser beam acts to keep the particle in the spot

In their scheme the position of a laser beam spot was constantly moved to encircle the particle. The particle was captured three-dimensionally in the light field surrounding the particle as if in a cage.

In the case of the trapping in two dimensions, a micrometer-sized metallic particle on a substrate can be trapped by a strongly focused laser beam [9,10,11]. This is explained by the optical absorption of the metallic particle. When the particle is located below the laser beam spot at a distance equal to the particle diameter, the net force on the particle due to optical absorption tends to pull the particle into the optical axis of the beam. In this case we can trap a metallic particle on a substrate in the lateral direction, but cannot lift the particle away from the substrate in the axial direction. Two-dimensional trapping of a metallic particle has also been utilized to hold a metallic probe particle for near-field microscopy [12].

3 Laser Trapping of Metallic Particles

For near-field microscopy, smaller particles are better if they are to be used as a near-field probe. If the size of a metallic particle is sufficiently small compared with the wavelength of the laser beam, the particle can be trapped in three dimensions by the radiation force induced by a strongly converging laser beam [5,13].

3.1 Radiation Forces on Metallic Rayleigh Particles

If the diameter of the probe particle is much smaller than the wavelength of the trapping laser, the force exerted on such a particle can be described by summation of the scattering force $\boldsymbol{F}_{\mathrm{scat}}$ and the gradient force $\boldsymbol{F}_{\mathrm{grad}}$ [1,5,14] in the following form:

$$\boldsymbol{F} = \boldsymbol{F}_{\mathrm{scat}} + \boldsymbol{F}_{\mathrm{grad}} \,. \tag{1}$$

The scattering force $\boldsymbol{F}_{\mathrm{scat}}$ always pushes the particle along the propagation direction of the light. In the case of a weakly absorbing particle such as a metallic particle, the force generated by light absorption is dominant in the scattering force [15]. The force due to absorption $\boldsymbol{F}_{\mathrm{abs}}$ is given by

$$|\boldsymbol{F}_{\mathrm{abs}}| = \frac{8\,\pi^2\,r^3\,n_1^2}{c\,\lambda}\,\mathrm{Im}\left(\frac{m^2-1}{m^2+2}\right) I \,, \tag{2}$$

where n_1 is the refractive index of the surrounding medium, m is the relative refractive index of the particle against the surroundings, and r is the radius of the particle; c, λ and I are the velocity of light, the wavelength of the light, and the power density of the light, respectively. $\mathrm{Im}\,()$ indicates the imaginary part of a quantity.

The gradient force $\boldsymbol{F}_{\mathrm{grad}}$ acts on a particle according to the gradient of the electromagnetic field around the particle. The gradient force $\boldsymbol{F}_{\mathrm{grad}}$ is expressed by

$$\boldsymbol{F}_{\mathrm{grad}} = \frac{1}{4}\, n_1\, \alpha \,\mathrm{grad}\left(|\boldsymbol{E}|^2\right), \tag{3}$$

where α is the polarizability of the particle and $\boldsymbol{E}$ is the electric field. We assume that the particle is spherical, then the polarizability α is given as follows:

$$\alpha = 4\pi\varepsilon\epsilon_0\, \frac{m^2-1}{m^2+2}\, r^3 . \tag{4}$$

Teh polarizability has a complex value in general. When the real part of the polarizability is positive, the gradient force pulls the particle into a stronger light field.

Table 1 shows the polarizabilities of various metallic and dielectric particles. A gold particle has a positive value of the real part of the polarizability. The magnitude of the real part of the polarizability is 13.4 times as large as that of a glass particle. This means that the gradient force on a gold particle is more than ten times larger than that on a glass particle. So if the particles is much smaller than the wavelength of light, a gold particle is much easily trapped by a laser beam than a glass particle is. A silver particle has the same behavior as a gold particle. At a wavelength of 488 nm, the polarizability of a gold particle still has a large real part, although the imaginary part of the polarizability is also large. This causes the scattering force exerted by light absorption to become large. Consequently, a gold particle is hardly trapped at this wavelength.

Table 1. Polarizabilities of various particles. The refractive indices of the metallic particles are taken from [16]

Particle	Refractive index	α/r^3 (10^{-10})	$\mathrm{Re}(\alpha)/\alpha_{\mathrm{glass}}$
Gold in water ($\lambda = 1047\,\mathrm{nm}$)	0.272 – 7.07i	$2.19 - 1.85 \times 10^{-2}\mathrm{i}$	13.4
Gold in water ($\lambda = 488\,\mathrm{nm}$)	0.916 – 1.84i	1.13 – 2.85i	6.9
Silver in water ($\lambda = 1047\,\mathrm{nm}$)	0.226 – 6.99i	$2.20 - 1.60 \times 10^{-2}\mathrm{i}$	13.4
Silver in water ($\lambda = 488\,\mathrm{nm}$)	0.130 – 2.88i	4.12 – 0.339i	25.2
Glass in water	1.50	0.164	1

3.2 Radiation Force in a Laser Beam Spot

Let us consider the trapping force on a metallic Rayleigh particle located in a spot formed by a strongly converging laser beam. Figure. 2 shows a schematic diagram of the laser trapping of a Rayleigh particle. For a particle to be trapped, the gradient force, which pulls the particle towards the spot, must be stronger than the scattering force, which repels the particle from the spot. In this section we discuss the magnitude of the gradient force and of the scattering force on a metallic particle in a beam spot.

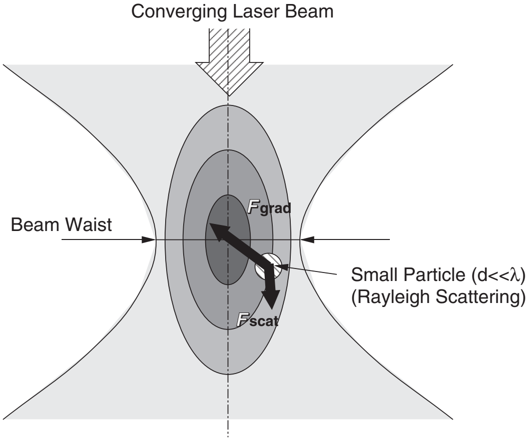

Fig. 2. Radiation force on a metallic Rayleigh particle. The scattering force repels the particle from the laser beam. The gradient force pulls the particle towards the laser spot

A laser beam focused with an aberration-free objective is assumed. The field distribution around the beam spot can be obtained by the integration of spherical waves with a circular aperture. The intensity distributions of the electric field along the transverse axis and along the longitudinal axis are given by [17]

$$|E(x,0,0)|^2 = |E_0|^2 \left|\frac{2J_1(gx)}{gx}\right|^2 , \tag{5}$$

$$|E(0,0,z)|^2 = |E_0|^2 \left|\frac{\sin(hz)}{hz}\right|^2 , \tag{6}$$

where $g = (2\pi/\lambda)NA$ and $h = (2\pi/\lambda n_1)NA^2$. NA is the numerical aperture of the objective. E_0 represents the electric field at the origin of the axes.

The gradient force on a particle located on the x axis but shifted in the lateral direction pulls the particles towards the spot. The magnitude of the transverse force is given by substitution of (5) into (3) as

$$F_{\mathrm{grad},x}(x,0,0) = n_1 \alpha g \,\frac{gxJ_1(gx)[J_0(gx) - J_2(gx)] - 2J_1(gx)^2}{(gx)^3}\,|E_0|^2 . \qquad (7)$$

Figure 3a shows the calculated result for the transverse force on a Rayleigh particle on the x axis. The magnitude of the transverse force has a minimum and a maximum at $x = -1.49/g$ and $x = 1.49/g$, respectively.

When the particle is located on the optical axis, the radiation force on the particle acts in the direction of the axis. The magnitude of the gradient force is given by

$$F_{\mathrm{grad},z}(0,0,z) = n_1 \alpha h \,\frac{hz\cos(hz)\sin(hz) - \sin^2(hz)}{2(hz)^3}\,|E_0|^2 . \qquad (8)$$

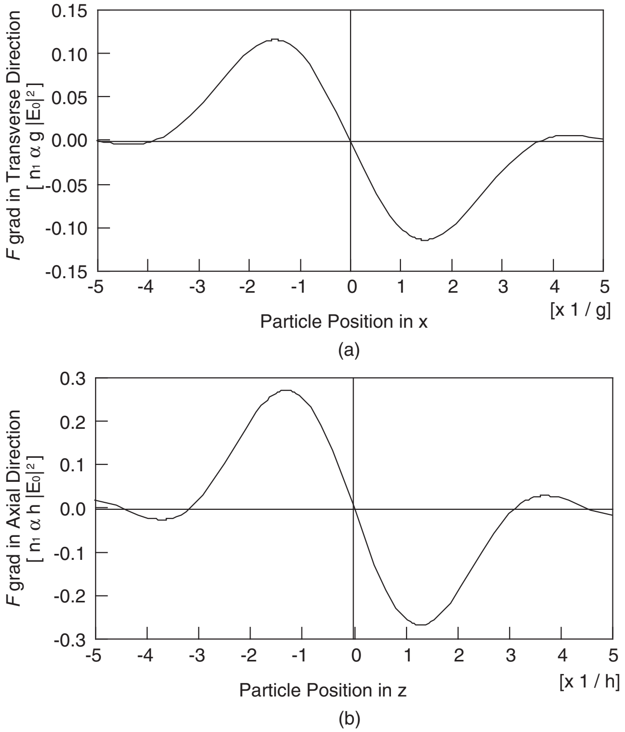

Fig. 3. Magnitude of gradient force exerted on Rayleigh particle: (**a**) gradient force in x direction, (**b**) gradient force in z direction. The magnitude of the force is normalized by $\alpha n_1/g$ and $\alpha n_1/h$, respectively

Figure. 3b depicts the axial-force distribution along the optical axis. The magnitude of the axial force has a minimum at $z = -1.30/h$ and a maximum at $z = 1.30/h$.

As an example, we can examine the laser trapping of a gold particle ($r = 20\,\mathrm{nm}$, $n_{\mathrm{Au}} = 0.272 - 7.07\mathrm{i}$ at $\lambda = 1047\,\mathrm{nm}$ [16]) in water by a near-infrared laser beam (100 mW power, 1047 nm wavelength) focused with an objective of numerical aperture 1.3. We neglect aberrations of the objective for simplicity. The polarizability of this particle is $(1.75 - 0.0148\mathrm{i}) \times 10^{-32}$, so that the gradient force pulls the particle into the focal spot of the laser beam. The maximum values of the gradient force are 5.81 pN in lateral the direction and 1.66 pN in the axial direction. On the other hand th scattering force on the particle has a maximum value of 0.0164 pN at the focal spot. This value is clearly smaller than that of the gradient force so that the particle can be trapped near the focal spot in three dimensions.

3.3 Experiment on 3-D Laser Trapping of a Gold Particle

Three-dimensional laser trapping of a gold particle can be achieved with an ordinary laser-trapping apparatus. The following is on example from the author's experiments [7]. An Nd:YLF laser ($\lambda = 1047$ nm, 2.5 W) was used as the laser light source for trapping. The laser beam was focused into a sample cell with a microscope objective (×100, numerical aperture 1.3). Gold colloidal particles of diameter 40 nm (British BioCell) dispersed in distilled water were used as particles to be trapped.

Figure 4 shows microscopic images of a gold particle trapped by the Nd:YLF laser beam. First the gold particle was trapped in two dimensions at the bottom of the sample cell as shown in Fig. 4a. Then the sample stage

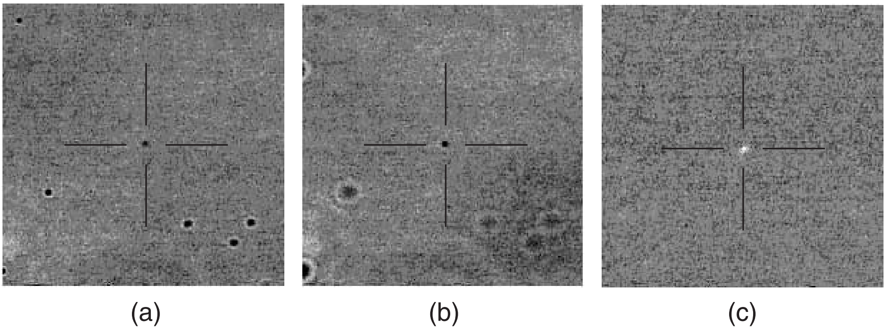

Fig. 4. Laser-trapped metallic particle (gold colloidal particle, diameter 40 nm). The crosshairs in each image show the spot position of the Nd:YLF laser beam. The trapped particle (at the center of each image) is seen as a dark spot in (**a**) and (**b**) and as a bright spot in (**c**). (**a**) A gold particle is trapped on the bottom of the sample cell. (**b**) sample stage was moved down by approximately 1 µm. (**c**) An Ar ion laser beam irradiates the trapped particle

was moved down by approximately 1µm from its position in Fig. 4a. The gold particle was still in focus after the stage movement, as shown in Fig. 4b, although other particles were out of focus. After the laser beam used for trapping was interrupted, the gold particle moved quickly out to the focal position owing to Brownian motion. These observations show that the gold particle was trapped by the laser beam in three dimensions.

Figure 4c shows a similar gold colloidal particle trapped by an Nd:YLF laser beam, simultaneously irradiated by a focused Ar ion laser beam. The bright spot seen in the center of the picture is the Ar ion laser light scattered by the particle. The Nd:YLF laser light scattered by the particle could not observed with the CCD camera, owing to the use of a dichroic mirror and an IR cutoff filter. The total power of the Ar ion laser light on the particle was attenuated here with a neutral-density filter to less than 1/100 of the light power of the Nd:YLF laser, so that no mechanical effect induced by the Ar ion laser beam could be seen on the trapped particle.

3.4 Feedback Stabilization of Probe Position

Because of thermal energy, a probe particle moves continuously in a laser-trapping potential as a result of collisions with water molecules (Brownian motion). Owing to the Brownian motion, the intensity of the light scattered from a particle such as is seen in Fig. 4c changes with time. This will cause noise in the measured signal when we use the trapped particle as a near-field probe. This noise affects the maximum resolving power of the laser-trapping NSOM. Consequently, it is necessary to reduce the fluctuation of the probe position in order to enhance the resolution of the NSOM. To reduce the fluctuation of the particle position, a feedback stabilization technique can be used [6].

In the feedback stabilization technique, information about the particle position is fed back to the spot position of the trapping laser beam. The position of the probe particle is monitored by detection of the spot position, as seen in Fig. 4c. The spot position can be sensitively detected with a four-segment detector and two sets of differential amplifiers used to calculate the displacement signals of the spot in the x and y directions. To shift the spot position of the trapping laser beam, two galvanomirrors are used. The angles of the galvanomirrors are changed to minimize the displacement signals in both the x and the y directions. The displacement signals in the x and y directions are captured by a personal computer.

Figure 5 shows displacement diagrams which depict the movements of a probe particle. Figure 5a shows the result recorded without feedback of the displacement signal to the galvanomirror and Fig. 5b shows the result recorded with feedback. The time interval between displacement measurements was 10 ms. The probe particle was a polystyrene latex particle which had a diameter of 1µm. The standard deviation of the particle position was about 13 nm in the case without feedback (Fig. 5a), while with feedback the

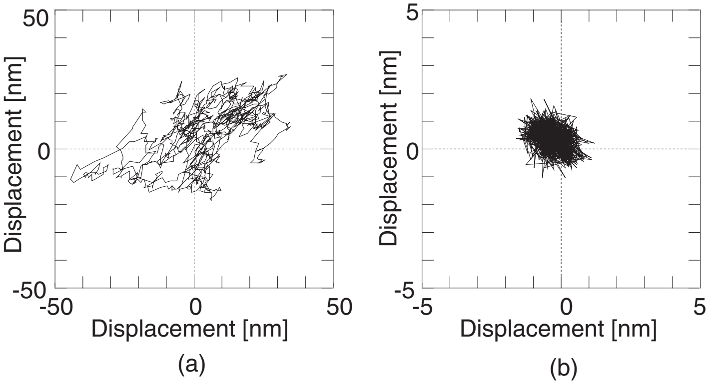

Fig. 5. Particle displacement in optical trap (experimental data): (**a**) without feedback stabilization of the probe particle, (**b**) with feedback stabilization

standard deviation of the particle position was reduced to 0.45 nm. From these results, we see that the feedback method is effective for stabilizing the position of a probe particle.

4 Scattering Properties of Metallic Particles

We estimate the scattering efficiencies of various particles in this section to evaluate the effect of a metallic probe particle. For simplicity a plane electromagnetic wave is assumed to be incident on a spherical particle.

4.1 Scattering Efficiencies

In such a case we can describe the scattering phenomena with a theory of electromagnetic scattering first developed by Mie [15,18]. The scattering efficiency Q_{scat} of a spherical particle is given by

$$Q_{\mathrm{scat}} = \frac{2}{(k_1 r)^2} \sum_{n=1}^{\infty} (2n+1) \left(|a_n|^2 + |b_n|^2 \right) , \tag{9}$$

where a_n and b_n are expansion coefficients given by

$$a_n = \frac{\psi_n(k_1 r)\, \psi_n'(m\, k_1 r) - m\, \psi_n(m\, k_1 r)\, \psi_n'(k_1 r)}{\zeta_n(k_1 r)\, \psi_n'(m\, k_1 r) - m\, \psi_n(m\, k_1 r)\, \zeta_n'(k_1 r)} , \tag{10}$$

$$b_n = \frac{m\, \psi_n(k_1 r)\, \psi_n'(m\, k_1 r) - \psi_n(m\, k_1 r)\, \psi_n'(k_1 r)}{m\, \zeta_n(k_1 r)\, \psi_n'(m\, k_1 r) - \psi_n(m\, k_1 r)\, \zeta_n'(k_1 r)} . \tag{11}$$

Here m is the relative refractive index of the particle with respect to the surrounding medium, r is the radius of the particle, k_1 is the wavenumber of the incident wave in the surrounding medium and $\psi_n(z)$ and $\zeta_n(z)$ are Ricatti–Bessel functions [15]. A prime indicates the derivative of the function.

Table 2 shows the calculated results for the scattering efficiencies of gold and silver particles. The particles are assumed to be homogeneous with a diameter of 40 nm and to be irradiated by a plane electromagnetic wave of wavelength 488 nm. According to the calculation, the scattering efficiency of a gold particle in air is 25 times as great as that of a glass particle in air. In case of particles in water, the scattering efficiency of a glass particle is smaller than it is in air because the relative refractive index of the particle in water is smaller than that in air. The scattering efficiency of the gold particle in water, however, is larger than it is in air because the index of the gold particle has an imaginary part. So the scattering efficiency of the gold particle in water is 348 times as great as that of the glass particle in water. Other metallic particles also have greater scattering efficiencies than that of a glass particle. In particular the scattering efficiency of a silver particle is larger than that of a gold particle. Although a silver particle is one of the best particle for a near-field probe, silver particles have less chemical stability. Accordingly, gold particles are more frequently used as a near-field probe in the laser-trapping NSOM.

Table 2. Scattering efficiencies of various particles. The wavelength is assumed to be 488 nm

In air	Gold	Silver	Glass
Q_{scat}	0.0258	0.0289	0.00101
$Q_{\mathrm{scat}}/Q_{\mathrm{scat\ glass}}$	25.3	28.4	1
In water	**Gold**	**Silver**	**Glass**
Q_{scat}	0.0854	0.228	0.000245
$Q_{\mathrm{scat}}/Q_{\mathrm{scat\ glass}}$	348	930	1

4.2 Near-Field Distributions Around a Metallic Particle

The near-field distribution around the probe particle affects the maximum resolving power of the NSOM. In particular, for fluorescence observations with the NSOM, the point spread of the image is strongly dependent on the near-field distribution around the probe. Therefore, we analyzed the near-field intensity distribution around a metallic particle. For simplicity we assumed a spherical particle irradiated with a plane-polarized electromagnetic wave. The scattering phenomena in such a problem can be described by the Mie scattering theory. We can derive an expression for the electromagnetic field around a probe particle from the Mie scattering theory simply [15].

Figure 6 shows the calculated results for the field intensity distribution around a gold particle with a diameter of 40 nm irradiated with a plane electromagnetic wave of wavelength 488 nm. The incident light is linearly polarized in the x direction and propagates in the z direction. Figures 6a,b show cross sections of the field intensity distribution in the x–z plane and the y–z plane, respectively. In the x–z plane there is a strong-intensity region of the field on the surface of the particle. The strong-intensity region is dependent on the polarization direction, so that the strong region is spread out in the x direction and narrow in the y direction. When a thin sample is put on a plane toucheing the particle at the position $z = -r$ (r is the radius of the particle), the sample can be irradiated by the strong-intensity region, which is nearly equal in size to the particle. The distribution of the field intensity on this plane ($z = -r$) is shown in Fig. 6c. The intensity distribution has two strong regions split by about $r/2$ in the x direction and concentrated within the size of the particle. Furthermore, the intensity of the concentrated field decreases exponentially with increasing distance from the particle. We conclude that the strong-intensity region around the particle is a near-field component generated by the particle.

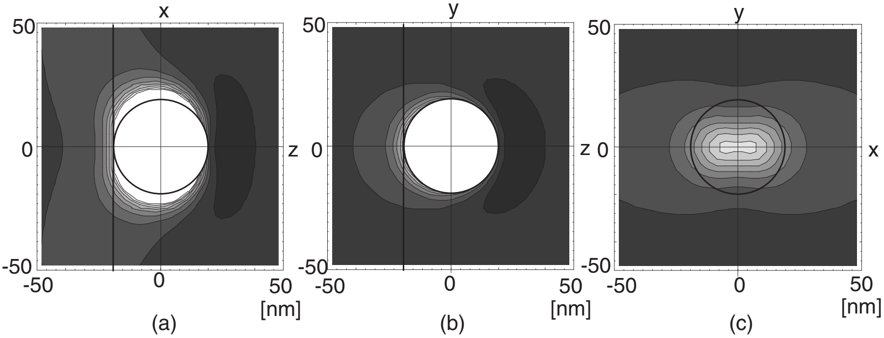

Fig. 6. Near-field intensity distribution around a particle ($d = 40$ nm). (**a**) x–z plane ($z = 0$), (**b**) y–z plane ($z = 0$) and (**c**) x–y plane ($z = -r$). The brighter parts indicates stronger field intensity. The incident light (polarized in the x direction) propagates in the z direction (from $-z$ to $+z$)

5 Laser-Trapping NSOM

As previously mentioned, we can use a particle trapped by a laser beam as a probe in scanning-probe microscopy. This idea was first demonstrated by *Ghislain* and *Webb* for atomic force microscopy [19]. These authers successfully demonstrated force measurement by observations of the scattered light from a polystyrene particle suspended near a sample surface. Later a near-field scanning optical microscope using a laser-trapped particle was reported by *Kawata* et al. [3]. In the experiments of *Kawata* et al.the near-field probe was also a polystyrene particle, which had a diameter of 1µm and was irradiated by an illuminating laser beam in a total-internal-reflection condition. Scattered light from the particle and fluorescence emission from the sample were measured and used to perform scattering imaging and fluorescence imaging, respectively. *Sasaki* et al. [20] applied this probing method to produce a tiny chemical sensor which could measure pH in nanometer regions.These authors utilized specially designed fluorescent beads which changed their fluorescence intensity with pH as a probe. *Saski* et al.trapped a single fluorescent bead with a laser beam and detected the fluorescent emission from the bead. They demonstrated a change in the fluorescence intensity when the pH of the surroundings was changed. In 1997 *Sugiura* et al.developed a laser-trapping NSOM with a three-dimensionally trapped metallic particle [3,5].

5.1 Principle of the Laser-Trapping NSOM

Figure 7 shows a schematic illustration of our laser-trapping NSOM a metallic probe particle. An intense near-infrared laser beam is focused with a microscope objective so as to trap a metallic particle. A single metallic particle is suspended near the focal spot of the laser and approaches the sample surface from beneath. A gold colloidal particle with a diameter of several tens of nanometers is used as a near-field probe.

Another laser beam, which has a wavelength in the visible range, is focused onto the particle simultaneously. This laser beam is used for illumination of the sample. The illuminating laser beam is scattered by the probe particle, and then the scattered light diverges like radiation from a point light source as small as the diameter of the particle. When the particle is sufficiently close to the sample surface, the scattered light illuminates a part of the sample as small as the size of the probe particle and interacts with the material of this region. The scattered light is collected by the objective and is detected

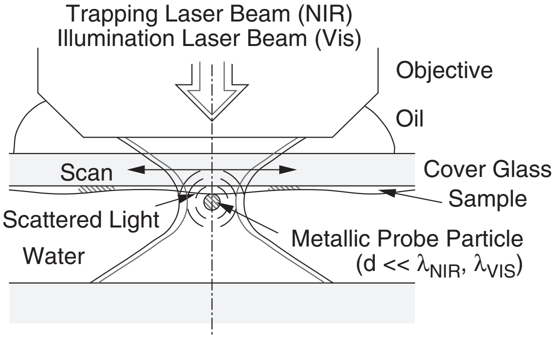

Fig. 7. Schematic illustration of laser-trapping NSOM with a metallic probe particle

through a pinhole placed in the image plane of the objective. The detected intensity of the scattered light contains local information about the sample; therefore the microscope gives information about the structure and material distribution of the sample with a higher lateral resolution than the diffraction limit of the light.

This microscope has the following advantages. (1) Since the spring constant for holding a probe particle is so weak, the sample is rarely damaged mechanically. (2) There is no need to regulate the distance between the probe particle and the sample, because the probe particle touches the sample surface during scanning. (3) Observation with this microscope is done under water. This is quite useful for biological applications [21] such as fluorescence in situ hybridization (FISH) [22]. (4) Because of to the use of a metallic particle, the light intensity scattered by the particle is expected to be much greater than that from a dielectric particle.

5.2 Experimental Setup

Figure 8 shows the experimental setup of our NSOM. The laser used for optical trapping is an Nd:YLF laser (TFR, Spectra-Physics, 2.5 W, wavelength 1047 nm). This laser beam goes into the microscope optics and is focused with an oil immersion objective (UPlan Apo, 100×, 1.35 NA, Olympus). The component labeled DM1 in the microscope optics is a dichroic mirror which reflects the light of the Nd:YLF laser and transmits visible light. Owing to this mirror, almost no light from the Nd:YLF laser penetrates to the upper part of the microscope optics.

The laser used for sample illumination is an air-cooled Ar ion laser (Uniphase, 20 mW, wavelength 488 nm). The beam from this laser also enters the microscope optics and is focused onto the probe particle. The spot position of the Ar ion laser corresponds to that of the Nd:YLF laser. Scattered light from the probe particle is collected with the objective, formed into an image at the position of the pinhole and detected with a photomultiplier tube (PMT) behind the pinhole. The pinhole eliminates undesired light from other parts of the sample. Sample scanning is done by changing the voltage applied to a piezo tube. A CCD camera is used for observation of the sample surface under conventional microscope conditions.

5.3 Observations of Various Samples

5.3.1 Surface of Cover Glass

Figure 9 shows an observed image of the surface of a cover glass. The probe particle used for this observation was a gold colloidal particle with a diameter of 40 nm, the same as in the trapping experiment. The probe particle was scanned over the glass surface while pushing it onto the glass. The contrast of the image in Fig. 9 has been enhanced to show the fine structure of the

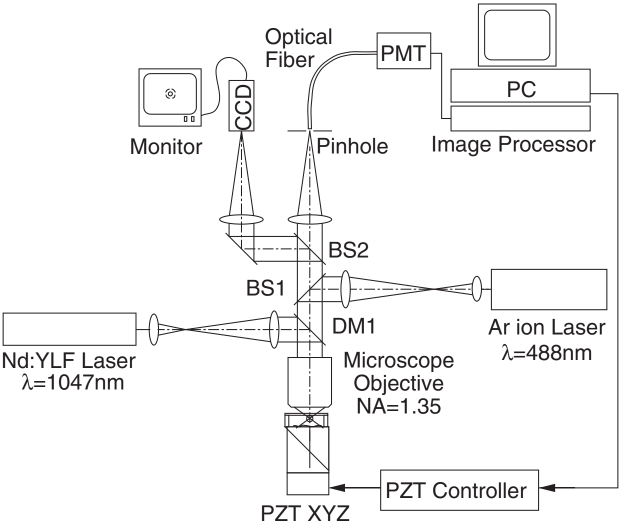

Fig. 8. Experimental setup of laser-trapping NSOM

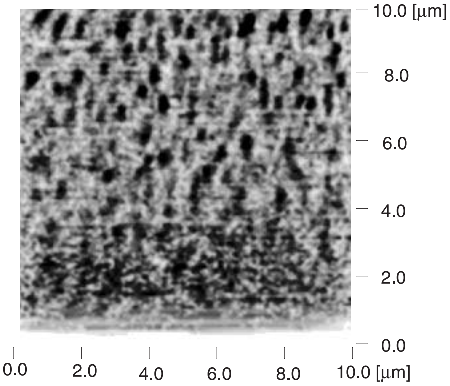

Fig. 9. Observation of the surface of a cover glass

image. The original contrast of the image (= $(I_{\max} - I_{\min})/(I_{\max} + I_{\min})$) was around 0.02. In the image, many round structures with diameters of 200 nm to 500 nm are seen. After observation with the NSOM, we also investigated the same sample with an atomic force microscope (Dimension-3000, Digital Instruments); structures of the same shape were observed, with almost same range of sizes. These structures were small dips with a depth of approximately 10 nm. We suggest that the round structures in Fig. 9 came from the dip structures on the surface of the cover glass.

5.3.2 Gold Colloidal Particles Adsorbed on a Glass Surface

Figure 10 shows an observed image of gold colloidal particles (diameter 40 nm) adhering to a cover glass. The probe particle was the same kind as was used in Fig. 9. The bright and dark structure in the center of the image is due to an aggregate of gold particles. Although th finer structure of this aggregate cannot be seen in this picture, we guess that the contrast mechanism may be dependent on the relative positions of the particles. Also, we could observe the same kinds of round shapes as in Fig. 9 in the flat part of this image after contrast enhancement.

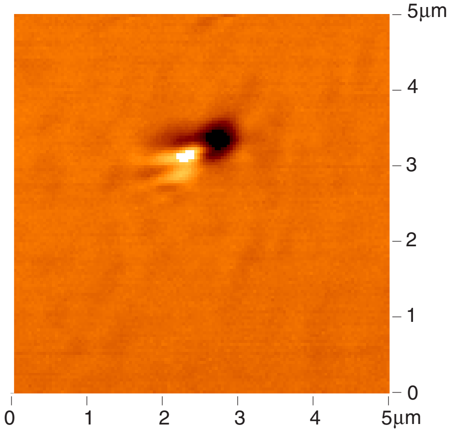

Fig. 10. Gold colloidal particles on a cover glass

5.3.3 Polystyrene Latex Particles

Figure 11 shows an observed image of dispersed polystyrene particles (diameter 100 nm) on a glass substrate. The image was taken by detection of light scattered from a gold particle 40 nm in diameter. There are two dark regions in the picture indicating the existence of particles on the surface. One dark region, in the upper part of the image, is regarded as being due to two particles, and the other dark region, in the middle part of the image, is regarded as being due to a single particle. These particles were observed as dark spots because the intensity of illumination on the probe particle is reduced by scattering by a polystyrene particle on the substrate. Consequently the intensity of light scattered from the probe particle located near a polystyrene particle is smaller than that from the probe particle on a bare glass substrate.

5.3.4 Fluorescent Beads

We observed fluorescent beads on a glass substrate to demonstrate the fluorescence-imaging capability. Figure 12 shows an observed result for fluores-

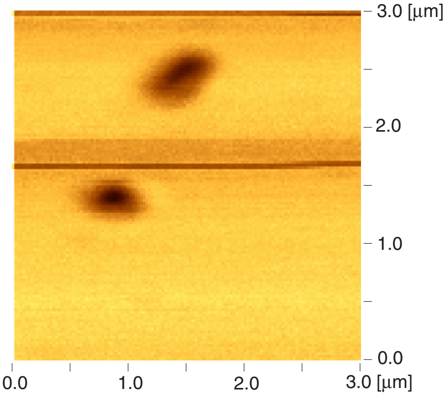

Fig. 11. Polystyrene particles (d = 100 nm) on a cover glass

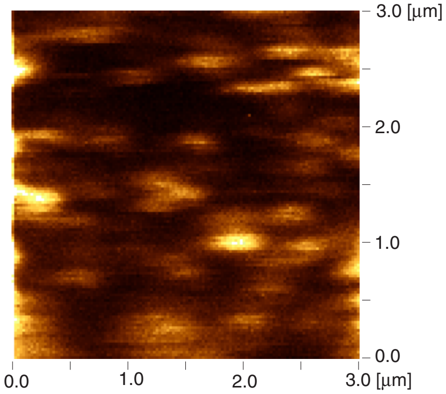

Fig. 12. Aggregated fluorescent beads ($d = 100$ nm)

cent beads ($d = 100$ nm). The excitation wavelength for the fluorescence was 488 nm, from an argon ion laser, and the fluorescence emission was filtered with a dichroic mirror and an absorption filter (cutoff wavelength $\lambda_{\mathrm{cut}} = 515$ nm) to cut out the light scattered by the probe particle. The probe particle was a gold colloidal particle 40 nm in diameter. The fluorescent beads were fixed on cover glass coated with silane. In Fig. 12 many particles are seen as bright spots. These particles were expected to be aggregated on the substrate from the condition of the sample preparation.

Figure 13 shows an observed result for fluorescent beads with a diameter of 50 nm. There are many bright spots in the image. Each spot corresponds to a single fluorescent particle. The line plot shown on the right of the image is the result of a scan across one of these bright spots. The center of the plot corresponds to a bright spot. From this line plot, we see that the spot has a sharp peak in the center. We suggest that the sharpness of the spot is due to the effect of the near-field component around the probe particle.

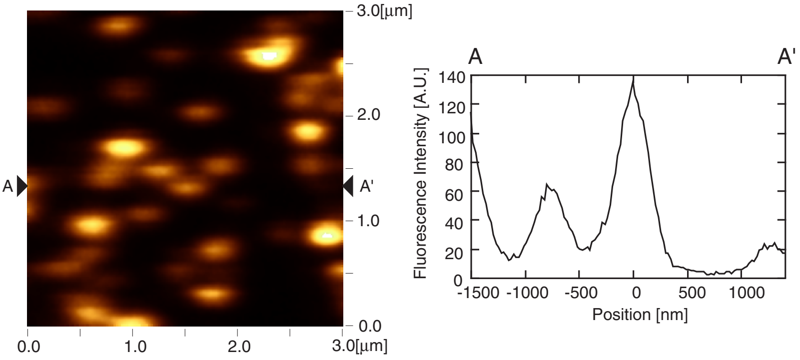

Fig. 13. Single fluorescent beads ($d = 50\,\mathrm{nm}$) and a line plot of the data

5.4 DNA Molecules Stained with YOYO-1 Iodide

An observation of DNA molecules was also performed. The DNA molecules were stained with YOYO-1 iodide dye (Molecular Probes, Inc.) to visualize them by fluorescence emission. This dye has an absorption peak at 491 nm wavelength and an excitation peak at 509 nm wavelength and has high affinity for binding to DNA molecules. The efficiency of fluorescent emission from the dye molecule significantly increases after binding to DNA.

DNA molecules from a calf thymus (Sigma Chemical Co.) were used for a test sample. The sample was prepared as follows. First the DNA was dissolved in water and stained with YOYO-1 iodide. Then the DNA solution was dropped onto cover glass coated with silane. After five minutes the glass was rinsed with deionized water ten times to wash away unadsorbed DNA molecules.

Figure 14 shows an observed result for DNA molecules stained with YOYO-1 iodide. In the middle of the picture an entangled DNA molecule

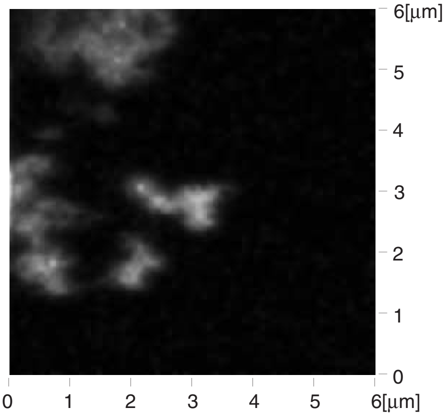

Fig. 14. Single fluorescent beads ($d = 50\,\mathrm{nm}$) and a line plot of the data. DNA molecules stained with YOYO-1 iodide

can be seen. Also, in the upper part, many aggregated DNA molecules can be observed. These results demonstrate that the laser-trapping NSOM has the ability to image biomolecules fixed on a substrate.

6 Summary

We have discussed the principle and mechanism of laser trapping of metallic particles for near-field microscopy and showed experimental verifications of laser trapping of colloidal gold particles. The trapping force on a gold particle is even greater than that on a glass particle when these particles are sufficiently small compared with the wavelength of light. This is due to the magnitude of the polarizability of gold particles. Laser-trapped metallic particles have been utilized as probes for near-field microscopy. An NSOM with a laser-trapped particle performed scattering imaging and fluorescence imaging of various samples. Some images taken with the NSOM were presented.

Metallic particles have many important features for near-field imaging, for example high scattering efficiency and a large enhancement factor of the near field. Also, gold and silver particles have the potential to be easily modified on their surfaces by molecular self-assembly. Surface modification of particles may enable us to add specific functionalities to the particles, such as pH sensing by a change of fluoresence intensity. This feature may introduce additional capabilities into the laser-trapping NSOM. For example, nanometric chemical sensors which detect specific ions with ultrahigh sensitivity, and fluorescence probing of specific biomolecules on a cell membrane by use of conjugate materials fixed on the particle are possible candidates for application of the laser-trapping NSOM. I hope that the laser-trapping technique for metallic particles will provide new tools for nanometric technology.

References

1. A. Ashkin, J. M. Dziedzic, J. E. Bjorkholm, S. Chu, Observation of a single-beam gradient force optical trap for dielectric particles. Opt. Lett. **11**, 288–291 (1986) 143, 145
2. A. Ashkin, J. Dziedzic, and T. Yamane, Optical trapping and manipulation of single cells using infrared laser beams, Nature **330**, 769–771 (1987) 143
3. S. Kawata, Y. Inouye, T. Sugiura, Near-field scanning optical microscope with a laser trapped probe, Jpn. J. Appl. Phys. **33**, L1725–L1727 (1994) 143, 154
4. S. Kawata, Y. Inouye, Near-field scanning optical microscope with a metallic probe tip, Opt. Lett. **19**, 159–161 (1994) 143
5. T. Sugiura, T. Okada, Y. Inouye, O. Nakamura, S. Kawata, Gold-bead scanning near-field optical microscope with laser-force position control, Opt. Lett. **22**, 1663–1665 (1997) 143, 145, 154
6. T. Sugiura, T. Okada, Near-field scanning optical microscope with an optically trapped metallic Rayleigh particle, SPIE Proc. **3260**, 4–14 (1998) 143, 150

7. T. Sugiura, S. Kawata, T. Okada, Fluorescence imaging with a laser trapping scanning near-field optical microscope, J. Microsc. **194**, 291–294 (1999) 143, 149
8. K. Sasaki, M. Koshioka, H. Misawa, N. Kitamura, H. Masuhara, Optical trapping of a metal particle and a water droplet by a scanning laser beam, Appl. Phys. Lett. **60**, 807–809 (1992) 144
9. S. Sato, Y. Harada, Y. Waseda, Optical trapping of microscopic metal particles, Opt. Lett. **19**, 1807–1809 (1994) 145
10. H. Furukawa, I. Yamaguchi, Optical trapping of metallic particles by a fixed Gaussian beam, Opt. Lett. **23**, 216–218 (1998) 145
11. P. C. Ke, M. Gu, Characterization of trapping force on metallic Mie particles, Appl. Opt. **38**, 160–167 (1999) 145
12. P. C. Ke, M. Gu, Image enhancement in near-field scanning optical microscopy with laser-trapped metallic particles, Opt. Lett. **24**, 74–76 (1999) 145
13. K. Svoboda, S. M. Block, Optical trapping of metallic Rayleigh particles, Opt. Lett. **19**, 930–932 (1994) 145
14. K. Visscher, G. J. Brakenhoff, Theoretical study of optical induced forces on spherical particles in a single beam trap, I: Rayleigh scatters, Optik **89**, 174–180 (1992) 145
15. M. Kerker, *The Scattering of Light and Other Electromagnetic Radiation* (Academic Press, New York 1969) 145, 151, 152
16. E. D. Palik, *Handbook of optical constants of solids* (Academic Press, London 1985) 146, 149
17. M. Born, E. Wolf, *Principles of Optics* (Pergamon, New York 1980) 147
18. G. Mie, Beiträge zur Optik trüber Medien, speziell kolloidaler Metallösungen, Ann. Phys. (Leipzig) **25**, 377–445 (1908) 151
19. L. P. Ghislain, W. W. Webb, Scanning-force microscope based on an optical trap, Opt. Lett. **18**, 1678–1680 (1993) 153
20. K. Sasaki, Z. Shi, R. Kopelman, H. Masuhara, Three-dimensional pH microprobing with an optically-manipulated fluorescent particle, Chem. Lett., 141–142 (1996) 154
21. G. A. Valaskovic, M. Holton, G. H. Morrison, Biological near-field scanning optical microscopy – instrumentation and sample issues for shear-force feedback, Ultramicrosc. **57**, 212–218 (1995) 155
22. M. R. P. Moers, W. H. J. Kalle, A. G. T. Ruitter, J. C. A. G. Wiegant, A. K. Raap, J. Greve, B. G. Grooth, N. F. Van Hulst, Fluorescence in situ hybridization on human metaphase chromosomes detected by near-field scanning optical microscopy, J. Microsc. **182** 40–45 (1996) 155

Surface-Enhanced Infrared Absorption

Masatoshi Osawa

Catalysis Research Center, Hokkaido University
Sapporo 060-0811, Japan
`osawam@cat.hokudai.ac.jp`

Abstract. Molecules adsorbed on metal island films or particles exhibit 10–1000 times more intense infrared absorption than would be expected from conventional measurements without the metal. This effect is referred to as surface-enhanced infrared absorption (SEIRA) to emphasize the similarities with surface-enhanced Raman scattering (SERS). The electromagnetic interactions of the incident photon field with the metal and molecules play predominant roles in this effect. The chemical interactions of the molecules with the surface can give additional enhancement. The enhancement mechanisms and some applications of SEIRA.

1 Introduction

The optical properties of molecules are dramatically changed when they are adsorbed on rough metal surfaces, metal island films, or metal particles. The best-known example is surface-enhanced Raman scattering (SERS), in which the Raman scattering of molecules is enhanced by millions of times compared with free molecules [1,2,3,4]. A quite similar effect occurs in the mid-infrared region: molecules on metal surfaces show infrared absorption 10–1000 times more intense than would be expected from conventional measurements without the metal [5,6,7,8]. This effect is referred to as surface-enhanced infrared absorption (SEIRA) to emphasize the analogy to SERS.

Since the discovery of this effect in 1980 [5], a number of SEIRA spectra have been observed on various metals. The SEIRA effect is characterized as follows:

1. Enhanced spectra can be observed in the transmission [9,10], attenuated-total-reflection (ATR) [5,6,7], external-reflection [11], and diffuse-reflection modes [12]. In ATR and external-reflection measurements, the observed band intensities depend on the polarization and angle of incidence of the infrared radiation [11,13,14].
2. The enhancement depends greatly on the morphology of the metal surface [15]. Vacuum-evaporated [5,6,7] and electrochemically deposited [16,17,18,19] metal island films, and metal colloids [20,21] are good enhancers. In the case of island films, the largest enhancement is observed when the islands are densely crowded but not touching each other.
3. Both physisorbed and chemisorbed molecules exhibit enhancement. In general, chemisorbed molecules show a larger enhancement than physisorbed molecules.

S. Kawata (Ed.): Near-Field Optics and Surface Plasmon Polaritons,
Topics Appl. Phys. **81**, 163–187 (2001)

4. The enhancement is significant for the first monolayer directly attached to the surface and decays sharply within about 5 nm from the surface [10,22,23,24,25].
5. Vibrational modes that have dipole moment derivative components perpendicular to the surface are preferentially enhanced [26]. This surface selection rule is the same as that in the so-called infrared reflection absorption spectroscopy [27]. The molecular orientation can be determined by using the surface selection rule [28,29,30].
6. Metal island films that exhibit SEIRA have a very broad absorption extending from the visible to the mid-infrared, on which the enhanced absorption bands of the adsorbed molecules are superposed [10]. There exists a linear relationship between the absorption of the metal and the enhancement [10,15].

At least two different mechanisms, the electromagnetic (EM) and chemical mechanisms, are supposed to contribute to the total enhancement [10,31,32] as in the case of SERS [1,2,3,4]. The infrared absorption (A) may be written as

$$A \propto |\partial \boldsymbol{\mu}/\partial Q \cdot \boldsymbol{E}|^2 = |\partial \boldsymbol{\mu}/\partial Q|^2 |\boldsymbol{E}|^2 \cos^2 \theta \tag{1}$$

where $\partial \boldsymbol{\mu}/\partial Q$ is the derivative of the dipole moment with respect to a normal coordinate Q, $\boldsymbol{E}$ is the electric field that excites the molecule, and θ is the angle between $\partial \boldsymbol{\mu}/\partial Q$ and $\boldsymbol{E}$. It should be noted that the intensity of the electric field $|\boldsymbol{E}|^2$ at the surface is not the same as that of the incident photon field: a coupling of the incident photon field to the metal surface can enhance the field [1,2,3,4,33,34]. The EM mechanism assumes an increase of the local electric field at the surface [8,26,35]. The experimental evidence that the enhancement extends to several monolayers away from the surface provides a strong argument that a relatively short-ranged enhanced EM field (i.e. the near field) contributes to the SEIRA effect. On the other hand, the chemical mechanism assumes an increase of $|\partial \boldsymbol{\mu}/\partial Q|^2$ (i.e. the absorption coefficient) due to chemical interactions between the molecule and the metal surface. For example, CO chemisorbed on metal surfaces has an absorption coefficient 2–6 times larger than condensed CO (i.e. overlayers) [36,37,38]. Adsorbed molecules are often oriented in a specific direction with respect to the surface. Since the space average of $\cos^2 \theta$ is $1/3$ for randomly oriented molecules, the orientation effect gives an additional enhancement by a factor of three at maximum for vibrational modes that have dipole changes parallel to $\boldsymbol{E}$.

SEIRA spectroscopy (SEIRAS) is now appearing with a wide range of applications. Infrared spectroscopy has been established as a routine molecule-specific technique for qualitative and quantitative purposes. However, the relatively low absorption coefficients of molecules in the infrared region limit its use in many applications. Therefore, SEIRAS techniques that lower the detection limit of infrared spectroscopy are of great interest. Trace amount of molecules, ranging from picograms to nanograms [9,39,40], and very thin organic and bioorganic films, including Langmuir–Blodgett films and self-assembled monolayers (SAMs) [22,41,42,43,44,45] have been analyzed. SEIRAS can also be used for chemical sensing [18,45,46,47,48]. Since fine metal particles have high catalytic activity in many reactions, SEIRAS is very promising for catalysis research [16,17,19,49,50,51]. Surfaces of nonmetallic materials, such as polymers, semiconductors, glass, human skin, and agricultural products, can also be analyzed by this technique [11,52,53]. Among several applications, great success has been achieved in its application to dynamic studies of electrochemical interfaces [8,25,54,55,56,57,58].

2 Enhancement Mechanisms

2.1 Electromagnetic Mechanism

Vacuum-evaporated thin metal films are used most frequently for SEIRA experiments. Thin metal films that show strong SEIRA are not continuous but consist of metal islands smaller than the wavelength of light, as shown in Fig. 1. The sample shown here is a 10 nm thick (in mass thickness) Ag film on Si. The average dimension of the islands is about 30 nm. If the islands are modeled by ellipsoids of rotation, the aspect ratio of the islands (the ratio of the major to the minor diameter) ranges from 3 to 5. The density, shape, and size of the islands depend on the mass thickness, the evaporation conditions, and the chemical nature of the substrate [15]. As the mass thickness increases, the islands grow in size, contact each other, and eventually form a continuous film. Connection of the islands significantly reduces the enhancement, suggesting that the small metal islands play an important role in the enhancement.

The metal islands are polarized by the incident photon field through the excitation of collective electron resonance, or localized plasmon, modes, and the dipole p induced in an island generates a local EM field stronger than the incident photon field around the island [2,3,33,34], as illustrated in Fig. 2. A detailed theoretical treatment of the local EM field has been given in [33]. It

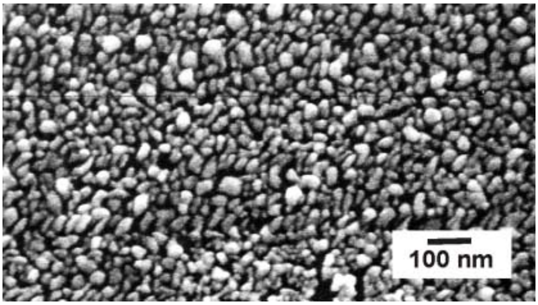

Fig. 1. SEM image of a 10 nm thick Ag film vacuum-evaporated on Si

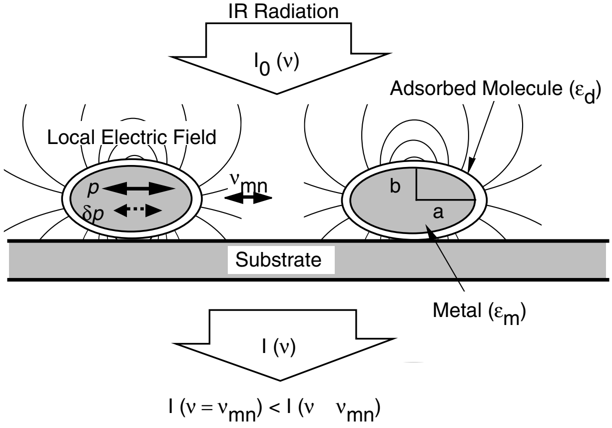

Fig. 2. Schematic representation of the electromagnetic mechanism of SEIRA on metal island films. See text for details. In simulations, the island film is modeled as a set of ellipsoids of rotation with a dielectric function ε_{m}, and the adsorbed molecules are modeled by a thin layer with a dielectric function ε_{d} covering the ellipsoids. The aspect ratio of the ellipsoids is defined as $\eta = a/b$

has been well established that the enhanced EM field strongly enhances the Raman scattering of adsorbed molecules. Figure 3 shows a set of transmission spectra of vacuum-evaporated Ag films on CaF_2 [10]. The strong band around 500 nm is attributed to the collective electron resonances of isolated Ag particles. As the mass thickness increases, the absorption band shifts to longer wavelengths and becomes broader owing to the dipole coupling between islands [59]. It is noteworthy that the tail of this absorption extends

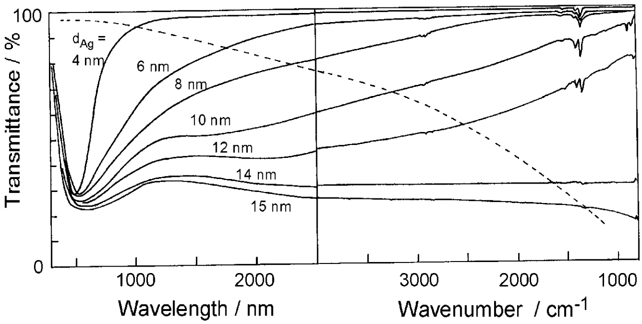

Fig. 3. Transmission spectra of Ag island films evaporated on CaF_2. The mass thickness of each film is shown in the figure. The peaks in the mid-infrared region are of p-nitrobenzoate adsorbed on the island films. The *dashed trace* is the spectrum of a 10 nm thick Ag film calculated from the Fresnel formula and the dielectric function of bulk Ag under the assumption that the film is continuous

well into the mid-infrared region. The observed spectra are very different from the spectrum shown by the dashed line, which was calculated using the dielectric function of bulk Ag and the Fresnel formula [60] under the assumption that the film is continuous. This result suggests that the collective electron resonance is excited even in the mid-infrared region and that the enhanced EM field enhances the infrared absorption of adsorbed molecules. A contribution of such EM effect to SEIRA was suggested also by the linear relationship between the enhanced band intensity and the average EM field intensity within the metal film [13,14].

The intensity of the enhanced EM field decays sharply as the distance from the surface (d) increases, as represented by the following equation [33,61]:

$$|E_{\text{local}}|^2 \propto \left(\frac{a}{a+b}\right)^6 , \tag{2}$$

where a is the local radius of curvature of the island. In addition, the local EM field is essentially polarized along the surface normal at every point on the surface of the islands [34] (Fig. 2). Therefore, this model is quite convenient for explaining the relatively short-ranged enhancement and the surface selection rule. However, the EM field enhancement theoretically estimated is only ten-fold or less in the mid-infrared region [10,43] owing to the large imaginary part of the dielectric constants of metals (i.e. the strong damping of localized plasmon modes). Therefore, the total enhancement of up to 1000 cannot be explained by this field enhancement only.

In the case of SERS on island films, the Raman-scattered light polarizes the metal islands and strong Raman scattered light is emitted from the dipoles induced in the metal islands [1,2,3,4,33]. A similar situation may be considered in SEIRA; that is, adsorbed molecules induce additional dipoles δP in the metal islands and perturbe the optical properties of the metal. Since the perturbation is larger at vibrational frequencies of the molecule than at other frequencies, the spectrum of the metal island film should be nearly identical to the spectrum of the molecule. The absorption coefficients of metal islands are smaller than those of the corresponding bulk metals in the infrared region, as revealed by infrared spectroscopic ellipsometric measurements [62], but are still larger than those of molecules. In addition, the volume of the metal in the island film is much larger than that of a monolayer adsorbate. Consequently, the vibrational spectrum of the adsorbate will be observed much more strongly than would be expected from conventional measurements without the metal. That is, a metal island is believed to function as an amplifier in SEIRA. The linear relationship between the band intensity of the adsorbed molecule and the background absorption of the metal can be understood with this assumption.

If the system is assumed to be a continuous composite film consisting of metal particles, adsorbed molecules, and voids (or host medium), the transmittance or reflectance of the composite film can be calculated easily by using the Fresnel equations [60]. The effective (i.e. space-averaged) dielectric function of the composite film can be connected with the polarization susceptibility (α) of the metal islands by using an effective-medium approximation (EMA) [63]. For the sake of simplicity, a metal island film is modeled as a set of ellipsoids of rotation with a uniform size, as shown in Fig. 2. The rotation axis is perpendicular to the surface. The molecules are assumed to cover the ellipsoid surfaces uniformly.

Among several models, the EMAs proposed by *Maxwell-Garnett* (MG) [64] and *Bruggemann* (BR) [65] are the best known. In the MG model, the effective dielectric function, $\varepsilon_{\mathrm{MG}}$, is connected with α by the following equation [63].

$$\varepsilon_{\mathrm{MG}} = \varepsilon_{\mathrm{h}} \left(\frac{3 + 2F\alpha}{3 - F\alpha} \right) , \tag{3}$$

where F is the filling factor of the metal within the composite layer and ε_{h} is the dielectric constant of the surrounding host medium. The value of α for an ellipsoid coated with molecules can be expressed as a function of the dielectric functions of the bulk metal (ε_{m}), the adsorbed molecule (ε_{d}), and the host as follows [66]:

$$\alpha_{\parallel,\perp} = \left\{ \frac{x}{y} \right\}_{\parallel,\perp} , \tag{4}$$

$$x = (\varepsilon_{\mathrm{d}} - \varepsilon_{\mathrm{h}})[\varepsilon_{\mathrm{m}} L_1 + \varepsilon_{\mathrm{d}}(1 - L_1)] + Q(\varepsilon_{\mathrm{m}} - \varepsilon_{\mathrm{d}})[\varepsilon_{\mathrm{d}}(1 - L_2) + \varepsilon_{\mathrm{h}} L_2] ,$$
$$y = [\varepsilon_{\mathrm{d}} L_2 + \varepsilon_{\mathrm{h}}(1 - L_2)][\varepsilon_{\mathrm{m}} L_1 + \varepsilon_{\mathrm{d}}(1 - L_1)] + Q(\varepsilon_{\mathrm{m}} - \varepsilon_{\mathrm{d}})(\varepsilon_{\mathrm{d}} - \varepsilon_{\mathrm{h}}) L_2 (1 - L_2),$$

where Q is the ratio of the volume of the core to the volume of the coated particle ($= V_1/V_2$), through which the size of the particle and the thickness of the adsorbed layer can be incorporated into the calculation. The depolarization factors of the core and the coated ellipsoid (L_1 and L_2, respectively) are solely a function of the aspect ratio of the ellipsoid η ($= a/b$; a and b are the radius along the major and minor axes of the ellipsoid, respectively) [67]. The subscripts $\parallel$ and $\perp$ refer to the cases where the applied electric field of the incident light is parallel ($\parallel$) and perpendicular ($\perp$), respectively, to the substrate surface.

The MG model includes weak interactions between the islands only through the Lorentz field and thus provides a good description for very thin island films in which the metal islands are well separated from each other. When the islands are densely packed (i.e. for thicker island films), dipole interactions between islands cannot be neglected. In such a case, the BR model provides a better approximation. In the BR model, the effective dielectric function is represented as [63]

$$\varepsilon_{\mathrm{BR}} = \varepsilon_{\mathrm{h}} \frac{3(1 - F) + F\alpha'}{3(1 - F) - 2F\alpha'} , \tag{5}$$

This model assumes that the metal islands are embedded in the effective medium [65]. Thus, α and ε_h in (5) must be replaced by α' and ε_BR, respectively, in this case.

Transmission spectra of a model molecule layer on 5 and 8 nm thick Ag island films simulated with both the MG and the BR models, are shown by the solid curves in Fig. 4 [26]. The thickness of the adsorbed molecular layer and the particle size ($2a$) were assumed to be 1 and 25 nm, respectively. The filling factors were taken from experimental data [68]. The dielectric function of Ag was calculated from the Drude model,

$$\varepsilon_\mathrm{m}(\omega) = 1 - \frac{\omega_\mathrm{p}^2}{\omega(\omega + \mathrm{i}/\tau)}\,, \tag{6}$$

where the plasma frequency ω_p equals $1.15 \times 10^{16}\ \mathrm{s}^{-1}$ and the relaxation time τ is 1×10^{-15} s for Ag [69]. The dielectric function of the adsorbed molecule was approximated by a damped harmonic dipole given by

$$\begin{aligned} \varepsilon_\mathrm{d}(\nu) &= \varepsilon'(\nu) + \varepsilon''(\nu)\,, \\ \varepsilon'(\nu) &= n_\infty^2 + \frac{B(\nu_0^2 - \nu^2)}{(\nu_0^2 - \nu^2)^2 + \gamma^2\nu^2}\,, \\ \varepsilon''(\nu) &= \frac{B\gamma\nu}{(\nu_0^2 - \nu^2)^2 + \gamma^2\nu^2}\,, \end{aligned} \tag{7}$$

where ν is the frequency in wavenumbers (cm^{-1}), n_∞ is the refractive index at a frequency far from the band center ν_0, and γ is the bandwidth. B is a constant related to the band intensity. These parameters were tentatively

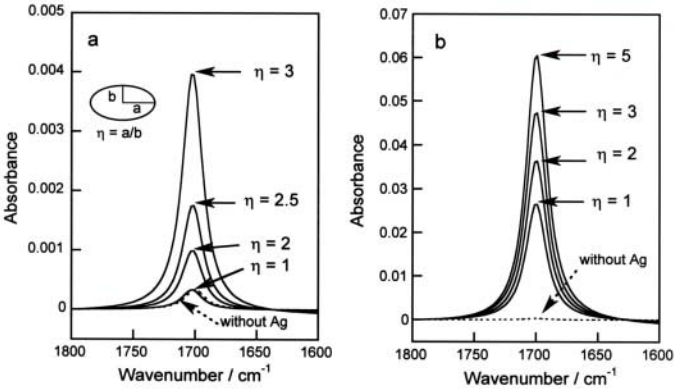

Fig. 4. SEIRA spectra of a model molecule adsorbed on Ag island films simulated by using the Maxwell-Garnett (**a**) and Bruggemann (**b**) effective-medium models. The mass thickness of the Ag film is 5 nm for (**a**) and 8 nm for (**b**). The *dashed trace* is the spectrum of a molecular layer on the substrate ($\mathrm{CaF_2}$) without a metal film. η represents the aspect ratio of the metal ellipsoid (Fig. 2). See text for details

assumed to be $n_\infty = 1.77$, $B = 30000\,\mathrm{cm}^{-2}$, $\nu_0 = 1700\,\mathrm{cm}^{-1}$, and $\gamma = 20\,\mathrm{cm}^{-1}$.

The dashed spectra in the figure correspond to a molecular layer formed directly on the substrate (CaF_2) without a metal film. The simulations clearly demonstrate that the molecular vibrations are observable very strongly in the presence of metal islands and that the enhancement depends on the shape of the islands (i.e. on η). For the 5 nm thick Ag film (Fig. 4a), the intensity for $\eta = 1$ (sphere) is as small as that without metal islands, but increases with η. For $\eta = 3$ (a typical value for vacuum-evaporated 5 nm thick Ag films), the enhancement factor, defined by the ratio of band intensities with and without a metal, is about 15. Larger enhancement factors are calculated with the BR model for the 8 nm thick Ag film (Fig. 4b). This factor reaches about 150 for $\eta = 3$. Such a large enhancement cannot be calculated if the MG model is used instead of the BR model, implying that interactions between metal islands play an important role in SEIRA. This result may be consistent with the fact that the tail of the collective electron resonance extends well into the mid-infrared region for thicker films owing to the dipole interactions between the islands (Fig. 3).

The enhancement factors calculated here are slightly smaller than the experimental values for the symmetric NO_2 stretching mode of p-nitrobenzoate adsorbed on Ag island films (about 50 and 500 at Ag thickness of 5 and 8 nm, respectively) [10]. Since this molecule is known to be oriented with the C_2 axis perpendicular to the surface, an enhancement factor of $(15\text{–}150) \times 3 = 45\text{–}450$ can be calculated for this mode by taking the orientation effect into account. This value is in reasonable agreement with the experiments.

The EM model can also simulate well some SEIRA spectra measured with the ATR and external-reflection geometries [11,70].

Despite the large simplification, the EM model explains well several characters intrinsic to SEIRA. The solid curve in Fig. 5 shows the band intensity of a model molecular layer calculated with the MG EMA as a functionof its thickness (d_mol) [35]. The intensity rises sharply as d_mol increases and then decreases slightly, whereas it increases linearly with d_mol on a metal-free substrate, as shown by the dashed line (the Lambert–Beer law). The result clearly demonstrates that the enhancement is a short-range effect limited to a few nanometers away from the surface. It should be noted that the EM simulation can be applied only to small d_mol values, because the voids between metal islands are completely filled with molecules at a certain d_mol and further deposited molecules form an overlayer on the composite layer. Hence, the experimentally observable curve of intensity versus d_mol should be the sum of the solid curve and the dashed line. The simulation is in good agreement with several experiments [10,22,23,24,25].

SERS, which is observed in the visible and near-infrared regions, is significant on free-electron metals (Au, Ag, and Cu) but is hardly observable on transition metals owing to the strong damping of plasmon modes (i.e. the

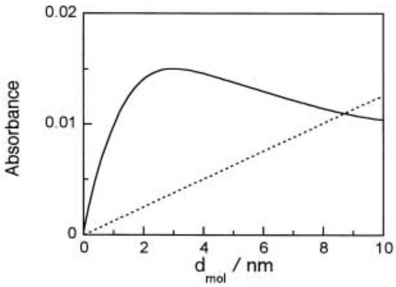

Fig. 5. Simulated peak intensity of a model molecule on a 5 nm thick Au island film plotted as a function of the thickness of the molecular layer, d_{mol}. The *dashed line* is the result without the metal film. The experimentally observable dependence of the band intensity on d_{mol} represented by the sum of the two components shown

large imaginary part of the dielectric constant) [1,2,3]. In contrast, the EM calculations predict an enhancement of infrared absorption on transition metals as strong as that on coinage metals [26]. In fact, several recent experiments have demonstrated the SEIRA effect on many other metals such as Pt, Pd, Rh, Ru, Ir, Sn, Fe, In, Pb, and Pt–Fe alloys [16,17,19,32,49,50,70,71,72,73]. Since the dielectric constants of these metals do not differ greatly from those of coinage metals in the infrared region, these results may be a reasonable consequence.

Asymmetric and bipolar (i.e. derivative-like) band shapes are often observed in SEIRA spectra [19,32,49]. In some cases, molecular vibrations are observed as negative absorption peaks, i.e. as reflectance maxima [16,17,19]. Very recently, it has been demonstrated that such spectral features can be simulated with the an EM calculation using the Bergman EMA [19].

2.2 Chemical Mechanisms

Molecules chemisorbed on a metal surface show a larger enhancement than do physisorbed molecules, suggesting some chemical effect between the molecule and the surface. It is known that the absorption coefficients of chemisorbed molecules are larger than those of condensed overlayers [38]. Interactions between adsorbed molecules also affect the intensity [36,37]. Some theories predict that charge oscillations between molecular orbitals and the metal surface enlarge the absorption coefficients of adsorbates by ‘intensity borrowing’ from the charge-oscillations [36,37,74]. There exist some experimental results that seem to support such chemical mechanism [32,75,76]. For example, CO adsorbed on Fe island films evaporated on MgO(001) shows a very asymmetric SEIRA band [32]. An enhancement factor of about 100 was estimated for this system. The band shape and enhancement were theoretically explained by assuming a Fano-type resonance of the molecular vibration with electronic transitions between the metal and the adsorbate [32]. The simulation agrees quite well with the observed spectra and the enhancement factor of 100 was ascribed to the chemical origin. Nevertheless, it should be noted that the asymmetric band shape can be explained also by an EM mechanism [19] as described previously. In addition, the chemical enhancement factor of 100 is one order of magnitude larger than that observed for CO on bulk metal surfaces (where the factor is less than 10). Although the difference in the electronic conditions between the island metal surface and the bulk metal surface might have a strong effect on the enhancement, the details are still unclear. Further theoretical and experimental studies of the chemical mechanism are necessary.

3 Electrochemical Dynamics Monitored by SEIRAS

Recent research in electrochemistry has increasingly involved the use of surface-sensitive analytical techniques in combination with conventional electrochemical techniques. The chief reason for this development is that electrochemical techniques inevitably measure the sum of all surface processes. The results primarily provide kinetic information, and no direct molecular information on the species involved in the reactions can be obtained. SEIRAS has been applied very successfully to examine molecular events occurring at the electrochemical interface. The achievements before 1997 have been reviewed in [8]. In this section, the basic aspects of this technique are summarized first and then some recent developments are described.

3.1 Experimental Technique

So far, the so-called infrared reflection absorption spectroscopy (IR-RAS) technique (Fig. 6a) has been used for in situ infrared studies of the electrochemical interface [77]. P-polarized infrared radiation passing through the solution phase is reflected at the electrode surface at a high incidence angle. The working electrode is pushed against an infrared-transparent cell window to reduce the strong absorption of the electrolyte solution. The thickness of the solution layer between the electrode and the window is typically 1–10 µm. An advantage of this technique is that well-defined single-crystals can be used as working electrodes, as well as poly-crystals. However, this technique has two serious problems when it is used for dynamic studies. One is that the thin-layer structure of the cell prevents mass transportation between the thin-layer and the reservoir, and the system does not respond quickly to changes of the externally applied potential owing to the large solution resistance. Hence, this technique can be used only under static or quasi-static conditions. The other is the interference from the bulk solution. Although the solution layer is very thin, it is still much thicker than a monolayer on the electrode. Thus the signal from the adsorbate is superposed on the solution background, which is about three orders of magnitude stronger. The

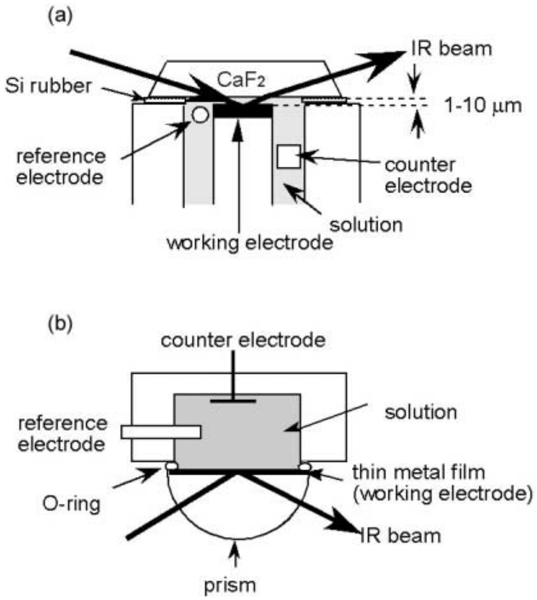

Fig. 6. In situ monitoring of the electrochemical interface with IR-RAS (**a**) and ATR-SEIRAS (**b**)

solution background can be removed to a large extent by measuring potential difference spectra [77], but its complete subtraction is very difficult.

These problems intrinsic to IR-RAS can be removed by using the ATR configuration illustrated in Fig. 6b. A thin metal film deposited on a prism (Si, Ge, or ZnSe) is used as the working electrode. The infrared radiation passed through the prism is totally reflected at the electrode/electrolyte interface. Since the evanescent wave penetrates only a few hundred nanometers into the solution phase [78], it is not necessary for the solution phase to be thin and further the solution background can be significantly reduced compared with that in IR-RAS. On the contrary, the absorption of species adsorbed on the electrode surface is enhanced by the SEIRA effect. Consequently, the signals from the adsorbate and solution are comparable in this configuration, which facilitates the complete subtraction of the solution background [70].

The details of the experimental setup and procedures have been described in [70,79]. Although the electrodes used in ATR-SEIRAS must be island films, relatively thick (15–20 nm) island films prepared by vacuum evaporation have a conductivity good enough for electrochemistry. It should be noted that slow deposition of the metal is crucial in preparing SEIRA-active thin-film electrodes by vacuum evaporation [15]. Evaporated metal films are generally polycrystalline, except for Au. The Au surface has a tendency such that facets with (111) crystallographic orientation preferentially appear on the surface when it is evaporated very slowly. A short (about 10 s) annealing of the film with a hydrogen–oxygen flame accelerates the recrystallization of the surface toward the (111) orientation [80]. A prolonged annealing of the film generally reduces the enhancement. The electrodes are used after cleaning their surface in the solution by repeated potential sweeps between the surface oxidation and hydrogen evolution potentials. Oxidation–reduction cycles in solutions containing halogen ions, which are very often used for observing SERS [1,3], are not recommended, to avoid complex electrochemistry. The surface can be kept clean for several hours if ultrapure water and chemicals are used.

3.2 Comparison of ATR-SEIRAS and IR-RAS

The ATR-SEIRAS technique has been applied very successfully to several electrochemical systems [8,28,29,30,49,50,56,57,58,80,81,82,83]. To highlight the difference between IR-RAS and ATR-SEIRAS, infrared spectra of pyridine adsorbed on Au electrodes measured with the two techniques [28,84] are compared in Fig. 8. The electrode used in the IR-RAS measurements was an Au(111) single-crystal, whereas in the ATR-SEIRAS measurement it was a vacuum-evaporated preferentially (111)-oriented 20 nm thick Au film. The infrared reflection absorption (IR-RA) spectra are represented by the relative reflectance change, defined as $\Delta R/R = (R_{\text{sample}} - R_{\text{ref}})/R_{\text{ref}}$, where R_{sample} and R_{ref} are the reflectivities of the electrode at the sample and reference potentials, respectively. On the other hand, the ATR spectra are represented in absorbance units, defined by $A = -\log(R_{\text{sample}}/R_{\text{ref}})$. In both measurements, the reference potential was –0.75 V versus a saturated calomel electrode (SCE), at which potential the molecule is totally desorbed from the surface. Therefore, the adsorbate on the electrodes gives down-going bands in the IR-RA spectra and up-going bands in the SEIRA spectra.

Several adsorbate bands are clearly identifiable in both sets of spectra, but the band intensities in the ATR spectra are about 20 times greater than those in the IR-RA spectra. Note that $\Delta R/R = 0.0005$ corresponds to 0.0002 absorbance units. Of course, the difference in surface area between the single-crystal and island film electrodes contributes to the different intensities. However, the roughness factor of the island film, estimated by electrochemical techniques, was only about 2.5. Considering that IR-RAS has a sensitivity over 10 times higher than transmission spectroscopy [27], an enhancement factor of about 100 or more is estimated for the evaporated Au electrode.

The IR-RA spectrum is characterized by a strong up-going band at 1445 cm^{-1}. Since the adsorption of the molecule onto the electrode surface reduces its concentration in the thin solution layer, the up-going band is ascribed to pyridine in the solution. Pyridine in the solution has another strong band at 1594 cm^{-1}, which deforms the spectral features around 1600 cm^{-1}. The down-going band at 1601 cm^{-1} is a ghost produced by the superposition of the up-going solution band at 1594 cm^{-1} and down-going band of adsorbed pyridine at 1593 cm^{-1}.

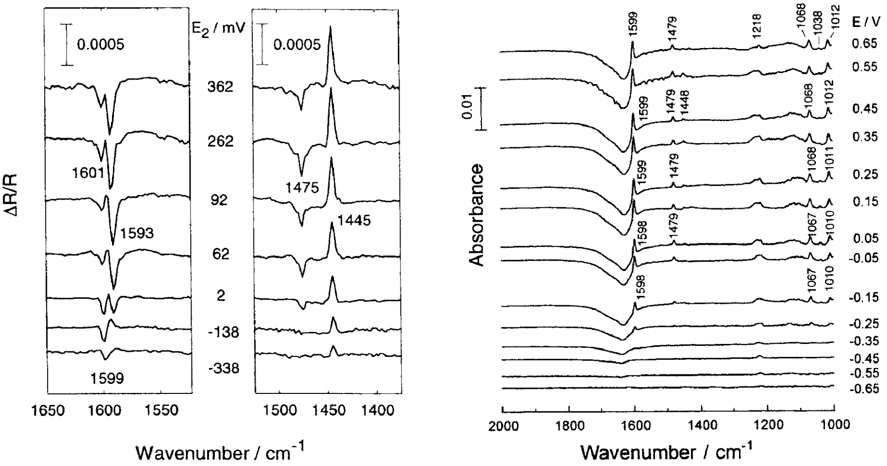

(a) (b)

Fig. 7. IR-RA and ATR-SEIRA spectra of pyridine adsorbed on an Au(111) single-crystal electrode (**a**) [84] and on a vacuum-evaporated (111)-oriented 20 nm thick Au film electrode (**b**) [29], respectively. Solutions: (**a**) 0.1 M $KClO_4$ + 3 mM pyridine, (**b**) 0.1 M $NaClO_4$ + 1 mM pyridine. The Reference potential was 0.75 V versus SCE in both measurements

The ATR-SEIRAS technique is free from this problem and only the vibrational modes of adsorbed pyridine are observed owing to its higher surface-sensitivity. Even the very weak band at 1448 cm^{-1} located very close to the solution band can be identified. In the SEIRA spectrum, a very broad negative-going band, assignable to the bending mode of water, is observed at 1620 cm^{-1}, which is not seen in the IR-RA spectrum because D_2O was used as the solvent to avoid strong interference from the solution. This band decreases in intensity with increasing potential, concomitantly with the growth of the pyridine bands. Thus, this band can be ascribed to water molecules that were removed from the interface by pyridine adsorption. This explanation is supported by the considerably lower frequency of this band than that of bulk water (1645 cm^{-1}) [79,81]. The observation of water molecules at the interface also demonstrates the high surface-sensitivity of this technique.

In summary, the ATR-SEIRAS technique is useful for observing only the interface without interference from the solution. On the other hand, IR-RAS can provides information on molecules both at the interface and in the bulk solution, although the superposition of the bands of both species often makes the spectral analysis difficult except in cases where the spectrum of the adsorbate is greatly changed by adsorption.

When solution bands are well separated from adsorbate bands, they can be used for semi-quantitative estimation of the amount of molecules adsorbed on the surface [84]. The intensity of the 1445 cm^{-1} band in Fig. 7a was shown to be proportional to the Gibbs surface excess (Γ) of pyridine determined by chronocoulometry.

On the other hand, the intensities of adsorbate bands are usually not proportional to the surface coverage, as shown in Fig. 8. The intensity of the 1597 cm^{-1} band in Fig. 7b (circles in Fig. 8) does not track the Γ versus potential curve (solid line) [85]. Although pyridine adsorption occurs at potentials more positive than −0.7 V, this band is observed at potentials more positive than −0.4 V, where Γ reaches a plateau. On the basis of the surface selection rule, the result is interpreted as showing that the pyridine ring is parallel to the surface at negative potentials and rises up as the potential increases. This potential-dependent reorientation of pyridine deduced by SEIRAS has been confirmed by in situ scanning tunneling microscopy [28].

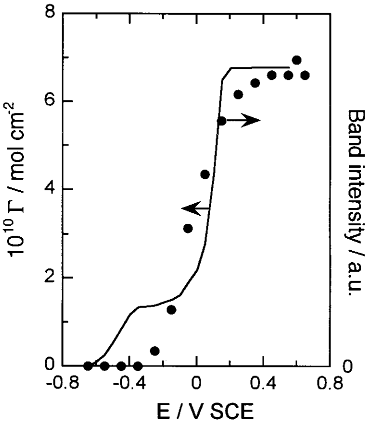

Fig. 8. The intensity of the 1599 cm^{-1} band in Fig. 7b plotted as a function of the potential (*circles*). The solid line represents the Gibbs surface excess (Γ) of pyridine measured as a function of the applied potential, which was taken from [85]

3.3 Time-Resolved Monitoring of Electrode Dynamics

Since the signal-to-noise ratio of a spectrum is proportional to the square root of the number of interferograms added together (in the case of FT-IR spectroscopy), one will recognize immediately that the high sensitivity of ATR-SEIRAS facilitates real-time or time-resolved monitoring of dynamic processes at the interface. The quick response of the electrochemical cell in the ATR configuration is also quite convenient for such measurements. In general, a signal-to-noise ratio good enough for detailed analysis of monolayer adsorbates can be obtained by adding fewer than 50 interferograms, which requires acquisition times of less than 10 s for most FT-IR spectrometers. For strongly absorbing molecules, high-quality spectra can be obtained without addition of interferograms. The short acquisition time enables us to accumulate a series of spectra successively under potential-sweep conditions together with electrochemical data. If the reactions to be investigated are reversible or repeatable, they can be monitored with microsecond time-resolution by using a step–scan FT-IR technique [54,56,58]. By applying two-dimensional correlation analysis (i.e. the so-called 2D-IR analysis) to a series of time-resolved spectra, detailed information on the reactions and dynamics that is not readily accessible with conventional one-dimensional spectra can be extracted [55,81].

A comparison of spectral and electrochemical data is quite important for obtaining deeper insights into electrochemistry [25,28,29,56,58,82]. As an example, a time-resolved SEIRA study of underpotential deposition of Cu on an Au(111) surface is shown in Fig. 9 [58]. Underpotential deposition is a phenomenon in which a monolayer or submonolayer amount of metal atoms is adsorbed on the surfaces of a different metal at a potential more positive than the equilibrium potentials. The inset in Fig. 9a shows a typical cyclic voltammogram for an Au(111) electrode in 0.1 M H_2SO_4 containing 1 mM

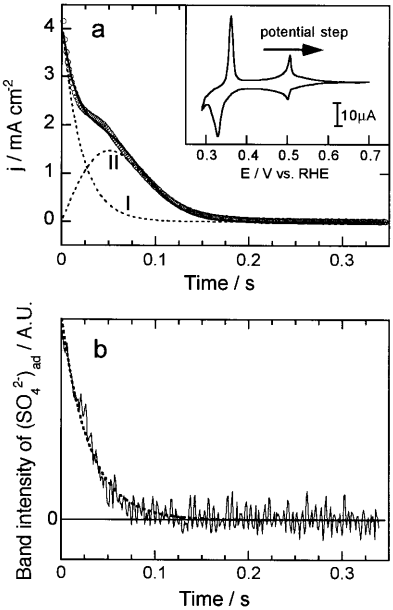

Fig. 9. (**a**) Current transient for a potential step from 0.45 to 0.6 V at an Au(111) electrode in 0.1 M H_2SO_4 containing 1 mM $CuSO_4$, and (**b**) the simultaneously measured transient of the band intensity of sulfate adsorbed on the electrode. The infrared data were taken from a series of ATR-SEIRA spectra measured with a 1 ms time-resolution. The *inset* shows a cyclic voltammogram recorded at a scan rate of $2\,\mathrm{mVs^{-1}}$

$CuSO_4$. Adsorption and desorption of Cu adatoms and sulfate ions provides the current flow. The sharp cathodic peaks at 0.5 and 0.33 V correspond to the formation of well-ordered phases. The two anodic peaks correspond to the reverse processes. The ordered phase formed in the potential range between 0.4 and 0.5 V is called the honeycomb $(\sqrt{3} \times \sqrt{3})$ phase, in which two-thirds of a monolayer (ML) amount of Cu adatoms are arranged in a honeycomb structure and one-third of a monolayer ML amount of sulfate anions are coadsorbed in the center of the honeycomb (see Fig. 10).

Figure 9a shows the current transient for the dissolution of the honeycomb $(\sqrt{3}\times\sqrt{3})$ phase triggered by a potential step from 0.45 to 0.6 V. The transient curve can be simulated by a combination of two kinetic terms as follows:

$$j(t) = k_1 \exp(-k_2 t) + k_3 t \exp(-k_4 t^2)\,. \tag{8}$$

The first term (curve I) corresponds to a Langmuir (i.e. random) process, and the second term (curve II) to a nucleation-and-growth process. The time constants k_2 and k_4 are 49 s^{-1} and 193 s^{-2}, respectively. This simulation indicates that the dissolution of the honeycomb $(\sqrt{3}\times\sqrt{3})$ phase takes place via two different successive processes, but conventional electrochemical measurements do not provide any detailed molecular information on these processes. Figure 9b represents the corresponding transient of the band intensity of coadsorbing sulfate, which was taken from a series of SEIRA spectra measured with a time-resolution of 1 ms. This transient can be simulated with a

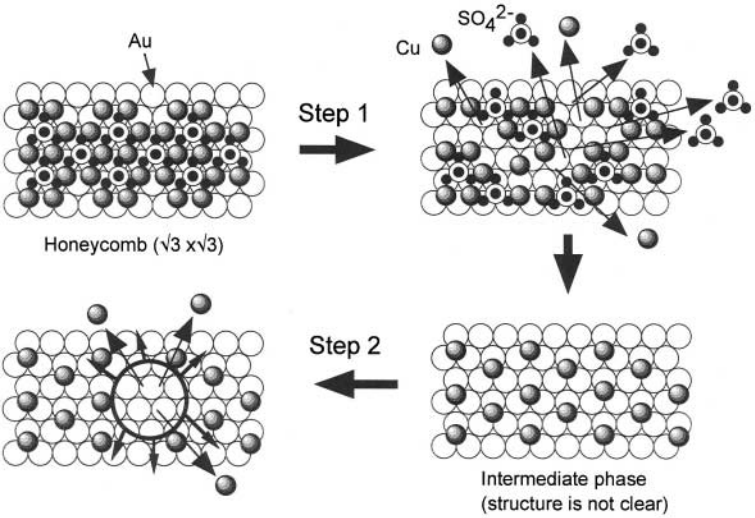

Fig. 10. Schematic representation of the dissolution dynamics of the honeycomb $(\sqrt{3} \times \sqrt{3})$ phase on an Au(111) electrode surface deduced from the data shown in Fig. 9. One half of the Cu adatoms and all sulfate ions are desorbed in step 1 with Langmuir kinetics. The remaining half of the Cu adatoms are desorbed in step 2 with nucleation-and-growth kinetics

single Langmuir term with a rate constant of 35 s^{-1}, which is nearly identical to that of the first process found in the current transient. The results indicate that sulfate ions are totally desorbed from the surface in the initial process and that the subsequent process involves desorption of Cu adatoms only. By integrating curves I and II in Fig. 9a, the charge densities passing during the first and second processes have been measured to be 85 and 125 μC cm^{-2}, respectively. A charge density of 125 μC cm^{-2} corresponds to that required for desorption of 1/3 ML of Cu adatoms (one-half of the Cu adatoms in the honeycomb phase). Accordingly, it is concluded that 1/3 ML of Cu and all sulfate ions are desorbed in the initial process, and then the remaining 1/3 ML of Cu adatoms is desorbed in the subsequent process. The smaller charge density of 85 μC cm^{-2} for the initial process is accounted by the superposition of a negative charge of 40 μC cm^{-2} required for desorption of the sulfate. The processes are schematically represented in Fig. 10.

3.4 A New Approach to Electrode Dynamics

When the electrode potential is changed, current flows across the interface to charge-up the double-layer. The time-constant for the double-layer charging is typically a few milliseconds for electrodes of ordinary size (millimeter to centimeter in diameter). Owing to the interference from the double-layer charging current, reactions that have time-constants equivalent to or smaller than that of the double-layer charging cannot be examined by conventional electrochemical techniques. Fortunately, spectroscopic measurements are not interfered with by the double-layer charging. Molecular absorption/desorption at electrodes within the time-region of the double-layer charging has been investigated by ATR-SEIRAS with a 100 μs time-resolution [56]. The change of the actual potential across the interface during the double-layer charging has also been measured from spectral changes of a SAM of 4-mercaptopyridine on Au [57].

Since electrochemical reactions are limited by double-layer charging, diffusion, and several other slow processes, it is impossible to determine rate constants of faster processes by any time-domain approaches. To overcome this limitation, measurements in the frequency domain are often used in electrochemistry. In ac impedance spectroscopy, for example, the potential is modulated and the phase shift of the corresponding current flow with respect to the modulation is measured, from which kinetic parameters can be obtained. However, reactions with rate constants larger than $\sim 10^3 s^{-1}$ cannot be measured even with this method, owing to the double-layer charging. Since spectroscopic measurements are not interfered with by the double-layer charging, very fast processes should be accessible if electrochemical measurements are replaced by spectroscopic measurements. This idea has been realized in the UV–visible region [86]. Unfortunately, the molecular specificity of UV–visible spectroscopy is not high enough. The use of FT-IR spectroscopy has also been examined for this purpose [87,88]. However, the relatively low sensitivity of infrared spectroscopy, the thin-layer structure of the electrochemical cell, and some other technical problems have prevented its practical use. Very recently, these problems were removed by coupling potential-modulated FT-IR with ATR-SEIRAS [57].

A block diagram of the experimental setup used for potential-modulated FT-IR spectroscopy is shown in Fig. 11. The electrode potential is modulated with a sinusoidal wave generated by a waveform generator, and the in-phase and quadrature (90° out-of-phase) components of the modulated IR signal are analyzed with a lock-in-amplifier. The dc component of the signal is used as the reference. The crosstalk between Fourier frequencies and the potential modulation frequency can be removed by the use of a step–scan FT-IR spectrometer.

Typical potential-modulated spectra for a 4-mercaptopyridine SAM on an Au electrode are shown in Fig. 12. The solid and dashed curves correspond to the in-phase and quadrature spectra, respectively. The bipolar band around 1470 cm^{-1} implies a shift of the vibrational frequency with potential. On the other hand, the 1618 cm^{-1} band changes only in its intensity. The peak intensities of the 1618 cm^{-1} band in the in-phase and quadrature spectra measured at modulation frequencies ranging from 41 Hz to 50 kHz form a semicircle in the complex plot (Cole–Cole plot), as in the Cole–Cole plots of ac impedance. A theoretical analysis of the infrared data revealed that the spectral changes occur at a rate of $\sim 5 \times 10^5 \mathrm{s}^{-1}$, which is much larger than the time constant of the double-layer charging ($1.9 \times 10^3 \mathrm{s}^{-1}$) [57].

Potential-dependent spectral changes, as shown in Fig. 12, are observed for many molecules adsorbed on electrode surfaces. Two mechanisms have been proposed for CO, the Stark-tuning and back-donation models [77]. The Stark-tuning model predicts that the change of the electric field across the double-layer changes the vibrational properties of the adsorbate. The back-donation model predicts that the change in the potential (that is, the Fermi

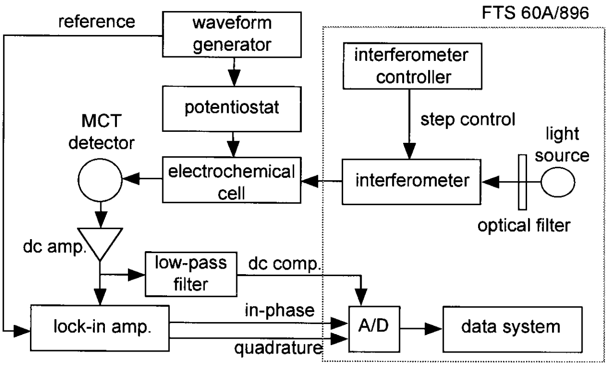

Fig. 11. Experimental setup for potential-modulated FT-IR spectroscopy

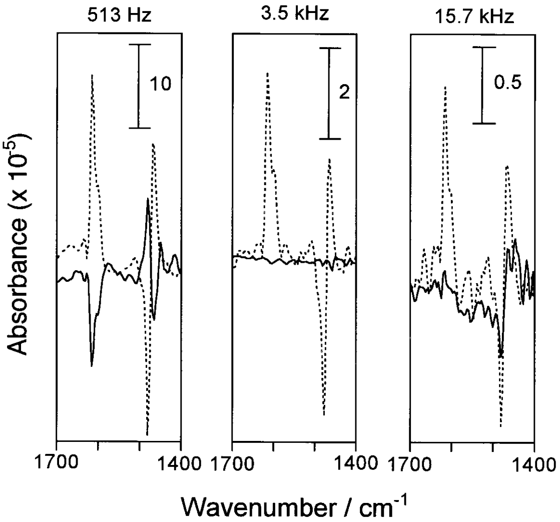

Fig. 12. In-phase (*solid lines*) and quadrature (*dashed lines*) spectra of a 4-mercaptopyridine self-assembled monolayer on an Au thin-film electrode in 0.1 M $HClO_4$ measured by potential-modulated FT-IR spectroscopy at the modulation frequencies indicated in the figure

level of the electrode surface) changes the amount of charge back-donated from the metal to the $2\pi^*$ orbital of CO, resulting in the spectral changes. If the Stark-tuning effect is dominant, the rate of the spectral changes should be the same as that of the double-layer charging (i.e. of the actual potential change at the interface). If this is not the case, the rate may be different (presumably, much faster). In the case of 4-mercaptopyridine, the rate of the spectral changes is much faster than that of the double-layer charging, indicating that the charge-transfer mechanism rather than the Stark-tuning mechanism contributes to the spectral changes.

4 Summary and Remarks

In summary, SEIRA is a phenomenon similar to SERS and is characterized by a 10–1000 times enhancement of the infrared absorption of molecules adsorbed on metal island films or small metal particles. The local electric field around the metal islands produced by the coupling of the incident photon field with the metal excites an adsorbed molecule. The excited molecule perturbs the optical properties of the metal, and the molecular vibrations are observed through a change of the transmittance or reflectance of the island film. Since the absorption coefficient and volume fraction of the metal are larger than those of the molecules, the molecular vibrations can be observed more strongly than would be expected from conventional measurements without the metal. Molecular vibrations that change the dipole moment along the surface normal are selectively enhanced. Preferential orientation of the molecules on the surface provides an additional enhancement by a factor of three at maximum. Chemical interactions of molecules with the surface can give additional enhancement, but the details are still unclear. Among several applications, SEIRAS has been applied most successfully to electrochemical systems. Thanks to developments in FT-IR instrumentation and data analysis techniques such as 2D-IR, SEIRAS has enabled us to study electrode dynamics that is not readily accessible by conventional electrochemical techniques.

Despite twenty years of history, SEIRA has received less attention than SERS. This is probably due to the smaller enhancement factor of SEIRA. However, infrared spectroscopy basically has a higher sensitivity than Raman spectroscopy, and hence the sensitivities of SEIRAS and SERS are comparable. It is emphasized that SEIRAS and SERS are not competitive but are supplementary to one other, as in the case of normal infrared and Raman spectroscopy. A comparison of SEIRA and SERS spectra is very helpful for detailed analysis of both spectra [42,44,72]. The use of SEIRAS in tandem with other analytical techniques will also be very fruitful for surface chemistry and surface electrochemistry, as described in Sect. 3.2. In electrochemistry, the combined use of SEIRAS and STM is becoming popular [28,29,30,83,89].

References

1. R. K. Chang , T. E. Furtak, *Surface Enhanced Raman Scattering* (Plenum, New York 1982) 163, 164, 167, 171, 174
2. H. Metiu, Surface Enhanced Spectroscopy, Prog. Surf. Sci. **17**, 153-320 (1984) 163, 164, 165, 167, 171
3. M. Moskovits, Surface-enhanced spectroscopy, Rev. Mod. Phys. **57**, 783–826 (1985) 163, 164, 165, 167, 171, 174
4. A. Otto, I. Mrozeck, H. Grabhorn, W. Akemann, Surface-enhanced Raman scattering, J. Phys. Condens. Matter **4**, 1143–1212 (1992) 163, 164, 167
5. A. Hartstein, J. R. Kirtley, J. C. Tsang, Enhancement in the infrared absorption from molecular monolayers with thin metal overlayers, Phys. Rev. Lett. **45**, 201–204 (1980) 163
6. A. Hatta, T. Ohshima, W. Suëtaka, Observation of the enhanced infrared absorption of p-nitrobenzoate on Ag island films with an ATR technique, J. Appl. Phys. A **29**, 71–75 (1982) 163
7. A. Hatta, Y. Suzuki, W. Suëtaka, Infrared absorption enhancement of monolayer species on thin evaporated Ag films by use of a Kretschmann configuration, Evidence for two types of enhanced surface electric fields, Appl. Phys. A **35**, 135–140 (1984) 163
8. M. Osawa, Dynamic processes in electrochemical reactions studied by surface-enhanced infrared absorption spectroscopy (SEIRAS), Bull. Chem. Soc. Jpn. **70**, 2861–2880 (1997) 163, 164, 165, 172, 174

9. Y. Nishikawa, K. Fujiwara, T. Shima, A Study of the qualitative and quantitative analysis of nanogram samples by transmission infrared spectroscopy with the use of silver island films, Appl. Spectrosc. **45**, 747–751 (1991) 163, 164
10. M. Osawa, M. Ikeda, Surface-enhanced infrared absorption of p-nitrobenzoic acid deposited on silver island films: contribution of electromagnetic and chemical mechanisms, J. Phys. Chem. **95**, 9914–9919 (1991) 163, 164, 166, 167, 170
11. Y. Nishikawa, K. Fujiwara, K. Ataka, M. Osawa, Surface-enhanced external reflection spectroscopy at low reflective surfaces and its application to surface analysis of semiconductors, glasses, and polymers, Anal. Chem. **65**, 556–562 (1993) 163, 165, 170
12. S. J. Lee, K. Kim, Diffuse reflectance infrared spectra of stearic acid self–assembled on fine silver particles, Vib. Spectrosc. **18**, 187–201 (1998) 163
13. M. Osawa, M. Kuramitsu, A. Hatta, W. Suëtaka, H. Seki, Electromagnetic effect in enhanced infrared absorption of adsorbed molecules on thin metal films, Surf. Sci. Lett. **175**, L787–L793 (1986) 163, 167
14. Y. Suzuki, M. Osawa, A. Hatta, W. Suëtaka, Mechanism of absorption enhancement in infrared ATR spectra observed in the Kretschmann configuration, Appl. Surf. Sci. **33/34**, 875–881 (1988) 163, 167
15. Y. Nishikawa, T. Nagasawa, K. Fujiwara, M. Osawa, Silver island films for surface-enhanced infrared absorption spectroscopy: effect of island morphology on the absorption enhancement, Vib. Spectrosc. **6**, 43–53 (1993) 163, 164, 165, 173
16. G.-Q. Lu, S.-G. Sun, S. P. Chen, L.-R. Cai, Novel properties of dispersed Pt and Pd thin layers supported on GC for CO adsorption studied using in situ MS–FTIR reflection spectroscopy, J. Electroanal. Chem. **421**, 19–23 (1997) 163, 165, 171
17. G.-Q. Lu, S.-G. Sun, L.-R. Cai, S.-P. Chen, Z.-W. Tian, In situ FTIR spectroscopic studies of adsorption of CO, SCN–, and poly(o–phenylenediamine) on electrodes of nanometer thin films of Pt, Pd, and Rh: Abnormal infrared effects (AIREs), Langmuir **16**, 778–786 (2000) 163, 165, 171
18. H. D. Wanzenböck, B. Mizaikoff, N. Weissenbacher, R. Kellner, Surface enhanced infrared absorption spectroscopy (SEIRA) using external reflection on low-cost substrates, Fresenius J. Anal. Chem. **362**, 15–20 (1998) 163, 165
19. A. E. Bjerke, P. R. Griffiths, W. Theiss, Surface-enhanced infrared absorption of CO on platinized platinum, Anal. Chem. **71**, 1967–1974 (1999) 163, 165, 171, 172
20. S. Y. Kang, I. C. Jeon, K. Kim, Infrared absorption enhancement at silver colloidal particles, Appl. Spectrosc. **52**, 278–283 (1998) 163
21. J. A. Seelenbinder, C. W. Brown, P. Pivarnik, A. G. Rand, Colloidal gold filtrates as a metal substrates for surface-enhanced infrared absorption spectroscopy, Anal. Chem. **71**, 1963–1966 (1999) 163
22. T. Kamata, A. Kato, J. Umemura, T. Takenaka, Intensity enhancement of infrared attenuated total reflection spectra of stearic acid Langmuir–Blodgett monolayers with evaporated silver island films, Langmuir **3**, 1150–1154 (1987) 164, 165, 170
23. A. Hatta, N. Suzuki, Y. Suzuki, W. Suëtaka, Infrared absorption of polycyanoacrylate enhanced by Ag island films in the Kretschmann's ATR geometry, The coverage dependence, Appl. Surf. Sci. **37**, 299–305 (1989) 164, 170

24. E. Johnson, R. Aroca, Surface-enhanced infrared spectroscopy of monolayers, J. Phys. Chem. **99**, 9325–9330 (1995) 164, 170
25. M. Osawa, K. Yoshii, In situ and real–time surface-enhanced infrared study of electrochemical reactions, Appl. Spectrosc. **51**, 512–518 (1997) 164, 165, 170, 177
26. M. Osawa, K. Ataka, K. Yoshii, Y. Nishikawa, Surface-enhanced infrared spectroscopy: the origin of the absorption enhancement and band selection rule in the infrared spectra of molecules adsorbed on fine metal particles, Appl. Spectrosc. **47**, 1497–1502 (1993) 164, 169, 171
27. F. M. Hoffmann, Infrared reflection-absorption spectroscopy of adsorbed molecules, Surf. Sci. Rep. **3**, 107-192 (1983) 164, 174
28. W.-B. Cai, L.-J. Wan, H. Noda, Y. Hibino, K. Ataka, M. Osawa, Orientational phase transition in a pyridine adlayer on gold(111), Langmuir **14**, 6992–6998 (1998) 164, 174, 176, 177, 182
29. H. Noda, T. Minoha, L.-J. Wan, M. Osawa, Adsorption and ordered phase formation of 2,2'-bypyridine on Au(111): a combined surface-enhanced infrared and STM study, J. Electroanal. Chem. **481**, 62–68 (2000) 164, 174, 175, 177, 182
30. L.-J. Wan, M. Terashima, H. Noda, M. Osawa, Molecular orientation and ordered structure of benzenethiol adsorbed on gold(111), J. Phys. Chem. B **104**, 3563–3569 (2000) 164, 174, 182
31. G. T. Merklin, P. R. Griffith, Influence of chemical interactions on the surface-enhanced infrared absorption spectrometry of nitrophenols on copper and silver films, Langmuir **13**, 6159–6163 (1997) 164
32. O. Krauth, G. Fahsold, A. Pucci, Asymmetric line shapes and surface enhanced infrared absorption of CO adsorbed on thin Fe films on MgO(001), J. Chem. Phys. **110**, 3113–3117 (1999) 164, 171
33. A. Wakaun, Surface-enhanced electromagnetic processes, in *Solid State Physics*, H. Ehrenreich, D. Turnbull (Eds.) (Academic, New York, 1984) **38**, pp. 223–294 164, 165, 167
34. J. I. Gersten, A. Nitzan, Photophysics and photochemistry near surfaces and small particles, Surf. Sci. **158**, 165–189 (1985) 164, 165, 167
35. M. Osawa, K. Ataka, Electromagnetic mechanism of enhanced infrared absorption of molecules adsorbed on metal island films, Surf. Sci. Lett. **262**, L118–L122 (1992) 164, 170
36. B. N. J. Persson, R. Ryberg, Vibrational interaction between molecules adsorbed on a metal surface: the dipole–dipole interactions, Phys. Rev. B **24**, 6954–6970 (1981) 164, 171
37. B. N. J. Persson, A. Liebsch, Collective vibrational models of isotope mixture of CO on Cu(111) and Cu(001), Surf. Sci. **110**, 356–368 (1981) 164, 171
38. P. Dumas, R. G. Tobin, P. Richards, Study of adsorption states and interactions of CO on evaporated noble metal surfaces by infrared absorption spectroscopy. 1. Silver, Surf. Sci. **171**, 555–578 (1986) 164, 171
39. Y. Nishikawa, K. Fujiwara, T. Shima, Quantitative analysis of nanogram samples with Fourier transform infrared transmission surface electromagnetic wave spectroscopy, Appl. Spectrosc. **44**, 691–694 (1990) 164
40. S. A. Johnson, N.-H. Pham, V. J. Novick, V. A. Maroni, Application of surface-enhanced infrared absorption spectroscopy as a sensor for volatile organic compounds, Appl. Spectrosc. **51**, 1423–1426 (1997) 164

41. K. Ito, K. Hayashi, Y. Hamanaka, M. Yamamoto, T. Araki, K. Iriyama, Infrared and Raman scattering spectroscopic study on the structures of Langmuir–Blodgett monolayers contacting a merocyanine dye, Langmuir **8**, 140–147 (1992) 165
42. M. Osawa, N. Matsuda, K. Yoshii, I. Uchida, Charge transfer resonance Raman process in surface-enhanced Raman scattering from p-aminothiophenol adsorbed on silver: Herzberg-Teller contribution, J. Phys. Chem. **98**, 12702–12707 (1994) 165, 182
43. C. Kuhne, G. Steiner, W. B. Fischer, R. Salze, Surface-enhanced FTIR spectroscopy on membranes, Fresenius J. Anal. Chem. **360**, 750–754 (1998) 165, 167
44. R. Aroca, R. Bujalski, Surface-enhanced vibrational spectra of thymine, Vib. Spectrosc. **19**, 11–12 (1999) 165, 182
45. G. T. Merklin, L.-T. He, P. R. Griffiths, Surface-enhanced infrared absorption spectrometry of p-nitorothiophenol and its disulfide, Appl. Spectrosc. **53**, 1448–1453 (1999) 165
46. R. Kellner, B. Mizaikoff, M. Jakusch, H. D. Wanzenböck, N. Weissenbacher, Surface-enhanced vibrational spectroscopy: A new tool in chemical IR sensing?, Appl. Spectrosc. **51**, 495–503 (1997) 165
47. H. D. Wanzenböck, B. Mizaikoff, N. Weissenbacher, R. Kellner, Multiple internal reflection in surface enhanced infrared absorption spectroscopy (SEIRA) and its significance for various analyte groups, J. Mol. Struct. **410-411**, 535–538 (1997) 165
48. C. W. Brown, Y. Li, J. A. Seelenbinder, P. Pivarnik, A. G. Rand, S. V. Letcher, O. J. Gregory, and M. J. Platek, Immunoassays based on surface-enhanced infrared absorption spectroscopy, Anal. Chem. **70**, 2991–2996 (1998) 165
49. Y. Zhu, H. Uchida, M. Watanabe, Oxidation of carbon monoxide at a platinum film electrodes studied by Fourier transform infrared spectroscopy with attenuated total reflection technique, Langmuir **15**, 8757–8764 (1999) 165, 171, 174
50. M. Watanabe, Y. Zhu, H. Uchida, Oxidation of CO on a Pt–Fe alloy electrode studied by surface-enhanced infrared reflection-absorption spectroscopy, J. Phys. Chem. **104**, 1762–1768 (2000) 165, 171, 174
51. S. Sato, K. Kamada, M. Osawa, Surface-enhanced IR absorption (SEIRA) on small Pt particles deposited on an island Au film, Chem. Lett., 15–16 (1999) 165
52. Y. Nishikawa, K. Fujiwara, M. Osawa, K. Takamura, Trace analysis of human skin secretions by surface-enhanced infrared spectroscopy: Detection of Lactate, Anal. Sci. **9**, 811–815 (1993) 165
53. Y. Nishikawa, K. Fujiwara, K. Takamura, Trace analysis of residual additives on the surface of cultivated fruits by surface-enhanced infrared spectroscopy, Bunseki Kagaku **43**, 425–429 (1994) 165
54. M. Osawa, K. Yoshii, K. Ataka, T. Yotsuyanagi, Real-time monitoring of electrochemical dynamics by submillisecond time-resolved surface-enhanced infrared attenuated-total-reflection spectroscopy, Langmuir **10**, 640–642 (1994) 165, 177
55. M. Osawa, K. Yoshii, Y. Hibino, T. Nakano, I. Noda, Two-dimensional infrared correlation analysis of electrochemical reactions, J. Electroanal. Chem. **426**, 11–16 (1997) 165, 177

56. H. Noda, K. Ataka, L.-J. Wan, M. Osawa, Time-resolved surface-enhanced infrared study of molecular adsorption at the electrochemical interface, Surf. Sci. **427–428**, 190-194 (1999) 165, 174, 177, 179
57. K. Ataka, Y. Hara, M. Osawa, A new approach to electrode kinetics and dynamics by potential–modulated Fourier transform infrared spectroscopy, J. Electroanal. Chem. **473**, 34–42 (1999) 165, 174, 179, 180
58. K. Ataka, G. Nishina, W.-B. Cai, S.-G. Sun, M. Osawa, Dynamics of the dissolution of an underpotentially deposited Cu layer on Au(111): A combined time-resolved surface-enhanced infrared and chronocoulometric study, Electrochem. Commun. **2**, 417-421 (2000) 165, 174, 177
59. S. Yoshida, T. Yamaguchi, A. Kimbara, Optical properties of aggregated silver films, J. Opt. Soc. Am. **61**, 62 (1971) 166
60. W. N. Hansen, J. Opt. Soc. Am. **58**, 380 (1968) 167, 168
61. P. N. Sanda, J. E. Demuth, J. C. Tsang, J. M. Warlaumont, Coverage dependence, in *Surface Enhanced Raman Scattering*, R. K. Chang, T. E. Furtak (Eds.) (Plenum, New York 1982), pp. 189–221 167
62. A. Röseler, E.-H. Korte, The optical constant of metallic island films as used for surface enhanced infrared absorption, Thin Solid Films **313-314**, 732–736 (1998) 167
63. G. A. Niklasson, C. G. Granqvist, Optical properties and solar selectivity of coevaporated Co–Al2O3 composite films, J. Appl. Phys. **55**, 3382–3410 (1984) 168
64. B. A. Maxwell–Garnett, Philos. Trans. Royal. Soc. A **203**, 385–420 (1904) 168
65. D. A. G. Bruggemann, Berechnung verschiedener physikalischer Konstanten von heterogenen Substanzen, Ann. Phys. (Leipzig) **24**, 636–664 (1935) 168, 169
66. C. F. Eagen, Nature of the enhanced optical absorption of dye-coated Ag island films, Appl. Opt. **20**, 3035–3042 (1981) 168
67. E. C. Stoner, The demagneitizing factors for ellipsoids, Philos. Mag. **7**, 803–820 (1945) 168
68. T. Yamaguchi, S. Yoshida, A. Kimbara, Continuous ellipsometric determination of optical constants and thickness of a silver film during deposition, Jpn. J. Appl. Phys. **8**, 559–567 (1969) 169
69. M. R. Johnson, W. W. Christy, Optical constants of the noble metals, Phys. Rev. B **6**, 4370 (1972) 169
70. M. Osawa, K. Ataka, K. Yoshii, T. Yotsuyanagi, Surface-enhanced infrared ATR spectroscopy for in situ studies of electrode/electrolyte interfaces, J. Electron Spectrosc. Relat. Phenom. **64/65**, 371–379 (1993) 170, 171, 173
71. M. Osawa, K. Ataka, M. Ikeda, H. Uchihara, R. Nanba, Surface-enhanced infrared absorption spectroscopy: Mechanism and application to trace analysis, Anal. Sci. **7** (Suppl.), 503–506 (1991) 171
72. R. Aroca, B. Price, A New Surface for surface-enhanced infrared spectroscopy: Tin island films, J. Phys. Chem. B **101**, 6537–6540 (1997) 171, 182
73. T. Yoshidome, T. Inoue, S. Kamata, Intensity enhancement of the infrared transmission spectra of p-nitrobenzoic acid by the presence of the Pb films, Chem. Lett. **6**, 533–534 (1997) 171
74. J. P. Devlin, K. Consani, Metal surface spectroscopy, Charge transfer and totally symmetric mode activity, J. Phys. Chem. **85**, 2597–2598 (1981) 171

75. T. Wadayama, T. Sakurai, S. Ichikawa, W. Suëtaka, Charge-transfer enhancement in the infrared absorption of thiocyanate ions adsorbed on a gold electrode in the Kretschmann configuration, Surf. Sci. **198**, L359–L364 (1988) 171
76. T. Wadayama, Y. Momota, A. Hatta, W. Suëtaka, Polarization modulation IR spectroscopic study of electrochemically generated species from TCNQ at a gold electrode in the Kretschmann ATR geometry, J. Electroanal. Chem. **289**, 29–36 (1990) 171
77. R. J. Nichols, IR spectroscopy of molecules at the solid–solution interface, in Adsorption of molecules at metal electrodes, J. Lipkowski, P. N. Ross (Eds.) (VCH, New York 1992) Chap. 7 172, 173, 180
78. K. P. Ishida, P. R. Griffiths, Theoretical and experimental investigation of internal reflection at thin copper films exposed to aqueous solutions, Anal. Chem. **66**, 522-530 (1994) 173
79. K. Ataka, T. Yotsuyanagi, M. Osawa, Potential–dependent reorientation of water molecules at an electrode/electrolyte interface studied by surface-enhanced infrared absorption spectroscopy, J. Phys. Chem. **100**, 10664–10672 (1996) 173, 175
80. S.-G. Sun, W.-B. Cai, L.-J. Wan, M. Osawa, Infrared absorption enhancement for CO adsorbed on Au films in perchloric acid solutions and effects of surface structure studied by cyclic voltammetry, scanning tunneling microscopy, and surface-enhanced IR spectroscopy, J. Phys. Chem. **103**, 2460–2466 (1999) 174
81. K. Ataka, M. Osawa, In situ infrared study of water–sulfate coadsorption on gold(111) in sulfuric acid solution, Langmuir **14**, 951–959 (1998) 174, 175, 177
82. K. Ataka, M. Osawa, In situ infrared study of cytosine adsorption on gold electrodes, J. Electroanal. Chem. **460**, 188–196 (1999) 174, 177
83. I. Taniguchi, S. Yoshimoto, Y. Sunatani, K. Nishiyama, Potential and pH dependencies of adsorbed species of 2,4–pyridinethiol and 2–pyrimidinethiol on Au(111) electrode, Electrochem. **67**, 1197–1199 (1999) 174, 182
84. M. Hoon–Khosla, W. R. Fawcett, A. Chen, J. Lipkowski, B. Pettinger, A SNIFTIR study of the adsorption of pyridine at the Au(111) electrode–solution interface, Electrochim. Acta **45**, 611–621 (1999) 174, 175
85. L. Stolberg, S. Morin, J. Lipkowski, D. E. Irish, Adsorption of pyridine at the Au(111)–solution interface, J. Electroanal. Chem. **307**, 241–262 (1991) 176
86. Z. Q. Feng, T. Sagara, K. Niki, Application of potential-modulated UV–visible reflectance spectroscopy to electron transfer rate measurements for adsorbed species on electrode surfaces, Anal. Chem. **67**, 3564–3570 (1995) 179
87. J.-N. Chazalviel, V. M. Dubin, K. C. Mandel, F. Ozanam, Modulated infrared spectroscopy at the electrochemical interface, Appl. Spectrosc. **64/65**, 1411–1416 (1993) 180
88. C. M. Pharr, P. R. Griffiths, Step–scan FT–IR spectroelectrochemical analysis of surface and solution species in the ferricyanide/ferocyanide redox couple, Anal. Chem. **69**, 4665–4672 (1997) 180
89. L.-J. Wan, H. Noda, Y. Hara, M. Osawa, Effect of solution pH of a 4–mercaptopyridine monolayer self–assembled on Au(111), J. Electroanal. Chem. (2000) (in press) 182

Excitation of Surface Plasmon Polaritons by a Focused Laser Beam

Hiroshi Kano

Department of Electrical and Electronic Engineering
Muroran Institute of Technology
Mizumoto-cho 27-1, Muroran, Hokkaido 050-8585, Japan
`h-kano@elec.muroran-it.ac.jp`

Abstract. In this chapter, the idea of the localized surface-plasmon-polariton (SPP) is described. The excitation method of the localized SPP and some theoretical analyses of its field distributions on a metallic surface for some varieties of light incidence are shown. As an application of the localized SPP, local thickness measurement of ultra-thin films is introduced. Visualization of the refractive index distribution on a metallic surface using the localized SPP is also described.

1 Introduction

The surface plasmon polaritons (SPPs) excited on a 'flat' metallic surface are an interesting and important topic in the area of near-field optical sensing. This is because optical properties such as the refractive index or absorption of a medium in the near field of the metallic surface can be measured with high sensitivityby means of SPPs. For example, an SPP sensor based on the measurement of the effective refractive index of a metallic surface has achieved a density measurement of particular molecules or ions in a gaseous or liquid sample [1,2]. This sensor also accomplished the detection of antigens which reacted with antibodies fixed on the metallic surface [3,4]. Further, this sensor has proven to be useful for measuring the refractive index and thickness of Langmuir–Blodgett–Kuhn (LBK) films deposited onto metals [5].

For the optical configuration of the SPP sensor, the Kretschmann–Raether configuration [6] is utilized in most cases. As shown in Fig. 1, the Kretschmann–Raether configuration consists of a prism made glass with a high refractive index such as BK7, a metallic thin film, and a dielectric medium (the sample to be measured) with a lower refractive index than that of the prism. The reason for using the glass prism is that the dispersion relation (the relationship between angular frequency and propagation constant) of SPPs does not correspond tp the region of propagating light but to the region of evanescent light. To couple the incident light to the SPPs, the light needs to be evanescent. Under conditions of total reflection, the light incident on the interface between the prism and the metal is converted to evanescent light on the metallic surface facing the sample and satisfies this requirement.

S. Kawata (Ed.): Near-Field Optics and Surface Plasmon Polaritons,
Topics Appl. Phys. **81**, pp. 189–206, 2001.

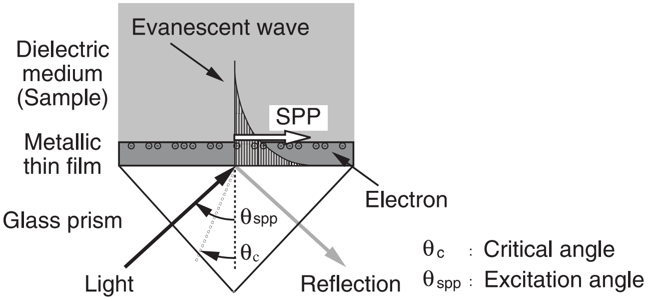

Fig. 1. The Kretschmann–Raether configuration

To measure the refractive index of the sample with the Kretschmann–Raether configuration, the incidence angle for which SPP excitation occurs must be investigated. Because the propagation constant of the SPPs depends strongly on the refractive index in the near field of the metallic surface, the excitation angle is affected by the refractive index of the sample. The excitation angle can be measured by finding the incidence angle which gives the minimum reflection, because SPP excitation absorbs light energy.

This sensing principle has been applied to microscopy as well [7]. In the original microscope using this principle, a plane light wave illuminated the metallic surface of a Kretschmann–Raether configuration through the glass prism, and the reflection from the metallic surface was imaged onto an image detector. When the incident light satisfied the excitation condition of the SPPs at the incident point, the incident light was absorbed by SPP excitation. This light absorption gave the image contrast. This SPP microscope was proven to be capable of imaging the thickness variation of a Langmuir–Blodgett film (cadmium arachidate) deposited on a silver surface. Some other varieties of SPP microscope have also been proposed [8,9].

Though these SPP microscopes achieved high sensitivities in measuring the distribution of the refractive index on a metallic surface, the achieved spatial resolution was not high enough. In typical cases, the resolution was a few tens of micrometers. The limitation of the spatial resolution arose from a property of the SPPs used as the sensing probe. Because the illumination light was a plane wave with a particular angle of incidence, the excited SPPs propagated in a certain direction and sensed over the region in which they had propagated. Consequently, the spatial resolution of the SPP microscope was determined by the propagation length of the excited SPP, which was a few tens of micrometers [10].

In order to overcome this limitation, localization of SPPs [11] can be used. Figure 2 shows this concept of localization. In the conventional method, the excited SPPs propagate in a certain direction as shown in Fig. 2a. In this case, the SPPs produce a uniform electric field on the metallic surface. On the other hand, in the method of localization, the excited SPPs gather at

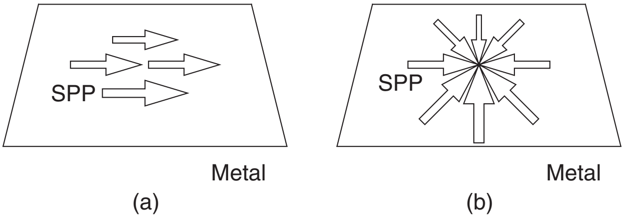

Fig. 2. Concept of localized SPPs. (**a**) Conventional method; (**b**) Method of localization

a certain point on the metallic surface as shown in Fig. 2b. In this case, the SPPs interfere with one another and form a localized electric field. The dimensions of the localized area are on the order of the wavelength.

In this chapter, we give an overview of the method of exciting localized SPPs and their properties [11]. Applications of localized SPPs [12,13] are also described.

2 Theory of Localized SPPs

Figure 3 shows optical arrangement for SPP excitation. The arrangement is based on the Kretschmann–Raether configuration and consists of a glass substrate, a metallic thin film, and a dielectric medium (the sample). The difference from the ordinary use of this configuration is that a coupling prism, which is normally attached to the dielectric substrate, is not used. An objective lens with a high numerical aperture (NA > 1) and immersion oil play the same role in the present arrangement. The illumination light is focused by the objective lens at the interface between the substrate and the metallic film. When the focused light contains plane wave components which satisfy the SPP excitation condition [10], SPPs are excited on the metal surface.

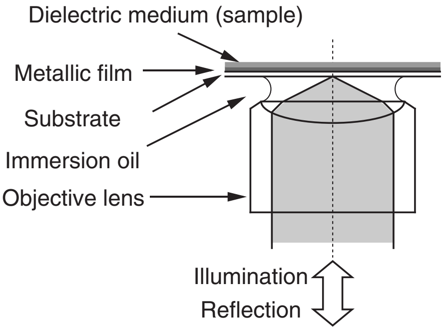

Fig. 3. Optical arrangement to excite localized SPPs

To explain the detailed function of this optical arrangement, the simplest case of SPP excitation will be assumed, a cover slip for an optical microscope as a dielectric substrate, a silver film with a thickness of 50 nm as the metal part, and a vacuum as the sample. Linearly polarized light with a wavelength of 632.8 nm and a numerical aperture of NA = 1.4 are also assumed. Under these assumptions, the excitation condition with respect to the incidence angle of the light is satisfied on a at the pupil plane of the objective lens. Thus, p-polarized components of the illumination light which pass through this ring can excite SPPs on the silver surface facing to vacuum. The excited SPPs travel along the surface in many directions, according to the position where the excitation light passes through the pupil plane. These SPPs interfere with one another and form a localized electric field around the geometrical focus of the objective lens.

To take a close look at the electric-field distribution, the field produced under this condition will be calculated. First, the incident field is given at the entrance pupil. The coordinates of the pupil plane are shown in Fig. 4a. When linearly polarized light illuminates the pupil plane of the objective lens, the electric-field components at the pupil plane can be expressed as

$$\begin{aligned} E_{\mathrm{p}}(\varrho,\varphi) &= E_{\mathrm{i}}\cos\varphi \quad (0 \le \varrho \le 1.4)\,, \\ E_{\mathrm{s}}(\varrho,\varphi) &= E_{\mathrm{i}}\sin\varphi \quad (0 \le \varrho \le 1.4)\,, \\ E_{\mathrm{p}}(\varrho,\varphi), \quad E_{\mathrm{s}}(\varrho,\varphi) &= 0 \qquad\qquad (\mathit{otherwise})\,, \end{aligned} \tag{1}$$

where E_{i} represents the incident amplitude. In this equation, ϱ and φ represent the radial and the azimuthal coordinates, respectively, at the pupil plane, and the ϱ axis is normalized by th wavenumber of the incident light in vacuum. The light passing any particular position (ϱ, φ) of the pupil plane is converted to a corresponding plane wave by the objective lens and illuminates the Kretschmann–Raether configuration. Here, E_{p} and E_{s} correspond to illumination of the interface by p-polarized and s-polarized light, respectively.

In the Kretschmann–Raether configuration, multiple reflections arise from each plane wave. To consider this effect, the amplitude transmission coeffi-

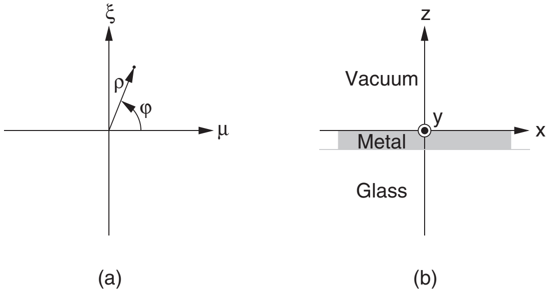

Fig. 4. Coordinates used in the calculation

cient of a three-layered system is introduced and is given by

$$T_m(\varrho) = \frac{t_{01}^m(\varrho) r_{12}^m(\varrho) \, \exp\left[\mathrm{i}k_{1z}(\varrho) d_1\right]}{1 - t_{10}^m(\varrho) r_{12}^m(\varrho) \, \exp\left[\mathrm{i}k_{1z}(\varrho) d_1\right]} \, , \qquad m = \mathrm{p}, \mathrm{s} \, , \tag{2}$$

where t_{ab}^m and r_{ab}^m are the Fresnel reflection and transmission coefficients at an interface beetween two materials a and b for light that is incident from material a; they depend on the relative permittivities of the materials on both sides. In this equation, k_{1z} denotes the z (normal to the interfaces) component of the wave vector in the silver film, and d_1 denotes the thickness of the silver film.

From (1) and (2), the amplitude components produced by light passing the location (ϱ, φ) of the pupil plane are obtainable. Thus, the functions E_ϱ^{SPP}, E_φ^{SPP} and E_z^{SPP} are introduced to represent the components which oscillate in the radial (ϱ), azimuthal (φ), and z directions in the sample. With the coordinates shown in Fig. 4b, these functions can be expressed as

$$\begin{aligned}
&E_\varrho^{\mathrm{SPP}}(x, y, z, \varrho, \varphi) = \\
&\quad \exp\left\{\mathrm{i}\left[k_{2x}(\varrho, \varphi)x + k_{2y}(\varrho, \varphi)y + k_{2z}(\varrho)z\right]\right\} \times \frac{k_{2xy}(\varrho)}{k_2} E_{\mathrm{p}}(\varrho, \varphi) T_{\mathrm{p}}(\varrho) \, , \\
&E_\varphi^{\mathrm{SPP}}(x, y, z, \varrho, \varphi) = \\
&\quad \exp\left\{\mathrm{i}\left[k_{2x}(\varrho, \varphi)x + k_{2y}(\varrho, \varphi)y + k_{2z}(\varrho)z\right]\right\} \times E_{\mathrm{s}}(\varrho, \varphi) T_{\mathrm{s}}(\varrho) \, , \\
&E_z^{\mathrm{SPP}}(x, y, z, \varrho, \varphi) = \\
&\quad \exp\left\{\mathrm{i}\left[k_{2x}(\varrho, \varphi)x + k_{2y}(\varrho, \varphi)y + k_{2z}(\varrho)z\right]\right\} \times \frac{k_{2z}(\varrho)}{k_2} E_{\mathrm{p}}(\varrho, \varphi) T_{\mathrm{p}}(\varrho) \, ,
\end{aligned} \tag{3}$$

where

$$\begin{aligned}
k_2 &= \frac{\omega}{c} \left(\varepsilon_2\right)^{1/2} \, , \\
k_{2x}(\varrho, \varphi) &= k_2 \varrho \cos\varphi \, , \\
k_{2y}(\varrho, \varphi) &= k_2 \varrho \sin\varphi \, , \\
k_{2xy}(\varrho) &= k_2 \varrho \, , \\
k_{2z}(\varrho) &= k_2 \left(1 - \varrho^2\right)^{1/2} \, .
\end{aligned} \tag{4}$$

The Componts in terms of the Cartesian coordinate system, can be expressed as

$$\begin{aligned}
E_x^{\mathrm{SPP}}(x, y, z, \varrho, \varphi) &= E_\varrho^{\mathrm{SPP}}(x, y, z, \varrho, \varphi) \cos\varphi - E_\varphi^{\mathrm{SPP}}(x, y, z, \varrho, \varphi) \sin\varphi \, , \\
E_y^{\mathrm{SPP}}(x, y, z, \varrho, \varphi) &= E_\varrho^{\mathrm{SPP}}(x, y, z, \varrho, \varphi) \sin\varphi + E_\varphi^{\mathrm{SPP}}(x, y, z, \varrho, \varphi) \cos\varphi \, .
\end{aligned} \tag{5}$$

Finally, the intensity I_{spp} of the electric field in the sample is obtained by integrating the amplitude produced by each plane wave with respect to the oscillation direction; it is given by

$$I^{\mathrm{SPP}}(x, y, z) = \left| \int E_x^{\mathrm{SPP}}(x, y, z, \varrho, \varphi) \, \varrho \, \mathrm{d}\varrho \, \mathrm{d} \; varphi \right|^2$$

$$+\left|\int E_y^{\mathrm{SPP}}(x,y,z,\varrho,\varphi)\ \varrho\ \mathrm{d}\varrho\ \mathrm{d}\varphi\right|^2$$
$$+\left|\int E_z^{\mathrm{SPP}}(x,y,z,\varrho,\varphi)\ \varrho\ \mathrm{d}\varrho\ \mathrm{d}\varphi\right|^2 . \tag{6}$$

In carrying out this calculation, the values of relative permittivity shown in Table 1 were used.

Table 1. Relative permittivities used in the calculation

Material	Relative permittivity	
	($\lambda = 488\,\mathrm{nm}$)	($\lambda = 632.8\,\mathrm{nm}$)
Glass (BK7)	$(1.522)^2$	$(1.515)^2$
Silver	$-7.901 + 0.7361\mathrm{i}$	$-15.87 + 1.073\mathrm{i}$
Vacuum/Air	$(1.000)^2$	$(1.000)^2$
$\mathrm{S_iO}_x$	$(1.460)^2$	$(1.460)^2$
PMMA	$(1.495)^2$	$(1.485)^2$

Figure 5 shows the calculated intensity distribution of the electric field as a sectional view ($1\,\mu\mathrm{m} \times 1\,\mu\mathrm{m} \times 1\,\mu\mathrm{m}$). The intensity is normalized by the sum of the incident-light intensities at the pupil plane. In this figure, the xy plane at $z = 0$ corresponds to the metal surface. The x axis denotes the direction of polarization of the incident light. One sees an electric field of SPPs around the geometric focus (the origin of this figure) of the objective lens. The field consists of one main peak and some side lobes. Taking the counterpart of this

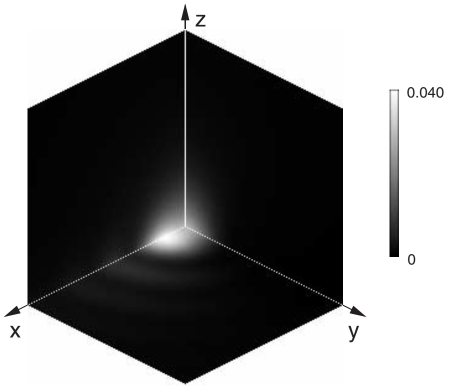

Fig. 5. Calculated electric-field intensity produced by localized SPPs, shown as a sectional view. The calculated region occupies $1\,\mu\mathrm{m}$ in the x, y and z directions. The incident light is polarized in the x direction

main peak (in the region $x < 0$) into account, these main peaks are spread over a region of size 0.6µm × 0.4µm, which is almost the same as the size of the diffraction-limited spot at this wavelength. One can see that the electric field is also confined to the near field of the metallic surface because the electric field accompanying an SPP has an evanescent-decaying nature in the direction normal to the surface. This is an electric field produced by localized SPPs. This calculated result reveals that a microscope utilizing SPPs excited by this method has a possibility of probing a 0.6µm × 0.4µm region in the near field of a metallic surface.

As mentioned above, incident light which passes through a ring of a particular size at the pupil plane can excite SPPs. This means that such light mainly contributes to the formation of the field, while the other light does not. To observe this effect, annular pupil illumination was investigated.

For this annular pupil illumination, linearly polarized light in the region $1.03 < \varrho < 1.04$ was assumed. Figure 6 presents the result, which shows a peak at a higher intensity. This means that one can expect further field-enhancement from annular illumination. This is because the efficiency of SPP excitation is higher than for circular pupil illumination, in which most of the incident light is just reflected. The profile of the electric field exhibits a good similarity to that in Fig. 5. This behavior can be easily understood by evaluating (2), which describes the contribution of the incident light to the formation of the electric-field as a function of ϱ. The result shows that p-polarized light which satisfies the dispersion-matching dominantly condition contributes to the field formation. Thus, a restriction at the pupil plane to annular illumination does not make a great difference to the result with respect to the profile of the field distribution.

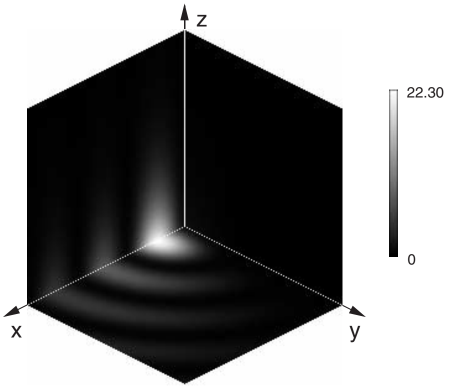

Fig. 6. Calculated electric-field intensity for linearly polarized light on a silver surface. A Kretschmann–Raether configuration and annular pupil illumination were assumed in the calculation

To appreciate further the nature of SPP excitation, the electric-field-intensity distribution for the same model (circular pupil illumination) but without the metallic film was also calculated (Fig. 7). In this image, two peaks are found in the center again. It is noteworthy that the SPPs enhance the electric-field strength by 7.5 times, from a comparison of the maximum intensities in Figs. 6 and 7.

Other types of incident polarization at the pupil plane were also examined. Figures 8a–c correspond to a radial polarization [14,15], an radial polarization [14,15], and a linear polarization with the phase of the incident light delayed by π in the region $x < 0$, respectively.

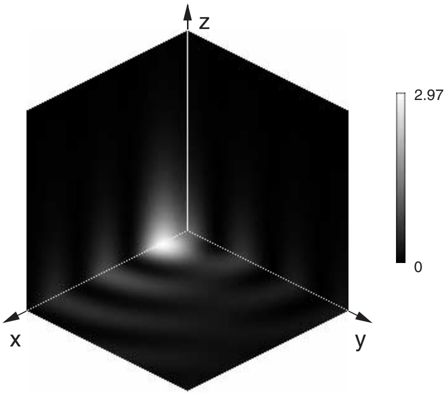

Fig. 7. Calculated electric-field intensity for linearly-polarized light on a glass surface. A glass–vacuum configuration and annular illumination were assumed in the calculation

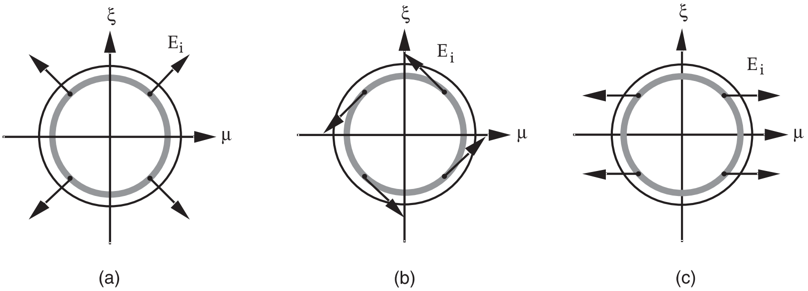

Fig. 8. Incident polarization at the pupil plane of the objective lens: (**a**) radial polarization, (**b**) azimuthal polarization, and (**c**) linear polarization but with the phase in the region $\mu < 0$ delayed by π

Figure 9a–c presents the corresponding electric-field distributions on the metal surface, with Fig. 9a showing a single peak on the optical axis. In this case, the electric-field component along the z direction interferes and maximizes its amplitude along the optical axis. Here, the maximum intensity is the highest among the cases investigated, because the whole of the incident light satisfies the SPP excitation condition. The electric field is localized in a $0.3\mu\mathrm{m} \times 0.3\mu\mathrm{m}$ area. In Fig. 9b, a weak peak is found because the light with the radial polarization illuminates the metal surface as s-polarized light and does not excite the SPPs. In Fig. 9c, a peak on the optical axis and sidelobes besides the central peak appear. In this case, the z component interferes and has a maximum on the optical axis. The peak intensity is almost half as strong as the peak intensity obtained with the radial polarization because half of the incident light illuminates the metal surface as p-polarized light.

The Fourier spectrum of the reflection light was also calculated. In this calculation, the condition expressed in (1) was assumed again for the incident light. In this case the reflectance of the Kretschmann–Raether configuration for a plane wave is considered instead of the transmittance; the reflectance is given by [10]

$$R_m(\varrho) = \frac{r_{01}^m(\varrho) + r_{12}^m(\varrho)\ \exp\left[\mathrm{i}2k_{1z}(\varrho)d_1\right]}{1 + r_{01}^m(\varrho) r_{12}^m(\varrho)\ \exp\left[\mathrm{i}2k_{1z}(\varrho)d_1\right]}\,, \qquad m = \mathrm{p}, \mathrm{s}\,. \tag{7}$$

The reflected plane wave is converged at $(\varrho, \varphi + \pi)$ of the pupil plane. Consequently, the light intensity at the pupil plane is obtained by

$$I(\varrho, \varphi) = \left|E_\mathrm{p}(\varrho, \varphi - \pi) R_\mathrm{p}(\varrho)\right|^2 + \left|E_\mathrm{s}(\varrho, \varphi - \pi) R_\mathrm{s}(\varrho)\right|^2\,. \tag{8}$$

Figure 10 shows a calculated Fourier spectrum of the reflected light which is observable at the exit pupil plane of the objective lens. One can see a pair

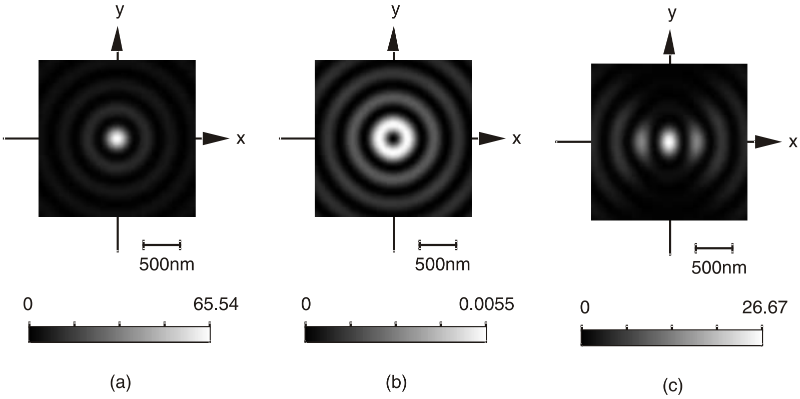

Fig. 9. Calculated results for the electric-field intensity for various types of incident polarization: (**a**) radial polarization, (**b**) azimuthal polarization, and (**c**) linear polarization but with the phase in the region $\mu < 0$ delayed by π. The Kretschmann–Raether configuration and annular illumination were assumed in the calculations

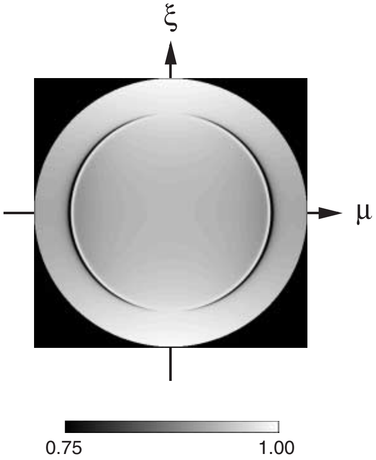

Fig. 10. Calculated Fourier spectrum at the pupil plane of the objective lens for linearly polarized incident light. The incident light is polarized in the μ direction

of dark arcs, which indicates absorption of the light energy by the th SPP excitation. This ring appears at $\varrho = k_{\mathrm{SPP}}$, which is given by

$$k_{\mathrm{SPP}} = \frac{\omega}{c}\sqrt{\frac{\varepsilon_{\mathrm{m}} n_{\mathrm{s}}^2}{\varepsilon_{\mathrm{m}} + n_{\mathrm{s}}^2}}\,, \tag{9}$$

where $\varrho = k_{\mathrm{SPP}}$, represents the propagation constant for SPPs, ε_{m} is the relative permittivity of the metal, and n_{s} is the refractive index of the sample. This equation shows a strong dependence of the curvature of the arcs on the refractive index. Thus, by finding the curvature, the local refractive index over the region of the SPP field distribution is obtainable.

3 Observation of Localized SPPs

As shown in the previous section, SPPs can be localized around the focal point of the incident light. In this section, an experiment which confirmed this localization is described.

First, a Kretschmann–Raether configuration was fabricated on cover slips, of the type used in normal microscopes. Silver was chosen as the material for the metallic film. By a vacuum evaporation technique, the cover slips were coated with silver so that the final thickness of metal was 50 nm. These substrates were examined for SPP excitation by measuring the relationship between reflectance and incidence angle with a conventional SPP sensor [5]. The substrates were then used for the following SPP experiment.

To confirm the existence of localized SPPs, a microscatterer was introduced onto the silver surface and scanned over the region of the focused spot of the beam. Figure 11 shows the optical setup of this experiment. An Ar^+ laser with a wavelength of 488 nm was used as the primary light source. The

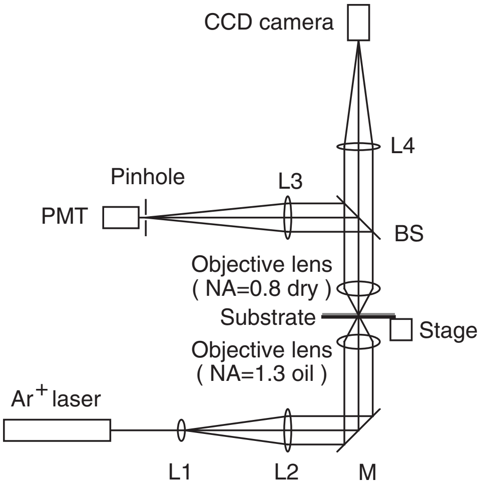

Fig. 11. Experimental setup used to confirm the existence of localized SPPs

laser beam was focused on the silver surface with an oil immersion objective lens (NA = 1.3). Latex beads with a size of 1.48 μm were used as the microscatterer. The density of the beads was 1 bead per $100\mu\mathrm{m}^2$. The whole substrate was scanned with a motorized stage in the lateral directions, instead of the scatterer being scanned over the focus region. To measure the scattered light, another objective lens (NA = 0.8,dry), which collected the scattered light towards a 200 μm pinhole placed in front of a photomultiplier tube, was introduced. The purpose of the pinhole was to reduce the amount of stray light; it hardly provided any spatial resolution in the imaging system. A CCD camera and white-light illumination were also used to observe the silver surface. These devices were used for sample alignment.

Figure 12 shows the experimental result. The size of the image is $3.8\mu\mathrm{m} \times 3.8\mu\mathrm{m}$. In the figure, one can see an image of a latex bead, which confirms the existence of localized SPPs. The bead image is extended in the polarization direction (y direction). However, the two peaks are not clear in this image.

In Fig. 13, an image from an area where the beads were more concentrated is also shown. Many well-separated beads are visible. This result again supports the existence of localized SPPs.

4 Thickness Measurement of LBK Films with Localized SPPs

As shown in the calculations above, a characteristic pattern appears in the Fourier spectrum of the reflected light. From this characteristic pattern, one can extract information concerning the effective refractive index of the metal surface. One of the most important applications of this measuring technique

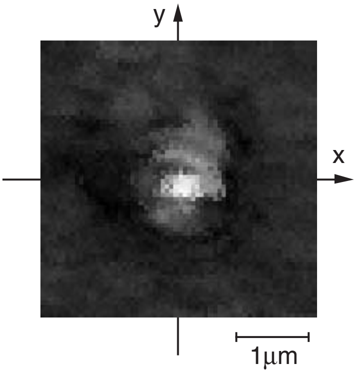

Fig. 12. Image obtained when a microscatter was scanned around the beam spot. The incident light is polarized in the y direction. The silver surface with a single bead is observed

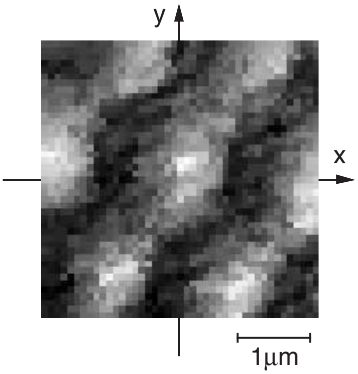

Fig. 13. Image obtained when a microscatter was scanned around the beam spot. The incident light is polarized in the y direction. The silver surface with many beads is observed

is local thickness determination of LBK films. In this section, thickness measurements of LBK films [12] are described.

For this experiment, polymethylmethacrylate (PMMA) films were prepared by using the Langmuir–Blodgett–Kuhn deposition technique. The films were multilayer assemblies of 4, 8, and 12 monolayers. These films were deposited onto substrates that consisted of a glass cover slip, a thin silver film, and an SiO_x coating. The thin silver film was prepared by vacuum evaporation again. The thickness of the silver film was 49 nm. The SiO_x layer, with a thickness of 18.3 nm, was evaporated onto the thin silver film. The purpose of the SiO_x layer was to protect the silver from chemical contaminations while the LBK films were deposited. The SiO_x layer was precoated so as to have a hydrophobic surface property, with HMDS (hexamethyldisilazane).

These samples were characterized by a conventional method [5] in which, the reflectance as a function of incidence angle was measured. The results are shown in Figure 14. These measurements were carried out by using a He–Ne laser with a wavelength of 632.8 nm. The thicknesses of the films were determined by fitting the data sets with theoretical curves. The fitting parameters used are shown in Table 1. From these measurements, the thicknesses of the films were estimated as 3.4 nm, 7.2 nm, and 11.2 nm.

Figure 15 shows the optical setup for the thickness measurement using localized SPPs. An Ar^+ laser operating at a wavelength of 488 nm was used as the light source. The laser beam was expanded by lenses in order to illuminate the pupil plane of the objective lens uniformly. An oil immersion (oil: Zeiss Immersionsoel 518C), infinity-corrected objective lens with NA = 1.3 was used to focus the light onto the metal surface. The reflected Fourier spectrum at the pupil plane was observed through a beam splitter and an imaging lens. The Fourier spectrum was transferred to a personal computer by using a CCD camera and a frame grabber.

Figure 16 shows the experimental results. Figures 16 a–d show the Fourier spectra for the samples with no, 4, 8, and 12 PMMA-layers, respectively. In the images, one can identify dark arcs as seen in the calculated results. In addition, rings fitted to the arcs are indicated. In each of the images, the larger ring corresponds to $\varrho = 1.3$ because the numerical aperture of the objective lens is 1.3. The smaller ring corresponds to the value of ϱ for excitation of SPPs. By comparing the ring radii, the values of ϱ for excitation of SPPs were found to be 1.163, 1.187, 1.216, and 1.251 for the sample with no LBK film and for the 4, 8, and 12 monolayer assemblies, respectively. The film thicknesses were derived from the value of ϱ for excitation by using the parameters shown in Table 1. Thicknesses of 3.5 nm, 7.3 nm and 11.5 nm for the 4, 8, and 12

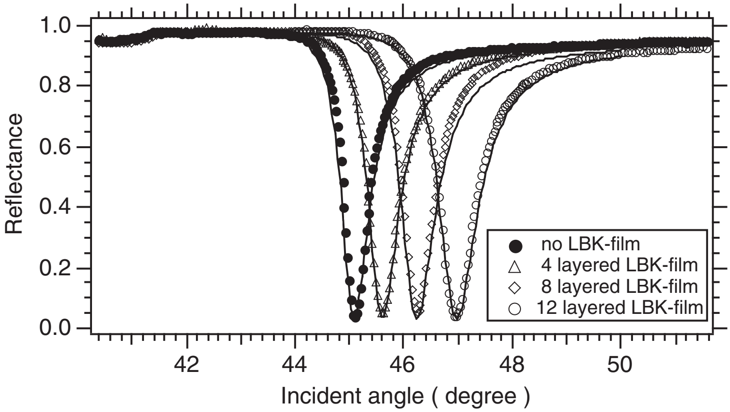

Fig. 14. Measured reflectance of the samples prepared for thickness measurement, as a function of incidence angle; p-polarized light with $\lambda = 632.8$ nm was used in the measurement. The experimental data sets were fitted by theoretical curves

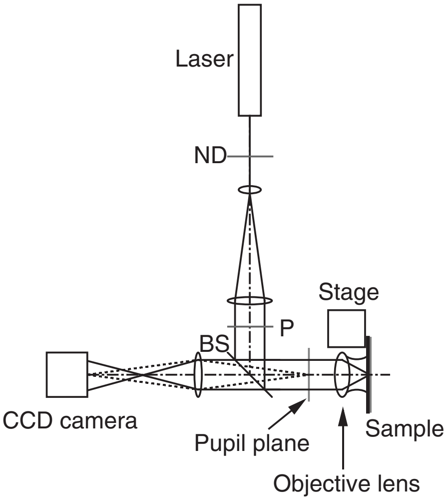

Fig. 15. Experimental setup for thickness measurement of LBK films using localized SPPs. ND, P, and BS represent a neutral-density filter, polarizer, and beam splitter, respectively

monolayer assemblies were found. These results coincide well with the values obtained by the conventional method. Differences on the order of a fraction of a nanometer remain. This is probably because of differences in the sample spots observed. These experiments, however, confirm the nanometer-order resolution in thickness determination.

Reflection Fourier spectra were also observed with circularly polarized light. In this case, complete dark rings were observed. The measured thicknesses were the same as those measured with linearly polarized light.

5 Microscopy with Localized SPPs

In this section, the two-dimensional observation of the refractive-index distribution on a metallic surface with localized SPPs is described [13].

For this experiment a scanning SPP microscope was developed which was based on the optical setup shown in Fig. 10. The differences were in the wavelength of the laser ($\lambda = 632.8\,\mathrm{nm}$) and the numerical aperture of the objective lens (NA = 1.4). The sample stage was also different from that in the earlier setup. For sample scanning, a three-dimensional piezo stage with a feedback system (Melles Griot, Nano-block system) was used. With this stage, the sample was scanned in two-dimensions and the focus position was controlled.

For the experiment, microparticles with diameters of $4.0\,\mu\mathrm{m}$ and $1.5\,\mu\mathrm{m}$ were used as samples. The material of these particles was silica. These particles were dispersed on silver films, each of which was evaporated on a cover

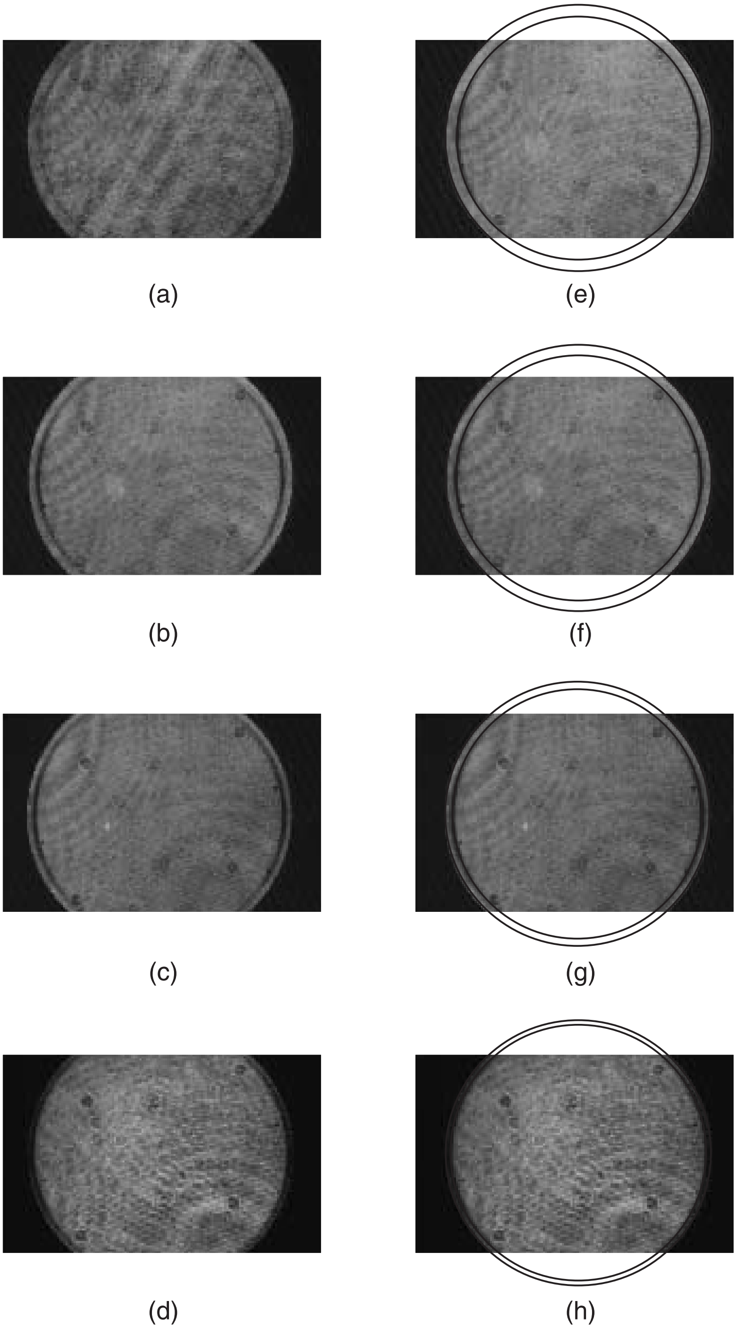

Fig. 16. Observed Fourier spectra: (**a**)–(**d**) for raw data and (**e**)–(**h**) for data with fitted rings: (**a**) and (**e**) no LBK-film; (**b**) and (**f**) 4; (**c**) and (**g**) 8; and (**d**) and (**h**) 12 monolayers, respectively, of PMMA

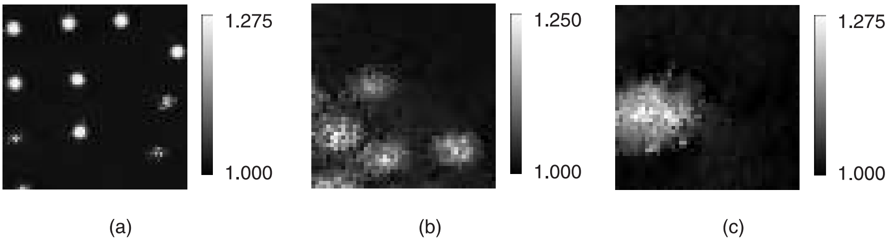

Fig. 17. Images obtained from (**a**) a sample with scattered particles (diameter 4.0 µm) in a 15µm × 15µm area, (**b**) a sample with particles (diameter 1.5 µm) in a 5µm × 5µm area, (**c**) a sample with a single particle (diameter 1.5 µm) in a 2.5µm × 2.5µm area

slip of the kind used for optical microscopes. The thickness of each silver film was 50 nm.

With these samples, two-dimensional Fourier spectra were obtained with a CCD camera. In the Fourier spectra, again, the characteristic arcs were found. With a simplex algorithm, the central position and the radius of the arcs were estimated by evaluating the cross section between the ring and the spectrum. The estimated radius corresponds to the propagation constant of the SPPs. The propagation constant was transformed to a local effective refractive index by using (9) in reverse. The whole set of Fourier spectra obtained was processed according to this procedure and an image was produced.

Figure 17 shows the images obtained for particles with a diameter of 4.0 µm in a 15µm × 15µm area, particles with a diameter of 1.5 µm in a 5µm × 5µm area, and a single particle with a diameter of 1.5 µm in a 2.5µm × 2.5µm area. In Fig. 17 a one can clearly see the particles as bright spots. The size of the spots seen in the figure is approximately 1.5 µm not 4.0 µm, which is the diameter of the particles. This is because the SPPs probe only the near field of the metallic surface and do not probe the whole of the particle. In Fig. 17 b, one can see four individual particles close to one another. This image proves that the present microscope can resolve 1.5 µm particles. Each particle occupies an area of about 1.5µm × 1.0µm. Again, this is because the probe is localized in the near field of the metal surface. This image suggests that the particles have been scanned by a distorted probe. As shown in Fig. 17 c, a single particle can be visualized as well. The direction of the distortion shows good coincidence with the direction of the polarization. These results are supported by the theoretical calculations.

In the theoretical calculations, it was found that the field distribution of the localized SPPs excited by linearly polarized light of $\lambda = 632.8\,\text{nm}$ was spread over a region of size 0.6µm × 0.4µm. However, the spatial resolution for the microscope did not reach this value. At this moment, a 1.5 µm particle is the smallest particle which gives a proper image. A further increase of the spatial resolution is expected.

The SPP microscope described here is expected to contribute particularly to the study of interfaces between metals and thin films. For example, higher resolution will provide a good chance to determine the local morphology of Langmuir–Blodgett–Kuhn films.

Instead of using localized SPPs, some researchers are currently pursuing research to increase the spatial resolution of SPP microscopes by using local-mode plasmons as a sensing probe [16,17,18]. When one tries to increase the spatial resolution by using a small particle such as gold particle with a radius of 10 nm, the electric field produced by the resonance between the incident light and electron oscillation within the metallic particle is scattered or diffracted by the fine structure of the sample and affects the original resonance. As a result of this nonlinear effect, the theory of image formation becomes complicated. This prevents us from evaluating the local refractive index, though this method can provide higher spatial resolution than the method described here.

6 Further Development of Localized SPPs

One of the most interesting possibilities which has not yet been reported on is the application of the field enhancement by localized SPPs. Unlike the case of enhancement by propagating SPPs, one can expect also a focusing effect of the incident light energy. With this enhancement, the incident light can interact more efficiently with materials. Nonlinear optics, such as multiphoton absorption phenomena, is one of the fields to which localized SPPs could be suitably applied [19]. The polarization of incident light will surely play an important role in achieving the maximum enhancement as shown in the theoretical calculations.

References

1. C. Nylander, B. Liedberg, T. Lind, Sens. Actuators **3**, 79 (1982/83) 189
2. K. Matsubara, S. Kawata, S. Minami, Appl. Spectrosc. **42**, 1375 (1988) 189
3. B. Liedberg, C. Nylander, I. Lundström, Sens. Actuators **4**, 299 (1983) 189
4. S. Löfås, B. Johnsson, J. Chem. Soc. Chem. Commun. **21**, 1526 (1990) 189
5. W. Knoll, Guided Wave Optics for the Characterization of Polymeric Thin Films and Interfaces, in *Handbook of Optical Properties*, Vol II, *Optics of Small Particles Interfaces, and Surfaces*, R. E. Hummel, P. Wissmann (Eds.) (CRC, Boca Raton 1997) 189, 198, 201
6. E. Kretschmann, H. Raether, Z. Naturf. **23**, 2135 (1968) 189
7. B. Rothenhäusler, W. Knoll, Nature **332**, 615 (1988) 190
8. T. Okamoto, I. Yamaguchi, Opt. Commun. **93**, 265 (1992) 190
9. H. Knobloch, G. von Szada–Borryszkowski, S. Woigk, A. Helms, L. Brehmer, Appl. Phys. Lett. **69**, 2336 (1996) 190
10. H. Raether, *Surface Plasmons on Smooth and Rough Surfaces and on Gratings*, Springer Tracts Mod. Phys. **111** (Springer, Berlin, Heidelberg 1988) 190, 191, 197

11. H. Kano, S. Mizuguchi, S. Kawata, J. Opt. Soc. Am. B **15**, 1381 (1998) 190, 191
12. H. Kano, W. Knoll, Opt. Commun. **153**, 235 (1998) 191, 200
13. H. Kano, W. Knoll, Opt. Commun. **182**, 11 (2000) 191, 202
14. R. Yamaguchi, T. Nose, S. Sato, Jpn. J. Appl. Phys. **28**, 1730 (1989) 196
15. M. Stalder, M. Schadt, Opt. Lett. **21**, 1948 (1996) 196
16. U. C. Fisher, D. W. Pohl, Phys. Rev. Lett. **62**, 458 (1989) 205
17. Y. Inouye, S. Kawata, J. Microsc. **178**, 14 (1995) 205
18. T. Okamoto, I. Yamaguchi, Jpn. J. Appl. Phys. Lett. **36**, L166 (1997) 205
19. H. Kano, S. Kawata, Opt. Lett. **21**, 1848 (1996) 205

Index